An investigation of air motion and heat transfer in a motored indirect injection diesel engine

Tawfig, Mohammed Elmustafa

Award date:
1991

Awarding institution:
University of Bath

AN INVESTIGATION OF AIR MOTION AND HEAT TRANSFER IN A MOTORED INDIRECT INJECTION DIESEL ENGINE

Submitted by **Mohammed Elmustafa Tawfig** for
the degree of Doctor of Philosophy in the
School of Mechanical Engineering of
the University of Bath 1991

COPYRIGHT

ProQuest LLC
789 East Eisenhower Parkway
P.O. Box 1346
Ann Arbor, MI 48106-1346

ABSTRACT

This thesis presents a computational and experimental investigation of air motion and heat transfer in the swirl chamber of a motored indirect-injection diesel engine.

An experimental study was carried out on an indirect-injection Ford 1.6 litre passenger car engine which has a standard Ricardo Comet MkVb combustion system. Air swirl has been measured by paddle wheel and hot wire anemometry. A fast response resistance thermometer was used to measure the instantaneous gas temperature in the swirl chamber.

A mathematical model was developed to simulate the thermodynamic and fluid dynamic processes in the IDI diesel engine. The model makes use of energy, mass and momentum conservation equations, which are integrated numerically to simulate the engine cycle.

The experimental data was used to verify the accuracy of the model predictions. The agreement between the experimentally measured and computed pressure and gas temperature in the swirl chamber was good. The swirl ratio was overpredicted because no account was taken of the drag caused by the glow plug.

The mathematical model was used to perform a parametric study of the effects of engine geometry and material properties on swirl and heat transfer. In addition the model was used to study the effects of throat area and volume ratio on swirl chamber pumping power and swirl. The results confirm that the swirl ratio is a function only of the geometry of the swirl chamber and throat and is almost completely independent of the engine speed. Insulating the swirl chamber would help both cold starting and ignition.

ACKNOWLEDGEMENTS

The author gratefully acknowledges the valuable help and guidance given by his supervisor, Dr Steve Charlton, throughout the course of this research work

Thanks also to Mr. Peter Prest for his fruitful discussions and help in the setting up of the instrumentations involved in the project.

The assistance of Dr M Tindal of King's College, University of London with the manufacture of hot wire probes in the early stages of the work is greatly appreciated.

The author would also like to thank the following technicians at Bath University who helped to build up the experimental rig; G. Bonwick, E. Brain, L. Dudderidge and M. Tanner.

Table of Contents

List of Tables

List of Figures

The figures are situated at the end of each chapter

Chapter 1

Chapter 2

Chapter 3

Chapter 4

Chapter 5

Chapter 6

Chapter 7

Chapter 8

Notation

Unless otherwise stated in the text, symbols are defined as follows:

Symbols

A	Geometric area
C_p	specific heat at constant pressure
D_{cyl}	cylinder diameter
D_{th}	swirl chamber throat effective diameter
h	specific enthalpy
I	effective momentum of inertia of swirl chamber contents
k	Thermal conductivity
m	mass
R	specific gas constant
R_{sw}	swirl chamber effective radius
R_{th}	swirl chamber throat effective radius
R_1	$=(R_{sw}-R_{th})$
	eccentricity of throat
p	pressure
p_1	total pressure upstream
t	time
T	temperature
T_1	total temperature upstream
U_{th}	velocity of flow through the throat
u	specific internal energy
V	Volume
γ	ratio of specific heat
ρ	density
ω	angular velocity of swirl
ω_e	angular velocity of crank shaft
ω/ω_e	swirl ratio

Subscripts

e	engine
i	flow into a control volume
m	main chamber
o	flow out of a control volume
sw	swirl chamber
th	swirl chamber throat
v	constant volume

CHAPTER 1

INTRODUCTION

1.1 General Background

Passenger car diesel engine sales have for a decade enjoyed a period of uninterrupted growth. In some countries where the price of diesel fuel is about half of that of petrol the diesel car has taken over 25% of the market. Most of today's taxis use diesel engines where gains in economy, reliability and longer overhaul periods, particularly under start-stop conditions are highly favourable compared to the petrol engine.

This introduction of the diesel engine into the passenger car market has demanded high standards in terms of prime cost, speed and torque performance, as well as low exhaust emissions and noise. Compared to the petrol engine, the diesel engine is more efficient due to its high compression ratio and absence of throttling, and has lower running costs because of cheaper fuel. Since air/fuel mixture in the diesel engine is always weak of stoichiometric, it emits less carbon monoxide. However, because of inefficient air utilisation, due to insufficient time for complete mixing and combustion of the fuel, the diesel engine suffers from a limited maximum operating speed and smoky and odorous exhaust. It also suffers from noise and difficult cold starting.

There are two main types of diesel engine combustion system which are suitable for high speed applications : (i) divided-chamber (or indirect injection, IDI) and (ii) open chamber (or direct injection, DI). In divided-chamber engines fuel is sprayed into the prechamber where combustion starts. Burning gases travel through the passageway connecting the prechamber to the main chamber (the volume above the piston) for the combustion process to be completed. In open chamber engines fuel is injected directly

into the combustion chamber which is formed by the volume bounded by the surfaces of the cylinder head and the piston, which takes the form of a cavity or bowl in the piston crown. Both systems are shown in Figure 1.1.

The direct injection diesel engine requires high injection pressures to achieve adequate air/fuel mixing (between 350 - 1000 bars compared to 150 - 350 bars for the IDI engine) and also a specially designed inlet port to generate air swirl. It suffers from high exhaust emissions, high combustion noise and its speed range is restricted compared to the IDI engine. However, according to Monaghan (1981), it has a potential benefit of a 10% gain in fuel economy over the IDI engine . Watson and Kamel (1979), attributed the lower efficiency of the IDI engine with respect to the DI engine to : (i) high thermal losses from the combustion system, due to its large exposed combustion chamber surface area, which dictates the use of high compression ratios, typically 22:1, and an electrical starting aid which is required at ambient temperatures below 25°C (ii) pumping losses because of the flow through the throat (iii) late injection which causes combustion to continue until later in the expansion stroke.

It is therefore useful to develop analytical and experimental techniques that can furnish new insights required for the design of an improved IDI engine. This has stimulated the research described in the present thesis to focus around the development and experimental validation of mathematical models which define the details of the air motion and heat transfer in the IDI engine.

1.2 Indirect Injection Diesel Engine Characteristics

Nearly all current passenger car diesel engines use indirect injection combustion systems because of the economic and technical ease with which they can be made compatible with existing petrol engines. There are two types of IDI system, the prechamber and the swirl chamber. These are illustrated in Figure 1.2. The prechamber system relies on high levels of turbulence to enhance air/fuel mixing. The swirl chamber system, relies

on an ordered air motion to increase mixing and combustion rates. Almost all of the current manufacturers employ the Ricardo Comet system or variants of it, as reported by Watson (1982), which dates back to the 1930s. The swirl chamber system is used more than the prechamber system, partly because of the wealth of accumulated operating experience and its favourable characteristics.

1.2.1 General Performance

A naturally aspirated IDI engine produces typical outputs of 24 kW/litre, compared with 37 kW/litre for a similar petrol engine. This can easily be raised to 33 kW/litre if the diesel engine is turbocharged. It also produces a maximum BMEP of around 7.5 bar, where a petrol engine can easily reach 9 bar.

1.2.2 Exhaust Emissions

With the growing concern about the environment the legislation against passenger car emissions is becoming more severe. Diesel engine exhaust gases contain oxides of nitrogen (NO_x), a small amount of carbon monoxide (CO), unburnt hydrocarbons (HC) particulates and visible smoke.

It is firmly established that NO_x emissions contribute to photochemical smog. According to Heywood (1987), NO_x is formed from the reaction involving nitrogen and oxygen atoms, at the high temperatures attained during and immediately after combustion. In the short time available the reactions do not attain chemical equilibrium. The rate of production of NO_x is highly temperature dependent and most NO_x will be concentrated in the lean area of combustion where there is excess oxygen (O_2). During the rapid expansion, the burnt gases cool leaving NO_x concentrations to freeze out at their high temperature levels, as the decomposition of NO_x is relatively slower than the engine

emissions. Heywood (1987) stated that the second cause is less significant in IDI engines than with DI engines, but he added that other sources such as late fuel injection (secondary injection) can be significant.

Diesel particulates are defined as materials which are collected from a diesel engine exhaust on a filter paper, by diluting the exhaust gases with air at a temperature of < 325 K. They consist principally of carbon particles (soot) with absorbed high molecular weight hydrocarbons. As most of the particulate material is formed as a product of incomplete combustion of fuel hydrocarbons, particulates have the same origins as HC but with the addition of soot. Some particulates are caused by lubricating oil and fuel additives. Soot or black smoke is formed from the carbon in the diesel fuel as a result of incomplete combustion when the fuel-rich mixtures are subjected to high temperature. It increases with increase in mixture richness or temperature.

There is no problem for the passenger car IDI diesel engine to meet the current European and Japanese emissions limits which, according to Stone (1989), are applied only for NO_x and HC. But it has to satisfy the US Federal emissions limits which are the most severe in the world. Europe and Japan are likely to adopt these stringent US standards in the future. According to Lilley (1984), US Federal emissions limits for passenger cars (1985) are : 0.41 g/mile HC, 3.4 CO g/mile, 1.0 g/mile NO_x and 0.2 g/mile particulates.

1.2.3 Controlling Exhaust Emissions

As explained earlier, the formation of NO_x depends strongly on temperature. Thus, in order to reduce NO_x injection timing may be retarded, as this will lead to lower temperatures. At part load exhaust gas recirculation (EGR) may be used, as the inert gases will limit the combustion temperature and limit oxygen availability. According to Wade (1980), at heavy loads the amount of EGR is limited by the small amount of excess air that can be replaced with EGR.

With efficient combustion and good fuel injection equipment, there is no problem for an IDI diesel engine to meet 0.41 g/mile HC levels, but HC usually increases when injection timing is retarded in order to reduce NO_x. Figure 1.4 shows typical NO_x and HC concentration and the effect of retarded timing. According to Scott (1984), to achieve both acceptable NO_x and HC levels, a generally retarded injection has to be planned with local advance in order to avoid high HC levels. This can be achieved easily by using electronic timing control, but it might prove difficult with the limited abilities of existing hydromechanical timing control systems. With engines of more than 2.0 litres capacity, control by timing is not adequate and exhaust gas recirculation (EGR) has to be used.

Particulates can be reduced by injection retard but this will increase HC and fuel consumption. With the effect of EGR, which results in increased particulate emissions, two approaches are suitable for meeting the required levels: by introducing a filter into the exhaust system which traps and burns off the particulates or by improving engine combustion to reduce such emissions at source. Using filters in the exhaust suffers from cost, available space, cold start and efficiency considerations, and in addition exhaust gas temperatures are not sufficiently high in urban driving. Improving engine combustion can be achieved either by using an electronically-controlled system to optimise such parameters as fuel flow, injection timing and EGR ratio, or possibly by combustion chamber insulation, although results using ceramic swirl chambers are mixed.

1.2.4 Noise

The major source of noise in the diesel engine is attributed to the combustion characteristic, see Stone (1989). Figure 1.5 shows the relation between combustion noise and the peak rate of heat release. Noise levels generally increase with rate of pressure rise in the cylinder. IDI engines have lower noise levels than DI engines because combustion starts in the prechamber and does not directly excite the surfaces in the cylinder. In addition combustion in IDI engines is slower due to the transfer between chambers. Turbocharged engines are generally quieter as they have shorter ignition

delay which leads to a 'softer' pressure curve than naturally aspirated engines. Lilley (1984), reported that the European limit for 1985, being tested to EEC procedure, is 80 dB(A) with the Japanese limit at 81 dB(A) and no American legislation. He predicted that the European limit will be reduced to 75-77 dB(A), the Japanese to 78 dB(A) with the Americans following the European lead in the longer term. He also reported that four passenger car diesel engines gave an average drive-by noise level of 79.5 dB(A) compared with an average of 78.7 dB(A) for 16 petrol cars. Scott (1973) reported that the comet IDI engine produced a noise level of 79.5 dB(A) compared with 84.5 dB(A) for a DI version under the same engine conditions.

1.2.5 Advanced Swirl Chambers

The need to develop the IDI engine results from the fact that it faces a challenge for its future application in the passenger car market from future emissions regulations, and its main rivals; the petrol engine and the DI diesel engine. This has prompted some manufacturers to seek alternative techniques which might lead to improvement in the performance of the IDI engine to overcome the above mentioned obstacles. While current fuel economy and emissions could be improved by an optimised control system for EGR and injection timing modulation, alternative ways have to be found to improve the combustion processes in the IDI engine further.

Recently, there has been intensive research, and to some extent application, as reported by Yamaguchi (1986), into the use of ceramic materials in diesel engines to insulate the combustion chamber in order to improve combustion and exhaust emissions. Low heat loss (adiabatic) engines provide two main advantages for diesel engine efficiency. First, is the high exhaust temperature which leads to further improvement when the engine is turbocharged or turbocompounded. Second, is the gain in power at part load from the reduction of the cooling system requirements which also means a more compact

installation. This is unlikely to happen in the case of a petrol engine as it will lead to self-ignition and pre-ignition which would consequently drop the output and cause failure of components.

The use of ceramic materials in the swirl chamber seems attractive provided that the cost of manufacturing the ceramic swirl chamber (lower-half or full chamber) in terms of improving combustion efficiency and exhaust emissions can be justified. Moreover, the ceramic swirl chamber has to be fitted tightly in the cylinder head in order to prevent fuel and air leakage into crevices which might result in increased hydrocarbon levels, as reported by Shephard *et al* (1990).

Another approach would be to develop the Ricardo swirl chamber further. This might be achieved using a flush mounted starting aid (glow plug), instead of the current one which protrudes into the swirl chamber and thus retards the air motion in the swirl chamber. Such a solution may allow an increase in the throat area which would reduce pumping and heat losses and hence improve fuel economy. Tamura *et al* (1989) reported that a modified combustion system which improves fuel economy and exhaust emissions is feasible. This system has design features such as; high compression ratio, swirl chamber of enlarged radius and higher volume ratio for accelerated fuel-air mixture, enlarged jet passage area and refined jet-passage with larger jet passage angle inside the swirl chamber than in the main chamber to attain higher jet penetration into the main chamber. Further research work on this subject has been reported by French and Scott (1985), Furubayashi *et al* (1986), Tanaka *et al* (1986) and Greeves *et al* (1988).

1.3 Engine simulation

During the last decade engine modelling has been developed to a stage where it is now a well established and to some extent reliable technique. This has been triggered by the great demand for more efficient and cleaner engines, which has encouraged most engine manufacturers to invest in this field. The rapid progress in experimental techniques has

helped a great deal in the validation of these models and, ever developing computer technology has allowed more complex models which have led to a better understanding of the physical processes involved. As reported by Tabaczynski (1988), it is important to understand that none of the present models are totally predictive.

Heywood (1988), classified the models into two main types. One class is built around the first law of thermodynamics and time is the only independent variable. The other, more recent class is based on full analysis of the fluid motion where time and up to three spatial dimensions are considered.

1.3.1 Thermodynamic Models

These models are often called zero-dimensional (since geometry is not involved), phenomenological (more details, other than the energy conservation equation, are being added to represent the true phenomenon), and quasi-dimensional (where dimensions are added to the basic thermodynamic approach in order to mimic specific shapes e.g. diesel fuel spray combustion or the spark ignition engine flame). The air flow through the engine is modelled by using one of the following :

quasi-steady method;

filling and emptying method;

wave action models.

(i) Quasi-Steady Method :

In this method the engine manifolds and turbocharger are considered as a series of interconnected components. These components are connected by the air flow passing through them and by the pressure ratios across them. The flow is assumed to behave in the same manner as if it was steady, and the mass of the gas is not allowed to accumulate between the various components (i.e. the components are assumed to have negligible volume). The equations used are all algebraic and the method depends extensively on

experimental data. Winterbone (1986), described the complete engine system in this method as analogous to an electrical circuit with component characteristics, air flow and pressure ratios similar to non-linear resistances, current and potential difference respectively.

This method is rather restricted by the empirical data for a particular engine, but it provides a quick and cheap simulation. In addition, it is often used to calculate the flow into and out of the cylinder through the inlet and exhaust valves. Moreover, some quasi-steady models have been used for simulating turbocharged diesel engines on real-time transient models.

(ii) Filling and Emptying Method :

In this method the engine manifolds and cylinders are represented as separate control volumes. The control volumes are filled and emptied subsequently as mass flows through them. The gas state in each control volume is defined by applying the energy and continuity equations from which the rate of change of temperature, mass and equivalence ratio can then be calculated. Thus, by assuming values of temperature, mass and equivalence ratio for each control volume (initial values) the differential equations may be solved by numerical integration. Pressure is a dependant variable which can then be calculated by applying an equation of state.

This method is used prolifically in industry for engine design and turbocharger matching. It is more predictive than the quasi-steady method and requires less empirical data. However, the accuracy of the method is restricted only to short manifolds and manifolds of more compact shape, reported by Heywood (1987), as shown in Figure 1.6. The method is described in greater detail in Chapter three.

(iii) Wave Action Models :

In the case of engines with long manifolds and where wave effects are important, an error will be introduced if the exhaust manifold is treated as a simple thermodynamic control volume. In the pulse turbocharging system where a pressure wave is present, the instantaneous pressure at each end of the manifold at any instant is different. Hence a knowledge of the variation of the gas state spatially along the manifold will reduce such error. According to Watson and Janota (1982), this error will depend on how long it takes for the pressure wave to travel the length of the manifold. If this time is small the error will be small as in the case of a small pulse turbocharged engine.

To accommodate the phenomenon of wave action in long manifolds in simulation programs, equations for the compressible unsteady flow have to be set and solved. Usually these programs assume one-dimensional behaviour as this will not introduce a significant error since two and three dimensional flows i.e. diffusers with separation and tapered pipes are rarely encountered in engine practice. The equations used to describe the compressible flow in pipes are non-linear hyperbolic partial differential equations, which may be solved by applying mathematical techniques such as the method of characteristics. In simulation programmes wave action models are only applied to long manifolds with the rest of the engine system, such as cylinders often applying the filling and emptying method.

1.3.2 Fluid Dynamics Models

Fluid dynamics or multi-dimensional flow models, in principle, represent with their predictive capabilities the ultimate in engine simulation technique. They emerged in the early 1970s and have progressed since then producing encouraging results with a promise of further improvement with future developments in computer hardware and algorithms. The potential advantage of such models is that they are almost independent of empirical formulae and the prediction of engine cycle processes is achieved solely by solving the governing conservation equations. These models use finite difference and to a lesser

extent finite element techniques to solve partial differential equations for conservation of mass, momentum, energy and chemical species with respect to time and space. Additional equations which describe processes within the flow such as turbulent motion, heat transfer and chemical reactions are also added.

The partial differential equations are applied to discrete cells or control volumes (with a finite number of nodes) which together form a mesh or grid. The mesh which defines engine geometry has the ability to expand and contract, i.e. piston motion, as well as distort to adapt complex geometries like piston cup and swirl chamber as reported by Zellat *et al* (1990). Figure 1.7 shows an example of a swirl chamber three-dimensional mesh. The accuracy of the model increases with the use of finer meshes and reduced time steps. However this will increase computing time and pre-processing cost.

The finite difference technique is then used to substitute divided differences for the derivatives in the partial differential equations by finite difference operators. Thus, transforming the partial differential equations into linear algebraic equations. The linear algebraic equations are solved using iterative methods to obtain values of the unknown variables within each cell. The solution is then advanced in discrete time steps. Currently, turbulence is usually modelled using $\kappa - \varepsilon$ functions. According to Gosman (1989) the accuracy is moderate to poor for predicting turbulence intensity and length scale with the current models. This is expected to improve with alternative turbulence modelling such as large eddy simulation (LES).

Fluid dynamics models have the capability to predict flow dynamics and heat transfer in motored engines. However, engine combustion modelling is yet to be firmly established and detailed validation is seen as a limiting factor. In addition, the few existing models for emissions and particulates have yet to be fully validated. Another drawback is that these models are complex and not easy to develop, requiring some time until they are complete and ready to make a contribution. Also, they are not easy to use, require

substantial CPU time and suffer from the lack of initial or boundary conditions, which is solved sometimes by using data obtained experimentally or by zero-dimensional models. Gosman (1989) suggested that further improvement can be achieved in the future with development of ignition models which include turbulence effects. Combustion models for partially-premixed and diffusion burning also have to be developed along with models for particulates and gaseous emissions. Moreover, extensive validation has to be carried out in order to enhance the usefulness of the technique.

On the other hand phenomenological models can be relatively cheap and easy to develop. They are well established, more directed towards engines and can be extremely useful when linked with experimental work. This makes them more favourable and probably they will stay for some time to come in the engine research and development field.

1.4 Aims and Outline of the Present Work

The objective of this thesis is to present a detailed study of the air motion and heat transfer in the IDI diesel engine based on a motored Ford 1.6 litre IDI diesel engine.

In the present work, the engine has been modelled mathematically using the filling and emptying method with the swirl chamber considered as a control volume connected to the main chamber via an orifice (throat).

The gas motion in the swirl chamber has been predicted assuming a one dimensional quasi-steady, compressible gas flow through the swirl chamber throat. Solid body rotation (forced vortex) was assumed to prevail in the swirl chamber, since the swirling motion of the gas in the swirl chamber was induced by gas flow through the throat. The angular velocity was then calculated by the conservation equation of angular momentum.

Heat transfer between the working fluid of the IDI diesel engine and the swirl chamber walls was predicted by covering the three modes of heat transfer i.e. conduction, con-

vection and radiation. Transient heat conduction was calculated by using a finite difference approach to solve for swirl chamber wall temperature at a number of points through the wall. Heat convection was calculated using a conventional Nu-Re relationship and the calculated local gas velocity. The heat radiation (fired engines) calculation was based on the Stephan-Boltzman law, combined with assumptions for emissivity and radiation temperature for multi-atomic gases.

Experimental measurements were made on a motored Ford 1.6 litre IDI diesel engine fitted with a Ricardo Comet MkVb swirl chamber both with the standard swirl chamber and with different ceramic lower-half swirl chambers.

Air swirl ratio in the swirl chamber was estimated by mounting a small light weight aluminium paddle wheel in the hot plug. The speed of the paddle wheel was counted by employing an optical technique. The experimental work also included design, manufacture and use of hot wire anemometers to measure the velocity and temperature of the gas in the swirl chamber from which swirl could be inferred.

The thesis is arranged as follows. Previous theoretical and experimental studies on the IDI engine are reviewed in Chapter 2. Turbulence and cycle-to-cycle variation phenomena encountered in engines are also discussed with definition of the common techniques used for the calculations. Thermodynamic and mathematical techniques employed for the simulation of the IDI engine are presented in Chapter 3. Chapter 4 presents in detail the theory, design and development of hot wire anemometry as a useful tool for the measurement of air velocity and temperature. The test rig developed, details of instrumentation and the data acquisition system are described in Chapter 5. In addition, the methodology of data reduction along with samples of the results are presented. The experimental results are discussed in Chapter 6 and a comparison is made to assimilate the theoretical and experimental results. In Chapter 7 the model is used to make a

parametric study of the effects of engine geometry and material properties on swirl and heat transfer. Finally, a general discussion of the whole project is made and conclusions are drawn in Chapter 8.

1.5 Summary

This chapter has addressed the merits and demerits of the indirect injection diesel engine as a prime mover for the current passenger car with emphasis on cost premium, performance, reliability and low emissions. Attention is also drawn to the obstacles which the IDI diesel engine has to overcome in order to compete with the two other contenders; the petrol engine and the direct injection diesel engine.

The importance of engine simulation as a useful tool to increase the information available to the engine designer and a brief description of the different types of current engine models has also been reviewed.

Finally the chapter closes by outlining the theme of the whole project.

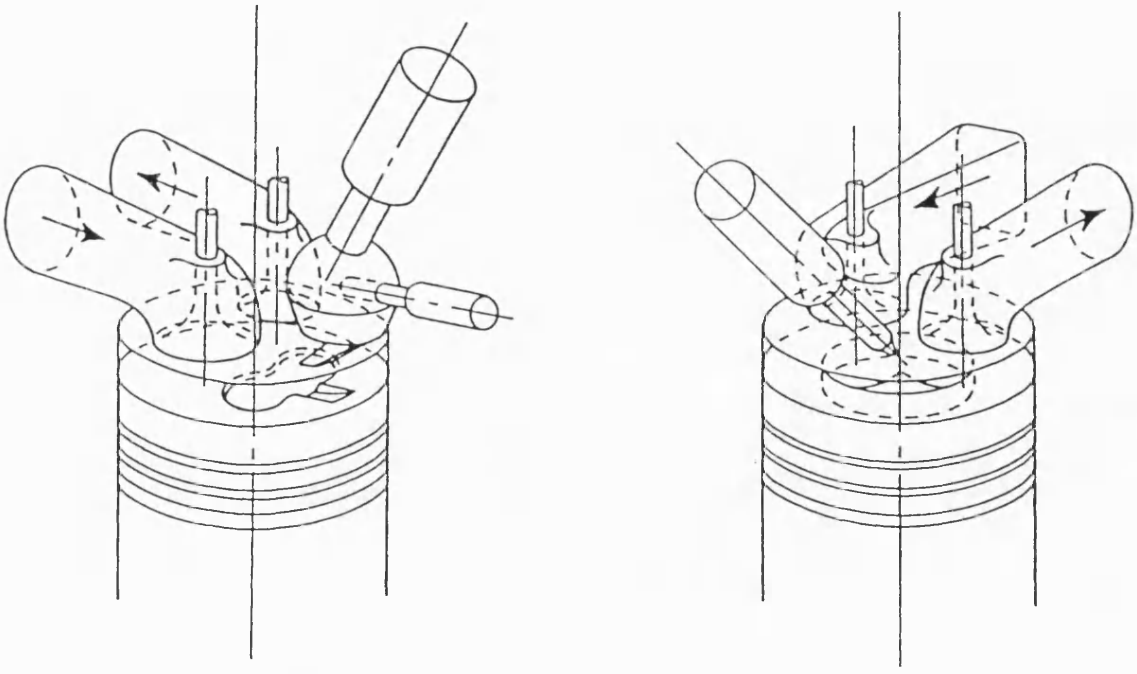

Indirect Injection Diesel Engine

Direct Injection Diesel Engine

Figure 1.1 High speed diesel engine systems, Manning (1984)

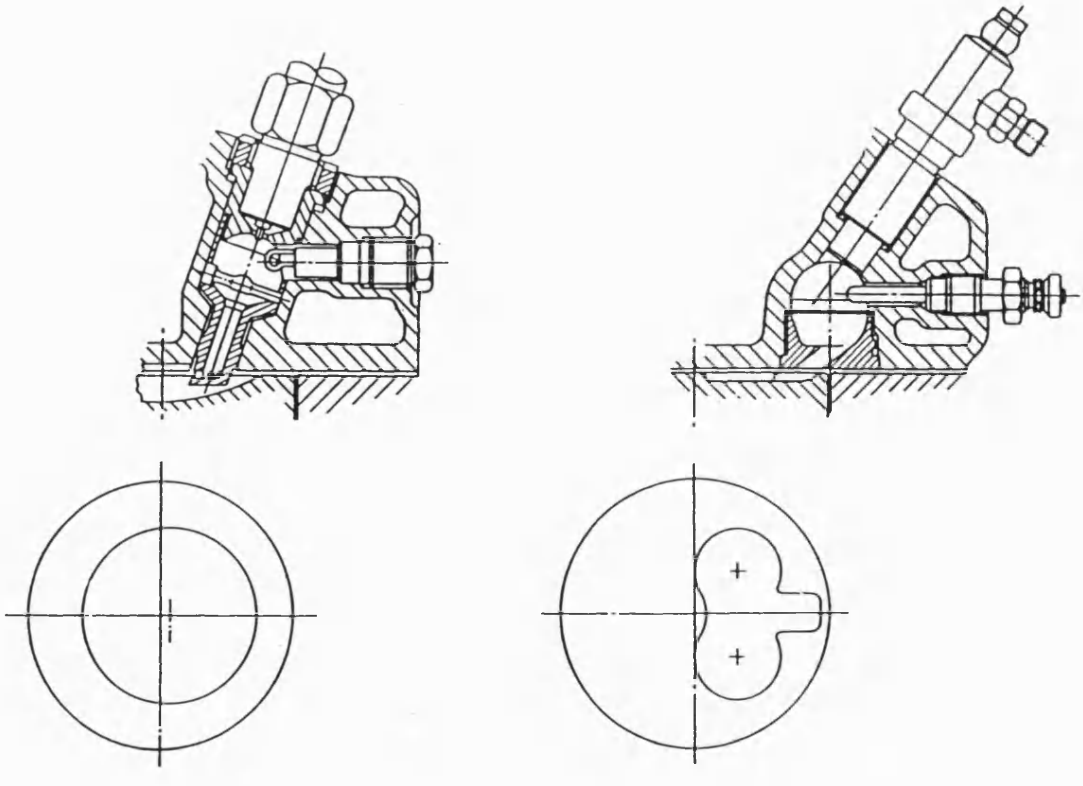

Daimler Benz prechamber

Ricardo Comet swirl chamber

Figure 1.2 Current combustion systems for IDI diesel engines, Lilley (1984)

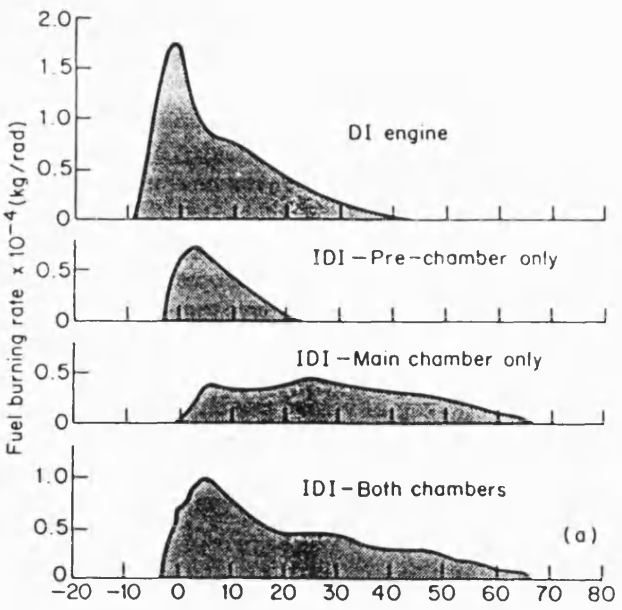

Figure 1.3 Comparison of rates of combustion for DI and IDI engines, Watson and Kamel (1979)

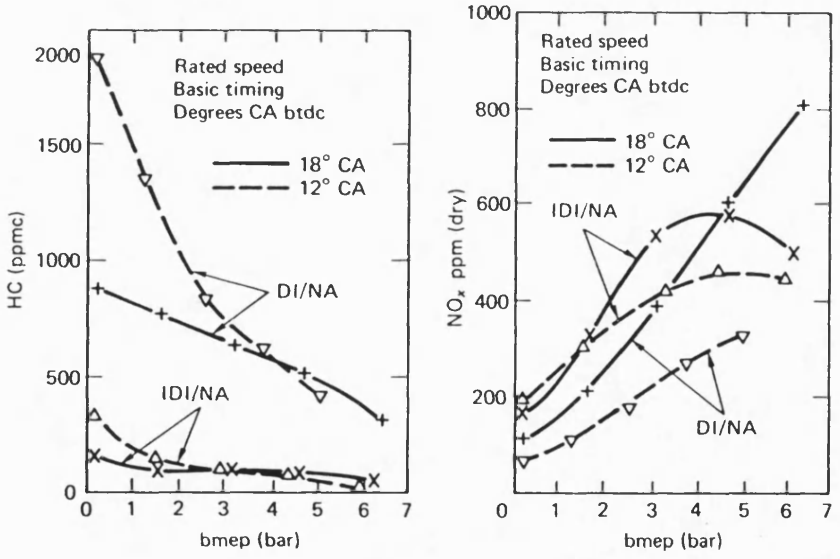

Figure 1.4 A comparison of emissions from naturally aspirated DI and IDI engines, Pischinger and Cartellieri (1972)

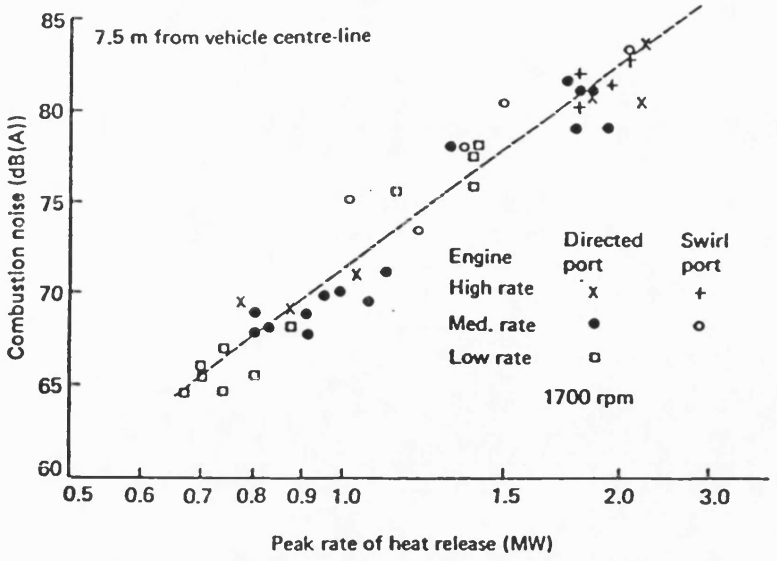

Figure 1.5 Relationship between combustion noise and peak rate of heat release, Glikin (1985)

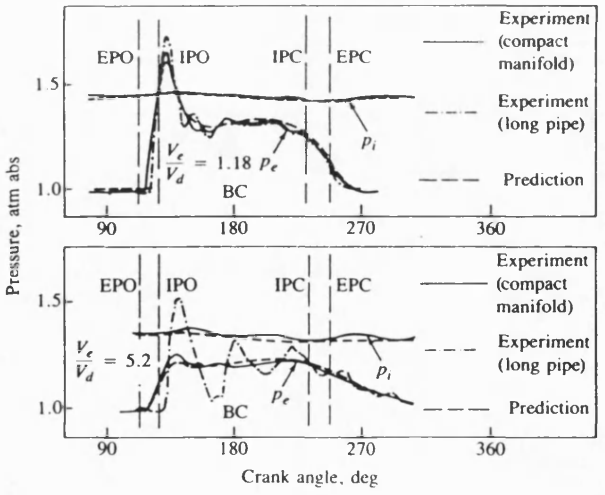

Comparison of intake and exhaust manifold pressures, p_i and p_e, predicted by filling and emptying model, with experimental data. Single-cylinder two-stroke loop-scavenged direct-injection diesel engine. Different ratios of exhaust system volume V_e to displaced volume V_d, and exhaust manifold shapes.[4]

EPO Exhaust port opens
IPO Inlet port opens
IPC Inlet port closes
EPC Exhaust port closes

Figure 1.6 Comparison of experimental and predicted results, Janota *et al* (1968)

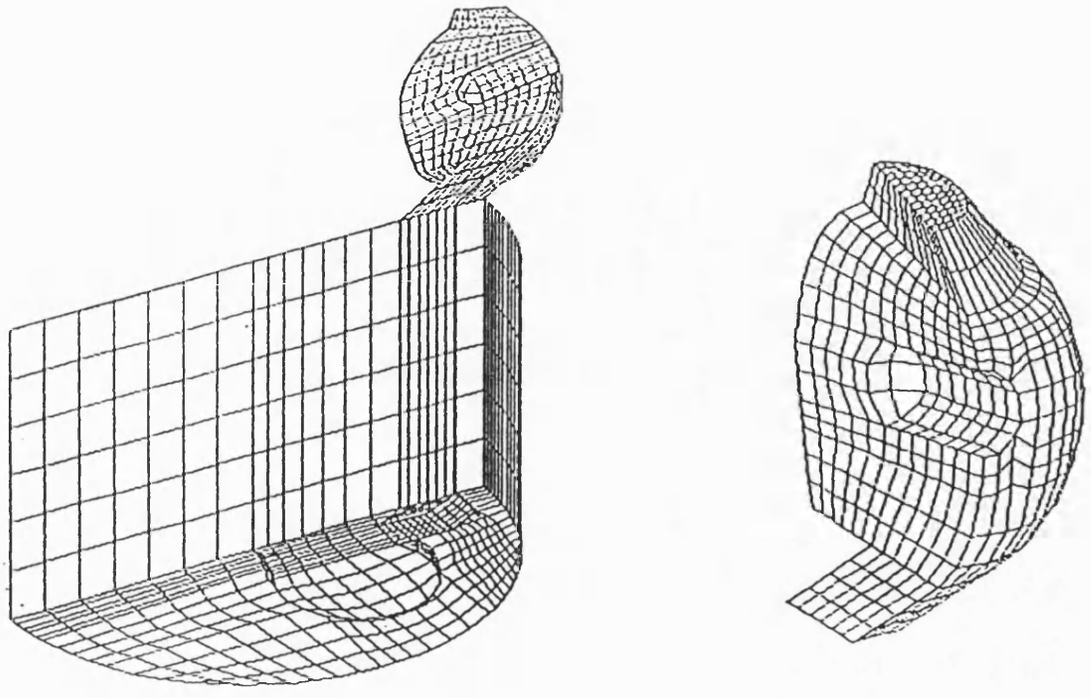

Figure 1.7 Combustion chamber computational mesh, Zellat *et al* (1990)

CHAPTER 2

LITERATURE REVIEW

2.1 Introduction

This chapter presents a critical review of the public domain literature relevant to the research presented in this thesis. Although the research is concerned, primarily, with the air motion and heat transfer in a motored engine, it is valuable to be aware of methods employed for the study of firing engines and to have an appreciation of the processes occurring during and before combustion. Consequently, the chapter begins with discussion of a detailed photographic study of combustion in the IDI diesel engine.

Predictive methods are presented, from the early days of computer modelling through to modern CFD studies. Experimental techniques for measuring the velocity inside engines are discussed. The chapter closes with a discussion of turbulence in engines and the inherent difficulty of separating mean velocity and fluctuating velocity in a cyclic flow.

2.2 Experimental Studies of IDI Combustion

The combustion process in the IDI engine has been investigated and explained by Alcock and Scott (1963), Nagao *et al* (1967) and Nakajima *et al* (1968). Their work provided a basis for better understanding of the complex combustion phenomena.

Hiroyasu *et al* (1986) used high speed photography to observe simultaneously the combustion process in the swirl chamber and main chamber of an IDI engine. Unlike Alcock and Scott (1963) who carried out similar work on a two-dimensional (cylindrical) swirl chamber, the swirl chamber design in this case was based on an actual Ricardo Comet MkVb swirl chamber with a plane wall on one side to allow for optical access. In order to observe the behaviour of flames in both chambers, the engine was modified

for optical access from the side of the swirl chamber and from the underside of the main chamber. The production engine had a compression ratio of 21.2, but this had dropped to 17.5 in the optical engine due to modification of the swirl chamber geometry. To compensate for the drop in the compression ratio, the inlet air and the swirl chamber wall temperatures were raised to 180 degC and 200 degC respectively. This maintained the ignition delay close to that of the production engine. The transparent piston and swirl chamber with optical access are shown in Figure 2.1.

The combustion photographs were taken with a high-speed camera at a film speed of about 8000 frames/second. When the photographs were taken, the engine was driven by an electric motor at 1000 rev/min prior to an injection of a fuel quantity of 33 mg/cycle. A piezo-electric pressure transducer was used to measure the pressure signal in the main chamber. Swirl ratio calculation was based on the moment of momentum into the swirl chamber. The study investigated the effects of fuel injection timing, cross-sectional area of the throat, injector location and the presence of a piston recess on engine performance.

The frames obtained during combustion sequences for the swirl chamber and main chamber (datum condition) are illustrated schematically in Figure 2.2. The authors reported that the calculated air velocity at the throat was 8.5 m/s and the swirl ratio was 35.2:1 at the fuel injection timing of 2 deg btdc. At 3 deg atdc the swirl ratio was 40:1 and the fuel spray, after impinging on the glow plug and the side wall, reached the bottom of the swirl chamber. At the same time, since the piston was descending, the fuel spray was just beginning to enter the throat where the air velocity was 10 m/s. Ignition occurred, at 10 deg atdc, at the bottom-left side of the swirl chamber. Immediately afterwards, at 12 deg atdc, the flame engulfed the vaporised fuel downstream of the ignition point and extended to the main chamber through the throat. Flame propagation in the main chamber almost finished at 15 deg atdc yet by 19 deg atdc the swirl chamber mixture was burning strongly with the flame jet spouting intensely from the throat producing twin vortices and raising the pressure rapidly in the main chamber. They reported that the flame in

the swirl chamber showed a swirling motion which can be described as a more complex pattern than a solid-body rotation. The estimated swirl ratio was about 20 to 25:1 at 20 deg atdc but it attenuated rapidly during the expansion stroke. The brown/sooty luminous flame gradually replaced a white/yellow flame as combustion continued until 45 deg atdc.

The investigation concluded that retarding injection timing will produce low NO_x and smoke emissions. However this will also result in a reduced BMEP and increased total unburnt HC, as shown in Figure 2.3a. Figure 2.3a also shows an improvement in engine BMEP and smoke emissions obtained as a result of recessing the piston top. Decreasing the throat area increased BMEP and decreased smoke emissions. This is due to the improved combustion because of better mixing. It also produced higher NO_x, because of higher gas temperatures, and slightly higher HC as shown in Figure 2.3b.

One can draw a few points from this study with regard to the significance of air swirl to combustion. Referring to Figure 2.2, too little air swirl would have accumulated the fuel at the bottom of the swirl chamber which will delay ignition and might even prove impossible at low injection pressures. Too much swirl will result in the fuel vapour and small droplets recirculating excessively. The vapour which ignites first will, after returning to its original location, blanket the arriving fuel droplets with burnt gas leading to soot formation. Therefore it is important to have an optimum air swirl, as shown in Figure 2.2, so that the products will be swept away. In addition, the increased air swirl in the swirl chamber will increase heat loss by convection.

2.3 Swirl Chamber Cycle Simulation Models

One of the earliest mathematical models of the IDI engine was attempted by Lyn *et al* (1970). They developed a program for thermodynamic analysis of the IDI engine. The

heat release was obtained by the sum of the net heat release and the heat loss from the cylinder contents. The disadvantage of that work was that the IDI swirl chamber and main chamber were treated as one control volume only.

One of the most extensive studies on the IDI engine was reported by Kamel (1977), Kamel and Watson (1979) and Watson and Kamel (1979). The engine was modelled as a series of control volumes connected together via orifices, as shown in Figure 2.4. A filling and emptying approach was employed to describe gas flow and changes in thermodynamic conditions, with the use of numerical techniques to integrate the governing thermodynamic equations. The heat transfer model was based on a Nu-Re correlation by Hassan (1968) with the characteristic velocity calculated by using the conservation of kinetic energy concept. A good agreement between predicted and measured heat fluxes in both chambers was achieved as shown in Figure 2.5. An extensive experimental program to obtain steady-state data was carried out. The ignition delay period and the pressure in both chambers were measured, from which the heat release diagram was calculated. The measured pressure has also been used in conjunction with a cycle simulation program to evaluate engine performance. Comparative thermodynamic efficiency between the IDI and the DI engine has also been published by Watson (1982).

Mansouri (1981) and Mansouri *et al* (1982) proposed a different approach for modelling the IDI engine. These workers used a stochastic mixing approach during the combustion and expansion processes to describe the non-uniform fuel-air ratio distribution within the engine including the way in which this distribution evolves with time. The combustion chamber was divided into three zones: the prechamber, the connecting passageway and the main chamber as illustrated in Figure 2.6. The prechamber and main-chamber were modelled as partially stirred reactors. In each zone, equal mass elements of air, fuel and fuel-air mixture are present in proportions which agree with the overall fuel-air ratio in that region. These elements mix and react according to rules

derived from classical models for turbulent reacting flows and combustion fundamentals. In this way, fuel-air ratio distribution during the mixing, combustion and emission formation processes can be followed as it evolves with time. To the author's knowledge this was the first phenomenological model that attempted to take account of turbulence during the mixing process, which should result in better prediction of combustion and emission formation. In this model the radiative heat flux was assumed to be proportional to the convective heat flux *i.e.* $Q_r = KQ_c$ where $0 \leq K \leq 0.3$ which is not realistic as the radiative heat flux is negligible during the induction, compression and exhaust strokes. The gas velocity in the prechamber was calculated by the conservation of energy equation. The model has been verified by experimental data generated on a single-cylinder 1979 GM IDI Diesel engine, as reported by Kort *et al* (1982). It has been used to examine the origin of No_x and soot emissions. Typical results are shown in Figure 2.7.

A more detailed multi-zone phenomenological model of diesel spray combustion in swirl chamber diesel engines has been developed by Hiroyasu *et al* (1982). The model is similar in concept to an earlier DI model by Hiroyasu and Kadota (1976), but has been extended to include an additional control volume for the swirl chamber. The fuel, which is injected into the swirl chamber as a spray predicted by a fuel injection simulator (Hiroyasu and Matsunari (1968)), is divided into many small packages, assuming no mixing among them, as shown in Figure 2.8. The packages are defined with respect to time and space. When a package moves away from the nozzle air entrains into it and fuel droplets evaporate so that the package now contains liquid fuel, vaporized fuel and air. The packages which impinge against the chamber wall change direction and their momentum decreases. Such packets will then move with the swirl, which is calculated by the conservation of angular momentum approach. When ignition occurs, after a delay period defined by an empirical correlation, it results in a high rate of pressure rise. If the pressure in the swirl chamber is higher than that in the main chamber, the package near the throat is transferred into the main chamber. The history of temperature and

equivalence ratio in each individual package is followed and the results of the events in the packages are synthesized to predict the engine performance and the concentrations of the exhaust emissions. The model has been validated against experimental results from a typical swirl chamber diesel engine, shown in Figure 2.9.

One of the most recent three-dimensional models of combustion and emissions in the IDI engine to emerge was reported by Pinchon (1989). The model was based on the KIVA computer code developed at Los Alamos National Laboratories. He found that the swirl ratio, calculated assuming solid body rotation, increases steadily during compression to a maximum at 15 degrees btdc and then decays rapidly. The swirl ratio obtained with the presence of the glow plug in the swirl chamber is less than half that without. This is shown in Figure 2.10. Although a $\kappa-\varepsilon$ turbulence model was used in the study, the effect of the presence of the glow plug in the swirl chamber on turbulence levels such as turbulence intensity was not reported. Zellat *et al* (1990) developed the model of Pinchon (1989) further. The model was then applied to a Renault J8S engine fitted with a Ricardo Comet swirl chamber. They used a crude mesh (20x22x36 cells) to represent the 3-dimensional combustion chamber configuration. The calculations started at intake valve closure and ended at 90 CA atdc. Temperature and pressure in both chambers were assumed initially uniform and the corresponding values were calculated using a zero-dimensional model. The fuel injection velocity was determined from measured injection pressures. The time evolution of the injected fuel quantity was approximated by a cosine law. Ignition delay, combustion and soot formation were predicted by implementing empirical models in the KIVA code. The model was then used to simulate air motion and combustion in the engine, in order to investigate the influence of injection timing and load on engine performance. The effect of the presence of the glow plug in the swirl chamber on swirl level was also simulated. Figure 2.11 shows clearly that the glow plug is obstructing the flow before injection whereas high levels of velocity are observed between the glow plug and the opposite wall. At tdc the velocity pattern in the swirl chamber is dominated by the fuel spray. A typical pressure

history from the simulation is shown in Figure 2.12, from which it can be seen that the computed values follow closely those measured. However, this has yet to be validated as they did not carry out any experimental measurements of velocity, temperature or emissions.

2.4 Air Motion Studies

Air motion in the IDI Diesel engine is of paramount importance since it influences the combustion efficiency and exhaust emissions. It also largely determines the convective heat flux. Today, air motion in internal combustion engines can be predicted to a good approximation by multi-dimensional models which represent the full spatial and temporal development of the flow processes, but they have their drawbacks as mentioned in section 1.3.2. A small number of detailed studies have been reported on flow modelling in the IDI engine. Two-dimensional modelling has been applied by Gosman *et al* (1979), Abou-Ellail and Elkotb (1981), Meintjes and Alkidas (1982) and Ikegami *et al* (1986). Most of the researchers seem to agree that the flow in the swirl chamber follows the solid body rotation (forced vortex) pattern during the compression stroke until the flame extends over the swirl chamber. During combustion the motion exhibits a more complex pattern than solid body rotation. Alcock and Scott (1963) reported that the angular velocity is roughly inversely proportional to the radius i.e. the linear velocity is roughly constant.

In the case of quasi-dimensional models, there are two concepts for the calculation of the gas velocity in the swirl chamber. Firstly, the concept of kinetic energy conservation, which assumes that the kinetic energy of the charge in the chamber remains constant unless kinetic energy is added by an additional inflow or dissipated by viscous friction. The gas velocity is calculated directly from the kinetic energy in the mean flow of the swirl chamber i.e.

$$V = (2E/m)^{1/2}$$

where E is mean flow kinetic energy and m is mass in the swirl chamber. Secondly, the concept of angular momentum conservation, which assumes that the angular momentum of the charge in the chamber remains the same unless further angular momentum is added or dissipated through viscous friction. The gas velocity is obtained, for example, by multiplying the angular velocity by the radius assuming solid body rotation i.e.

$$V = \omega r$$

where ω is angular velocity in the swirl chamber and r is the radius. As the flow in the swirl chamber is three-dimensional, unsteady and turbulent neither of the two concepts represent the actual velocity. The kinetic energy concept is a scalar quantity which takes all velocity components into consideration and gives an over estimate of the velocity. Moreover, it does not account for the inclination of the throat relative to the swirl chamber which determines the magnitude of the mean swirl velocity in the swirl chamber.

Alcock (1934) published the earliest theoretical model of air motion in the IDI engine. His analysis was based on the conservation of angular momentum concept. The model was rudimentary, since the throat velocity calculation was based on the piston speed. In addition there was no friction effect in the swirl chamber. Nevertheless the paper was very interesting as he explained the importance of production and utilisation of air swirl in diesel engines.

Ajakaiye (1976) and Ajakaiye and Dent (1981) carried out theoretical analysis and measurements of air velocities in low compression cylindrical swirl chambers of a motored IDI engine. The theoretical model was based on the conservation of angular momentum concept with no assumption of a throat flow coefficient of discharge. Their results show poor and inconsistent agreement between theory and experiment. They

justified the discrepancies as due to the disturbance to the flow caused by the probe and not using a discharge coefficient at the throat in the calculation. They also concluded that the assumption of solid body rotation is an over-simplification.

Previous prediction and measurements of air swirl in the IDI engine is summarised in Table 2.1.

2.5 Heat Transfer Studies

Heat transfer in the IDI diesel engine has been studied by Knight (1965). He used a resistance thermometer and a surface thermocouple to measure the gas and metal temperatures respectively in the swirl chamber. He calculated the gas velocity, using the conservation of kinetic energy concept, to obtain instantaneous heat transfer coefficients from empirical pipe flow equations. He compared the experimental and the theoretical heat fluxes under both fired and motored conditions at different engine speeds. His calculations over-estimated the effect of engine speed on the peak of the heat flux curve and he recommended the work to be carried further.

Hassan (1968) used hot wire and resistance thermometry to measure the velocity and temperature of the air and wall temperature in a motored low compression cylindrical swirl chamber. He derived a correlation for the heat transfer coefficient and calculated the heat flux. His work compared very well with the experimental evidence.

Kamel (1977) predicted the heat transfer in the IDI diesel engine. His model was based on the same correlation as that adopted by Hassan (1968) for the convective term but he calculated the gas characteristic velocity in the swirl chamber using the kinetic energy concept. The radiation term was predicted using the model of Oguri *et al* (1975). The theoretical work was supported by extensive experimental results under both motored and fired conditions.

Shephard *et al* (1990) examined the feasibility of using advanced engineering ceramic materials to insulate the swirl chamber of an IDI diesel engine. They carried out extensive dynamometer tests on both lower half and full swirl chamber designs. They reported that improved insulation of the swirl chamber has no significant advantage on engine performance over the standard swirl chamber design. Although their results seem to contradict earlier claims, they explained that their tests were carried on an engine which was designed with a well insulated standard swirl chamber.

2.6 Techniques of Measurements

The air motion in a diesel engine is unsteady as a result of the cyclic motion of the piston, accompanied by large changes of temperature and pressure. When fuel is injected a two-phase flow exists and during combustion the environment inside the engine is hostile and unpredictable. Because of these factors the task of measuring the air velocity in a diesel engine has proved to be extremely difficult even when only motoring the engine. A device for measuring the flow in a diesel engine has to be highly sensitive with very rapid response to resolve the high frequency fluctuations (2-3 kHz) encountered. It should be as unobstructive as possible in order not to disturb the flow, be stable and directionally sensitive to be able to measure all velocity components. Moreover it should be independent of fluid properties such as temperature and pressure. According to Gosman (1986) there are three main methods for measuring air motion in diesel engines viz. flow visualization or optical methods, global methods and local methods.

Flow visualization involves the use of a tracer or smoke to make the flow pattern visible so that it can be photographed or detected from outside. Also falling into this group are methods which make use of changes in the physical properties of the medium whilst passing a light beam through the gas i.e. Laser sheet, Schlieren technique, interferometery and shadowgraph methods. Flow visualization has been widely used in combustion

studies. Most of the results obtained are qualitative as the flow in engines is three-dimensional. These methods are limited because they are difficult and expensive to apply in engines because of the need for high quality quartz windows.

Global methods are used for assessing bulk flow characteristics or swirl measurement and include instrument such as the vane anemometer or impulse swirl meter. These methods are usually not used for in-cylinder air motion measurements but rather on steady-flow test rigs and swirl chambers. The vane anemometer employs a freely rotating vane carried on a spindle which passes through a sealing gland to an external counting mechanism as shown in Figure 2.13. According to Heywood (1988) the rotation rate of the paddle wheel depends on the location of the wheel and its design. In addition it does not provide a measure of the swirl, rather some kind of a mean of the swirl during the entire cycle. The impulse swirl meter, as shown in Figure 2.14, comprises a honeycomb flow straightner which measures the total torque exerted by the swirling flow. As the restraining torque equals the flux of angular momentum through the plane coinciding with the flow-straightner upstream face, it has the advantage of giving an indication of the swirl variation during the cycle. Although the inertia of both methods could be an obstacle for fast response, they have the advantage of being simple, cheap and can be very useful for providing information about mean swirl ratios.

Local methods are the most widely used because of the detailed information they can produce. The most familiar and widely used of these are hot-wire anemometry (HWA) and laser-doppler anemometry (LDA). The following is a brief description of their principles with an outline of their merits and demerits :

Hot Wire Anemometry

This technique has been used for measuring air flow since the start of this century. During the 1960s and early 1970 hot wire anemometry has been applied extensively to measure gas velocities and turbulence levels in motored engines. Amongst the most prominent

workers in this area are Tindal and Williams at King's College and Dent *et al* at Loughborough University. While the work at King's College concentrated on the DI engine, the work at Loughborough varied over the years between IDI and DI engines. More details of the theory and development of HWA will be given in Chapter 4.

This technique involves the use of a heated fine wire (2-10μm diameter), to minimise thermal inertia. The wire can be run in either of two modes; constant temperature or constant current anemometry. Because if its high frequency response, the constant temperature anemometer is preferred in air flow measurements in engines. The wire, in a constant temperature anemometer, is maintained at a constant temperature, and hence electrical resistance, in the fluid stream. When the wire temperature changes, by a small amount, due to a change in convective heat transfer (i.e. change of fluid velocity perpendicular to the wire axis) a control system varies the supply voltage to maintain the wire at a constant temperature.

Advantages of HWA

(i) It gives a continuous signal, good frequency response in addition to high signal-to-noise ratio.

(ii) The probes and electronic circuitry are generally simple to design and inexpensive to manufacture and repair.

Disadvantages of HWA

(i) It disturbs the flow.

(ii) The probes are delicate and liable to frequent breakage

(iii) It has no sense of direction of the flow.

(iv) The probes need to be calibrated before and after every test.

(v) It is limited in its ability to measure high levels of turbulence.

(vi) It is dependent on pressure and temperature.

Laser Doppler Anemometry

The optical arrangement of a typical laser doppler anemometer (LDA) system is shown in Figure 2.15a. The principle of operation of this technique is that; a coherent laser beam from a low power (typically 5-30 mW) gas laser source (usually Helium-Neon or Argon-Ion) is split into two parallel and equal beams by using either a rotating grating or beam splitter module. The two beams are passed through a lens where they cross in the flow at the focal point. An interference fringe pattern is created at the intersection region because of the wave structure of the incident light, as shown in Figure 2.16a. The fringe patterns, appear as straight light and dark lines, perpendicular to the lens axis, as shown in Figure 2.16b. The spacing between two adjacent fringes Δx is given by:

$$\Delta x = \frac{\lambda}{2\sin(\phi)}$$

where λ is the wave length of the laser light and ϕ is half the angle of the two intersecting beams. Scattered light is produced when small particles from the flow, preferably of $\Delta x/4$ diameter , cut across the fringes. A Doppler burst, shown in Figure 2.16c, from the scattered light will be picked up by a photomultiplier through a lens. The scattered light is collected by either a further lens, as shown in Figure 2.15a which is called a forward scatter mode or, by the same lens which is used to focus the incident laser beam, which is called back scatter mode, as shown in Figure 2.15b. The component of velocity of the particle normal to the fringes can be calculated from the Doppler burst frequency F as follows, see Witze (1980),:

$$V_p = F\Delta x$$

The pros and cons of LDA have been evaluated by Witze (1980) as the following :

Advantages of LDA

(i) It can be applied at all conditions of the flow i.e. independent of temperature and pressure.

(ii) It can measure the flow direction as it is only sensitive to the single component of velocity perpendicular to both the incident-beam optical axis and the fringes.

(iii) It can measure turbulence intensity to unlimited degree. Also, in principle, it has the potential to measure the velocity in a firing engine although some technical difficulties have to be overcome.

(iv) It does not disturb the flow and no calibration is needed.

Disadvantages of LDA

(i) It requires optical access which might be difficult in some cases.

(ii) The signal is intermittent as it is produced by a finite number of particles

(iii) It involves a high frequency signal which requires expensive processing equipment. Moreover it has low signal-to-noise ratio.

(iv) In engine applications the flow has to be seeded with small light-scattering particles.

A feasibility study has been carried out during this project to build a signal counter in-house. Although the cost was substantially reduced, it was still outside the budget of the project and consequently the idea was abandoned.

2.7 Turbulence

The flow inside reciprocating engines is highly turbulent i.e. randomly fluctuating as a result of high speeds and small dimensions encountered in engines. It is also periodical because of the piston motion. Thus the turbulent flow in engines is characterised as non-stationary (unsteady) as opposed to stationary (steady). The instantaneous fluid velocity, in a typical stationary turbulent flow, is conventionally decomposed into its time-average (mean) and fluctuating components, as reported by Heywood (1988) :

$$U(t) = \overline{U} + u(t) \tag{2.1}$$

where U(t) is the instantaneous velocity, $\overline{U}$ the mean velocity and u(t) the turbulent or fluctuating component. The mean velocity is obtained simply by :

$$\overline{U} = \frac{1}{T}\int_{t_o}^{t_o+T} U\,dt \tag{2.2}$$

In engine applications the mean velocity is not constant, rather it is time dependent. The mean velocity can vary significantly from one engine cycle to another. It is now more appropriate to define the instantaneous velocity in terms of crank angle position (θ), instead of time (t), for the case of engine cycle (i), that it is decomposed as

$$U(\theta, i) = \overline{U}(\theta, i) + u(\theta, i) \tag{2.3}$$

It is clear that the above equation is similar to (2.1) apart from $\overline{U}$ which is a function of crank angle position and cycle.

The task now is to find a suitable definition for the mean velocity as it varies from one engine cycle to another. The most common technique used for processing data acquired from engines is that of ensemble-averaging, as reported by Lancaster (1976), Witze (1977) and Rask (1979). In this technique the mean velocity is defined for N engine cycles as :

$$\overline{U}(\theta) = \frac{1}{N}\sum_{i=1}^{N} U(\theta, i) \tag{2.4}$$

where

$$U(\theta, i) = U(\theta + n\pi(i-1))$$

and n is the number of engine strokes. The fluctuating component, u, is usually expressed in terms of its root mean square level, the turbulence intensity, $u'(\theta)$, given by :

$$u'(\theta) = \sqrt{\frac{\sum_{i=1}^{N}[U(\theta,i) - \overline{U}(\theta)]^2}{N}} = \sqrt{\frac{\sum_{i=1}^{N}[u(\theta,i)]^2}{N}} \tag{2.5}$$

Although ensemble averaging seems acceptable in terms of producing the mean velocity over a number of cycles, it does not represent the true mean velocity of the individual cycle. This may result in misinterpretation of the quantity of the fluctuating component, $u(\theta)$, and hence the turbulence intensity $u'(\theta)$, as shown in Figure 2.17. The solution to this problem is to allow $\overline{U}(\theta)$ to vary from cycle to cycle. A cycle-to-cycle variation term is defined as the difference between the instantaneous average velocity and the average velocity obtained over many cycles by ensemble average, as reported by Rask (1979);

$$\hat{U}(\theta,i) = \overline{U}(\theta,i) - \overline{U}(\theta) \tag{2.6}$$

from which the instantaneous velocity can be expressed as

$$U(\theta,i) = \overline{U}(\theta) + \hat{U}(\theta,i) + u(\theta,i) \tag{2.7}$$

Different methods have been tried to define $\overline{U}(\theta)$ during an individual cycle. Lancaster (1976), assumed that $\hat{U}(\theta)$ is constant over a finite period of time during each cycle. He used a finite time interval of 45° crank angle. This proved unrealistic in engines as $\hat{U}(\theta)$ may vary significantly over different time intervals, according to the levels of non-stationary turbulence in a particular cycle. In addition, as reported by Gosman (1986), the choice of the finite time interval is arbitrary which will influence the results obtained.

Another method, used by Rask (1979), is to fit a smooth continuous curve over the engine cycle. The instantaneous turbulence component can then be defined as the difference between the actual signal and the smooth fit. He described this technique as applying a low-pass filter to the signal. Everything that does not go through the low-pass filter is assigned to turbulence. He suggested that one should start with too little smoothing and proceed until the exact amount of smoothing is achieved. Gosman (1986) commented on this technique by pointing out that no satisfactory basis are available for choosing the appropriate filter. Rask (1981) used this technique to study cycle-to-cycle variation by using cubic splines to fit data for velocity measurements obtained by laser-doppler anemometry in a motored engine. He then compared the cycle-by-cycle fitting procedure with the window and ensembled methods. He concluded that both the window and the ensemble methods are unable to distinguish between cyclic variations in mean velocity and turbulence. Moreover, the window method further suffers from an error introduced by the finite window size especially when large window sizes are used. On the other hand, the cycle-by-cycle fitting method proved to account for variations in mean velocity from one cycle to the next.

Knowledge of the mean velocity and turbulence intensity are not usually enough to describe the observed turbulence in engines, or turbulent flows. A number of length scales which define the structure of turbulence are also required in addition to other features. Figure 2.18 is a schematic representation of the jet issuing into the cylinder from the intake valve. Lancaster (1976) reported that the largest eddies in a turbulent flow are limited in size by the system boundaries. Gosman (1986) attributed their production to the shearing action of the flow and described them as inherently unstable. The larger eddies then break down into smaller eddies as a result of turbulent stresses created by velocity gradients. These smaller eddies break down into even smaller eddies until the process eventually ends in viscous dissipation. Hinze (1959) mentioned that a continuous supply of energy is required to maintain the turbulent motions, e.g. by external effects, otherwise these will decay in the course of time. Since turbulence is a broad

subject more details will be found in standard text books. However, the following is a brief summary of the important parameters encountered in turbulent flows, see Figures 2.18 and 2.19.

Correlations between the velocities at various points in the field of turbulence can give an interpretation of the scale of turbulence and its statistical properties as reported by Taylor (1935). Witze (1977b) described the auto-correlation coefficient as a measure of the coherence of the turbulent structure in a fluid flow. The characterisation of the eddy size distribution, at a point within a turbulent flow, can be determined by the auto-correlation of the velocity fluctuation, as reported by Lancaster (1976). Assume velocity measurements are made between two adjacent points in a turbulent flow separated by x distance a part. The auto-correlation coefficient R_x can be defined in terms of the fluctuating velocity u at a reference location o and values at distances x from it by

$$R_x = \frac{1}{N} \sum_{i=0}^{N} \frac{u(x_o)u(x_o + x)}{\sqrt{u'(x_o)u'(x_o + x)}} \tag{2.8}$$

where N is the number of measurements. According to Heywood (1988) due to the difficulty of measuring the velocity in engines at two adjacent points the common technique is to define the auto-correlation coefficient R_x in terms of time by

$$R_t = \frac{1}{N} \sum_{i=0}^{N} \frac{u(t_o)u(t_o + t)}{\sqrt{u'(t_o)u'(t_o + t)}} \tag{2.9}$$

Witze (1977a) defined the auto-correlation coefficient in terms of crank angle R_ϕ as

$$R_\phi(\theta) = \frac{1}{N} \sum_{i=1}^{N-1} \frac{u(\theta + in\pi)u(\phi + in\pi)}{u'(\theta)u'(\phi)} \tag{2.10}$$

where ϕ is the phase angle about which the computation is being made. He reported that; it must be noted that whenever $\theta > \phi$ equation (2.10) has no physical significance

as it correlates events in the future.

The integral, or macro, length scale is a measure of the largest scale structure of the flow field. Heywood (1988) defined the integral length scale l_x as the integral of the auto-correlation coefficient of the fluctuating velocity at two adjacent points in the flow at a variable distance apart. He also stated that measurements of velocity at two points x distance apart will correlate if x is significantly less than l_x and no correlation will exist when x is much greater than l_x. As shown in Figure 2.19 the integral length scale l_x is defined as the area under the curve

$$l_x = \int_0^\infty R_x dx \tag{2.11}$$

Dent and Salama (1975), described the integral length scale as a measure of the average size of the energy-containing eddies which are held responsible for the increased diffusion of momentum (and also heat).
The lifetime of these larger eddies is defined through the integral time scale which can be defined from the auto-correlation coefficient similarly as

$$l_t = \int_0^\infty R_t dt \tag{2.12}$$

Witze (1977a) expressed the integral time scale in terms of crank angle as

$$T_\phi = \frac{1}{\eta}\int_{-\infty}^0 R_\phi(\theta) d\theta \tag{2.13}$$

where η is the engine speed.

Under conditions where the mean velocity $\overline{U}$ is constant and the turbulence is relatively weak i.e. $\frac{u'}{\overline{U}} \gg 1$ Taylor (1938) proved that turbulence is isotropic i.e. has no preferred direction. Under such conditions Dent and Salama (1975) reported that the integral length and time scales are related by

$$l_x = \overline{U} l_t \tag{2.14}$$

Gosman (1986) advised that the above relation must be used with caution as the above conditions are seldom encountered in engines.

Taylor (1935) defined the microscale as "the average size of the smallest eddies," which are responsible for the dissipation of energy by viscosity. As shown in Figure 2.19 the microscale or Taylor microscale is defined by the distance between the origin and the point where the parabola, which follows the curvature of the auto-correlation curve, intersects the abscissa. Gosman (1986) defined Taylor microscale as a measure of the spacing between the smallest eddies which he expressed as

$$\lambda = -\frac{2}{(\delta^2 R_x/\delta x^2)_{x=x_o}} \tag{2.15}$$

Similarly the micro time scale can be defined, see Heywood (1988), as

$$\tau_M = -\frac{2}{(\delta R_t/\delta t^2)_{t_o}} \tag{2.16}$$

Witze (1977a) defined the micro time scale in terms of crank angle as

$$\tau_\phi^{-2} = -(\eta^2/2)\,[\delta R_\phi(\theta)/\delta\theta^2]_{\theta=\phi} \tag{2.17}$$

Similarly for the same conditions as that of equation (2.14) a similar relation exist between the micro length and time scales as

$$\lambda = \overline{U}\tau_M$$

The kinetic energy of the turbulence fluctuations can be analysed according to its distribution over the various frequencies occurring in these fluctuations as reported by Hinze (1959). Taylor (1938) defined a one-dimensional spectrum function F(n) which is a Fourier transform of the auto-correlation coefficient expressed as

$$F(n) = \frac{4}{U}\int_0^\infty R_x \cos\frac{2\pi n x}{U} dx \tag{2.15}$$

where n is the frequency. Hence by observing R_x the spectrum curve F(n) can be calculated and vise versa. The energy spectrum function, E(n), which represent the turbulent energy contained between frequencies n and n+dn is obtained from the Fourier transform of the average value of u^2 such that :

$$u'^2 = \int_0^\infty E(n)dn \tag{2.16}$$

The spectrum function, F(n), is related to the energy function, E(n), by

$$F(n) = \frac{E(n)}{u'^2} \tag{2.17}$$

Witze (1977a) defined the normalised one-dimensional energy spectrum in terms of crank angle and engine speed

$$E_\theta(n) = \frac{4}{\eta}\int_{-\infty}^0 R_\phi(\theta)\cos 2\pi f\frac{\theta}{\eta} d\theta \tag{2.18}$$

2.8 Summary

This chapter has looked at previous experimental and theoretical studies of the IDI diesel engine. Areas such as cycle simulation, air motion and heat transfer have been reviewed. The techniques used for measuring air velocity in engines have been presented with a description of their advantages and disadvantages. Turbulence encountered in engines has also been discussed. This included a review of the common techniques used for tackling the problem of cycle-to-cycle variation and definition of other parameters used to define turbulence in engines.

Author	Analytical Technique	Experimental Technique	Appr. Max. Swirl Ratio
Alcock (1934)	conservation of Angular Momentum		55.5
Lyn and Valdmanis (1962)		High speed Schlieren Photography	20
Alcock and Scott (1962)		High speed photography	64
Nakajima *et al* (1963)		Plasma tracer	38.1
Knight (1965)	conservation of Kinetic Energy		90.2
Hassan (1971)		Hot-wire anemometry	37.1
Kamel and Watson (1979)	conservation of Kinetic Energy		114.6
Ajakaiye and Dent (1981)		Hot-wire anemometry	83.3
Abou-Ellail and Elkotb (1981)	Finite-difference Technique	Hot-wire anemometry	50.25
Mansouri *et al* (1982)	conservation of Kinetic energy		19
Zimmerman (1983)		Laser Doppler Anemometry	20
Hiroyasu *et al* (1986)	conservation of angular momentum		35.2
Pinchon (1989)	Multi-dimensional modelling		47

Table 2.1 Summary of Published Work on Divided Chamber Engines

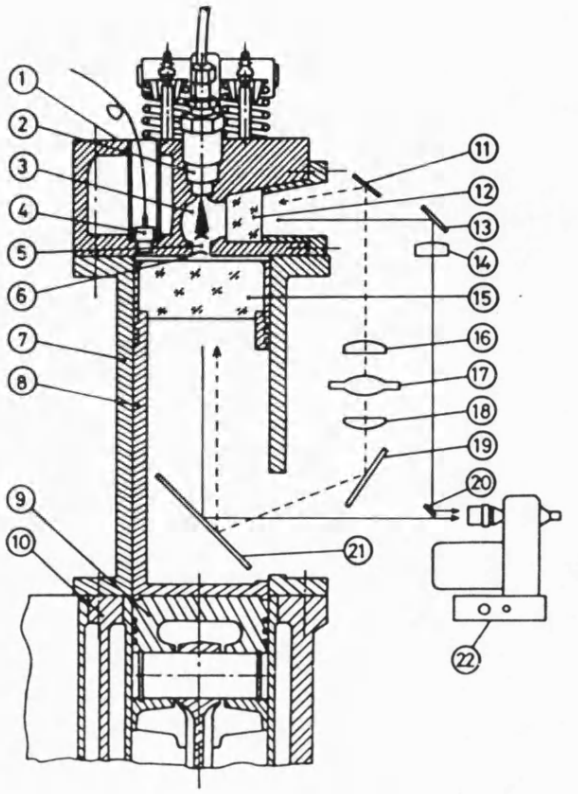

1 Cylinder Head
2 Fuel Injector
3 Prechamber
4 Pressure Transducer
5 Throat
6 Main Chamber
7 Elongated Cylinder Liner
8 Elongated Piston
9 Piston
10 Cylinder
11 Mirror
12 Transparent Window
13 Mirror
14 Convex Lens
15 Transparent Piston Crown
16 Convex Lens
17 Xenon Lamp
18 Convex Lens
19 Mirror
20 Mirror
21 Mirror
22 High-speed Camera

Figure 2.1 Section through the optical engine showing modifications to the combustion chamber, Hiroyasu *et al* (1986)

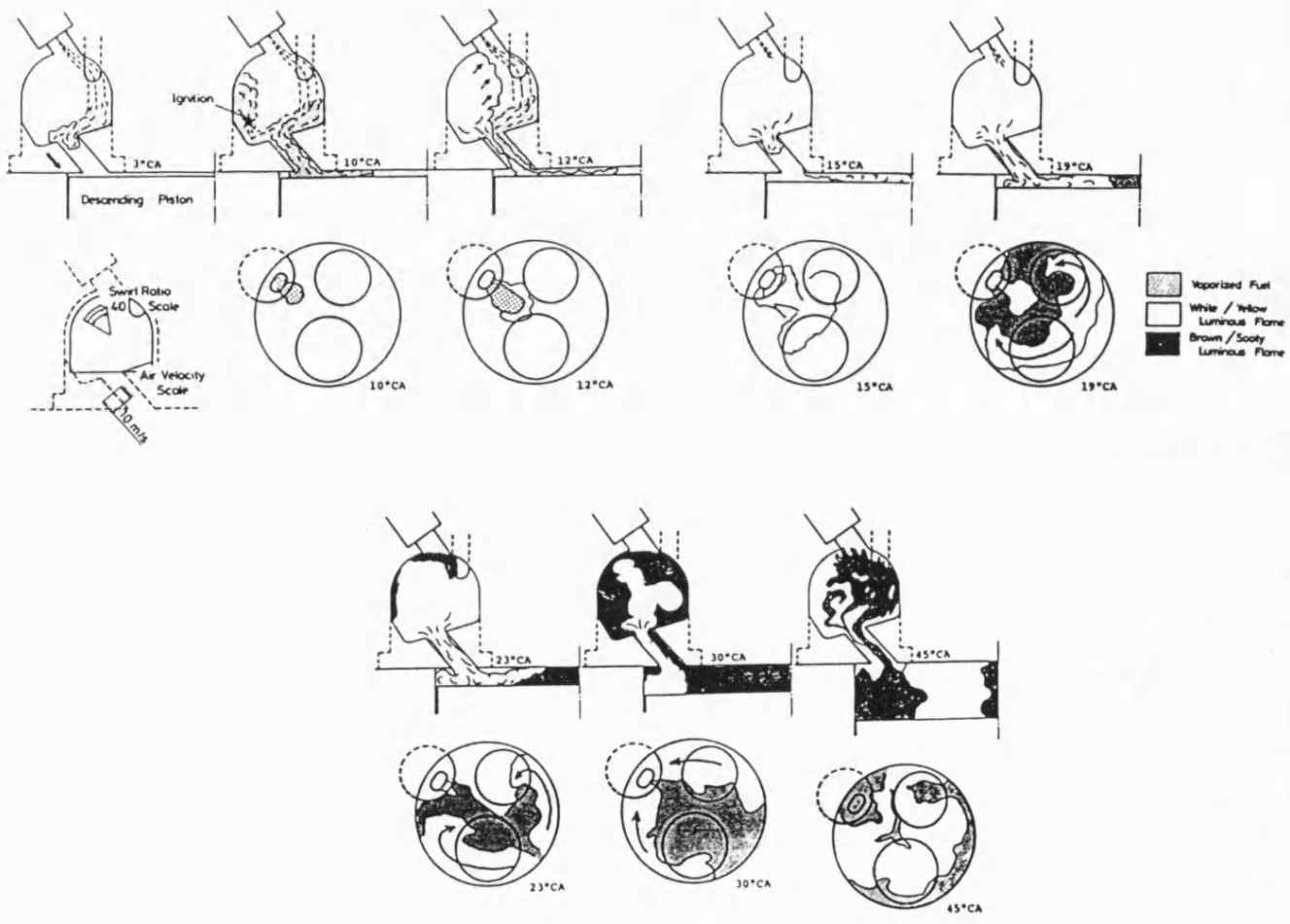

Figure 2.2 Development of combustion with injection timing 2 deg btdc, Hiroyasu *et al* (1986)

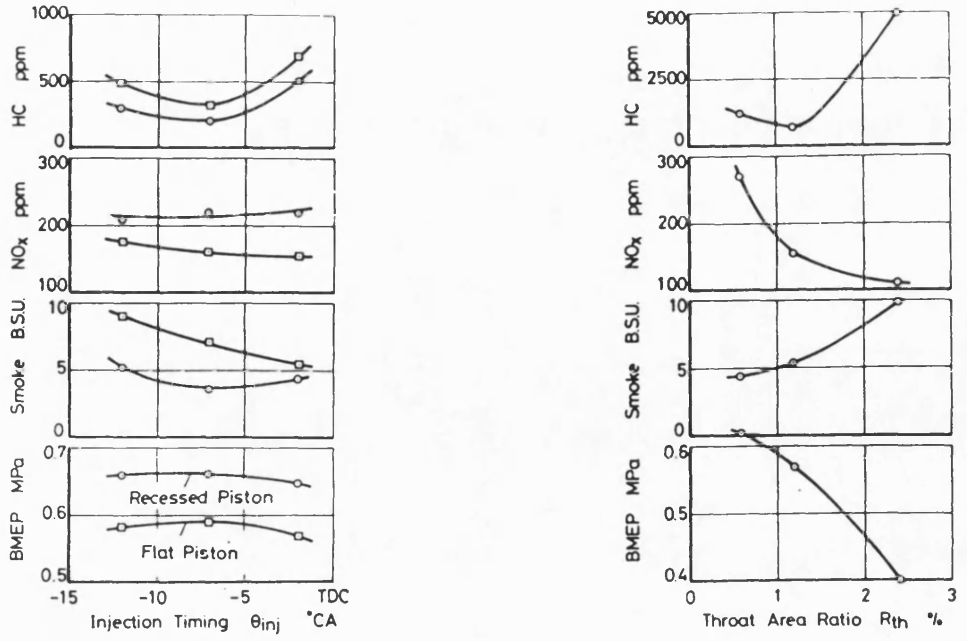

Figure 2.3 Engine Performance (a) Effect of injection timing and piston cavity (b) Effect of throat area ratio, Hiroyasu *et al* (1986)

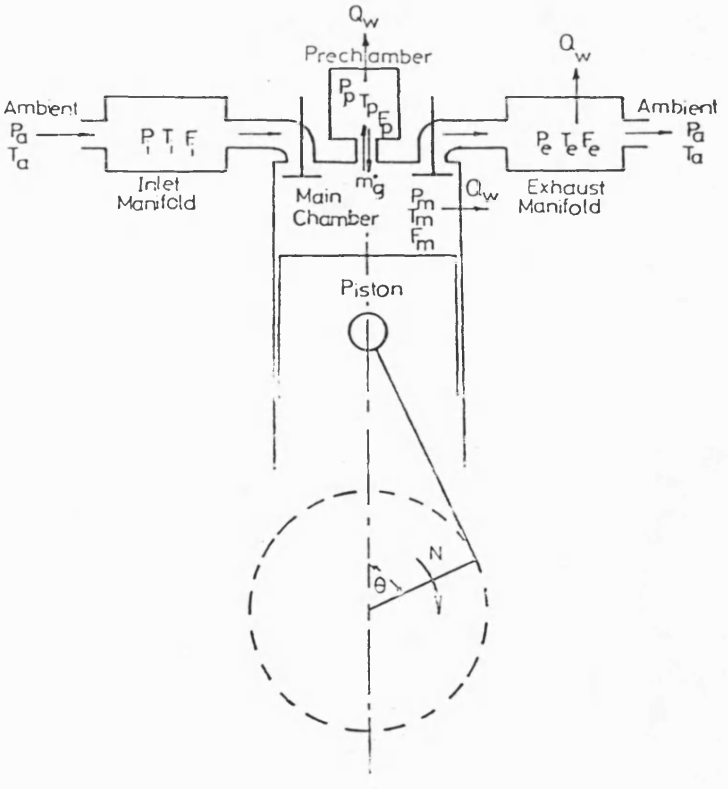

Figure 2.4 Engine thermodynamic simulation system, Watson and Kamel (1979)

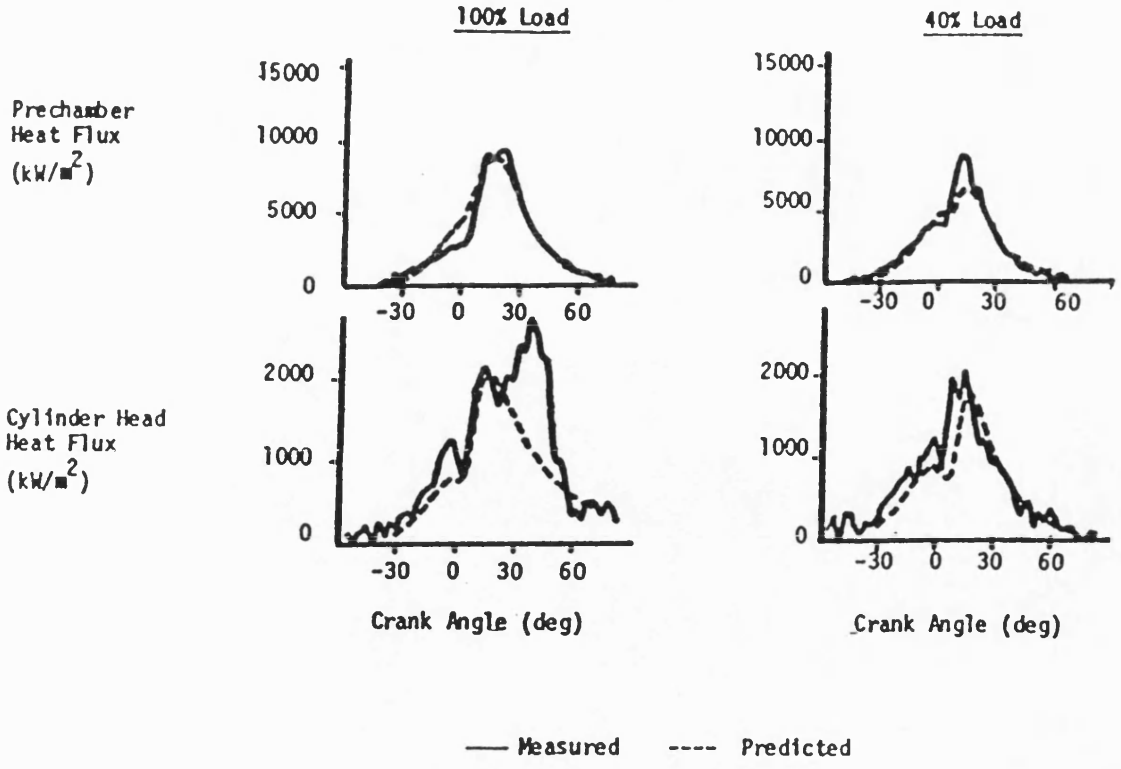

Figure 2.5 Measured and calculated heat fluxes, Kamel and Watson (1979)

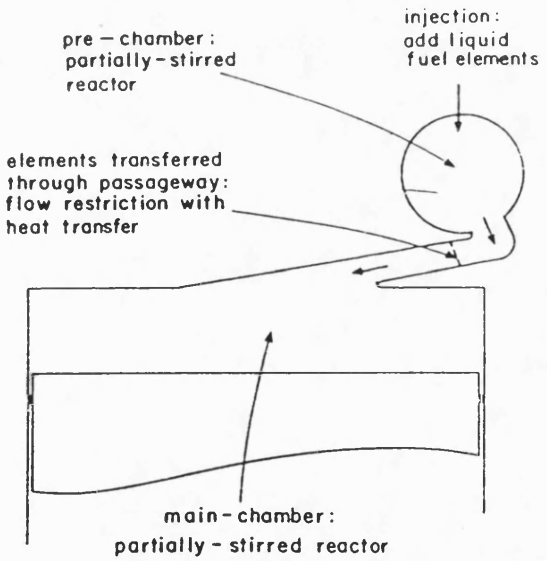

Figure 2.6 Schematic of IDI engine illustrating how stochastic mixing model is applied to prechamber, main chamber and passageway, Mansouri and Ekchian (1982)

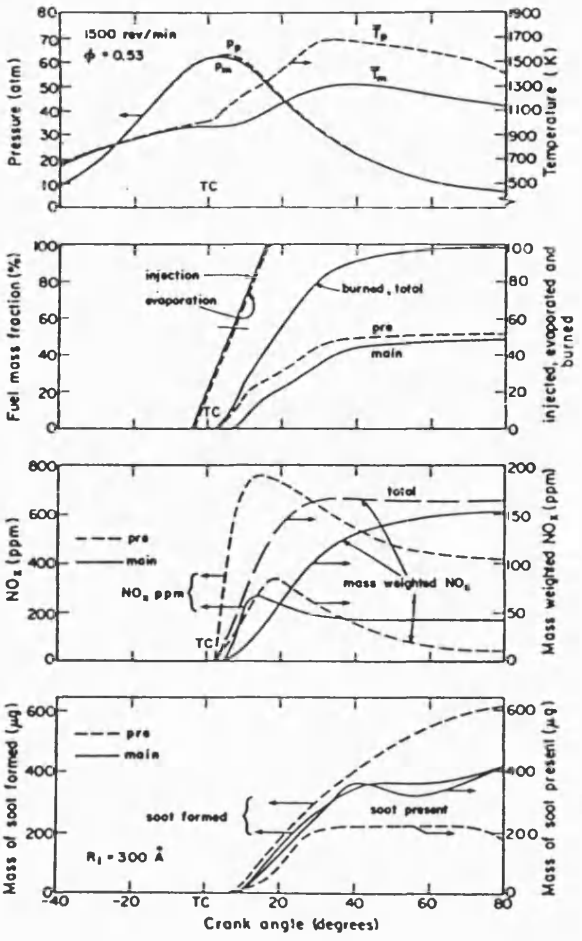

Figure 2.7 Example of simulation predictions through the engine operating cycle, Mansouri and Ekchian (1982)

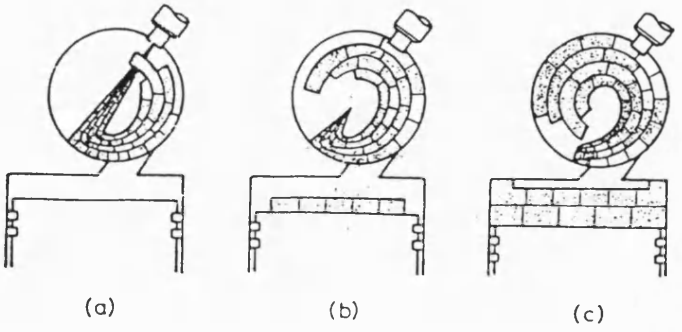

Figure 2.8 Schematic representation of divided package of the spray and combustion zones, Hiroyasu *et al* (1982)

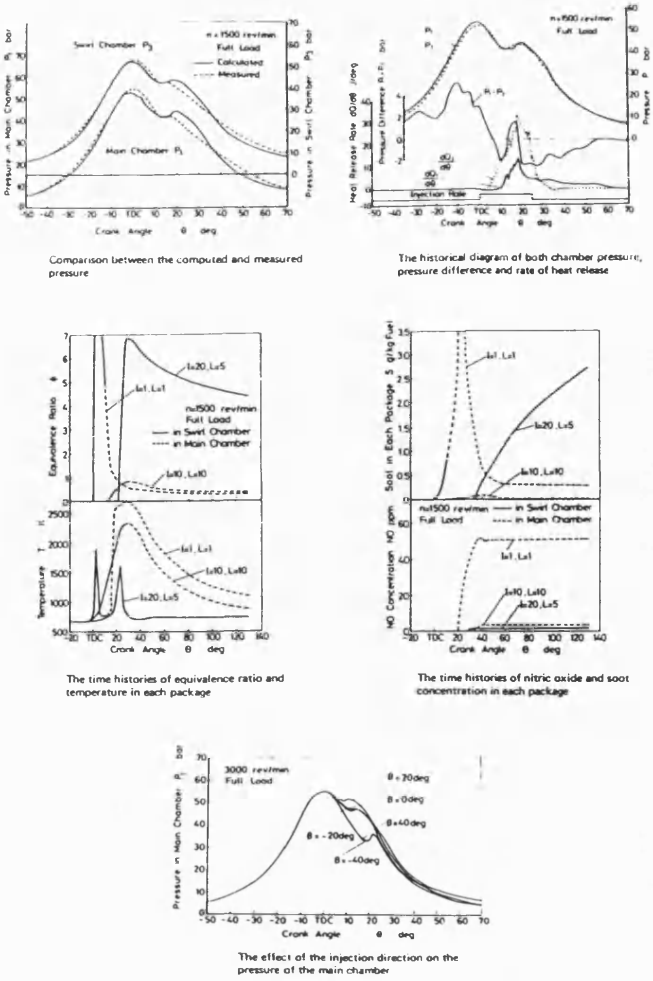

Figure 2.9 Comparison of measured and calculated results, Hiroyasu *et al* (1982)

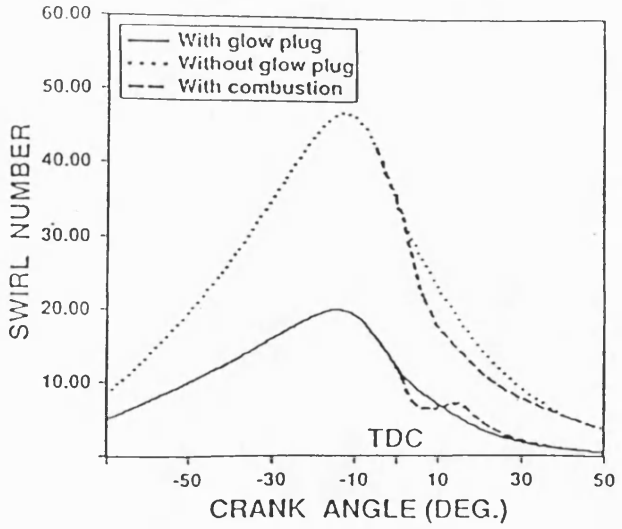

Figure 2.10 Evolution of the computed swirl number with crank angle, Pinchon (1989)

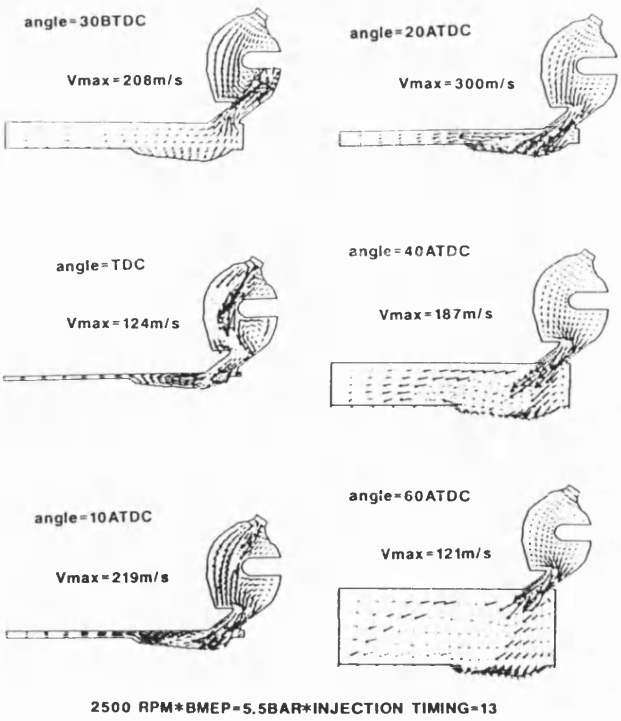

Figure 2.11 Velocity vector plots, Zellat *et al* (1990)

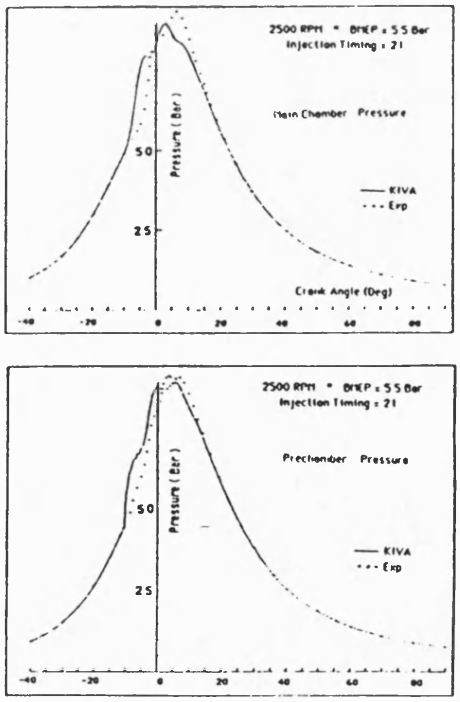

Figure 2.12 Experimental and computed pressure histories, Zellat *et al* (1990)

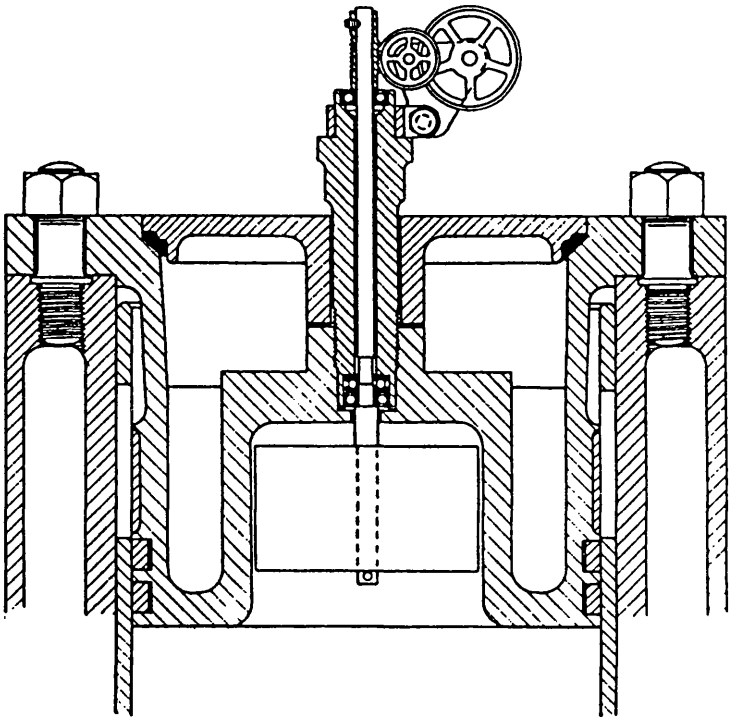

Figure 2.13 Ricardo swirl meter, Alcock (1934)

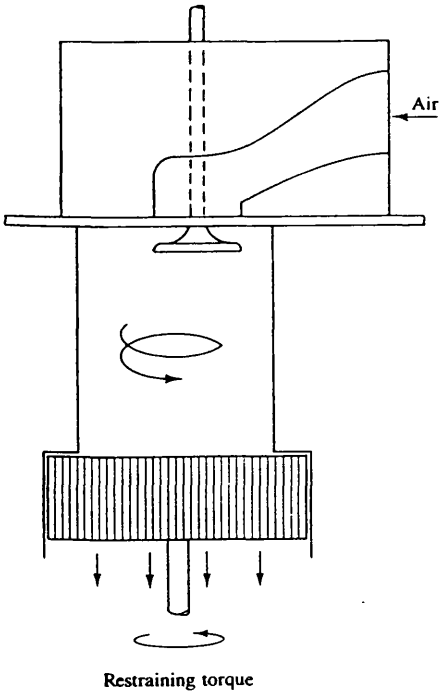

Figure 2.14 Impulse swirl meter, Heywood (1988)

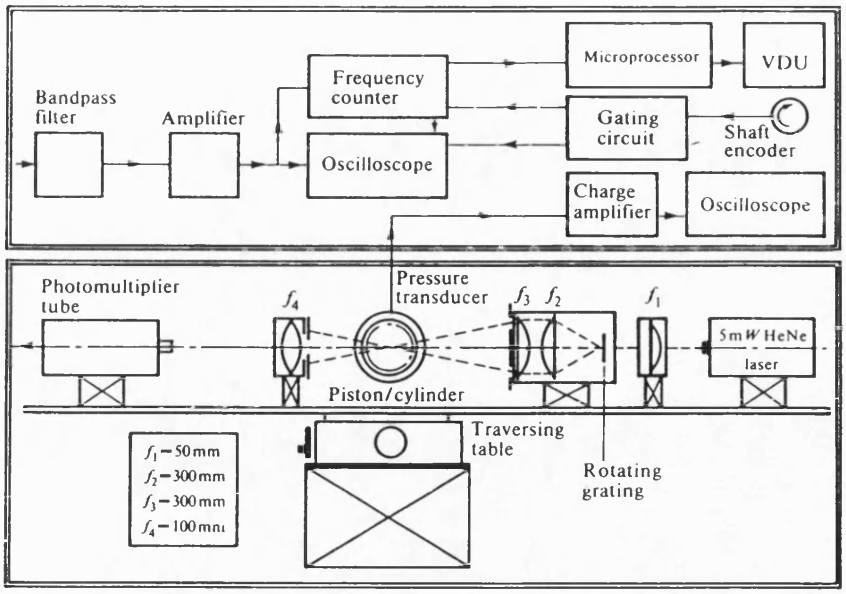

(a)

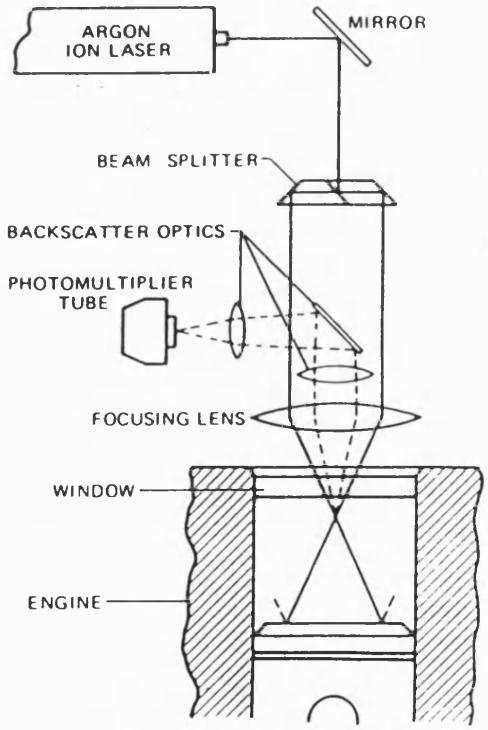

(b)

Figure 2.15 LDA arrangements (a) forward scatter, Gosman (1986) (b) backward scatter, Witze (1980)

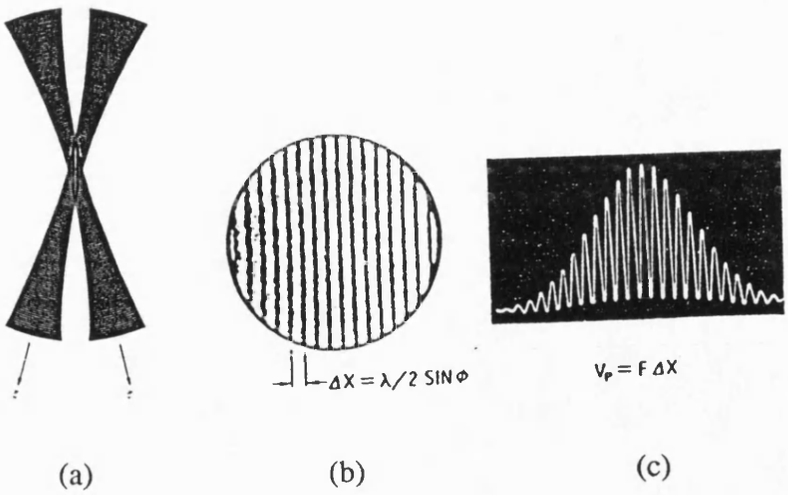

Figure 2.16 Principle of dual beam LDA, Witze (1980)

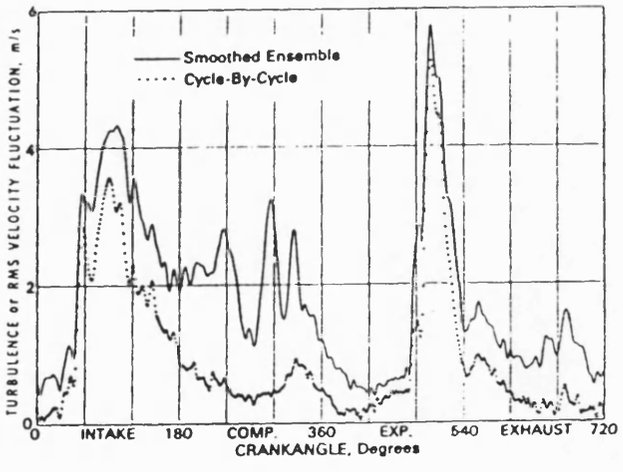

Figure 2.17 Cycle-to-cycle analysis, Rask (1979)

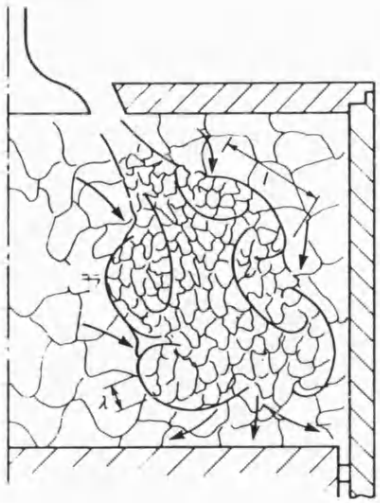

Figure 2.18 Turbulent eddy structure in the cylinder during induction, Gosman (1986)

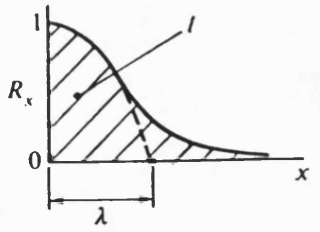

Figure 2.19 Variation of spatial correlation coefficient, with distance, and definition of integral and micro length scales, Gosman (1986)

CHAPTER 3

SWIRL CHAMBER SWIRL AND HEAT TRANSFER MODEL

3.1 Introduction

A mathematical model which represents the true physical phenomena of air motion and heat transfer in the IDI engine would be of great value in engine research and design. Such a model would constitute a solid foundation upon which predictions of heat release and exhaust emissions, that depend on correct predictions of the aforementioned two parameters, could be built. Workers at Bath University have developed a FORTRAN based package, named SPICE (Simulation Program for Internal Combustion Engines), for diesel engine simulation. This package is versatile in terms of its ability to simulate all types of DI engines including turbocharged and compound engines. However, it does not have the capability to simulate the complex combustion process in the IDI engine. At the start of this project it was realised that it would be unwise, and too time consuming, to develop a separate package for the simulation of the IDI engine. Accordingly, the decision was taken to use SPICE and to incorporate a mathematical model for the IDI engine simulation within it. This could be achieved by developing FORTRAN based modules for prediction of air motion and heat transfer in the IDI engine which could be integrated within SPICE.

In this chapter, the mathematical models used for the simulation of air motion and heat transfer in the IDI engine are presented. The chapter starts with the description of the structure of SPICE; this includes theoretical and empirical equations involved, numerical solution and flow chart. Then, the technique used to model the air motion in the swirl chamber is explained. This is followed by a detailed description of the heat transfer model which covers the three modes of heat transfer. Transient heat conduction through the walls of the swirl chamber, in addition to heat convection and radiation between the combustion gases and the chamber walls, are presented.

3.2 The Computer Program SPICE

At the start of this project the version of SPICE which existed could only be run on a main frame or a minicomputer. The IDI version of SPICE was developed on a VAX 11/750 minicomputer. Since then development was carried out to enable the program to run on personal computers. The latest IDI version of SPICE will run on IBM PC and compatible micro computers as well as Sun workstation.

The program SPICE considers the engine as a series of thermodynamic control volumes connected together via flow junctions and shafts. The user is able to construct an engine model easily using any combination of these components. As reported by Charlton (1986), many types of control volume, such as a slider-crank operated piston and a constant volume control volume (manifold, plenum or any air receiver), can be simulated in addition to other standard devices which can easily be added. Junctions available include; simple orifice, valve or port, simple reed valve, wastegate etc. Shaft types such as crankshaft and turbocharger rotor are also available. A wide range of engine types can then be simulated by linking the above mentioned elements, which are controlled by an input data file. Figure 3.1 illustrates some of the systems that may be modelled by using SPICE.

The filling and emptying concept, which is based on the principles of mass and energy conservation, is used to construct differential equations within each thermodynamic control volume. This set of first order non-linear ordinary differential equations is then solved at discrete time steps for each control volume. Empirical or theoretical sub-models are used, whenever necessary, to determine unknown terms required in the solution of the differential equations.

3.2.1 Basic Thermodynamic Relations for a Control Volume

For a motored engine, where air is the working fluid, the first law of thermodynamics when applied to any control volume, referring to Figure 3.2a, can be expressed as follows

$$\frac{dU}{dt} = -P\frac{dV}{dt} + \frac{dQ_w}{dt} + h_i\frac{dm_i}{dt} - h_o\frac{dm_o}{dt} \tag{3.1}$$

which is :

Rate of change of internal energy = Rate of work exchange with the surroundings + Rate of heat exchange with the surroundings + Rate of enthalpy added due to gas flow into the control volume + Rate of enthalpy subtracted due to gas flow out of the control volume.

The total rate of mass flow is given by

$$\frac{dm}{dt} = \frac{dm_i}{dt} - \frac{dm_o}{dt} \tag{3.2}$$

Since

$$\frac{dU}{dt} = \frac{d(mu)}{dt}$$

$$= m\frac{du}{dt} + u\frac{dm}{dt} \tag{3.3}$$

and neglecting dissociation effects $u = \phi(T)$

$$\frac{du}{dt} = \frac{du}{dT}\cdot\frac{dT}{dt} \tag{3.4}$$

Assuming perfect gas behaviour :-

$$pV = mRT$$

$$\therefore p = \frac{mRT}{V} \tag{3.5}$$

then by substituting (3.3), (3.4) and (3.5) into (3.1) and rearranging

$$m.\frac{du}{dT}.\frac{dT}{dt} = -\frac{mRT}{V}\frac{dV}{dt} + \frac{dQ_w}{dt} - u\frac{dm}{dt} + h_i\frac{dm_i}{dt} - h_o\frac{dm_o}{dt}$$

hence

$$\frac{dT}{dt} = \frac{1}{m\frac{du}{dT}}\left\{-\frac{mRT}{V}\frac{dV}{dt} + \frac{dQ_w}{dt} - u\frac{dm}{dt} + h_i\frac{dm_i}{dt} - h_o\frac{dm_o}{dt}\right\} \tag{3.6}$$

Equations (3.2) and (3.6) describe the mass transfer and temperature change respectively. They describe fully the control volume at any instant of time. To solve equation (3.6) the program evaluates all unknown terms at each time step of the solution. These terms together with the mathematical simulation technique are described in the following sections

3.2.2 Rate of Change of Cylinder Volume

The volume and liner area are calculated, for a cylinder control volume, according to the kinematics of a slider crank mechanism. The crank angle was chosen as the time base for the calculations, since the angular position of the crank shaft governs the state of each of the engine cylinders. The calculations are then converted to time by multiplying by the engine speed. Referring to Figure 3.3, the values are :

$$\frac{dV}{dt} = \frac{\pi d^2}{4}\left(R\sin\theta + \frac{R^2\sin 2\theta}{2\sqrt{(L^2 - R^2\sin^2\theta)}}\right) \times 6N$$

$$V = \frac{\pi d^2}{4}\left(R + L - R\cos\theta - \sqrt{(L^2 - R^2\sin^2\theta)} + \frac{2R}{(CR-1)}\right)$$

$$A_{wall} = \frac{4V}{d}$$

The geometry of orifices, manifolds and constant volume control volume is supplied by the user in the input data file. Valve areas are also supplied in the input data file as a function of crank angle position.

3.2.3 Heat Transfer

Heat transfer to the walls of a control volume is calculated by considering conduction, convection and radiation modes. Convective heat transfer is calculated using semi-empirical correlations such as Woschni, Annand and Hohenburg, see Charlton (1986). Conduction heat transfer is calculated by using either a constant wall temperature or a resistance option which allows up to ten regions of the chamber to have thermal resistance properties. Figure 3.4 shows the thermal resistance model for a combustion chamber. Since in a real engine the wall temperature needs many minutes to reach equilibrium, which is not practical in terms of computer time, this is overcome by applying thermal equilibrium at the end of each cycle.

3.2.4 Rate of Mass Flow

The rate of mass flow through an orifice to or from a control volume, is represented by one-dimensional quasi-steady compressible flow. The mass flow must be determined, in addition to the specific stagnation enthalpy of the flow, before the temperature differential equation is solved. Since the length of these junctions is relatively small, effects such as pressure waves and deviation from one-dimensional flow on the gas are neglected. A discharge coefficient, derived from steady flow tests, is multiplied by the instantaneous geometric area of the restriction to give the effective area of the flow. Simple junctions

such as an orifice have an invariable flow area. Effective flow area for a valve or a port is represented by a table of effective area versus crank angle or a table of flow areas versus pressure (reed valves and wastegates) and scaling factors, as reported by Charlton (1986).

When the kinetic energy downstream of the junction is fully dissipated, it is assumed that the static pressure at the throat is equal to the downstream stagnation pressure. The throat velocity and mass flow rate between the upstream conditions in the control volume at entry and the downstream conditions in the control volume at exit are given by

throat velocity

$$U_{th} = \sqrt{\left(2C_p T_1 \left(1 - \frac{P_{th}}{P_1}^{\frac{\gamma-1}{\gamma}}\right)\right)} \tag{3.7}$$

Mach number at throat

$$M_{th} = \frac{U_{th}}{\sqrt{\left(\gamma R T_1 \frac{P_{th}}{P_1}^{\frac{\gamma-1}{\gamma}}\right)}}$$

for continuity

$$\frac{dm}{dt} = \rho_{th} A^* U_{th}$$

hence

$$\frac{dm}{dt} = A^* \left(\frac{P_{th}}{P_1}^{\frac{1}{\gamma}} \frac{P_1}{RT_1} \sqrt{2C_p T_1 \left(1 - \left(\frac{P_{th}}{P_1}\right)^{\frac{\gamma-1}{\gamma}}\right)}\right) \tag{3.8}$$

when the pressure ratio $(\frac{P_{th}}{P_1})$ reaches the critical value i.e. $M = 1$ then

$$\frac{P_{th}}{P_1} = \left(\frac{2}{\gamma+1}\right)^{\frac{\gamma}{\gamma-1}}$$

At sonic flow rates in the orifice the throat velocity and mass flow rate will become

$$U_{th} = \sqrt{\left(2C_pT_1\left(\frac{\gamma-1}{\gamma+1}\right)\right)} \tag{3.9}$$

$$\frac{dm}{dt} = A^*\left(\frac{2}{\gamma+1}\right)^{\frac{1}{\gamma-1}} \frac{P_1}{RT_1}\sqrt{2C_pT_1\left(\frac{\gamma-1}{\gamma+1}\right)} \tag{3.10}$$

3.2.5 Gas Properties

Semi-Perfect gas behaviour and thermodynamic equilibrium within a control volume is assumed throughout the simulation. A homogeneous mixture of gases with no spatial variation is also assumed within the control volume. The properties of the gases are expressed as a series of fourth order polynomials obtained from thermodynamics tables, see Rogers and Mayhew (1980). Thermal conductivity is expressed as :

$$k = 0.0041 + 7.79E-5 \times T - 1.421E-8 \times T^2$$

3.2.6 The Numerical Solution

The energy and mass equations, derived above, are solved step-by-step using a numerical integration. The most commonly used methods in engine simulation are the Runge-Kutta and the modified Euler predictor-corrector. Kamel (1977) used the predictor-corrector method for simulating the cycle of the IDI engine. He justified his use of the predictor-corrector stating that it is more efficient and less prone to numerical instability during the gas exchange processes than the Runge-Kutta method. He added that the iterative methods provide estimates for the final truncation error which allows further

correction for a specified accuracy. Tarabad (1983) used the predictor-corrector method in his diesel engine cycle simulation programme. He reported that the Runge-Kutta method has the disadvantage that the error is unknown and several derivative calculations are required at each step.

The numerical method used by SPICE is the modified Euler predictor-corrector. The set of coupled first order differential equations require initial values in each control volume to be known. According to Charlton (1986) the step size may require to be reduced, particularly during the valve overlap period, when numerical difficulties arise. This is achieved automatically in the programme by reducing the step size by half if the number of iterations at a particular crank angle exceeds a prescribed number. The step size may be further reduced by half until a solution is found if the required convergence criteria is not encountered. Figure 3.5 shows the solution procedure schematically. The method uses the Euler type equation for providing first estimate of the function (predictor)

$$Y_1 = Y_o + \frac{dy}{dx_o}.\Delta x$$

A modified Euler type equation is used to obtain a better estimate of the function (corrector)

$$Y_1 = Y_o + \left[\left(\frac{dy}{dx}\right)_o + \left(\frac{dy}{dx}\right)_1\right]\frac{\Delta x}{2}$$

An iterative sequence is then applied until convergence is achieved. The difference between two successive iterations must be within a specified tolerance. According to Kamel (1977) reducing the step size does not yield significant improvement in accuracy. However experience in using SPICE suggests that the programme will run faster by using local step size reduction.

Figure 3.6 shows a flow diagram for the programme and a flow diagram for solution of the control volume is shown in Figure 3.7.

3.3 Mathematical Model for Air Motion in the Swirl Chamber

The calculation of the mean angular velocity in the swirl chamber is based on the principle of conservation of angular momentum and the assumption of solid body rotation. As reported by Tawfig *et al* (1991), the angular momentum is considered to be created by the linear momentum flux through the throat during piston ascent, as shown in Figure 3.2b. To this effect the swirl chamber is assumed spherical with the gas rotating as a solid body and the throat is assumed to be attached tangentially at a given radius. Thus the angular velocity is calculated by the conservation equation of angular momentum. According to Hunsaker and Rightmire (1947), the angular-momentum law states that: The resultant external torque on the matter momentarily occupying a fixed volume equals the rate of change of angular momentum of the matter inside the volume plus the net rate of outflow of angular momentum through the control surface.

Ajakaiye (1976) reported that the fixed volume in the above statement is the swirl chamber. The resultant external torque is the torque due to viscous friction and the net flow of angular momentum is due to the flow through the throat. The principle of angular momentum thus yields

$$\frac{d(I\omega)_{sw}}{dt} = -\mathrm{T}_v + \left(\frac{dm}{dt}\right)_{th} U_{th} R_1 \qquad (3.11)$$

where I is the moment of inertia of the air mass in the swirl chamber, ω is the angular velocity, T_v is the viscous torque, $\frac{dm}{dt}$ is obtained from equation (3.8) or (3.10), U_{th} is obtained from equation (3.7) or (3.9) and R_1 is the perpendicular distance between the axis of the swirl chamber and the axis of the throat. The moment of inertia of the air mass in the swirl chamber, assuming solid body rotation is expressed as

$$I = \frac{2}{5} m_{sw} R_{sw}^2 \tag{3.12}$$

where m_{sw} is the instantaneous mass of air in the swirl chamber, R_{sw} is the radius of the swirl chamber.

Consider an elemental strip of the wall surface of the swirl chamber of thickness $R\delta\theta$ and radius y as shown in Figure 3.8. The torque due to viscous friction at the surface of the elemental strip can be expressed as

$$\delta T_v = \tau A y \tag{3.13}$$

where τ is the wall shear stress and A is the elemental strip area which can be defined as

$$A = 2\pi y R \delta\theta$$

$$\tau = \frac{1}{2} C_F \rho (\omega y)^2 \tag{3.14}$$

The friction factor C_F, according to Heywood (1987), may be given by the flat plate formula

$$C_F = 0.037 \lambda Re^{-0.2} \tag{3.15}$$

where λ is an empirical constant to allow for differences between the flat plate and cylinder wall ($\lambda \approx 1.5$)

$$Re = \frac{\rho(\omega y)(2\pi y)}{\mu}$$

then substituting the above equations in (3.13) yields

$$\delta T_v = 0.0372\pi^{0.8}\lambda\rho^{0.8}\omega^{1.8}\mu^{0.2}R y^{3.6}\delta\theta \tag{3.16}$$

but since

$$y = R\sin\theta$$

then

$$\delta T_v = 0.0372\pi^{0.8}\lambda\rho^{0.8}\omega^{1.8}\mu^{0.2}R^{4.6}(\sin\theta)^{3.6}\delta\theta \tag{3.17}$$

the total viscous torque will be

$$T_v = 2\int_0^{\frac{\pi}{2}} \delta T_v$$

$$= 2\times 0.037\pi^{0.8}\lambda\rho^{0.8}\omega^{1.8}\mu^{0.2}R^{4.6}\int_0^{\frac{\pi}{2}}(\sin\theta)^{3.6}\delta\theta \tag{3.18}$$

For flow into the swirl chamber

$$\frac{d(I\omega)_{sw}}{dt} = -T_v + \left(\frac{dm}{dt}\right)_{th} U_{th}R_1 \tag{3.19}$$

Each 'packet' of mass flow leaving the swirl chamber is assumed to take with it a proportional amount of the total angular momentum in the swirl chamber. Consequently for flow out of the swirl chamber

$$\frac{d(I\omega)_{sw}}{dt} = -T_v - \left(\frac{dm}{dt}\right)_{th} \omega_{sw} R_{sw}^2 \qquad (3.20)$$

3.4 Heat Transfer Model

3.4.1 Introduction

Predicting the heat transfer from the gases to the walls of the internal combustion engine constitutes a significant application for engine mathematical modelling. It also plays an essential role in cycle calculations as it affects the energy balance equation, volumetric efficiency and the performance of the engine as a whole. Heat transfer is complex because the properties and the state of the gases in the engine vary with both time and location. This has made the task of detailed prediction of heat transfer very difficult. Nevertheless, the extensive engine research over the past sixty years has provided a better understanding of modes of heat transfer encountered in engines. It is now evident that all modes of heat transfer are present to varying degrees throughout the engine cycle. In a diesel engine, heat is transferred by forced convection between the gases and engine walls, by conduction through the walls to the coolant and by radiation from luminous flames due to the particles of soot and carbon burning within them. Forced convection is the most dominant mode of heat transfer in engines, and it depends on the local velocity and boundary layer behaviour. A number of empirical and semi-empirical correlations for predicting convective heat transfer have emerged over the years. Some of them, as early as the model of Eichelberg (1939), are still in current use. These correlations are derived from experimental data obtained from different engines. Therefore it is not surprising that large variations may occur when applied to a particular engine.

The heat transfer model for the swirl chamber has been divided into three separate sections; the upper half, the lower half (hot plug) and the throat, see Figure 3.9. Each

section has its own thermal properties. The overall heat transfer from the swirl chamber is calculated by adding the combinations of the three sections together. The following is a description of the heat transfer models for the swirl chamber.

3.4.2 Unsteady Heat Conduction

Subject to the periodic gas temperature and velocity fluctuations in the combustion chamber of the diesel engine, the heat flux into the exposed chamber walls varies through the cycle. This unsteady heat transfer, in turn causes the surface temperature of the walls to be continuously varying. However, this variation is damped out within a small distance from the wall surface (usually less than 1 mm). The result is that the temperature at the coolant side remains constant, as the transient components of the temperature flux die out within the wall.

For a three-dimensional solid body with constant thermal properties and without internal heat generation, heat conduction may be expressed by the following equation

$$\frac{\delta T}{\delta t} = \alpha\left(\frac{\delta^2 T}{\delta x^2} + \frac{\delta^2 T}{\delta y^2} + \frac{\delta^2 T}{\delta z^2}\right)$$

where

$$\alpha = \frac{k}{\rho c}$$

Measurements of surface temperature, by a surface thermocouple, have been reported by Annand (1963), Hassan (1968) and Kamel (1977). Their work has proved that the assumption of one-dimensional conduction was well justified for many locations within engines. Thus the above equation in the x-direction will yield

$$\frac{\delta T}{\delta t} = \alpha\left(\frac{\delta^2 T}{\delta x^2}\right) \tag{3.21}$$

Equation (3.21) is known as the Fourier heat conduction equation in one-dimension. This equation can be solved by analytical, graphical, numerical or experimental methods. In engine research the two favoured methods are as follows.

(i) Analytical Methods

In these methods the solution of the equation is derived mathematically with certain boundary conditions assumed. The basic equation is usually simplified and the solution is by no means exact as far as the physical problem is concerned. Nevertheless, this method has found popular support for internal combustion engine heat transfer. Assuming a sinusoidal variation of surface temperature (T_w) with time (t) the surface temperature can be expressed as

$$T_{(0,t)} = T_0 + \sum_{n=1}^{N} [A_n \cos(n\omega t) + B_n \sin(n\omega t)] \qquad (3.22)$$

where T_0 is the mean gas side temperature, A_n and B_n are Fourier coefficients, N is the number of harmonics and ω is the angular frequency in radians per second. With the boundary conditions ...

at $x = 0$ (gas side) $T = T_{(0,x)}$

at $x = l$ (coolant side) $T = T_l$ (oscillations heavily damped)

then the steady state temperature distribution will be given by

$$T_{(x,t)} = T_0 - (T_0 - T_l)\frac{x}{l}$$

and the total temperature distribution in the wall will be

$$T_{(x,t)} = T_0 - (T_0 - T_l)\frac{x}{l} + \sum_{n=1}^{N} e^{-\phi_n x} F_n(x,t) \tag{3.23}$$

where $F_n = A_n \cos(n\omega t - \phi_n x) + B_n \sin(n\omega t - \phi_n x)$ and $\phi_n = \sqrt{\left(\frac{n\omega}{2\alpha}\right)}$. The total fluctuation of heat flux with time can then be defined as

$$\dot{q}_x = -\kappa \frac{\delta T}{\delta x}$$

$$= \frac{\kappa}{l}(T_0 - T_l) + \kappa \sum_{n=1}^{N} \phi_n [(A_n + B_n)\cos(n\omega t) - (A_n - B_n)\sin(n\omega t)] \tag{3.24}$$

from which the instantaneous heat flux at the wall surface, $x = 0$, will be

$$\dot{q}_{x=0} = \kappa \frac{(T_0 - T_l)}{l} + \kappa \sum_{n=1}^{N} \left[A_n \cos\left(n\omega t + \frac{\pi}{4}\right) + B_n \sin\left(n\omega t + \frac{\pi}{4}\right) \right] \tag{3.25}$$

Hence we can deduce that the periodic heat flow leads the periodic temperature fluctuation by $\frac{\pi}{4}$.

(ii) Numerical Methods

These methods are usually based on finite difference or finite element numerical techniques. They derive an approximate numerical solution for the partial differential equations involved whose accuracy, according to Croft and Lilley (1977), can be increased to any desired degree. Such techniques offer solutions to problems that are often not easy to solve by analytical methods. The speed of current computers has made the use of this technique increasingly desirable. Accordingly the decision was taken to compute the temperature variation through the swirl chamber wall by the finite difference method.

3.4.2.1 Finite Difference Solution

Consider a one-dimensional engine wall divided into equally spaced columns and rows, as shown in Figure 3.10. The columns represent distance (i) and the rows represent time (j). Consider a control volume around node (P) and by applying the energy balance principles to this control volume; energy conducted across the boundary of the control volume will be :

$$Q_{i-1,j} + Q_{i+1,j} + Q_I = Q_{i,j+1} \tag{3.26}$$

where Q_I is the energy generated within the control volume and $Q_{i,j+1}$ is the energy change within the control volume. Now since

$$Q_{i-1,j} = -\kappa \Delta z \Delta y \frac{(T_{i,j} - T_{i-1,j})}{\Delta x} \tag{3.27}$$

$$Q_{i+1,j} = -\kappa \Delta z \Delta y \frac{(T_{i,j} - T_{i+1,j})}{\Delta x} \tag{3.28}$$

$$Q_{i,j+1} = mc_p \frac{dT}{dt}$$

$$= (\Delta x \Delta y \Delta z \rho) c_p \frac{(T_{i,j+1} - T_{i,j})}{\Delta t} \tag{3.29}$$

then by substituting (3.27), (3.28) and (3.29) in (3.26) and neglecting energy generated within the control volume, after rearranging yields

$$\frac{(T_{i,j+1} - T_{i,j})}{\Delta t} = \alpha \frac{(T_{i-1,j} - 2T_{i,j} + T_{i+1,j})}{\Delta x^2} \tag{3.30}$$

introducing Fourier number (Fo)

$$Fo = \alpha\frac{\Delta t}{\Delta x^2} = \frac{\text{Rate of conduction of heat}}{\text{Rate of storage of heat}}$$

then (3.30) after further rearranging becomes

$$T_{i,j+1} = Fo\left[T_{i+1,j} + T_{i-1,j} + \left(\frac{1}{Fo} - 2\right)T_{i,j}\right] \tag{3.31}$$

Thus if the temperatures at the time row (j) are known, the temperature at the time row ($j+1$) can be calculated. With the same method the temperature at the time row ($j+2$) can be calculated from the computed temperatures at the time row ($j+1$) and so on. This method is known as the explicit method.

Examining equation (3.31) indicates that the value of the Fourier number is very significant. When a high value of Fo is chosen the temperature at the time row ($j+1$) will increase indefinitely. In practice the calculations carried out to solve the finite difference equations have to be restricted to a finite number of decimal places which introduces round-off errors. For this reason, and in addition to other reasons with regard to the stability of the computed values of the finite difference equation, the maximum value of Fourier number in equation (3.31) is limited. Although the explicit method is computationally simple, according to Smith (1965), it is only valid for $0 < Fo \leq \frac{1}{2}$.

The limitation of $0 < Fo \leq \frac{1}{2}$ of the explicit equation is an undesirable constraint. This has lead to the derivation of other equations which are unconditionally stable for larger Fourier number. In the explicit method only the present (j) temperatures are used. A similar formulation, that consider other temperatures, has lead to what is known as the implicit equation. The implicit equation uses the temperature on the ($j+1$) time row. The implicit version of the finite difference equation, evaluating the terms at time row ($j+1$) is expressed as

$$T_{i,j+1} - T_{i,j} = Fo(T_{i+1,j+1} + T_{i-1,j+1} - 2T_{i,j+1}) \tag{3.32}$$

The above equation is stable regardless of the value of Fourier number. However, according to Croft and Lilley (1977), it is less accurate and the time required to advance one time-step in the solution process is considerably more than the explicit method.

A third method which uses the mean of the temperatures on the (j) and $(j+1)$ time rows was proposed by Crank and Nicolson (1947). According to Smith (1965), this method requires less time than the fully implicit method and it is both accurate and stable for all values of Fourier number. Thus by using the Crank-Nicolson method equation (3.26) will be

$$\frac{(T_{i,j+1} - T_{i,j})}{\Delta t} = \frac{1}{2}\left[\frac{\alpha(T_{i+1,j+1} - 2T_{i,j+1} + T_{i-1,j+1})}{\Delta x^2} + \frac{\alpha(T_{i+1,j} - 2T_{i,j} + T_{i-1,j})}{\Delta x^2}\right]$$

giving, after rearranging as before

$$-T_{i-1,j+1} + \left(\frac{2}{Fo} + 2\right)T_{i,j+1} - T_{i+1,j+1} = T_{i-1,j} + \left(\frac{2}{Fo} - 2\right)T_{i,j} + T_{i+1,j} \tag{3.33}$$

A generalised equation is obtained by taking a weighted average of the explicit and fully implicit equations

$$\frac{1}{Fo}(T_{i,j+1} - T_{i,j}) = \lambda(T_{i+1,j+1} + T_{i-1,j+1} - 2T_{i,j+1}) + (1-\lambda)(T_{i+1,j} + T_{i-1,j} - 2T_{i,j}) \tag{3.34}$$

where λ $(0 \le \lambda \le 1)$ is a weighting factor. Equation (3.34) becomes fully implicit when $\lambda = 1$, explicit when $\lambda = 0$ and Crank-Nicolson when $\lambda = \frac{1}{2}$.

Convective Boundary Condition

Consider the same one-dimensional case, as above, subject to a convective boundary condition at its left-hand edge, as shown in Figure 3.11. Assume that the fluid temperature and heat transfer coefficient are known. Applying the energy balance method as before gives

$$\Delta y \Delta z h(T_{f,j} - T_{1,j}) + \Delta y \Delta z k(T_{2,j} - T_{1,j}) = \frac{\Delta x \Delta y \Delta z}{2} \rho C_p \frac{(T_{1,j+1} - T_{1,j})}{\Delta t}$$

Introducing Biot number (Bi)

$$Bi = \frac{h\Delta x}{k} = \frac{\text{surface conductance}}{\text{thermal conductivity of solid}}$$

and multiplying by $\frac{\Delta x}{\Delta y \Delta z k}$, after some rearrangement, the above equation will be

$$T_{1,j+1} = 2Fo\left(T_{2,j} + BiT_{f,j} + \left(\frac{1}{2Fo} - Bi - 1\right)T_{1,j}\right) \tag{3.35}$$

for stability $\left(\frac{1}{2Fo} - Bi - 1\right)$ is to be positive i.e. $Fo \leq \frac{1}{2+2Bi}$.

Similarly for the right-hand edge

$$T_{n,j+1} = 2Fo\left(T_{n-1,j} + Bi_c T_{c,j} + \left(\frac{1}{2Fo} - Bi - 1\right)T_{n,j}\right) \tag{3.36}$$

The above equations are written explicitly as the temperature in the $(j + 1)$ time row is expressed in terms of the (j) time row temperatures. Similarly Crank-Nicolson convective boundary condition for the left-hand edge will be

$$-BiFoT_{f,j+1}+(BiFo+Fo+1)T_{1,j+1}-FoT_{2,j+1}=$$

$$BiFoT_{f,j}-(BiFo+Fo-1)T_{1,j}+FoT_{2,j} \tag{3.37}$$

and for the right-hand edge

$$-Bi_cFoT_{c,j+1}+(Bi_cFo+Fo+1)T_{n,j+1}-FoT_{n-1,j+1}=$$

$$Bi_cFoT_{c,j}-(Bi_cFo+Fo-1)T_{n,j}+FoT_{n-1,j} \tag{3.38}$$

The subroutines adopted for the solution of both methods, explicit and Crank-Nicolson, are presented in appendix A.

Since in finite difference methods derivatives are replaced by finite differences, a truncation error will be generated. This error, according to Croft and Lilley (1977), depends on Fourier number, boundary conditions, initial given temperature distribution and the choice of the finite difference scheme. In addition, the accuracy of the scheme is mostly affected by the truncation error when the finite difference scheme is stable. It is now well established that the Crank-Nicolson scheme is more accurate than the explicit and implicit schemes as its truncation error is the smaller. By refining the space-time grid the approximate computed solution approaches the exact solution. This is known as convergence. As the time step in this case will be governed by the time step needed for the rest of the simulation ($\leq 100\mu s$), convergence could only be achieved by refining the space grid.

To demonstrate this point a small exercise was carried out. As the time step in the current simulation is varied between $10\mu s$ and $100\mu s$ the value of the space grid required for different values of Fourier number is calculated. The results are shown in Table 3.1 for the case of cast steel. It can be seen from the results that the value of the space grid decreases as the value of Fourier number increases. This means an increase in the number

of grid points required, and hence more computing time, for a fixed wall thickness. Table 3.2 shows that a compromise could be achieved by choosing a suitable space grid, and hence number of grid points, and allowing the Fourier number to vary with the time grid.

Since the implicit method requires more time to converge, it has been excluded from the current study. In order to find out the suitability of the explicit and Crank-Nicolson methods for the current simulation, both methods have been employed for an engine cycle. The gas temperature was allowed to vary during the engine cycle while the coolant temperature was kept constant. The wall thickness was kept constant.

It is clear from Figure 3.12 that the solution by using either method is consistent, when Fourier number is valid for the explicit method. Figure 3.13 shows that the explicit method, as expected, requires less computer time than the Crank-Nicolson method. Different numbers of space grids have been tried in order to achieve convergence. It is apparent that no significant gain will be obtained beyond 128 space grids, as shown in Figure 3.14. As a result of the above study both methods have been included. For low engine speeds with a more refined space grid, when $Fo \leq \frac{1}{2}$, the Crank-Nicolson method should be used. In addition, the user may select, in the data file, the number of space grids according to the degree of refinement required.

3.4.3 Heat Convection

Heat transfer due to forced convection may be expressed by

$$Q_c = hA(T_g - T_w) \tag{3.39}$$

where h is the heat transfer coefficient due to convection, A is the surface area and T_g and T_w are bulk gas and wall surface temperatures respectively. From the definition of Nusselt number

$$Nu = h\frac{l}{\kappa}$$

where l is the characteristic length and κ is the thermal conductivity, the heat transfer coefficient can be obtained, provided Nu is known. For flat plate and pipe flow, the heat transfer coefficient is usually calculated using a Nusselt-Reynolds numbers correlation of the form :

$$Nu = aRe^{b}Pr^{c} \tag{3.40}$$

where a, b and c are constants, Re is Reynolds number and Pr is Prandtl number. For engine work the Prandtl number is assumed to be constant, approximately equal to 0.7, and absorbed within the constant 'a'. Thus equation (3.40) will be reduced to :

$$Nu = aRe^{b} \tag{3.41}$$

The above correlation has been used by many researchers in the engine field. However large variations in the values of the constants a and b have been reported in the literature.

According to Holman (1981), the most widely used relation for turbulent flow in smooth pipes takes the form :

$$Nu = 0.023Re^{0.8}Pr^{0.4} \tag{3.42}$$

when comparing the above equation with equation (3.30), after neglecting Pr, the values of the constants are $a = 0.023$ and $b = 0.8$. Hassan (1971), has obtained the same values for the constants a and b on experimental investigation in a motored IDI swirl chamber. Kamel and Watson (1979), further verified these values for a Ricardo Comet MkVb

swirl chamber type but with $a = 0.012$ for the main chamber. Mansouri *et al* (1980), used $a = 0.035$ and $b = 0.8$ for both chambers and $a = 0.025$ for the passageway. Hiroyasu *et al* (1982) used the same values for the swirl chamber but he adopted for the main chamber the model due to Woschni of the form :

$$h = 110.0B^{-0.2}p^{0.8}(C_1C_m)T^{-0.53}$$

where B is the cylinder bore, p pressure, C_m is average piston speed, C_1 is a constant and T is temperature.

It was decided, for the current work, to use the existing model in SPICE for the prediction of heat transfer in the main chamber, see section 3.2.2. The decision was justified by the fact that the model has been tested and proved accurate enough for the prediction of the heat transfer in the main chamber of a DI engine. Furthermore the work carried out by Hiroyasu *et al* (1982) proved that a good agreement between the theoretical and experimental results can be achieved using the model due to Woschni for the main chamber.

The approach in this work, for the swirl chamber prediction of convective heat transfer, was to give the user the liberty to choose between two models in the data file. The first model uses equation (3.41) with values of a and b similar to those used for turbulent flow in smooth pipes i.e. $a = 0.023$ and $b = 0.8$. The characteristic length was taken, according to Hassan (1971), as the circumference of the swirl chamber. The characteristic velocity was taken as the local gas velocity which has been calculated using the model based on conservation of angular momentum and solid body rotation as described in section 3.3. Gas properties were evaluated at bulk mean gas temperature.

The second model is based on the classic correlation of convective heat transfer over a flat plate. Consider the case of laminar flow of a fluid at a temperature T_∞ flowing with

a velocity U_∞ over a flat plate as shown in Figure 3.15. Assume that the fluid has $Pr >$ 1, as in the case of liquids. The velocity boundary layer(δ), which starts to develop at the leading edge of the plate, is thicker than the temperature boundary layer (δ_T), which starts to develop at $x = x_o$. According to Özisik (1985), the local Nusselt number N_x is given by

$$Nu_x = 0.332 Re_x^{1/2} Pr^{1/3} \qquad \text{(exact) for} \quad Re_x < 5 \times 10^5 \tag{3.43}$$

Although the above expression is derived on the assumption $Pr > 1$, Özisik (1985) stated that it is valid in the range $0.6 < Pr < 10$ which covers most gases and liquids. The average heat transfer coefficient h_m over the length of the plate from $x = 0$ to $x = L$ is defined as

$$h_m = \frac{1}{L} \int_0^L h_x dx$$

and since

$$Nu_x = h(x) \frac{x}{k}$$

which will lead to the definition of the average Nusselt number for laminar flow along a flat plate as

$$Nu_m = 0.664 Re_L^{1/2} Pr^{1/3} \qquad \text{(exact) for} \quad 0.6 < Pr < 10 \tag{3.44}$$

In a turbulent flow a transition takes place in the boundary layer from laminar to turbulent flow in the range of Reynolds numbers from 2 x 10^5 to 5 x 10^5 for flow over a flat plate. Above this value the flow in the boundary layer is turbulent and the Nusselt number can be expressed as

$$Nu_x = 0.029 Re_x^{0.8} Pr^{0.43} \quad (3.45)$$

valid for $Re_x > 2 \times 10^5$ to 5×10^5.

When the flow is turbulent over a flat plate the boundary layer is always initially laminar and the averaging must be performed over both regions. According to Özisik (1985), the average Nusselt number over the laminar and turbulent regions is

$$Nu_m = 0.036 Pr^{0.43} (Re_L^{0.8} - Re_c^{0.8}) + 0.664 Re_c^{0.5} Pr^{1/3} \quad (3.46)$$

valid for $Re_L > Re_c$, where $Re_L = \frac{U_\infty L}{\mu}$ and Re_c = critical Reynolds number for transition.

Figures 3.16a and 3.16b show the average heat transfer coefficient over the swirl chamber surface over the laminar and the laminar and turbulent regions respectively.

Convection heat transfer through the throat is modelled assuming a fully developed pipe flow i.e. equation (3.42)

The local velocity used above is calculated on the basis of motoring conditions. This has to be modified under fired operation as the fuel injected into the swirl chamber will affect the swirl motion of the air. Kamel *et al* (1979) have shown, Figure 3.17, that there is a considerable effect of velocity enhancement, due to the fuel jet, on the predicted heat flux for the swirl chamber. The method adopted for the current calculation could use the principle of conservation of angular momentum to work out the new value of the air velocity due to fuel injection. It may be assumed that the linear momentum flux of the fuel at the outlet of the injector will contribute to the angular momentum of the air in the swirl chamber. Thus the momentum of the fuel will be

$$= \frac{dm_f}{dt} V_f R_f$$

where $\frac{dm_f}{dt}$ is the fuel injection rate, V_f is the velocity of the fuel jet and R_f is the perpendicular distance between the injector axis and the swirl chamber axis. The velocity of the fuel jet is obtained from

$$V_j = \sqrt{2g\frac{\Delta p}{\rho_f}}$$

where Δp is the instantaneous pressure difference between the injection pressure and the swirl chamber pressure and ρ_f is the density of the fuel.

3.4.4 Heat Radiation

Although radiation is always present in diesel engines, it is negligibly small at low and medium temperatures (up to 1273 K, say). During an engine cycle the radiative heat transfer varies between 0 and over 30% of the total heat transfer for small and medium size engines. In very big diesel engines, over 1 m bore, the radiant component would account for up to 75% of the total heat transfer, see Oguri and Inaba (1972). As reported by Sato *et al* (1966), radiation from luminous flames is composed of the radiation from non-luminous or optically transparent gases such as carbon dioxide (CO_2), water vapour (H_2O) and carbon monoxide (CO) and the radiation from luminous or optically non-transparent soot particles formed in the combustion gas. According to Sitkei (1972), radiation in internal combustion engines appears of importance only in multi-atomic heteropolar gases such as CO_2 and H_2O, rather than gases with symmetrical molecules (hydrogen, oxygen, etc.).

The radiation heat transfer rate across an area A from a black body at temperature T_1 to another at temperature T_2 parallel to it through space containing no absorptive material can be defined as

$$Q_r = A\sigma(T_1^4 - T_2^4)$$

where $\sigma = 5.67 \times 10^{-}8W/(m^2.K^4)$ is the Stefan-Boltzmann constant. The spectral radiation intensity emitted by a real surface is always less than that of a black body. In order to compensate for this deviation a definition of gray body has been introduced as

$$Q_r = A\varepsilon\sigma(T_1^4 - T_2^4)$$

where ε is defined as the emissivity of the body ($0 \leq \varepsilon \leq 1$). In engine application the radiative heat flux, according to Kunitomo *et al* (1975), is given by

$$Q_r = \varepsilon_f\sigma(T_f^4 - T_w^4) \tag{3.47}$$

where T_f and T_w are flame and wall temperatures respectively, the flame emissivity ε_f is obtained by

$$\varepsilon_f = 1 - (1 - \varepsilon_s)(1 - \varepsilon_g) \tag{3.48}$$

where

$$\varepsilon_g = 1 - (1 - \varepsilon_{CO_2})(1 - \varepsilon_{H_2O}) \tag{3.49}$$

and ε_s is the soot emissivity.

The calculation of gas and soot emissivity procedure, adopted after Kamel and Watson (1979), is as follows :

The volume fraction y_i of CO_2 and H_2O is calculated from the overall excess air ratio ϕ and the specific gravity of fuel γ, after Kunitomo and Kodama (1974)

$$y_{CO_2} = 0.038\gamma - 2.619(1.01-\gamma)(\phi - 1.05)^2 + 0.092 \qquad for \quad \phi \le 1.1$$

$$= 0.075\phi + 0.033\gamma + 0.175 \qquad for \quad \phi > 1.1$$

$$y_{H_2O} = 0.126 - 0.72\{\phi + 0.887\gamma - 1.724 - 1.42(\phi - 0.805)^2\} \qquad for \quad \phi < 1.05$$

$$= 0.0783\phi - 0.068\gamma + 0.259 \qquad for \quad \phi \ge 1.05$$

from which the partial pressure $p(\theta)$ is evaluated

$$p(\theta) = x(\theta).y_i.p_c(\theta) \tag{3.50}$$

where $x(\theta)$ is the fuel fraction burnt, known from the assumed heat release pattern and $p_c(\theta)$ is the chamber pressure.

The gas emissivity is expressed by, after Stikei (1974), at atmospheric pressure i.e. $p_c(\theta) = 1$;

$$\varepsilon_{CO_2} = 0.711(p.L)^{0.333} \Big/ \left(\frac{T}{100}\right)^{0.5}$$

$$\varepsilon_{H_2O} = 0.707(p.L)^{0.6}(p)^{0.2} \Big/ \left(\frac{T}{100}\right)$$

where L is the radiation length which, according to Kamel and Watson (1979), is considered to be equal to swirl chamber diameter, T is the gas temperature and p ($p(\theta)$) is the partial pressure of each gas, obtained from equation (3.50).

Kunimoto *et al* (1975) expressed the soot emissivity as a function of gas emissivity, excess air ratio and chamber pressure :

$$\varepsilon_s = 1 - \exp\left[p_c^m(\theta).\ln\left\{1 - \varepsilon_{g_{p=1}}\left(\frac{0.09}{\phi^2 - \gamma^2 + 0.35\gamma - 0.38} + 6.8\gamma - 5.95\right)\right\}\right] \tag{3.51}$$

where

$$m = \frac{4.95}{\phi + 1.5} - 0.25$$

Kamel (1977) calculated the gas emissivities at high pressures by curve fitting mean absorption coefficients obtained by Abu-Romia and Tien (1967);

$$K_{CO_2} = 102.280 - 0.11108T_g + 0.42221E - 5T_g^2 - 5.36838E - 9T_g^3$$

$$K_{H_2O} = 52.054 - 0.08882T_g + 5.26603E - 5T_g^2 - 10.4314E - 9T_g^3$$

the gas emissivity can then be calculated, after Sitkei and Ramanaiah (1972),

$$\varepsilon_g = 1 - e^{KpL} \tag{3.52}$$

By substituting equations (3.51) and (3.52) into equation (3.48) the flame emissivity ε_f can be obtained.

3.5 Summary

This chapter has explained, in detail, the development of the mathematical model adopted for simulating the air motion and heat transfer in the IDI diesel engine. The computer program SPICE has been described. The numerical solution adopted in SPICE has been discussed and the program flow chart has been presented. The module used for calculating the air motion in the swirl chamber with its theoretical and empirical equations is presented. Transient heat conduction, convective and radiative heat transfer are also presented.

$Fo = 0.5$, $\alpha = 7.15E-6, m^2/s$, $x = 0.008, m$

$\Delta t, \mu s$	10	20	50	100
$\Delta x, m$	1.2E-5	1.7E-5	2.67E-5	3.78E-5
Number of space grid	670	474	300	213

$Fo = 0.25$, $\alpha = 7.15E-6, m^2/s$, $x = 0.008, m$

$\Delta t, \mu s$	10	20	50	100
$\Delta x, m$	1.69E-5	2.4E-5	3.78E-5	5.35E-5
Number of space grid	474	336	213	151

$Fo = 0.1$, $\alpha = 7.15E-6, m^2/s$, $x = 0.008, m$

$\Delta t, \mu s$	10	20	50	100
$\Delta x, m$	2.76E-5	3.78E-5	5.98E-5	1.2E-4
Number of space grid	300	213	135	96

$Fo = 0.01$, $\alpha = 7.15E-6, m^2/s$, $x = 0.008, m$

$\Delta t, \mu s$	10	20	50	100
$\Delta x, m$	8.5E-5	1.2E-4	1.9E-4	2.8E-4
Number of space grid	95	68	43.3	30

Table 3.1 Study of Variation of Space Grid with a Variable Fourier Number

Number of grid points = 128, $\alpha = 7.15E-6, m^2/s$, $x = 0.008, m$

$\Delta t, \mu s$	10	20	50	100
Fo	0.018	0.036	0.09	0.18

Table 3.2 Study of Variation of Fourier Number with Constant Space Grid

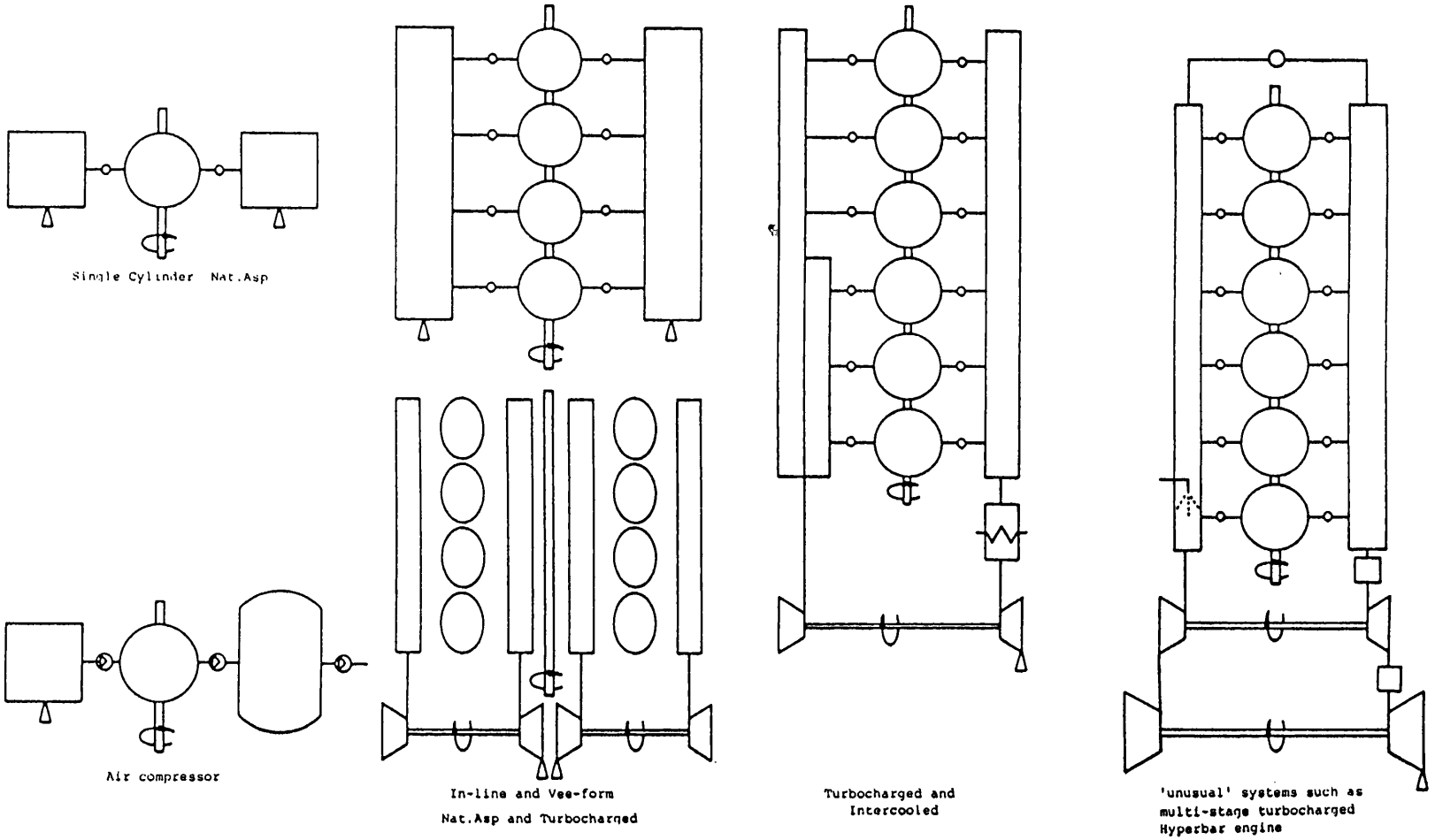

Figure 3.1 Some of the systems that may be modelled by using SPICE, Charlton (1986)

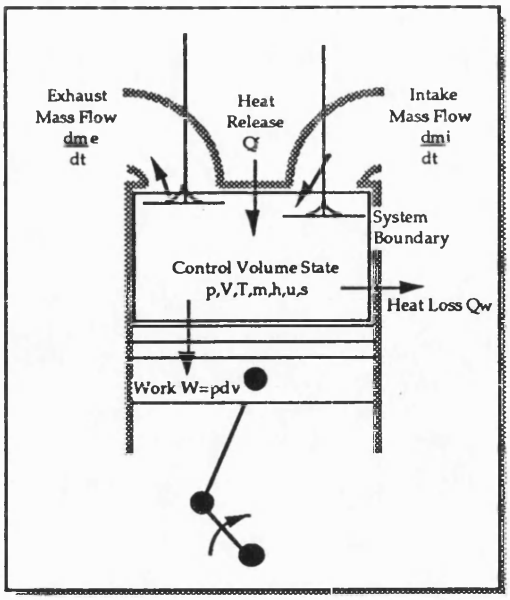

(a)

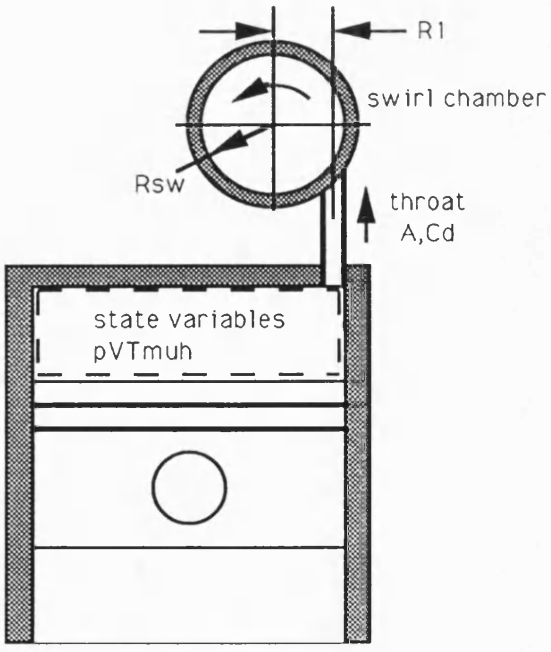

(b)

Figure 3.2 Thermodynamic control volume representation of (a) an engine cylinder

(b) the Comet swirl chamber

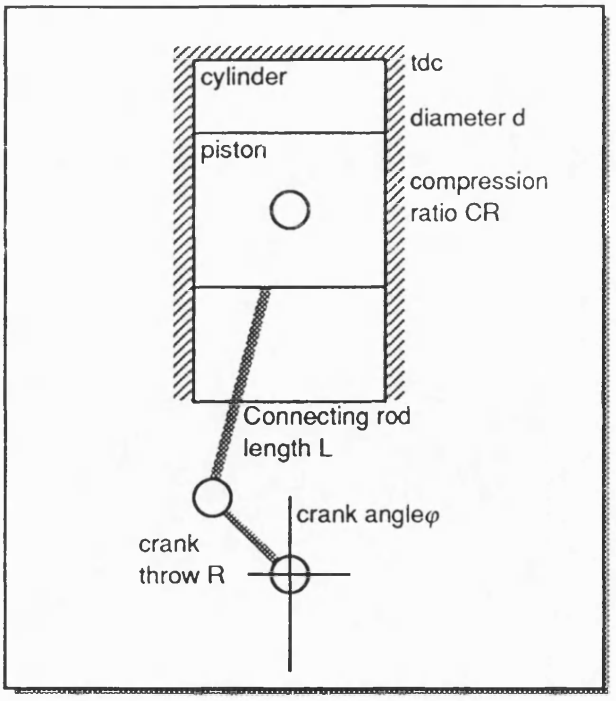

Figure 3.3 A slider crank mechanism, Charlton (1986)

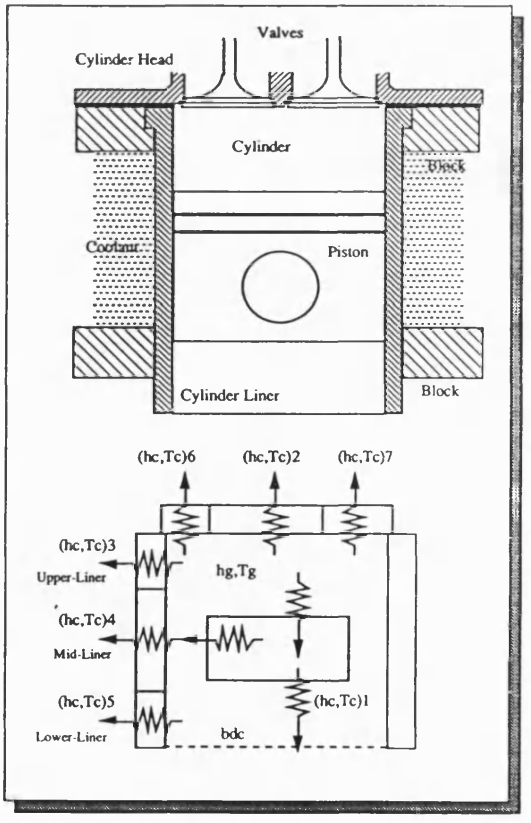

Figure 3.4 Thermal resistance analogue of combustion chamber, Charlton (1986)

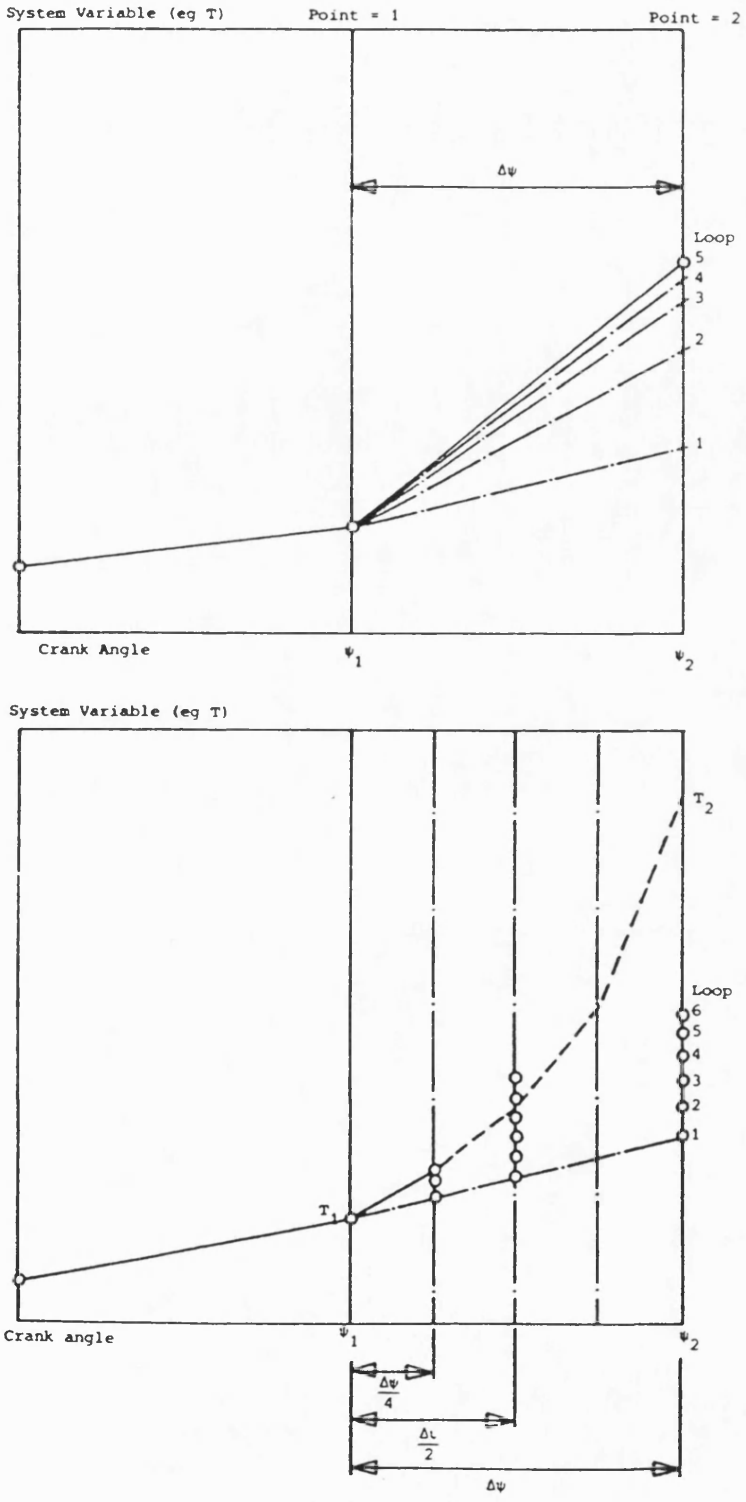

Figure 3.5 Graphical presentation of the predictor-corrector numerical solution within SPICE. Upper curve, solution found without reduction of step size. Lower curve, step-size reduced to $\frac{\Delta\psi}{4}$, Charlton (1986)

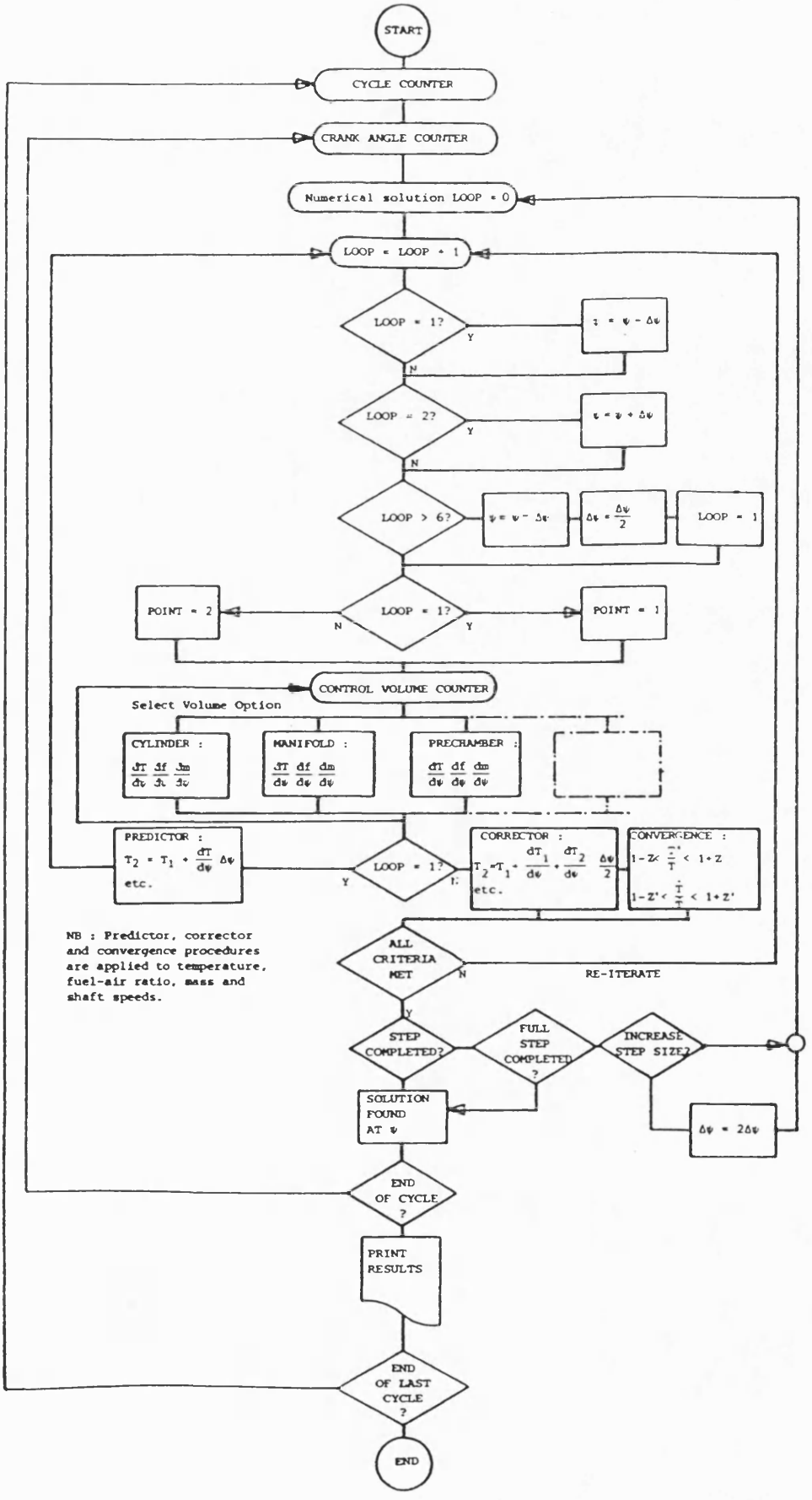

Figure 3.6 Flow diagram for SPICE, Charlton (1986)

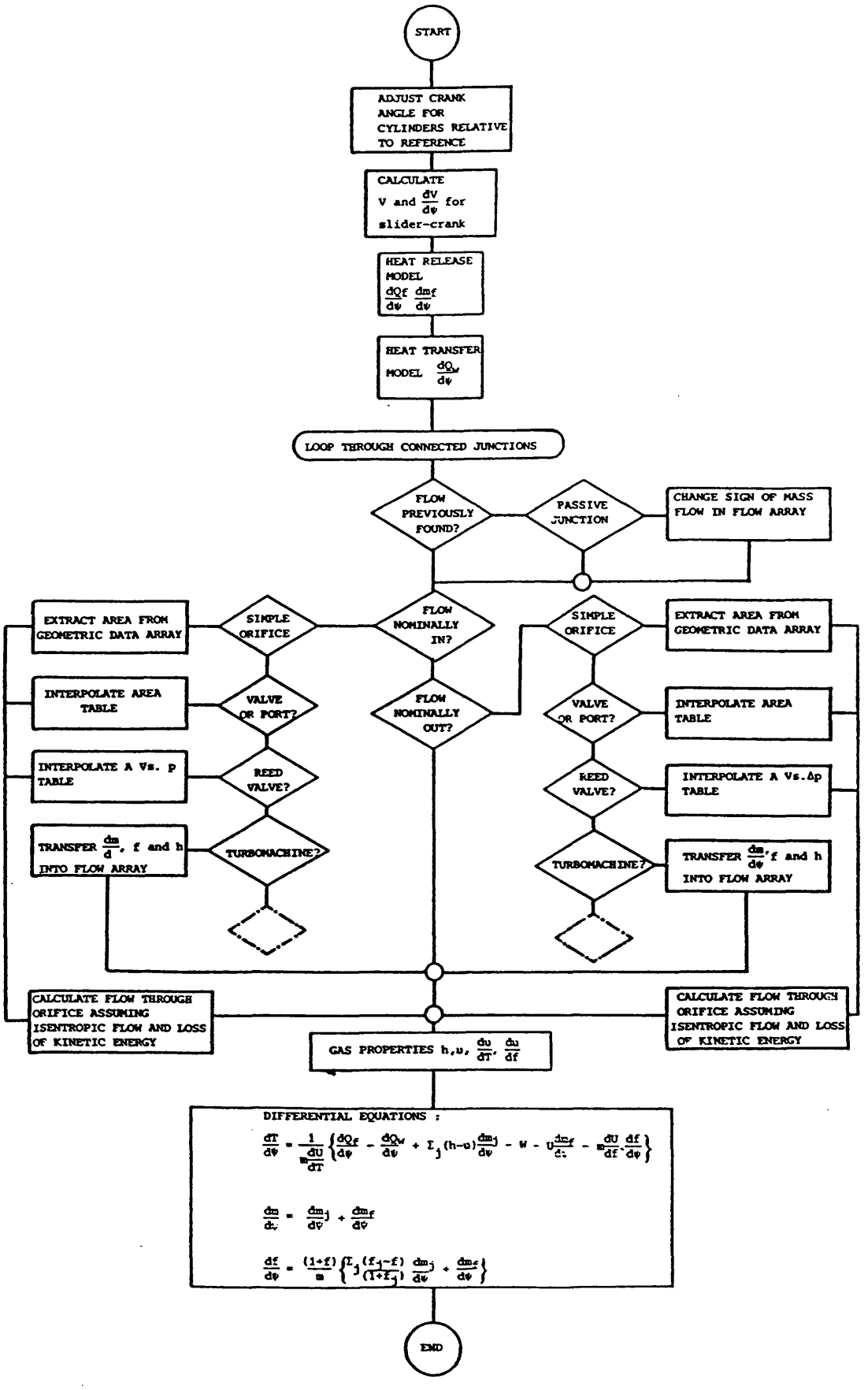

Figure 3.7 Control volume flow diagram, Charlton (1986)

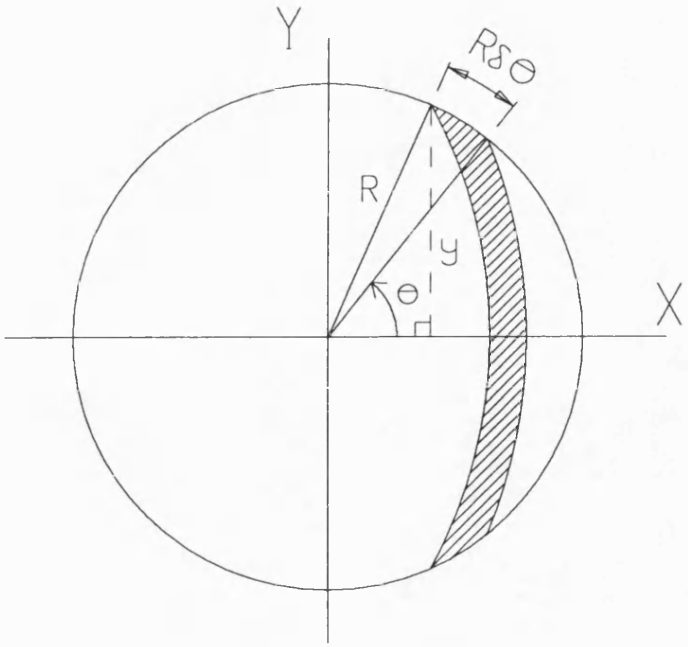

Figure 3.8 Elemental surface area in spherical swirl chamber

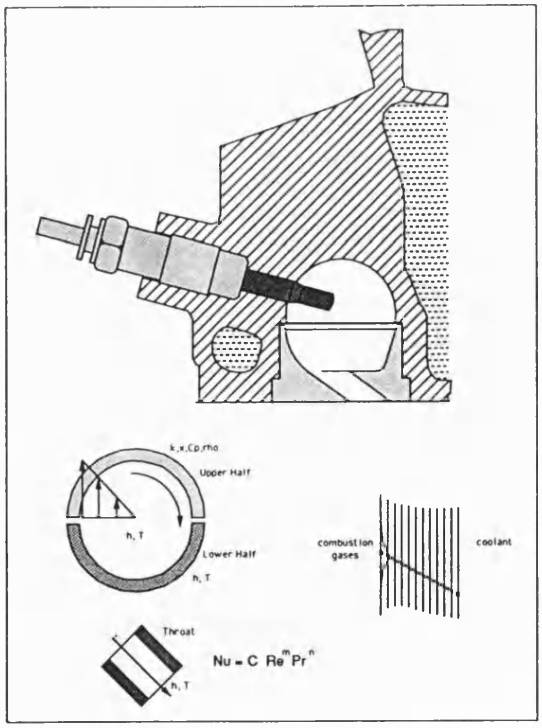

Figure 3.9 Heat transfer model of swirl chamber

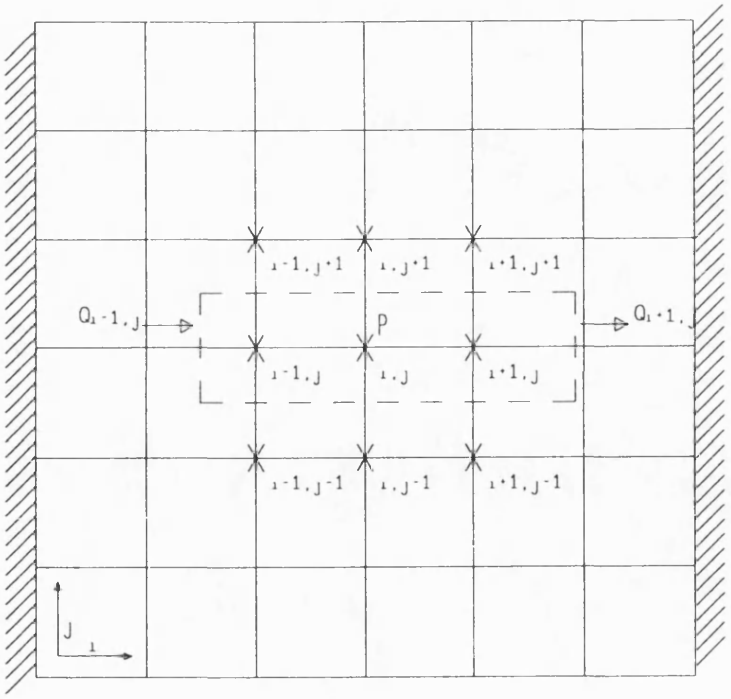

Figure 3.10 Transient heat conduction through an engine wall

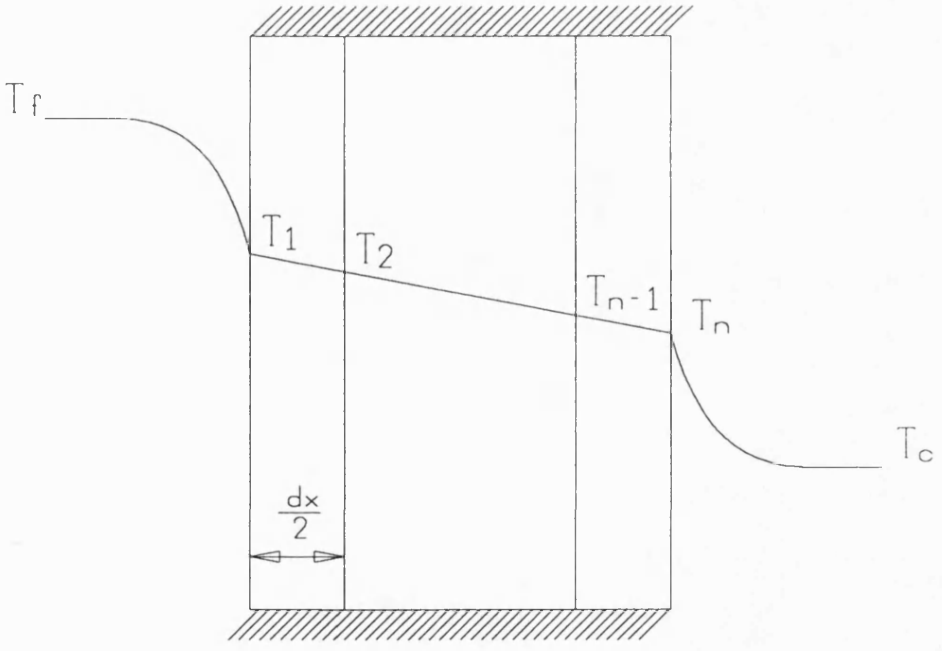

Figure 3.11 Temperature profile across a 1-D convective boundary surface

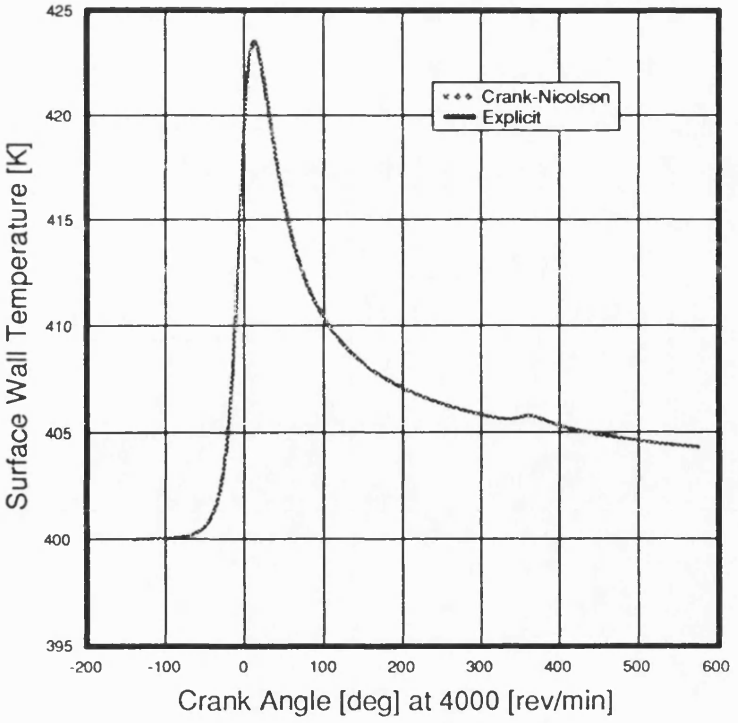

Figure 3.12 Comparison of Finite difference solution using Crank-Nicolson and Explicit methods

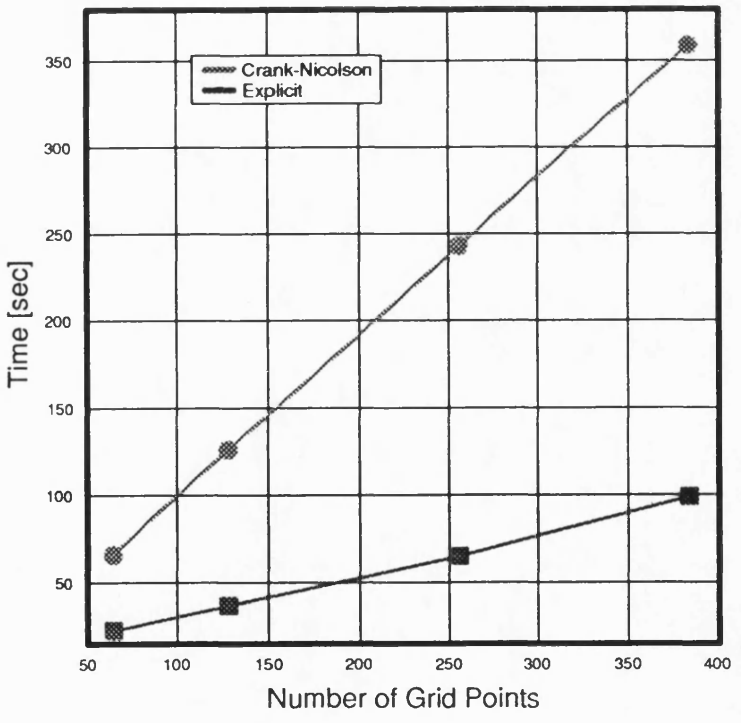

Figure 3.13 Effect of number of grid points on CPU time

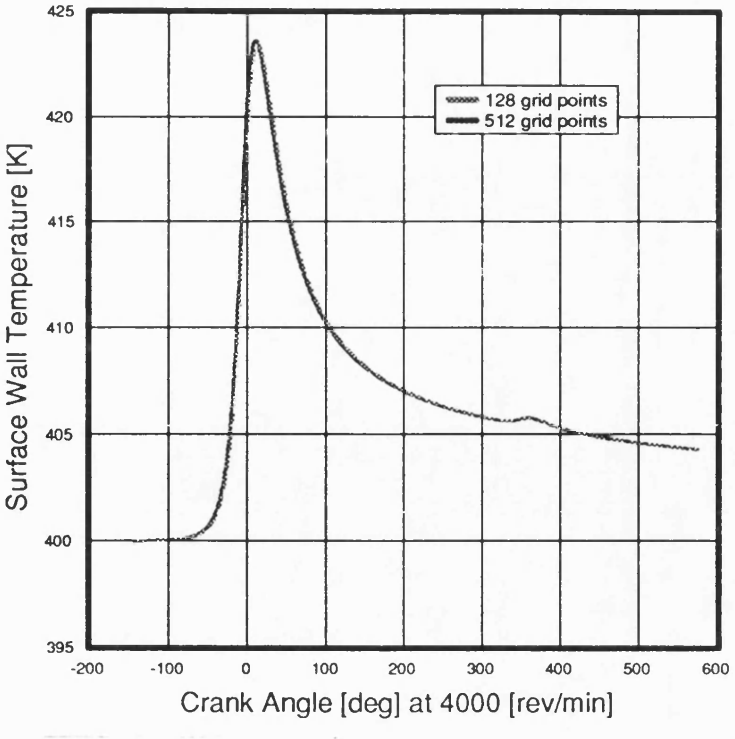

Figure 3.14 Effect of number of grid points on the finite difference solution

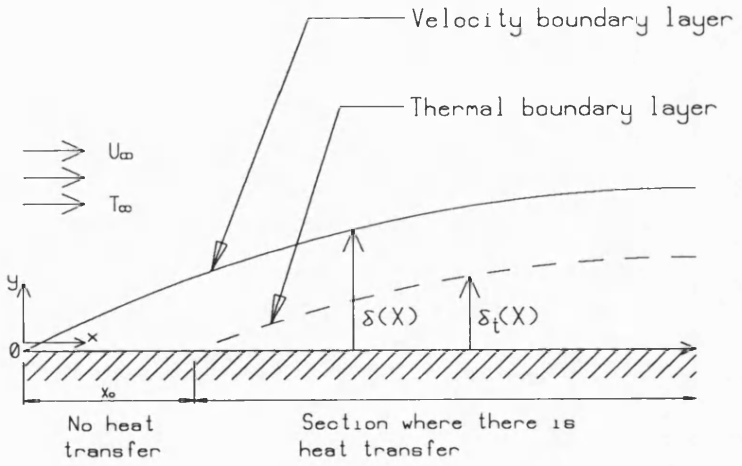

Figure 3.15 Velocity and Temperature boundary layer over a flat plate

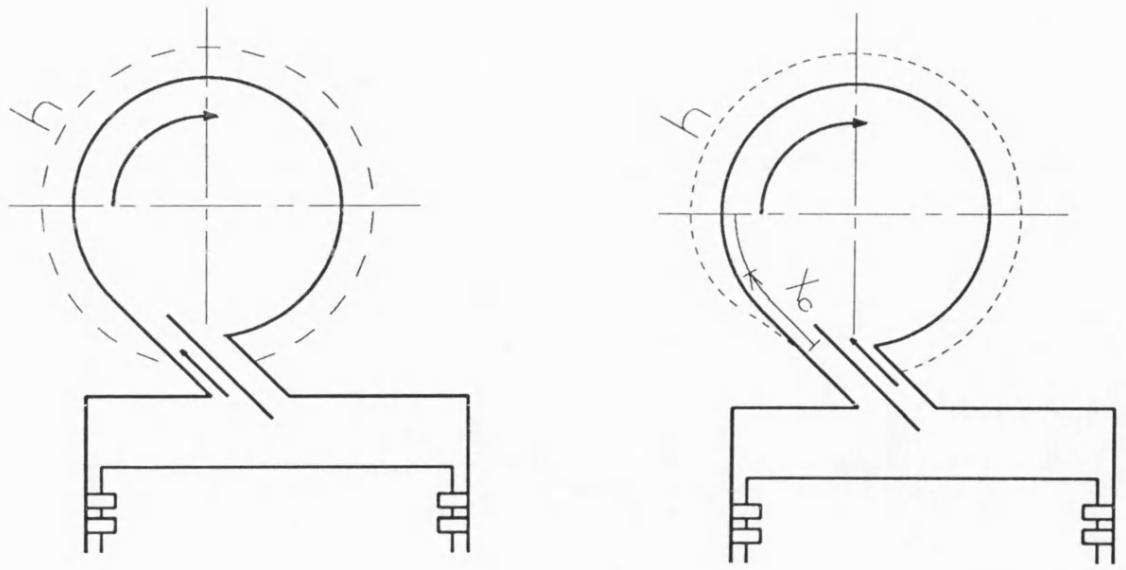

(a) (b)

Figure 3.16 Average heat transfer coefficient over swirl chamber surface (a) laminar (b) laminar and turbulent

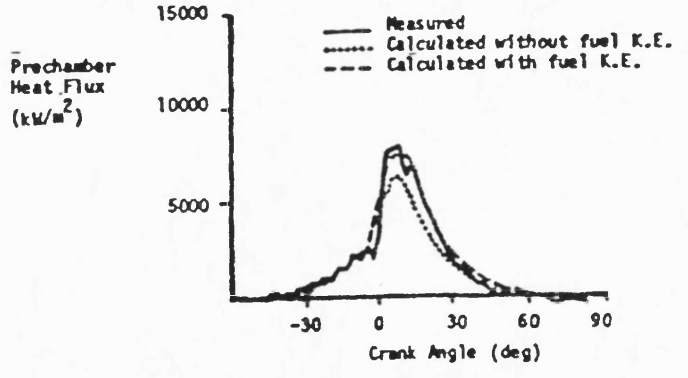

Figure 3.17 Effect of fuel kinetic energy (1320 rev/min and 40% load), Kamel and Watson (1979)

CHAPTER 4

HOT WIRE ANEMOMETRY

4.1 Introduction

Hot wire anemometry is a suitable technique for the measurement of instantaneous gas velocity and temperature in the swirl chamber of the motored IDI experimental engine. Although laser doppler anemometry is a more sophisticated technique for velocity measurements, it is less attractive in terms of its high cost and the requirement of optical access which might be difficult in the case of the swirl chamber of a small IDI engine. To the author's knowledge no one has attempted to measure gas velocity and temperature in an internal combustion engine at Bath before, and the hot wire anemometry equipment available had only been used to measure air flow in a wind tunnel, (Wood, 1981), and high swirl constant volume combustion rig, (Packer, 1983). Two Thermo-Systems Inc. (TSI) 6.3 micron single-wire Platinum-Iridium probes were purchased for the project. The first probe broke during calibration and the second one during the first cycles while running the engine. It was realised then that it will be costly and time consuming to send the probes to TSI for repair which prompted the decision to design and manufacture the probes in-house.

This chapter is intended to present in detail the application of hot wire anemometry to the measurement of instantaneous gas velocity and temperature in engines. This includes the theory of hot wire anemometry which covers heat transfer between the wire and the surroundings, directional sensitivity of the wire and methods used for temperature compensation. In addition, resistance thermometry and wire frequency response will be discussed.

4.2 Theory of Hot Wire Anemometry

The hot wire anemometer is operated in either of two modes. The first mode, which is the most widely used, is a constant temperature (resistance) mode in which the sensor wire is maintained at constant resistance, and hence temperature, by varying the heating current (by using a high gain feedback amplifier) in response to changes in flow velocity. The second mode is a constant current mode in which the sensor wire is supplied with a constant current, by a constant current power supply, and the changes in the wire resistance caused by the cooling effect of the flow is related to the flow velocity. The sensing element is normally inserted into one arm of a Wheatstone bridge circuit, with two fixed resistors and one adjustable resistor to complete the circuit. In the case of a constant temperature anemometer the bridge balance is adjusted by using a differential feedback amplifier. The circuits for both modes are shown in Figures 4.1 and 4.2. In the constant current mode the current has to be increased during high velocity measurements to acquire good sensitivity. Also it has to be decreased during low velocity measurements in order not to burn out the wire. According to Lomas (1986), (see section 4.7) the frequency response of the constant current anemometer is far too low to allow the probe to be used for turbulence measurements without frequency compensation. Consequently, the constant current mode, although simpler to build than the constant temperature anemometer, is not used for flow measurements where high velocity fluctuations are encountered.

4.3 Heat Transfer from an Electrically Heated Wire

Consider the thermal equilibrium of a differential element of length dx and cross-sectional area A of a fine electrically heated wire placed in a uniform flow of air as shown in Figure 4.3. Let the total wire length be equal to $2l$ and since the temperature profile of the wire in uniform flow will be symmetrical about the centre of the wire, let the origin

be at the mid-point of the wire length. It is assumed that there is no radial temperature gradient since the wire has a small diameter (order of 10^{-6}) and the thermal conductivity of the wire is larger than that of air, as reported by Davies and Fisher (1964).

Heat is generated in this element by the electrical current and dissipated to the fluid by convection and radiation. Close to the ends there will be conduction to the support needles to which the element is attached. In addition there is heat storage in the wire element.

Heat input due to electrical energy supplied to the element is

$$q_e = I^2 \frac{\rho_T}{A} dx \tag{4.1}$$

where I is the heating current and ρ_T is the resistivity of the wire at temperature T.

Heat convection to the fluid is

$$q_h = \pi d h (T - T_f) dx \tag{4.2}$$

where d is the wire diameter, h is the coefficient of heat transfer and T_f is the temperature of the fluid.

Heat radiation to the surroundings is

$$q_r = \pi d \sigma \varepsilon (T^4 - T_s^4) dx \tag{4.3}$$

where σ is Stephan-Boltzman constant, ε is the wire emissivity and T_s is the temperature of the surroundings.

Conduction heat transfer is

$$q_c = A\frac{\delta}{\delta x}\left(k_T\frac{\delta T}{\delta x}\right)dx \tag{4.4}$$

where k_T is the thermal conductivity of the wire material at temperature T.

Heat storage in the element of length dx is

$$q_s = \rho c A\frac{\delta T}{\delta t}dx \tag{4.5}$$

where ρ is the density of the wire, c its specific heat capacity and t is time.

Thermal equilibrium of the element will be expressed as

$$q_e - (q_h + q_r + q_c + q_s) = 0 \tag{4.6}$$

substituting from (4.1) to (4.5) into (4.6) yields after some rearrangement

$$A\frac{\delta}{\delta x}\left(k_T\frac{\delta T}{\delta x}\right) + I^2\frac{\rho_T}{A} - \rho c A\frac{\delta T}{\delta t} - \pi d h(T - T_f) - \pi d\sigma\varepsilon(T^4 - T_s^4) = 0 \tag{4.7}$$

4.3.1 Radiation Heat Transfer from Hot Wires

In general, radiation heat transfer from the wire to the surroundings is assumed to be negligible but to be certain it should be calculated for this project since relatively high wire temperatures are to be used (600°C). The emissivity of the wire has been determined by Schmidt and Cresci (1971). They constructed a wire with a very long length-to-diameter (aspect) ratio (of approximately 10^5) in order to drop the conduction heat loss from the wire. Then they placed the probe in a very low pressure environment (evacuated

bell jar) so that convection heat loss term can also be dropped. In this manner, all of the electrical heating is dissipated by radiation to the surroundings, and the effective emissivity can be computed (equation 4.3). By using the temperature resistance relationship (equation 4.9) and by setting the wire at different temperatures electrically they determined the emissivity by measuring the applied voltage. They found that the tests gave values of emissivity roughly two and a half times the previously accepted values. They attributed the discrepancy to the change in surface properties of the wire due to heating, collection of dust and erosion.

In order to calculate the radiation heat transfer from the whole wire length used in this project equation (4.3) can be modified assuming that the wire radiates as a black body:

$$q_r = \pi d l \sigma (T^4 - T_s^4)$$

Then for $d = 10E-6m$, $l = 2.5E-3m$, $\sigma = 5.67E-8 \frac{W}{m^2K}$

$$T = 873K, T_s = 293K$$

$$q_r = 3.96E-3W$$

At zero flow the electrical heat input to the wire will be at its minimum value and will yield typical values of

$I = 0.47A, R = 11.86\Omega$ which will give

$$q_e = I^2R$$

$$= 2.5W$$

2.62

Then % heat loss by radiation from total electrical input to the wire

$$= \frac{3.96E-3}{2.5} \times 100\%$$

$$= 0.15\%$$

4.3.2 Temperature Distribution along a Hot Wire

The total resistance of the wire is expressed as :

$$R = \frac{1}{A}\int_{-l}^{l} \rho_T dx \tag{4.8}$$

By assuming, after Davies and Fisher (1964), that radiation losses are negligible and that the wire temperature does not vary with time when operated in the constant temperature mode, the thermal conductivity of the wire material is constant and that the resistivity of the wire material obeys the simple relation,

$$R = R_o(1 + \alpha(T - T_o)) \tag{4.9}$$

after Hinze (1959). Where α is the temperature coefficient of resistance and the subscript o indicates some reference temperature.

then equation (4.7) will reduce to:

$$\frac{\delta^2 T}{\delta^2 x} + \left[\frac{\alpha I^2 R_o}{2Akl} - \frac{\pi dh}{Ak}\right](T - T_f) + \frac{I^2 R_o}{2Akl} = 0 \tag{4.10}$$

Since the fluid temperature is constant along the wire then,

$$\frac{\delta^2 T_1}{\delta x^2} + K_1 T_1 + K_2 = 0 \tag{4.11}$$

where

$$T_1 = T - T_o, \quad K_1 = \frac{\alpha I^2 R_o}{2Akl} - \frac{\pi dh}{kA} \quad and \quad K_2 = \frac{I^2 R_o}{2kAl}$$

With boundary conditions

$$\frac{dT}{dx} = 0 \qquad at \qquad x = 0$$

$$T = T_o \qquad at \qquad x = \pm l$$

If some mean value of h is assumed K_1 is a constant. For most values of h, K_1 is negative. The solution of (4.11) is then

$$T_1 = \frac{K_2}{K_1}\left[\frac{\cosh\sqrt{|K_1|}\,x}{\cosh\sqrt{|K_1|}\,l} - 1\right] \tag{4.12}$$

This equation represents the temperature distribution along a hot wire when convection and conduction effects are included. The temperature distribution along a wire has been calculated numerically and measured experimentally by Champagne, Sleicher and Wehrmann (1967). They used an infra-red radiometric microscope with a special resolution of 7.6 micron, as shown in Figure 4.4. A summary of the temperature distribution that they measured is shown in Table 4.1. Figures 4.5, 4.6 and 4.7 show the results of the temperature distribution along hot wires having aspect ratios of 99, 202 and 400 respectively. It can be noticed that the temperature along the wire becomes more constant as the aspect ratio of the wire increases. Equation (4.12) can further be integrated along the wire length to give the mean temperature of the wire :

$$\overline{T}_w = \frac{1}{l}\int_{-l}^{+l} T_w dx$$

$$\overline{T}_w = \frac{K_2}{K_1}\left[\frac{\tanh\sqrt{|K_1|}\,l}{\sqrt{|K_1|}\,l} - 1\right] \tag{4.13}$$

4.3.3 Conductive Heat Loss to the Wire Supports

Conductive heat loss to the two wire supports can be obtained from equation (4.4)

$$q_c = 2Ak_T\left|\frac{\delta T_1}{\delta x}\right|_l$$

The temperature gradients at the ends of the wire can be found by differentiating equation (4.12) to give conduction heat loss to the supports :

$$q_c = 2k_T A\frac{K_2}{\sqrt{|K_1|}}\tanh\sqrt{|K_1|}\,l \tag{4.14}$$

This equation can be solved by evaluating the constants K_1 and K_2. Lomas (1986), pointed out the difficulties of obtaining accurate values of physical properties ($k and R$), length and diameter of the wire and since K_1 contains h which cannot easily be measured this makes the calculation of conduction end loss of the wire difficult. Davies and Fisher (1964), calculated the heat loss to the wire supports by placing the hot wire probe in a vacuum chamber at a pressure less than $10^{-4} atm$ so that the heat generated by the wire is lost to the wire supports since convection and radiation (less than 0.5% of total losses) are then negligible. They solved equation (2.7) in a dimensionless form to obtain temperature distribution along the wire which is shown in Figure 4.8. The results of their calculations of the end loss expressed as a fraction of the total heat supply is shown in Figure 4.9. Schmidt and Cresci (1971), determined the thermal conduction loss by a

similar procedure as in the case of determining the radiation heat loss but their values where 20 percent higher than those given in various handbooks, this they also attributed to surface changes due to dust and erosion. Champagne *et al* (1967), determined the end conduction losses for wires with 99, 202 and 400 aspect ratios, which are shown in Table 4.1. It can be noticed that the end conduction loss decreases with increase of aspect ratio.

A rough estimation of the end conduction loss for the wires used in this project will be useful. Since conduction loss is maximum when h is zero (at zero flow). With typical values at zero flow of :

$I = 0.47 \quad A, \quad R_o = 6.1 \quad \Omega, \quad k = 38.0 \quad \frac{W}{mK},$

$\alpha = 0.0016 \quad /K, \quad d = 10 \quad \mu m, \quad 2l = 2.5 \quad mm$

which gives

$K_1 = 288.956E6$

$K_2 = 180.597E9$

substituting the above values in equation (4.14) to give conduction heat loss to the wire supports:

$q_c = 0.0634 \quad W$

As before % heat loss from the total electrical input to the wire:

$$= \frac{0.0634}{2.26} \times 100\%$$

$$= 2.81\%$$

Of course this value does not represent the true value as the observed voltage from the

bridge output includes also heat loss by natural convection since the wire was maintained at $873K$ and the air flow at $293K$.

4.3.4 Heat Loss by Convection to the Surroundings

In practice, the hot wire transfers the majority of its heat by convection to the surroundings. The heat loss by convection can be evaluated if the value of the convective heat transfer coefficient (h) in equation (4.2) can be determined. The task of determining h is not simple since it is a function of the fluid flow, thermal properties of the fluid and geometry of the wire. The hot wire transfers heat by conduction to the fluid layer immediately adjacent to it thus equation (4.2) can be rewritten for the whole length of the wire as :

$$q_h = \pi d l h (T - T_f) = -k_f \pi d l \left(\frac{\delta T}{\delta y}\right)_{y=0}$$

from which the dimensionless Nusselt number can be introduced as :

$$Nu = \frac{hd}{k_f} = -\frac{\left(\frac{\delta T}{\delta y}\right)_{y=0}}{(T - T_f)/d} \tag{4.15}$$

Many experimental heat-transfer correlations have been suggested. King (1914), proposed the most well-known heat transfer empirical relationship for a wire assuming potential flow of gas existed over the wire :

$$Nu = A + BRe^{0.5}$$

where A and B are constants to be evaluated by wind-tunnel calibration and

$$Re = \text{Reynolds Number} = \frac{\rho U d}{\mu}$$

Davies and Fisher (1964), offered a different correlation from that of King, indicating that the above correlation is not satisfactory because of conduction losses to the supports. They expressed the coefficient of local heat transfer as:

$$h_w = \frac{C_f \rho U c_v k_w}{\pi k_o}$$

where C_f is the skin friction coefficient and c_v is the specific heat at constant volume.

Hassan and Dent (1971), corrected the method of Davies and Fisher (1964) for operation of the wire at high temperature in a high temperature and density gas environment. They corrected the velocities computed by the above method as follows:

$$U = U_{D.F.} \left[\frac{T_w}{T_g}\right]^{0.3}$$

$$U = U_{D.F.} \left[\frac{T_m}{T_g}\right]^{0.5}$$

where $U_{D.F.}$ is the velocity computed by Davies and Fisher (1964) method and T_m is the mean film temperature defined as

$$T_m = \frac{T_w + T_g}{2}$$

The most widely used correlation, with various modifications, has been proposed by

Collis and Williams (1959) who recommended an expression of the form:

$$Nu\left(\frac{T_m}{T_g}\right)^{-0.17} = A + BRe^n$$

Tindal, Brown and Kyriakides (1982), after some experimental investigation of the flow at high pressure and temperature recommended the above correlation with different value of the index of the temperature loading factor

$$Nu\left(\frac{T_m}{T_g}\right)^{0.5} = A + BRe^n \tag{4.16}$$

At zero flow, heat is dissipated from the hot wire by conduction to the supports and by natural convection to the surroundings. By adopting the Davies and Fisher method at zero flow the natural convection term is not allowed for and all the heat will be dissipated to the wire supports which can be calculated using equation (4.14). In practice, equation (4.14) can not be used to obtain the heat loss to the wire supports, see section 4.3.3. Accordingly, it was decided to use equation (4.16) for the work in this project.

By operating the wire in the constant temperature mode, assuming that conduction and radiation losses are negligible and using (4.15) and (4.16) equation (4.7) becomes :

$$I^2R = \frac{V^2}{R} = k\pi l\left(\frac{T_f}{T_m}\right)^{0.5}(A + BRe^n)(T - T_f) \tag{4.17}$$

where V is the anemometer output voltage.

4.4 Directional Sensitivity of Probes

The heat loss by convection from a hot wire is a maximum for a given fluid velocity when the wire is placed perpendicular to the direction of this velocity. If the wire is

inclined to the flow as shown in Figure 4.10 the flow velocity vector can be resolved into two components, U_x which is normal to the wire and hence is mainly responsible for wire cooling by convection, and U_y which is parallel to the wire. If the angle θ (yaw angle) is the angle between the flow velocity vector and U_x then the effective velocity U_{eff} measured by the wire, suggested by Hinze (1959), is given by:

$$U_{eff}^2 = U^2(\cos^2\theta + k^2\sin^2\theta) \tag{4.18}$$

where k is a factor which depends on the aspect ratio and the yaw angle of the wire. Champagne *et al* (1967), found that k depends primarily upon the aspect ratio of the wire and that it is approximately 0.2 for $l/d = 200$ and effectively becomes zero at $l/d = 600$ as shown in Figure 4.11. For the present study the aspect ratio is around 250 which gives $k = 0.16$ from Figure 4.11. Thus, equation (4.18) can be approximated to

$$U_{eff} = U\cos\theta$$

From this equation it is apparent that an error of 10 degrees in the velocity direction will produce an error of 1.5% in velocity magnitude.

The hot wire anemometer is restricted in its ability to give direct indication of the flow direction. So, for a single-wire probe in order to measure accurately the velocity in a turbulent flow (mean plus fluctuating component) the direction of the mean flow must be known, *a priori*, and according to Witze (1977) the fluctuating velocity components must be much smaller in magnitude than the mean velocity. He indicated that the turbulence intensity $u/\overline{U}$ should be less than 20 percent, but this could be increased to 30 percent by a simple analytical correction according to Corrsin (1943). Also, Durst and Zare' (1974) have shown that directional ambiguity does not introduce a considerable error until the relative intensity exceeds 60 percent.

Williams and Tindal (1980) used shielded single-wire probes to determine the flow direction in a DI engine as shown in Figure 4.12. By taking a measurement with the shield on one side and then rotating the probe through 180° and taking another measurement this enabled them to determine the direction of the flow but this caused a considerable disturbance to the flow and they have to use unshielded probes for determining velocity magnitudes.

The flow in the swirl chamber of an IDI engine is assumed to follow closely the forced vortex pattern, see section 2.4. Hassan (1969) used single-wire probes to measure the air flow in a cylindrical swirl chamber of an IDI engine. Abou-Ellail and Elkotb (1981) measured the air flow and turbulence intensities in a swirl chamber of an IDI diesel engine using a single-wire probe. Ajakaiye (1976) used a three-wire probe with the wires set mutually perpendicular to measure the flow in a cylindrical IDI engine. He quoted an error between -5% to 15% in the measurement of the velocity magnitude. The cause of the error was due to the fact that it was difficult to weld three wires mutually perpendicular and slight bowing in the wires occurred during the welding process. Also, to keep the probe as small as possible most of the wires used had aspect ratio of 200 or less and as mentioned in section 4.3.3 end conduction losses become significant at aspect ratio less than 200. In addition he found it was not possible to make comparison between the three velocity magnitudes obtained thus he resolved the absolute velocity vectors in the direction of solid-body rotation.

Accordingly, it was decided to use a single-wire probe to measure the flow velocity in the swirl chamber of the IDI experimental engine.

4.5 Temperature Compensation

Unlike the flow conditions in a wind tunnel where uniform flow at atmospheric pressure and temperature takes place, the flow in an internal combustion engine undergoes a continuous variation ranging from near atmospheric flow conditions when both valves

are open to high temperature and pressure by the end of the compression stroke. Since the hot wire is sensitive to gas temperature and pressure as well as velocity variations it is necessary to apply corrections to the voltage signal obtained during wind tunnel calibration. The various methods of temperature compensation, as suggested by Tropea (1988), can be divided into four groups:

4.5.1 Calibration Method

The first method, which is ideal but not practical, is to calibrate the hot wire at the same conditions over the complete range that prevail in I.C. engines. This is hindered by the fact that it is a very time consuming operation to calibrate each individual probe over the whole of temperature and pressure encountered for every reading taken where the probe itself is liable to frequent breakage and short life. Also, a calibration rig which provides such facilities will be expensive to build and run which restricts its availability. Hassan (1971), calibrated hot wires at high temperature and pressure to check the validity of the corrections applied to the Davies and Fisher method, see section 4.3.4. He used a bank of air bottles at a pressure of 138 bar which were discharged through a reducing valve into a pipe line. The temperature of the air ahead of the test section could be raised by a hydrogen burner in the system.

Tindal *et al* (1982), calibrated hot wires at gas pressures up to 15 bar and temperature up to 450°*C* at Cranfield Institute of Technology to obtain a semi-empirical relation between Nu and Re numbers.

4.5.2 Automatic Compensation

This technique, used by El-Khafaji, Tindal and Williams (1974) and Abou-Ellail and Elkotb (1981), is achieved by adjusting the sensor temperature to maintain the same voltage at the same velocity of wind tunnel calibration. The wire resistance is made to vary with the gas temperature by installing a resistance thermometer in the bridge and

the value of the wire resistance will be determined by a signal from the resistance thermometer which measures the gas temperature in the engine. Figure 4.13 shows the resistance which is incorporated in a second bridge circuit. This technique is questionable as it does not account for pressure changes, which is required since *Re* number in equation (4.17) is a function of the gas pressure and temperature. Also, according to Witze (1977), the frequency response is not adequate.

4.5.3 Operation of velocity wire at different wire temperatures

In this method, described by Dent and Derham (1972), the wire is operated at two different temperatures in the engine. The method assumes there is little cyclic variation in the mean velocity in the engine and that the mean velocity will remain nearly the same during the two different readings. By using the voltage reading at one measurement the mean velocity can be calculated from the heat balance equation. This mean velocity is then applied to the heat balance equation to predict the voltage at the second operating temperature. A comparison can be made with the measured output voltage and a temperature correcting factor can be derived, if necessary, for the heat balance equation. The accuracy is increased by taking several measurements at different wire temperatures. This method suffers from low accuracy in engine application as only mean velocity can be measured and the assumption that cyclic variations in the mean velocity in engines is negligible is questionable.

4.5.4 Analytic Approach

The last and the most practical technique, reported by Williams and Tindal (1980) and Kyriakides (1984), is to calibrate the hot wire at ambient conditions in a wind tunnel and to correct engine measurements point by point using an analytical model which accounts for pressure and temperature variations. The instantaneous gas temperature may be measured (sometimes approximated by calculation if measurements prove to be

difficult) by a constant current anemometer. This technique is adopted in this study as both the gas pressure and temperature in the swirl chamber of the IDI engine can be acquired simultaneously.

By assuming that equation (4.17) holds for both measurements in engine and calibration and that mean wire temperature, wire resistance and Reynolds Number are the same in both cases then applying equation (4.17) for both cases we have

$$\frac{V_e^2}{R_W} = k_e \left(\frac{T_{g_e}}{T_{m_e}} \right)^{0.5} (A + BRe^n)(T_W - T_{g_e}) \tag{4.19}$$

$$\frac{V_c^2}{R_W} = k_c \left(\frac{T_{g_c}}{T_{m_c}} \right)^{0.5} (A + BRe^n)(T_W - T_{g_c}) \tag{4.20}$$

where suffixes e and c refer to engine and calibration conditions respectively.
From the above it can be seen that the output voltage obtained from the engine can be corrected to that of calibration conditions by multiplying by the factor

$$Fc = \sqrt{\frac{k_c}{k_e} \left(\frac{T_{g_c} T_{m_e}}{T_{g_e} T_{m_c}} \right)^{0.5} \left(\frac{T_W - T_{g_c}}{T_W - T_{g_e}} \right)} \tag{4.21}$$

With the thermal conductivity relation, after Collis and Williams (1959)

$$k = k_o \left(\frac{T}{T_o} \right)^{0.8} \tag{4.22}$$

substituting (4.22) in (4.21) we get

$$Fc = \sqrt{\left(\frac{T_{m_c}}{T_{m_e}}\right)^{0.8}\left(\frac{T_{g_c}T_{m_e}}{T_{g_e}T_{m_c}}\right)^{0.5}\left(\frac{T_W - T_{g_c}}{T_W - T_{g_e}}\right)} \qquad (4.23)$$

4.6 Resistance Thermometry

As mentioned in the previous section, measurement of the gas temperature in the swirl chamber has to be carried out. Lyn and Valdmanis (1967) mentioned that the choice of techniques for compression temperature measurement can be between; optical method, sonic velocity method and resistance thermometry. They stated that optical and sonic velocity methods require specially constructed engines and calibration presents some difficulty. On the other hand resistance thermometry has the advantage that it can be applied easily to any normal engine and can easily be calibrated. The main disadvantage is the finite time lag of the wire which will be discussed in section 4.6.1

In resistance thermometry the temperature is measured simply by using the relation between the sensing probe resistance and its temperature as described by equation (4.9). When a temperature measurement is needed, the sensor resistance is measured and equation (4.9) is used to calculate the temperature. Continuous temperature measurement can be achieved by using the sensing wire in either constant current or constant temperature mode at low overheat ratio. As reported by Lomas (1986); at too low overheat ratio neither the amplifier in the constant temperature anemometer nor the constant current source in the constant current anemometer have good stability. A comprise is necessary as increasing overheat ratio too much will introduce appreciable velocity sensitivity. Constant current anemometry is often chosen because of better stability. It was decided to operate the same type of probe used for velocity measurement in constant current mode to measure the gas temperature in the swirl chamber.

According to Lomas (1986), a Wheatstone bridge circuit is not necessary for constant current operation. Instead the probe can be powered directly by a constant current supply and the output voltage can be obtained by measuring the voltage drop across the probe. This is shown in Figure 4.14. This technique, known as the four wire method, is going to be adopted in this project. The advantage of this method is that the resistance of the wire is read directly with no effect of cable resistance or any resistance resulting from the connections in the circuit.

4.6.1 Thermal Lag

Since the wire of the resistance thermometer has a thermal inertia, the temperature indicated by the wire lags behind the true gas temperature as the frequency of the gas temperature variation increases. Kyriakides (1984) suggested that thermal lag can be minimised by using wires which are short and of small diameter. In addition he indicated that the errors are small in the region of tdc as the time constant is reduced because of high Reynolds number and the rate of change of temperature is comparatively low. Hassan (1968) discussed this subject thoroughly and he calculated a time constant $\tau = 0.33ms$ for a 5 μm tungsten wire used in his study from the following relation

$$\tau = \frac{\rho_w d c}{4h} \tag{4.24}$$

where ρ_w is the density of the wire, d is the wire diameter, c is the wire specific heat and h is the heat transfer coefficient. He found that at 1100 rev/min engine speed the calculated time constant was equivalent to 2.2 degCA phase lag.

Lyn and Valdmanis (1967) used the following relationship established by Scadion and Warshawsky (1952)

$$\frac{\tau_1}{\tau_2} = \left(\frac{p_2}{p_1}\right)^{\frac{1}{2}} \left(\frac{N_2}{N_1}\right)^{\frac{1}{2}} \tag{4.25}$$

where p is gas pressure in atmospheres and N is engine speed in rev/min. They produced theoretical curves for compression temperature in an engine running at 250 rev/min. The reference temperature was measured with a $10\mu m$ wire, which is shown in Figure 4.15. We can see that the time constant in the above equation is affected by relative changes in engine speed and gas pressure. Figure 4.16 shows the effect of engine speed on time constant. Hassan (1968) used the above equation to demonstrate the effect of gas pressure in time constant. By substituting the time constant ($\tau = 0.33ms$) obtained from (4.24) at $p_1 = 1$ in equation (4.25) the value of $\tau_2 = 0.129ms$ will be obtained at $p_2 = 7$. It will correspond to 0.8 degCA at 1100 rev/min. This shows that the time constant decreases near tdc region as stated by Kyriakides (1984) above.

4.7 Frequency Response of a Hot Wire Anemometer

When there are rapid variations in the local velocity, such as that in turbulent flows in engines, a finite time is needed for the hot-wire to respond to this sudden variation due to the thermal inertia of the hot-wire. In order to take accurate turbulence measurements, the frequency response of the hot-wire should be higher than the frequency of the velocity fluctuations. Hinze (1959), has discussed this topic in detail and his method of developing an expression for the frequency response of hot-wire anemometers in both cases i.e. constant current mode and constant temperature mode will be adopted here.

Consider the case of a wire with finite thermal inertia. Assume the wire is long enough such that there is no loss of heat by conduction and that radiation heat loss is negligible. Then equation (4.7) for heat balance will reduce to:

$$I^2\frac{\rho_T}{A}=\rho cA\frac{\delta T}{\delta t}+\pi dh(T-T_f) \tag{4.24}$$

using (4.8) and (4.9) we get

$$I^2R=\frac{\rho cAl}{\alpha R_o}\frac{\delta R}{\delta t}+\frac{\pi dhl}{\alpha R_o}(R-R_f) \tag{4.25}$$

with the relation between the compensating electronic current i and the resistance variation of the total wire r given by

$$i=-g_{tr}Ir \tag{4.26}$$

where g_{tr} is the transconductance of the electronic circuit.

By putting

$$h=A+BU^n$$

$$U=\overline{U}+u$$

$$R=\overline{R}+r$$

$$I=\overline{I}+i$$

where prime values are time-mean condition and lower case are fluctuating components. Substituting these quantities in equation (4.25) and neglecting small order terms yields

the following relations for the time-mean and fluctuating part respectively

$$I\overline{R} = (\overline{R} - R_f)(A + B\overline{U}^n) \tag{4.27}$$

$$2\overline{IR}i + \overline{I}^2 r = (A + B\overline{U}^n)r + (\overline{R} - R_f)nB\overline{U}^{n-1}u + \frac{\rho cAl}{\alpha R_o}\frac{\delta r}{\delta t} \tag{4.28}$$

substituting equation (4.26) into (4.28) will give after some arrangement

$$\frac{\delta r}{\delta t} + \alpha R\frac{A + B\overline{U}^n - \overline{I}^2 + 2g_{tr}\overline{I}^2\overline{R}}{\rho cAl}r = -\frac{\alpha R_o(\overline{R} - R_f)nB\overline{U}^{n-1}}{\rho cAl}u \tag{4.30}$$

by again substituting (4.27) into (4.30) will give

$$\frac{\delta r}{\delta t} + \frac{\alpha R\overline{I}^2}{\rho cAl}\left(\frac{R_f}{\overline{R} - R_f} + 2g_{tr}\overline{R}\right)r = -\frac{\alpha R_o(\overline{R} - R_f)nB\overline{U}^{n-1}}{\rho cAl}u \tag{4.31}$$

which may by written as

$$\frac{\delta r}{\delta t} + \frac{1}{\tau_{c.t.}}r = \phi(t)$$

where

$$\phi(t) = -\frac{\alpha R_o(\overline{R} - R_f)nB\overline{U}^{n-1}}{\rho cAl}u$$

and

$$\tau_{c.t.} = \frac{\rho c A l}{\alpha R_o \bar{I}^2 \left[\frac{R_f}{(\bar{R} - R_f)} + 2 g_{tr} \bar{R} \right]} \tag{4.32}$$

this expression for the time constant, $\tau_{c.t.}$, (the subscript c.t. refers to constant temperature) of the hot wire including the feedback of the electronic circuit, through the transconductance g_{tr}. Examination of the above equation indicates that the frequency response of the wire (reciprocal of the time constant) can be increased by decreasing the value of l, i.e. using a shorter wire. As using a shorter wire will increase heat loss to the supports, see section 4.3.3, the frequency response of the wire is increased electronically since, according to Hinze (1959), $g_{tr}\bar{R} \gg 1$. The dynamic response of constant temperature anemometer systems have been studied and evaluated by Davis (1970) giving a natural frequency of 16.7 kHz for 9.3 micron wire. Commercial probes, see DISA (1982) similar to the probe used in this study claim maximum frequency response up to 150 kHz in constant resistance mode and 500 Hz in constant current mode. The expression for the time constant of the hot wire at constant current mode, $\tau_{c.c.}$, will be,

$$\tau_{c.c.} = \frac{\rho c A l (\bar{R} - R_f)}{\alpha R_o R_f \bar{I}^2}$$

by omitting the term $2 g_{tr} \bar{R}$ in equation (4.32)

Hassan (1968) found that the ratio of the time constant in constant temperature mode to that in constant current mode, for the wire used in his study, is

$$\frac{\tau_{c.t.}}{\tau_{c.c.}} = \frac{1}{760}$$

4.8 Summary

This chapter has described the theory of hot wire anemometry. The difference between constant temperature and constant current anemometers and their applications was explained. The directional sensitivity of the wire is presented in addition to methods used for temperature compensation when using the wire for measuring air velocity in engines. Resistance thermometry and frequency response of the hot wire anemometer is also discussed.

Run no.	ℓ/d	a_w	α (°)	U_∞ (m/s)	Gradients (°C/cm) Upstream	Gradients (°C/cm) Downstream	% end conduction loss	Mean T check (%)	d_s/d_w
1	200	0·8	0	8·61	—	—	—	8	10
2	200	0·8	0	5·42	—	—	—	8	10
3	200	0·8	50	†	—	—	—	8	10
4	202	0·8	0	5·55	$2{\cdot}36 \times 10^3$	$2{\cdot}41 \times 10^3$	7·9	12	20
5	202	0·8	55	†	$2{\cdot}36 \times 10^3$	$2{\cdot}48 \times 10^3$	8·0	12	20
6	197	0·8	0	5·41	—	—	—	—	S.E.‡
7	197	0·8	45	†	—	—	—	—	S.E.‡
8	400	0·8	0	5·45	$2{\cdot}36 \times 10^3$	$2{\cdot}39 \times 10^3$	4·1	8	20
9	400	9·8	50	†	$2{\cdot}54 \times 10^3$	$2{\cdot}53 \times 10^3$	4·3	8	20
10	400	0·8	0	8·57	$2{\cdot}19 \times 10^3$	$2{\cdot}31 \times 10^3$	3·3	9	20
11	400	0·5	0	8·57	$1{\cdot}92 \times 10^3$	$1{\cdot}57 \times 10^3$	4·6	16·7	20
12	199	0·8	0	5·06	$3{\cdot}03 \times 10^3$	$3{\cdot}11 \times 10^3$	9·9	8	S.E.
13	199	9·8	55·	†	$2{\cdot}95 \times 10^3$	$3{\cdot}10 \times 10^3$	9·8	8	S.E.
14	199	0·5	0	4·98	$1{\cdot}37 \times 10^3$	$1{\cdot}51 \times 10^3$	7·3	14·1	S.E.
15	99	0·8	0	6·19	$3{\cdot}86 \times 10^3$	$3{\cdot}79 \times 10^3$	20·1	7	20
16	99	0·8	55	†	$3{\cdot}59 \times 10^3$	$3{\cdot}94 \times 10^3$	20·1	7	20
17	218	0·8	45	Probe 8·85	$2{\cdot}75 \times 10^3$	$2{\cdot}85 \times 10^3$	7·8	5	S.E.
18	199	0·8	45	8·75§	$2{\cdot}95 \times 10^3$	$3{\cdot}07 \times 10^3$	8·8	8	S.E.
19	199	0·8	30	8·75§	$3{\cdot}03 \times 10^3$	$3{\cdot}27 \times 10^3$	8·7	8	S.E.
20	400	0·8	0	5·20	$2{\cdot}19 \times 10^3$	$2{\cdot}31 \times 10^3$	4·0	9	20

† For inclined wire, wire voltage and resistance was maintained at $\alpha = 0°$ values.
‡ S.E. stands for special end as described in text.
§ Exceptions to a, as U_∞ for run 13 was 8·40 m/s.

Table 4.1 Summary of temperature distribution data, Champagne *et al* (1967)

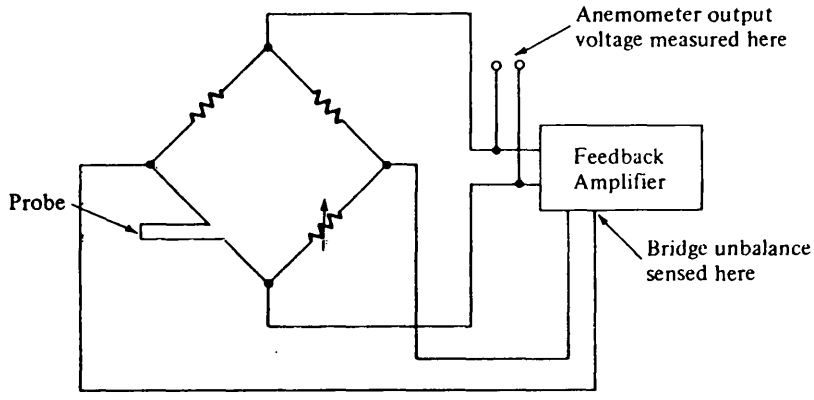

Figure 4.1 The block diagram of a constant temperature anemometer, Lomas (1986)

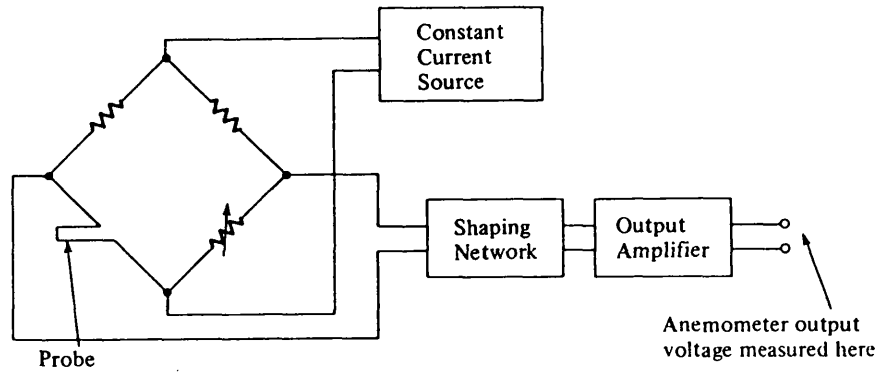

Figure 4.2 The block diagram of a constant current anemometer, Lomas (1986)

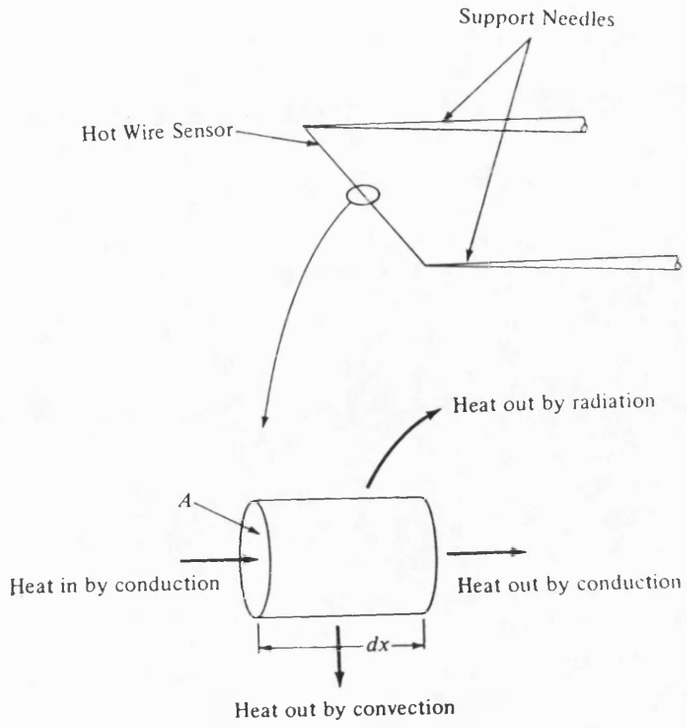

Figure 4.3 The differential element for a hot wire sensor, Lomas (1986)

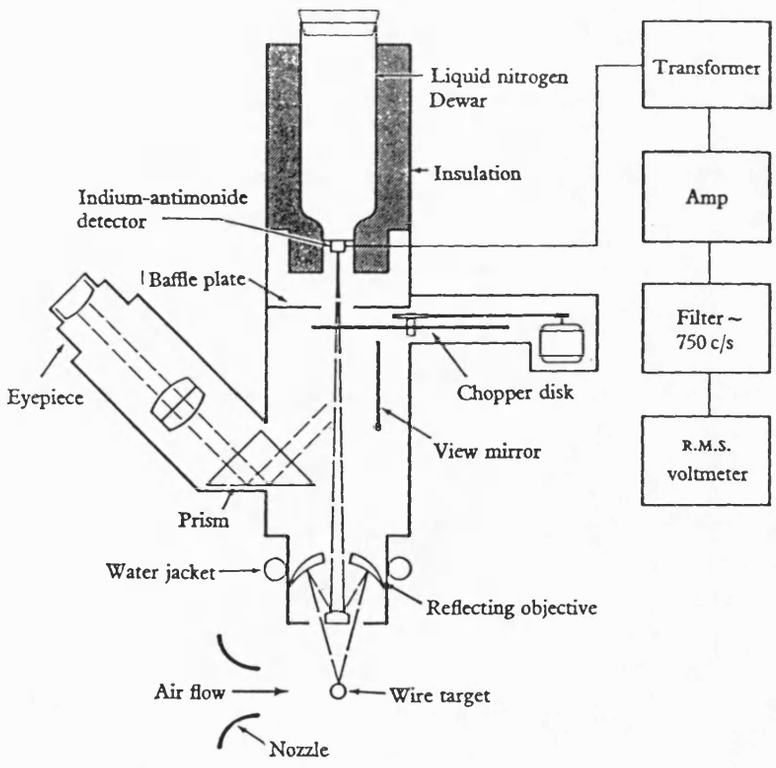

Figure 4.4 Schematic diagram of infra-red detector, Champagne *et al* (1967)

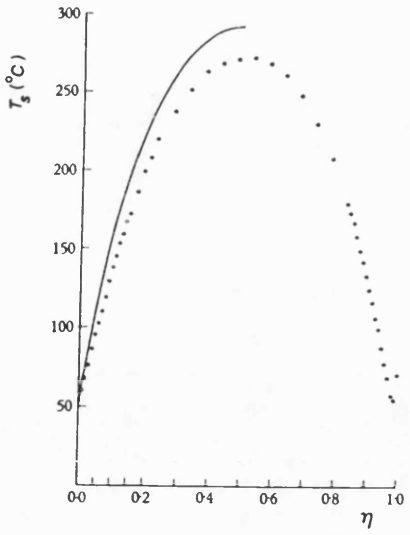

Figure 4.5 The temperature distribution along a hot wire sensor having an aspect ratio of 99, Champagne *et al* (1967)

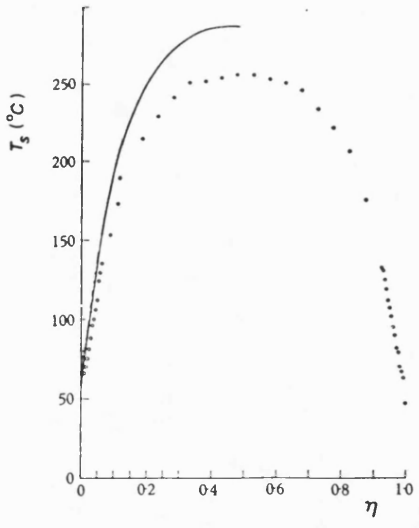

Figure 4.6 The temperature distribution along a hot wire sensor having an aspect ratio of 202, Champagne *et al* (1967)

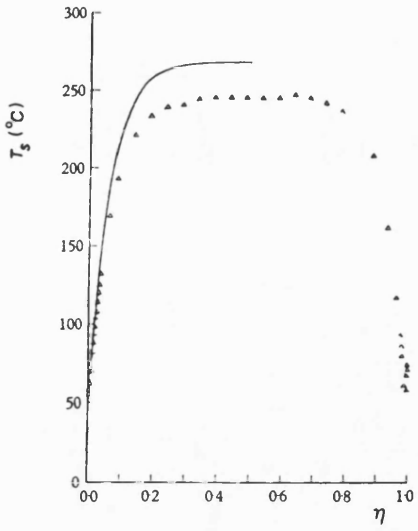

Figure 4.7 The temperature distribution along a hot wire sensor having an aspect ratio of 400, Champagne *et al* (1967)

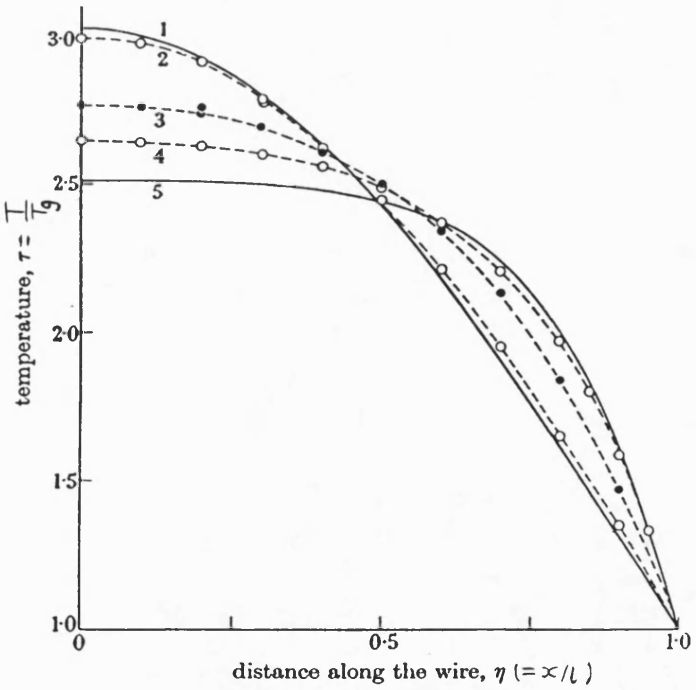

FIGURE 4.8 Comparison of various methods of calculating temperature distributions on hot wires. 1, wire *in vacuo*, (2·6*a*); 2, wire *in vacuo*, (2·9); 3, velocity 32 ft./s, (2·6*a*), h = const.; 4, velocity 32 ft./s, (2·9); 5, velocity 32 ft./s, (2·6*a*), $h = h_0(1 + 2\tau)$,

Davies and Fisher (1964)

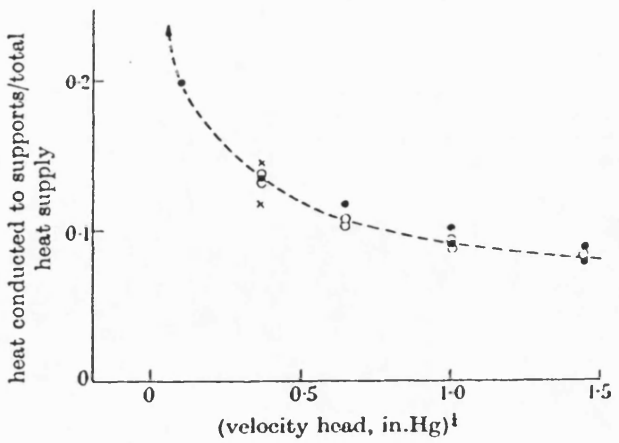

Figure 4.9 Conductive heat loss to hot-wire supports for a 5 μm hot wire. •, wire 0·2 cm long; ×, 0·25 cm long; ○, 0·3 cm long,

Davies and Fisher (1964)

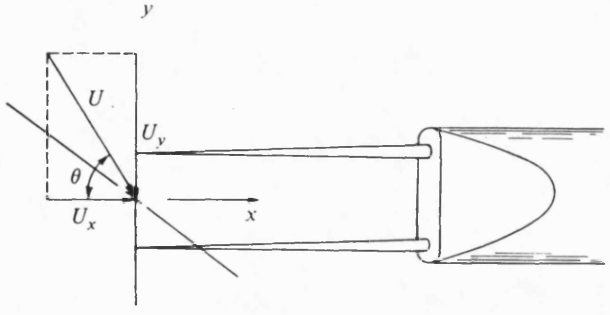

Figure 4.10 The yaw angle, θ, for a standard hot wire probe, Lomas (1986)

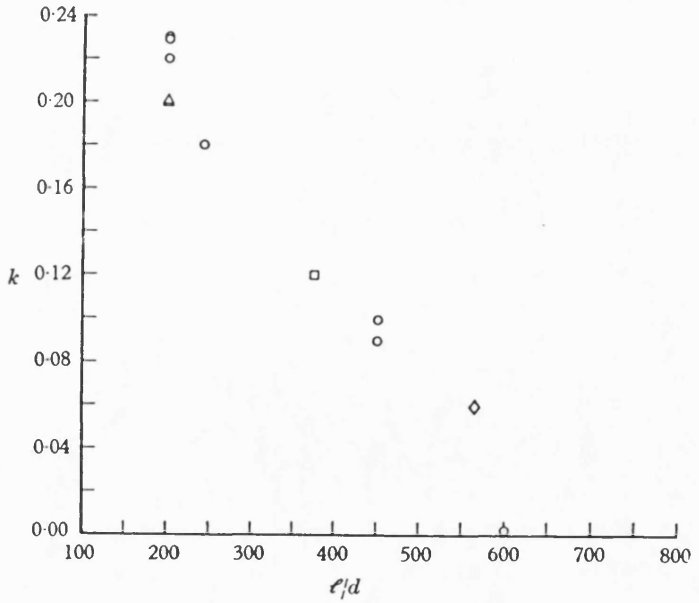

Figure 4.11 The variation in yaw factor for hot wire probes of different sensor aspect ratio, Champagne *et al* (1967)

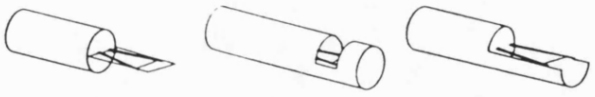

Figure 4.12 Types of shield used on single hot wire probes, Williams and Tindal (1980)

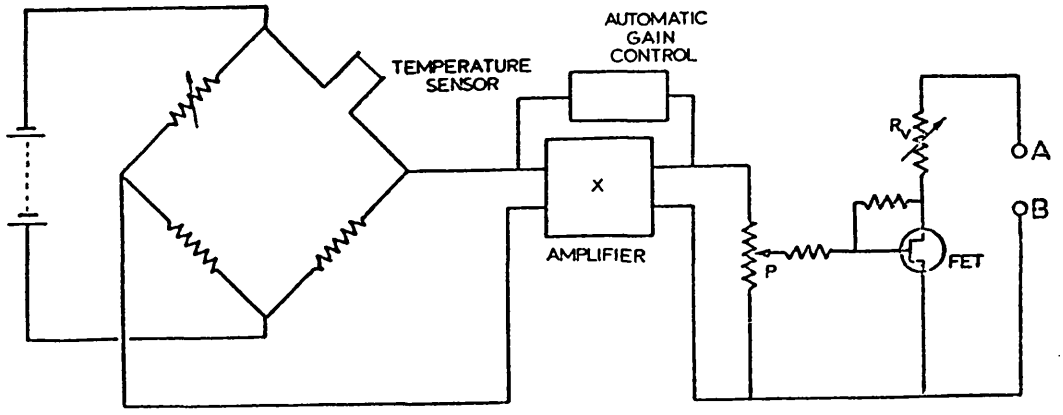

Figure 4.13 Temperature compensating circuit, El-Khafaji *et al* (1974)

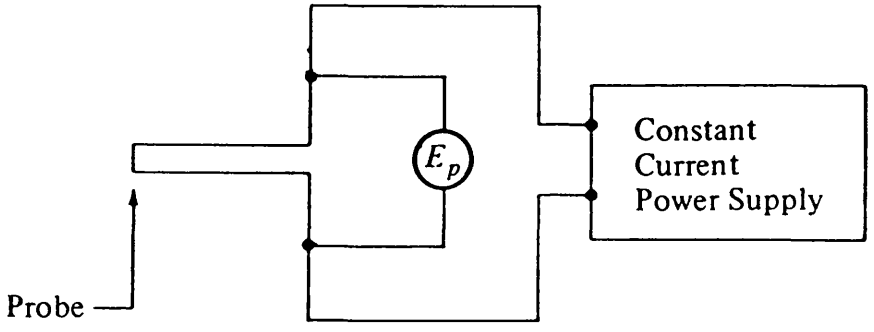

Figure 4.14 Constant current anemometer, Lomas (1986)

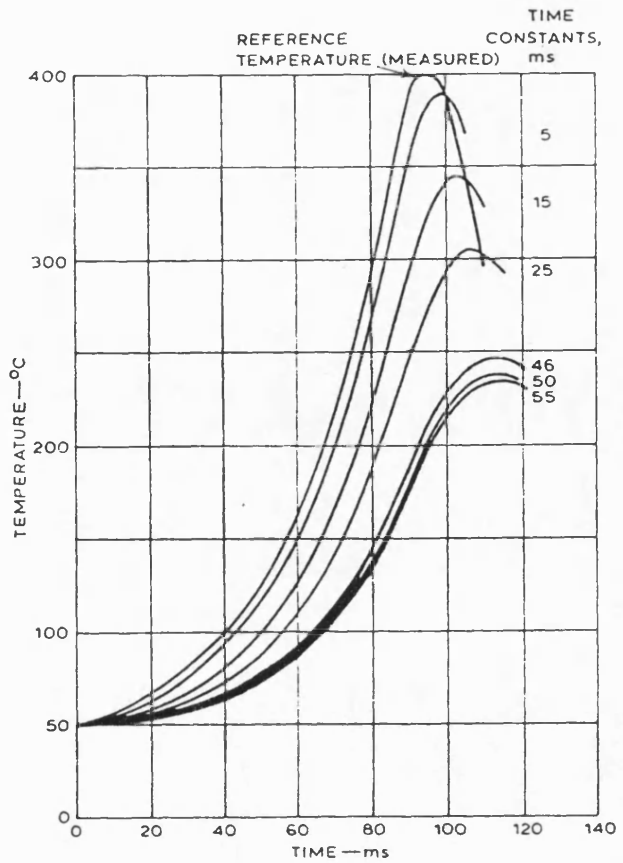

Figure 4.15 Compression temperature curves at 250 rev/min with different time constants, Lyn and Valdmanis (1967)

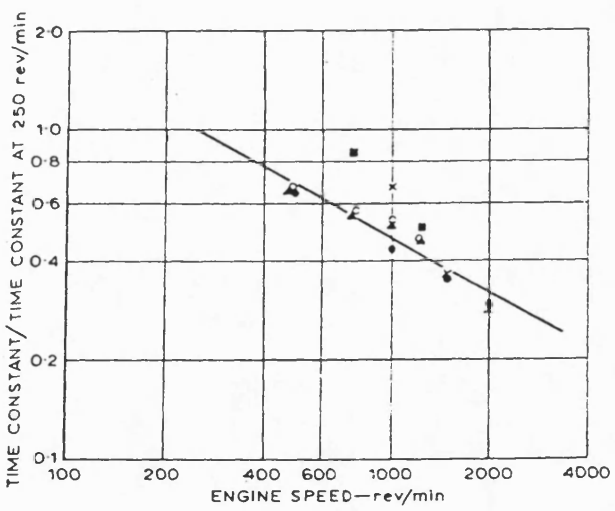

Figure 4.16 Relative change of time constant with engine speed, Lyn and Valdmanis (1967)

CHAPTER 5

DESCRIPTION OF EXPERIMENTAL FACILITY AND DATA PROCESSING

5.1 Introduction

The swirl chamber of an IDI diesel engine is located in the cylinder head and connected via one or more passages to the volume above the piston top. In the case of a Ricardo Comet type swirl chamber the lower half of the spherical chamber which contains the throat is made in the form of a loose member for heat insulation purposes. This configuration and the small size of the swirl chamber (usually about 25.4 mm in diameter) and the throat (approximately 5 mm diameter) make the task of flow measurements in the swirl chamber very difficult.

From the limited amount of work that has been published showing flow measurements in an IDI engine most previous workers have adopted a cylindrical swirl chamber, of the same diameter and volume as the production spherical swirl chamber, with low compression ratios to facilitate experimental procedures. Hassan (1971) and Ajakaiye and Dent (1981) used an air cooled single cylinder engine with a specially fabricated cylinder head in order to achieve the idealised cylindrical shape of the swirl chamber which was also used by Lyn and Valdmanis (1962). The purpose of the cylindrical swirl chamber is to minimise cycle to cycle variation by creating an 'ordered flow'. Zimmerman (1983), reported that there is very little difference in the gross flow noticed between cylindrical and spherical swirl chambers during a simulated compression stroke and that the flow in the cylindrical swirl chamber is more repeatable. He claimed that the combustion phenomena are quite repeatable from cycle to cycle in the cylindrical swirl chamber as verified by combustion movies. Table 5.1 shows previous experimental swirl chamber specifications.

In the present work, flow measurements have been made in the near-spherical Ricardo Comet MkVb swirl chamber. During the first part of the project the mean swirl ratio of the flow in the swirl chamber was measured using vane anemometry. The second part of the investigation covered the measurements of gas velocity, temperature and pressure in the swirl chamber using hot wire anemometry, resistance thermometry and a piezo-electric pressure transducer respectively.

In this chapter a description of the test engine and drive assembly is given. Details of the instrumentation and data logging system used to acquire data from the engine are presented.

5.2 The Engine Test Bed and Drive Assembly

The engine used was an indirect injection diesel engine fitted with a Ricardo Comet MkVb type swirl chamber. The engine data is given in Table 5.2. This engine had been used previously in the department for experiments under firing conditions. The engine was mounted on a fabricated steel frame with the facility of a subframe to allow the engine to slide thus allowing adjustment of the driving belt tension. Since the engine was previously used for firing tests, it was necessary to clean it thoroughly to prepare it for hot wire anemometry tests. The cylinder head was removed from the engine. The three cylinders that were used and their piston tops were cleaned by using Emery Cloth (wet and dry) and cleaning solution. The cylinder head was washed in a power washing unit after removing the swirl chamber lower half (hot plug). The cylinders and eventually the swirl chamber was washed with methylated spirits. This cleaning procedure was carried out three times during the project; each cylinder head (with ceramic and cast steel inserts) having previously been used in firing tests.

In order to motor the engine the fuel injectors were disconnected from the fuel injection pump and the fuel was allowed to circulate through the injection pump via an elevated fuel tank in order to maintain lubrication of the working parts. The engine water was cooled by an elevated water tank by thermo-syphon.

The engine was driven by a 14.9 KW (20 h.p.) 3-phase induction electric motor with a constant motor speed of 3000 rev/min. Since it was expensive to buy an electronic speed controller the decision was taken to use pulleys and belts in order to drive the engine at different speeds. A layshaft allowed the drive ratio to be varied over a wide range. The layshaft was mounted on two roller bearings so that it could transmit the drive from the electric motor to the engine. A safety guard was bolted to the frame around the intermediate shaft. Calculations were carried out to determine the maximum speed at which the engine could be driven with the existing power of the electric motor. Because of the electric motor starter limitations and the belt slippage losses the engine could only be driven at a maximum speed of 2140 rev/min. A number of pulleys were employed to achieve the required engine speeds. The pulleys had to be changed each time a new engine speed was required. During the project the following speeds were used: 670, 898, 1410 and 2140 rev/min. The engine test bed and drive assembly arrangement are shown in Figure 5.1 and 5.2.

5.3 Ceramic Lower-Half Swirl Chambers

It was decided to compare different types of lower-half inserts on the engine. Since the air motion in the swirl chamber of the IDI engine is not dictated by material type, it was decided to measure only the air temperature in the swirl chamber. Two types of ceramic inserts (Aluminium Titanate and Syalon) were to be compared with a standard cast steel insert. The thermal properties of the three materials are given in Table 5.3. A different cylinder head was used for each since the ceramic inserts were placed in a nimonic steel sleeve and could not be fitted into the standard cylinder head. The ceramic inserts and the cylinder head are shown in Figure 5.3. It was necessary to remove the ceramic inserts

from the cylinder head in order to carry out the cleaning procedure mentioned in section 5.2. This proved to be difficult as forcing the inserts out would probably have damaged the ceramic parts. It was decided to drop a circular shim (0.254 mm thick) coated with Araldite, through the injector hole, which is bigger than the swirl chamber throat to seal the throat of the swirl chamber. A bright light was shined to check that the shim has sealed properly. When the Araldite became hard the swirl chamber was then filled with grease and, after blocking the glow plug hole, a dummy injector was used to compress the grease using the hydraulic principle to extract the ceramic insert. This method proved to be successful in extracting the ceramic inserts undamaged.

5.4 Detailed Instrumentation

5.4.1 Vane Anemometry

One of the earliest methods used for the measurement of swirl in the swirl chamber, as reported by Alcock (1934), is to employ a freely rotating vane in the swirl chamber which by using a suitable counter, mechanical then, will give a measure of the mean value for the swirl during the entire cycle. A light weight (1.14 gm) aluminium paddle wheel with four blades, each blade 1 mm thick, was manufactured. The wheel was then mounted on a small shaft, 1.5 mm in diameter. The shaft was in turn mounted in P.T.F.E. Bearings (to withstand the high temperatures encountered in the swirl chamber) in the lower half of the swirl chamber. Figure 5.4 shows a picture of the paddle wheel and the flexible optical fibre cable used in this project.

The counter technique used was similar to that used to measure rotor speed in turbo-machines. The basic principle of this counter is to project light onto the rotating blades of the wheel. As the light is reflected back from the blades it is transduced by a

photo-detector to give an electrical signal. As each blade passes the light source an electrical pulse is produced by the photo-detector. The number of pulses divided by number of blades divided by time will give the speed of the wheel.

It was decided to employ optical fibres to transmit the light from the light source (light bulb) to keep the light bulb remote from the engine, as the engine temperature and engine vibration would reduce the life time of the light bulb. Also, optical fibres were used to transmit the reflected light from the blades of the wheel to the photosensor, again to keep the photosensor and electrical circuit remote from the engine.

Initially, an optical fibre cable with two channels was used to view the wheel through the injector hole. This cable has a separate inlet and outlet for each channel at one end (light bulb and photosensor end) and a common outlet and inlet at the swirl chamber end, see Figure 5.4. The light emitted by the bulb was transmitted by one channel to the blades of the wheel through a quartz window. A quartz window was chosen because it can withstand the high pressure and temperature encountered in the swirl chamber.

This method did not work as the light emitted was reflected back by the quartz window which gave false signals. It was decided then to employ two separate optical fibre cables one for transmitting the light emitted by the bulb, and the other for transmitting the reflected light from the blades of the wheel to the photosensor. A suitable adaptor was made for the optical fibre cable, that transmits the emitted light, with a quartz window into the swirl chamber through the glow plug hole. The light which was reflected from the blades of the wheel was transmitted through the other cable through the injector hole as shown in Figure 5.5.

A diagram of the electronic circuit used to interpret the optical signal obtained from the blades of the wheel is shown in Figure 5.6. A silicon photodiode light sensor was used in a photo voltaic mode. The diode gave a peak current in the order of $10^{-9}A$, which

was converted to a voltage pulse by means of an operational amplifier current to voltage stage. This voltage pulse was then compared with a preset threshold voltage translated to standard logic levels.

Due to the very small signal current an insulated gate FET operational amplifier (CA3140) was selected. This device has an input current of 10×10^{-12} A which can be neglected. To obtain a suitable amplifier output pulse of 1 volt a feedback resistor of $10^{9}\Omega$ was required. As this was not readily available an equivalent network was employed with values of $10K\Omega$, $1K\Omega$ and $100M\Omega$.

The amplifier output pulse was compared with the voltage threshold by a stage using an LM311 comparator. According to Lefferts (1978), unless the signal transition is fast, the comparator may burst into oscillation near the crossover-points due to the high gain and wide bandwidth of comparators such as the LM311. He suggested that the situation is improved if both comparator inputs see the same source impedance. He also suggested that, to avoid oscillation stray capacitance should be kept to a minimum and the leads between the resistors and the comparator inputs should be kept short. Hysteresis, (positive feedback around the comparator) was also used to reduce further the possibility of oscillation or false outputs due to noise.

A 40106B buffer which has low output impedance (less susceptible to noise picked up from other equipment in the area) was used to reduce the possibility of the comparator oscillating due to the load capacitance of the cable. A digital signal of 5 volts was obtained from the buffer output which was further processed to give the speed of the wheel.

This circuit was built in a metal box because of the sensitivity of the input amplifier to capacitively coupled noise. All chips were decoupled by $0.01\mu F$ ceramic capacitors.

5.4.2 Pressure Measurement

Swirl chamber pressure was measured by using a piezo-electric transducer, Kistler type 6121. A piezo-electric pressure transducer functions when a force is exerted on a quartz crystal in the transducer, an electrical charge is produced which is a function of the force that has been exerted. This type of transducer has good frequency response and linearity over a wide range. However, as reported by Kamel (1977), due to different thermal expansion coefficients and different thicknesses of the elements comprising the pressure transducer thermal shock effects could cause changes in sensitivity and drift. A sudden increase in the gas temperature results in an uneven expansion of the diaphragm of the transducer which in turn exerts force on the quartz crystal. This will result in an electrical charge which might wrongly be interpreted as pressure signal. Kyriakides (1984), employed air cooling to avoid overheating of the pressure transducer by passing air through an internal jacket. Kamel (1977), investigated experimentally the effect of thermal shock on pressure transducers. He concluded that recessing the pressure transducer would overcome some of the thermal shock effects, but a good overall behaviour can be obtained by using a thermally shielded transducer flush mounted.

In this project the pressure transducer was inserted into an adaptor, that resembles the glow plug shape, which was in turn screwed into the swirl chamber through the glow plug hole. Figure 5.7 shows the pressure transducer and adaptor. Usually the glow plug protrudes into the swirl chamber in order to pre-heat the air to aid engine starting. At a later stage in the project another adaptor, which was flush mounted, was manufactured in order to compare the two cases.

A Vibro-meter charge amplifier type LPC 630 was used to condition the signal from the pressure transducer. Calibration of the pressure transducer was carried out using high pressure (up to 100 bar) nitrogen gas at ambient temperature before every test.

5.4.3 Crank Angle Measurement

A commercial optical shaft encoder, model I58T manufactured by McLennan Limited, has been employed for measuring the instantaneous crank angle. It was connected at the free end of the crank shaft by a transversely flexible, but torsionally stiff, coupling. The encoder body was mounted on a steel bracket with the possibility of rotating the encoder for adjustment when it is not in operation. The steel bracket was rigidly bolted to the engine body to minimise relative vibration.

The encoder consists of a glass disc, with many teeth-like notches around its periphery at one radius, rotated between a long life light source and a photodiode. A sinusoidal voltage is produced by the photodiode because of the alternate light signal. The sinusoidal voltage is then transformed electronically into square wave pulses. A single pulse per revolution (gate pulse) can be obtained by an additional notch at a different radius. The crankshaft speed was measured by using this gate pulse divided by time. The gate pulse is also used for indicating tdc position. The engine was turned by hand to the tdc position. The shaft encoder was then rotated, after loosening the screws which hold it to the bracket, while the gate pulse was monitored on an oscilloscope. The screws were then tightened and the engine was motored for some time before checking for any variation. The static test was repeated before running the engine at each new speed.

The shaft encoder employed in this project can produce 1800 pulses per revolution (1/5° CA). An electronic circuit was built to allow the possibility of an output of 360, 180, 120 and 90 pulses per revolution (1, 2, 3 and 4 degree CA respectively). A diagram of the electronic circuit used is shown in Figure 5.8.

5.4.4 Anemometer Probe Manufacture

The design requirements for probes have been discussed in chapter four. The probe body was manufactured from a B.S. 316 stainless steel tube of 3.175 mm (1/8 in) outside

diameter, 0.254 mm (0.01 in) wall thickness and 140 mm length for easy handling. The steel tube was purchased in 2 m lengths which were then cut into 140 mm length tubes. The tube ends were shaped externally using a small grinding wheel and internally using a hand drill to clear any metal burrs.

The prongs of the probe were two stainless steel sewing needles made commercially by Millwards (size 9) which have a diameter of 0.4 mm. The points of the needles were ground by a small grinding wheel to give a flat surface to facilitate the process of welding the wire. The needles were annealed in order to permit more efficient welding of the wire. A thin copper single-wire with P.T.F.E. coating was welded to the 'eye' end of each needle using a thermocouple welder in the School of Material Science. The output end of the connecting leads was stripped to the copper wire to facilitate the attachment of connectors.

To hold the wire supports to the probe body an adhesive that could stand the high gas temperature and pressure encountered in engines, and maintaining good insulation was used. Packer (1983) used Araldite in the combustion bomb which proved to be effective in terms of standing the high pressure, but the temperature encountered was not high. A ceramic adhesive that has been used in the school to adhere ceramic piston crowns was tried. Although, it has survived the high temperature, testing it in the swirl chamber revealed that the ceramic adhesive had been pushed back along the tube and when the needles were pulled the adhesive disintegrated. Eventually an alumina base high temperature ceramic adhesive with the commercial name Ceramabond 552 was used, after recommendation from the Department of Mechanical Engineering of King's College. This adhesive has a shelf life of six months with a low temperature cure (93°C for 2 hours) and with a maximum working temperature of 1650°C.

The length of the pointed ends of the needles, which protrude out of the probe body, was decided according to the point of measurement in the swirl chamber. Too great a pro-

truding length of the probe will increase the possibility of vibration. Also, when taking measurements in a location close to the wall, the probe body has to be pushed back along the probe holder tube which will create a recess. This recess will generate local turbulence which might lead to errors in the wire reading. The protruding length of the needles in this project was between 5 and 9 mm.

After introducing the needles into the tube the Ceramabond is made to fill the whole length. Ceramabond is fluid before it is cured which enables the needles to be placed the correct distance apart. This was done by holding the probe body in a small vice and measuring the distance between the needles using a micrometer. The distance between the needles in this project was kept between 2.5 and 3.0 mm. After the ceramic adhesive was cured in an oven the probes were held again in the small vice and, using a digital-volt-meter (DVM), the needles and the tube wall were checked for electrical insulation and spacing. The faulty probes were discarded.

The above procedure proved to be very effective in terms of producing rigid probes which can be inserted into and removed from the swirl chamber with ease. The conducting wires were also well insulated inside the tube and their temperature was kept well below the gas mean temperature. This is because of the ceramic adhesive which served as a thermal and electrical insulator. More than thirty probes were manufactured during this project for a minor cost.

It was decided, that the measurement of the flow in the swirl chamber should be carried out in a fixed orientation to the flow assuming forced vortex flow therein. Since there was no need to rotate the probe and because of the awkward position of the injector hole in the cylinder head of the IDI engine, it was decided that a traversing mechanism would not be necessary. Instead, the probe direction and position in the swirl chamber were to be set before the probe was inserted into the swirl chamber. This was done by designing a probe holder which holds two probes; one for temperature and one for velocity

measurements. A probe holder assembly is shown in Figure 5.9. The probe holder has two parts which can be held together by two Allan screws. A rubber washer is used in the recess between the two parts of the probe holder in each of the two probe holes to ensure air tightness. The two probes were first introduced into the lower part of the probe holder, into the rubber washers and finally into the upper part of the probe holder. The protrusion of the probe is set, before the probe was introduced into the swirl chamber, by using a micrometer to measure the distance from the wire of the probe to the edge of the probe holder. The cylinder head was marked on both sides of the injector hole. The probe holder was tightened and two markers were drawn on the flat hexagonal top of the probe holder corresponding to the two markers on the cylinder head body. A line connecting the two markers was drawn on the flat hexagonal top of the probe holder. The direction of the wire was set by adjusting the wire parallel to the line connecting the two markers, with the aid of a rule held on the line. Figure 5.10 shows the probe holder with two probes and also a sample of a single-wire probe.

5.4.5 Welding Wire Sensors

The wire used in this project was a $10\mu m$, 90% platinum 10% rhodium alloy. The wire was supplied in 2 m length batches. It was decided that the variation in diameter of the wire over a length of 3 mm will be negligible and accordingly the diameter specified by the manufacturers (Dantec) has been used. The temperature coefficient of resistivity was determined using the standard oven test, see section 5.4.6, and the variation from the handbook values was found to be 5% which was attributed to experimental error.

The probe was short circuited using a small thick copper wire and the resistance of the leads was determined using the Prosser anemometer bridge. The flat surface of the point of the two needles was cleaned using Ethanol before welding the wire. The wire was welded onto the needles using a Dantec 55A12 welding power generator and Prior

micromanipulator in conjunction with a binocular microscope. The wire was welded at three points on the flat surface of each needle. Figure 5.11 shows the spot-welding equipment.

5.4.6 Hot Wire Calibration

Figure 5.12 shows a picture of the hot wire anemometer system used in this project which was manufactured by Processor. The calibration rig used in this study was built by Wood (1981), as shown in Figure 5.13. Air coming from a Bellis air compressor is maintained at 80 bar in the air receiver, it is then filtered through a one micron filter. As the original regulator did not give adequate regulation for the required velocity range, a pressure regulator was added to the system after the air filter. The air is discharged to the atmosphere through a B.S. nozzle upstream of which the air temperature was measured by a thermocouple and the air velocity, and hence Reynolds number, by a manometer. The hot wire probe was held vertically upwards downstream of the nozzle perpendicular to the direction of the flow.

The calibration rig was used to obtain a number of readings of anemometer output voltage versus Reynolds number. A computer program was written to determine the constants A, B and n, equation (4.20), from the calibration data.

5.4.7 Temperature measurement

The technique of resistance thermometry has been described in section 4.6. The same probe which was used for velocity measurements has also been used for temperature measurement. The electronic circuit used for temperature measurement is shown in Figure 5.14. A constant current of 2 mA is supplied by a constant current power supply. The temperature was measured by monitoring the voltage across the probe, which is directly proportional to the resistance. The output voltage was amplified by an adjustable gain, differential D.C. amplifier.

For the purpose of calibration the probe was mounted inside an enclosed porcelain tube placed in an electrically heated oven. A thermocouple was mounted near the probe inside the tube. Figure 5.15 shows the standard oven test arrangements. The oven was heated up to 500°*C* observed by the thermocouple and the corresponding voltage reading of the probe was recorded. The oven was left to cool down gradually to atmospheric temperature and the temperature readings of both the thermocouple and the probe were recorded in steps.

5.5 Data Acquisition Systems

The transient measurements which involved cylinder pressure, vane anemometry, resistance thermometry and hot wire anemometry were collected by an IBM AT microcomputer from the engine via an external interface. The microcomputer was fitted with a Computerscope ISC-16 analogue to digital converter (ADC) board. The ADC is designed to enable the microcomputer to fully emulate a digital storage oscilloscope through driver software. The 1 MHz ADC, multiplexed to give 16 channels has an input range of -10 to +10 volts with a maximum memory buffer size of 64 kbytes. Analogue signals from the engine are connected to the ADC through a 16 channel external interface box. The 12-bit resolution system is triggered externally by the gate pulse from the shaft encoder. The sampling rate was determined according to the crank angle signals coming from the shaft encoder. Figure 5.1 shows the instrumented engine with the data acquisition system (Computerscope) display.

Captured data is stored in two files; a binary data file (maximum of 131 kbytes) and a parameter file (1024 kbytes) on the hard disk. The data is then transferred to the Schools's VAX 11/750 for processing using the file transfer protocol Kermit.

5.6 Data Processing Technique

As mentioned earlier, the data acquired from the engine through the AIMS card and software was in binary files. These files were transferred through Kermit to the School's VAX 11/750 minicomputer for processesing. Unfortunately the VAX 11/750 was replaced by Sun4 workstations in the middle of the research project. All the data collected from the engine had to be saved on a 1/2 inch tape written on the VAX VMS operating system. A problem arose because the Sun4 workstations operate on the UNIX operating system. The 1/2 inch tape was then taken to the School of Mathematics to be read by a software program which then translates the data for the UNIX operating system and writes it to a cassette.

The following is a description of the procedure used to process the data acquired from the engine

5.6.1 Paddle Wheel Anemometer

The raw signal obtained from the vane anemometer is shown in Figure 5.16. Since the paddle wheel has four blades, four optical signals reflected by the blades represent one revolution of the paddle wheel. A program was written to identify the signal reflected by each blade. Two thresholds, upper and lower, were set as shown in Figure 5.16. A count is carried out when the signal is greater than the upper threshold on the positive slope and falls below the lower threshold on the negative slope. The difference in time between every fifth signal is considered as one revolution. Figure 5.17 shows the vane anemometer signal after processing.

5.6.2 Pressure

The pressure signal was multiplied by a constant obtained from the pressure calibration curve, to convert the signal from voltage to bar. It was decided to set the reference pressure equal to the atmospheric pressure. This choice was based on the fact that the

pressure in the swirl chamber was assumed to be equal to atmospheric pressure just before inlet valve closure. A mean value of the pressure signal at inlet valve closure of all the cycles was then obtained. The pressure signal was then offset by a value equal to the difference between the reference pressure and the mean value of the actual pressure signal at inlet valve closure.

Since the engine was motored, cycle-to-cycle variation in the pressure signal is insignificant according the reported literature. This proved to be true in the case of the current work as shown in Figure 5.18.

5.6.3 Temperature

Since the temperature probe is operated in constant current mode, equation (4.9) can be expressed in terms of voltage i.e.

$$V = V_o(1 + \alpha(T - T_o))$$

Rearranging the above equation the temperature T can be expressed as

$$T = T_o + \left(\frac{\frac{V}{V_o} - 1}{\alpha} \right)$$

Since T_o, V_o and α are constants which can be determined from the standard oven test. The gas temperature can be obtained from the measured output voltage by

$$T = \text{slope} \times V + \text{constant}$$

Figure 5.19 shows gas temperature variation over a single cycle and an ensemble average of 44 consecutive cycles.

5.6.4 Hot Wire Anemometer

The raw anemometer output voltage obtained from the engine is multiplied by the correction factor Fc, see section 4.5.4. This is shown in Figure 5.20. Since the constants A, B and n have been determined from the calibration tests, section 5.4.6, the velocity (obtained from Reynolds number) was calculated from equation (4.19). An ensemble average was then obtained from the data file of the velocity, as shown in Figure 5.21. The swirl ratio, which is the speed at which the air is rotating in the swirl chamber divided by the rotation of the engine crank shaft, was calculated from the velocity signal assuming solid body rotation. This is shown in Figure 5.22.

5.7 Summary

This chapter has described the experimental arrangements carried out during the project. The chapter starts by describing the commissioning of the engine and the suitable drive assembly adopted. Then a detail description of the instrumetnation employed is presented. Finally the techniques used for processing the data acquired from the engine are described.

Author	Cyl. Pre. Dia. [mm]	Compression ratio
Nakajima (1969)	33.0	7 : 1
Hassan (1969)	51.0	8 : 1
Ajakieya (1976)	25.5 and 51.0	12 : 1 and 7.8 : 1
Abou-Ellail *et al* (1981)	48.5	17 : 1

Table 5.1 Specification of IDI engines used in literature

Engine make and model	Ford, 1.6 Fiesta D.
Engine type	4-stroke, compression ignition, IDI, naturally aspirated engine.
Swirl chamber type	swirl chamber, Ricardo Comet MkVB
Number of cylinders	4
Bore	0.080 m
Stroke	0.080 m
Connecting rod length	0.18 m
$\frac{\text{Passage Area}}{\text{Piston Area}}\%$	1.03
$\frac{\text{Prechamber Volume}}{\text{Total clearance volume}}$	0.476
Engine Compression Ratio	21.5 : 1
Valve Timing	Exhaust Valve open 52 degCA bbdc Exhaust Valve close 16 degCA atdc Inlet Valve open 19 degCA btdc Inlet Valve close 49 degCA abdc

Table 5.2 Engine data

Material	Thermal conductivity $\kappa, W/m.K$	Density $\rho, Kg/m^3$	Specific heat $c, J/kg.K$	Thermal diffusivity $\alpha, m^2/s$
Aluminium Titanate	1.2	2840	940	4.5E-7
Syalon	21.3	3245	620	1.06E-5
Cast Steel	25.1	7612	461	7.15E-6

Table 5.3 Thermal properties of swirl chamber insert materials

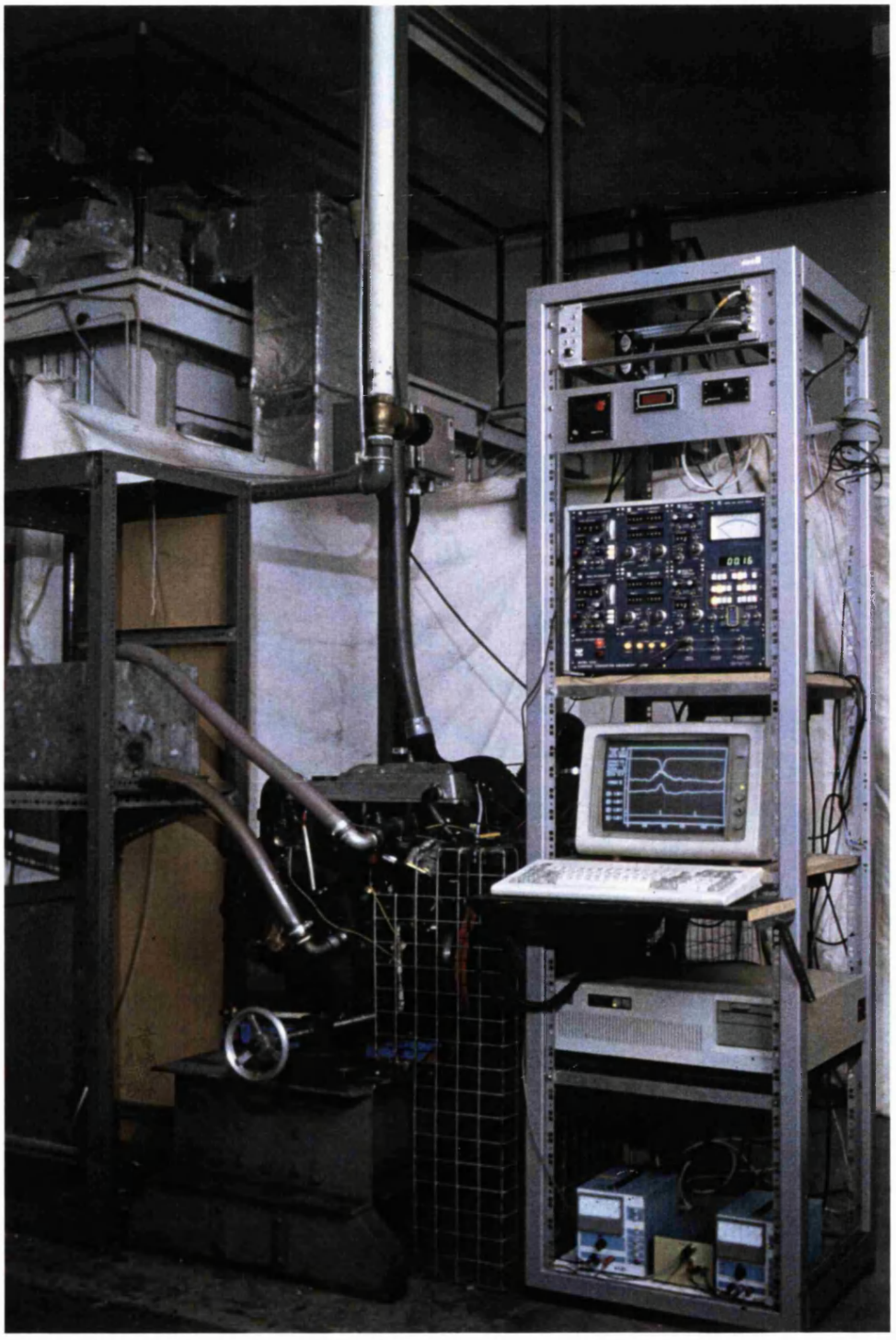

Figure 5.1 View of the engine and instrumentation

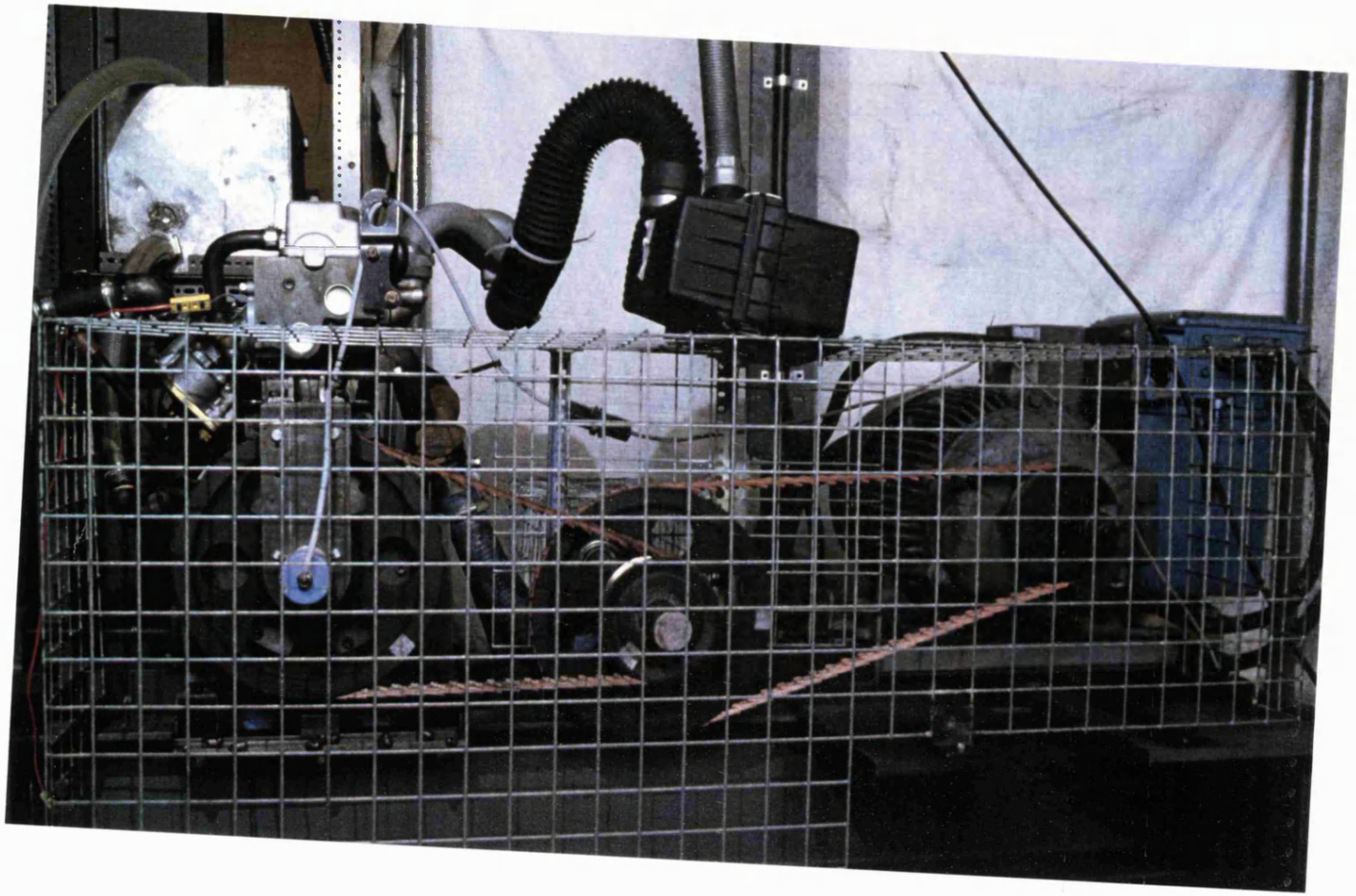

Figure 5.2 View of the motored engine

Figure 5.3 View of the cylinder head (top) and the ceramic insert (bottom)

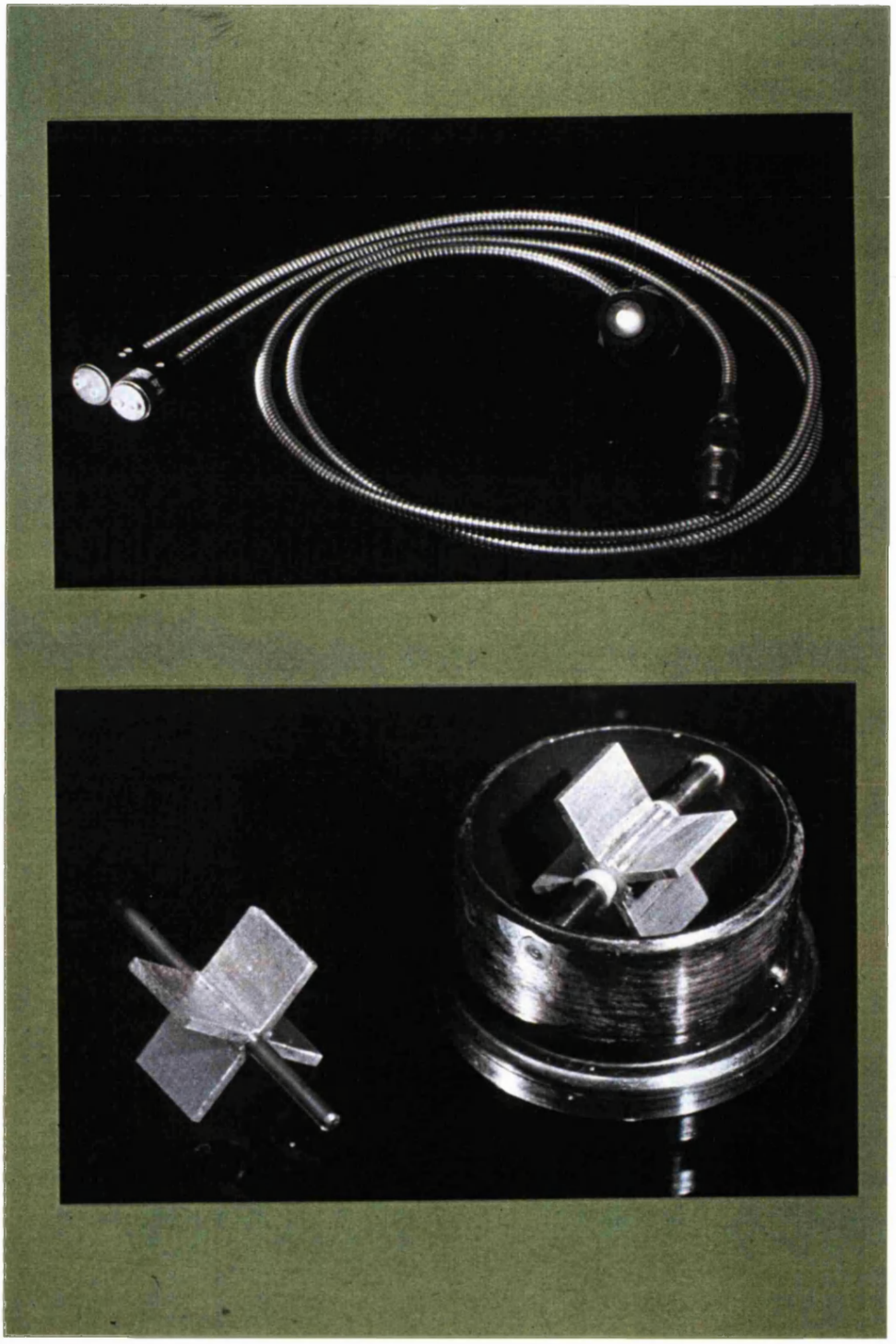

Figure 5.4 The flexible fibre optic cable (top)
and the paddle wheel (bottom)

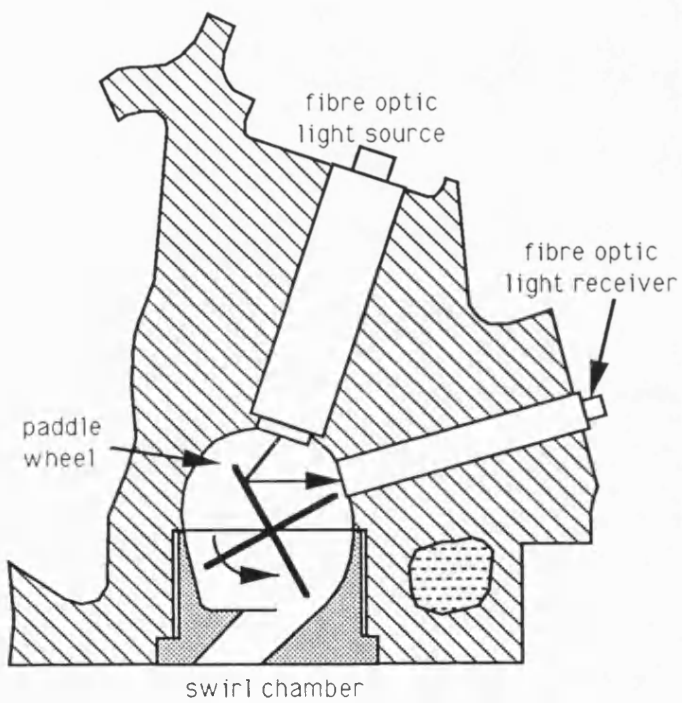

Figure 5.5 Paddle wheel anemometer installed in the swirl chamber

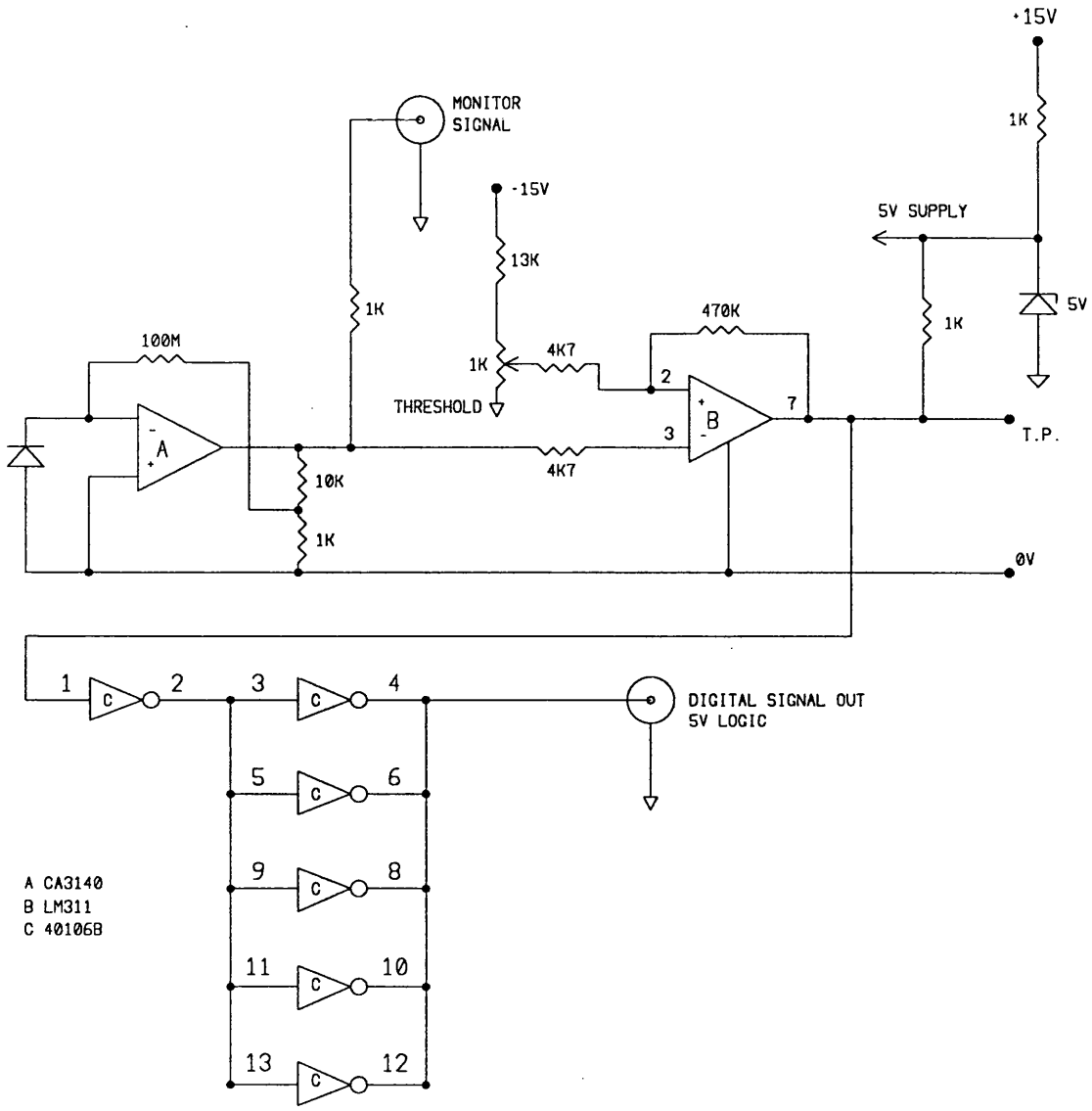

Figure 5.6 Paddle wheel anemometer circuit diagram

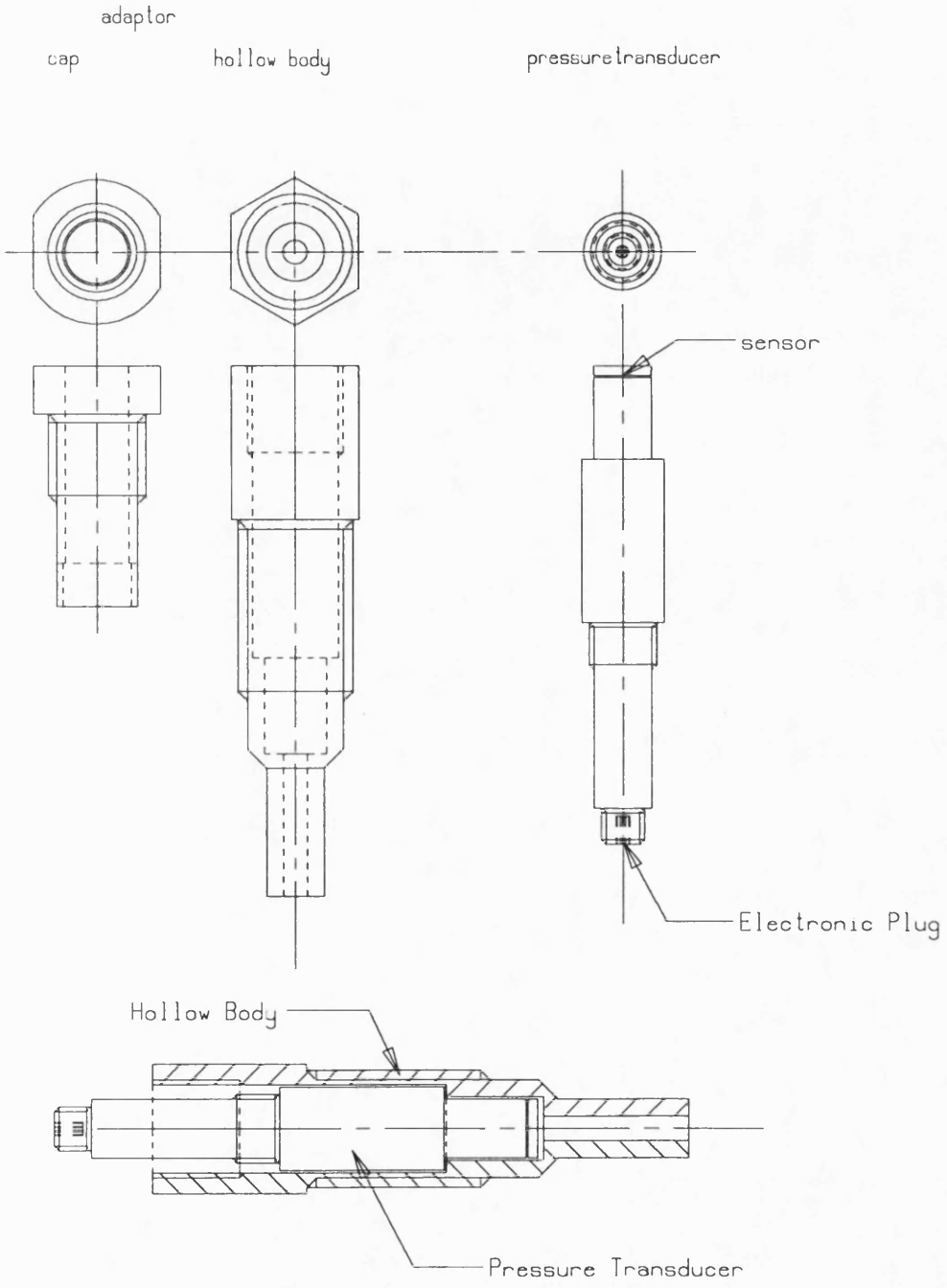

Figure 5.7 Pressure transducer and adaptor

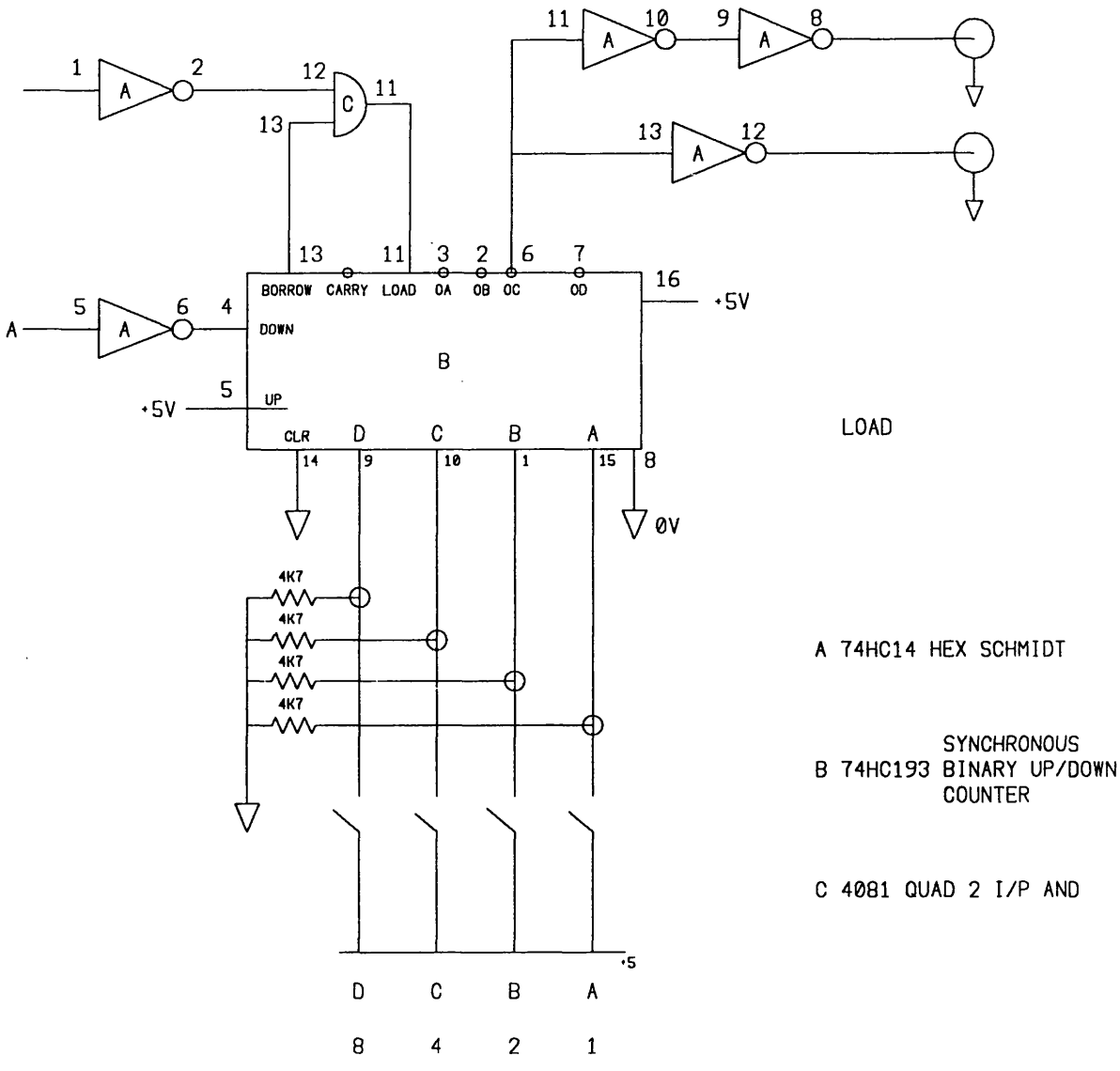

Figure 5.8 Shaft encoder circuit diagram

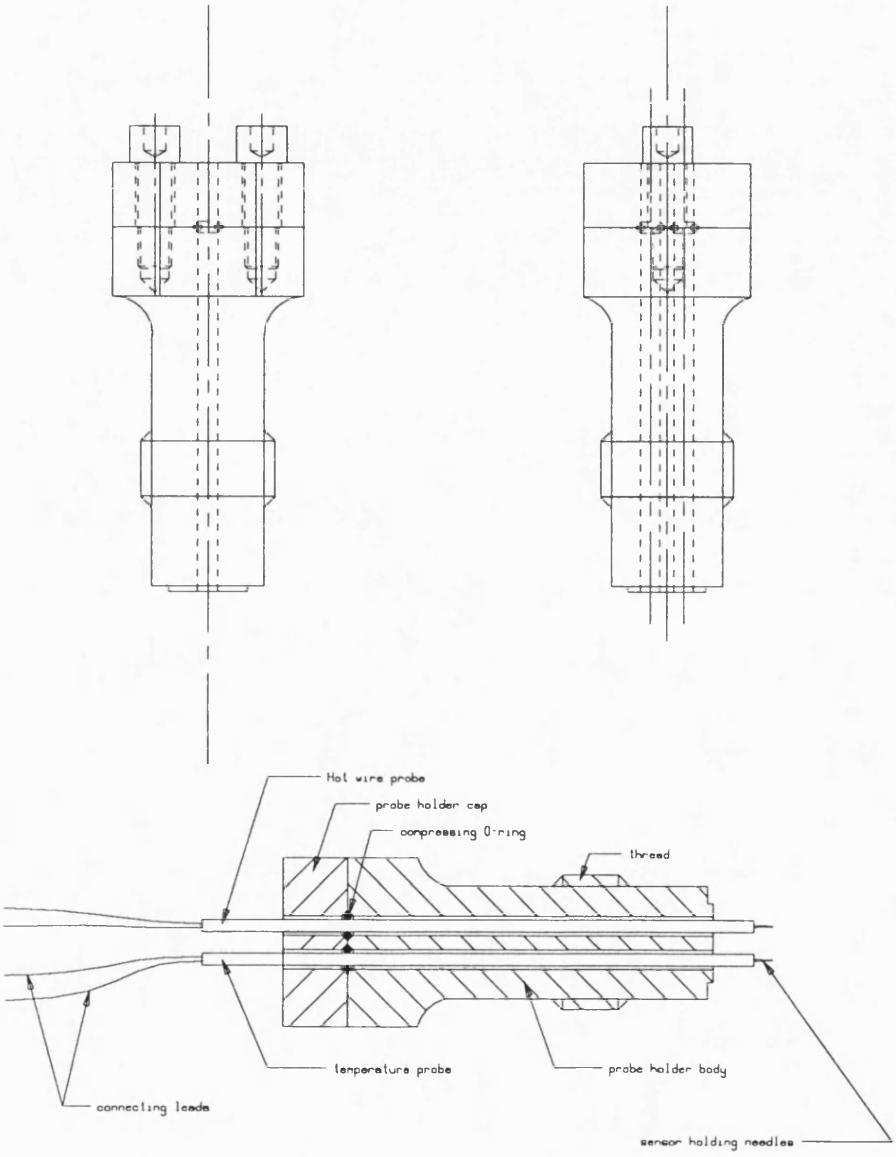

Figure 5.9 Probe holder assembly

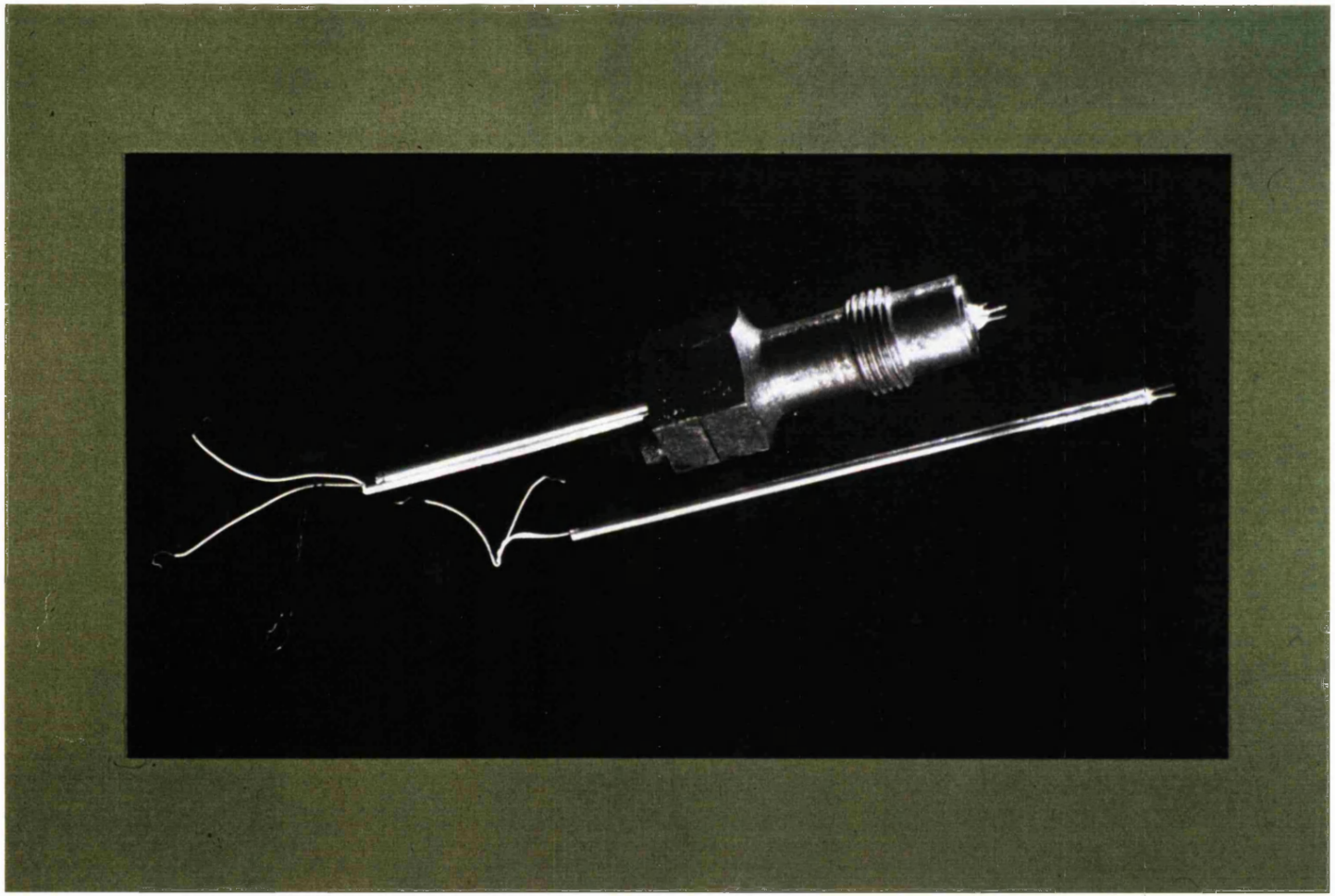

Figure 5.10 Hot wire probe and adaptor

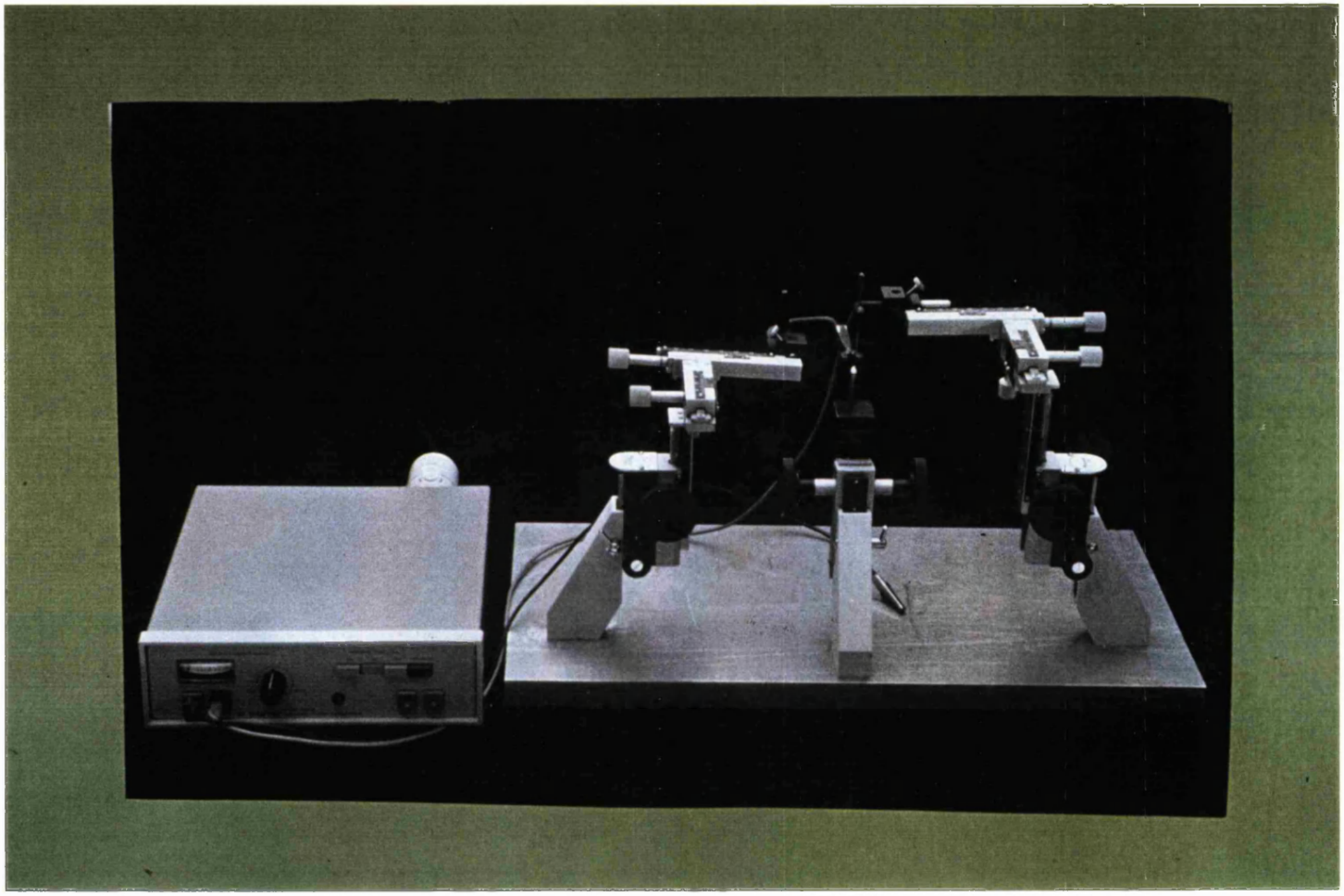

Figure 5.11 Spot-welding equipment

Figure 5.12 Prosser hot wire anemometer system

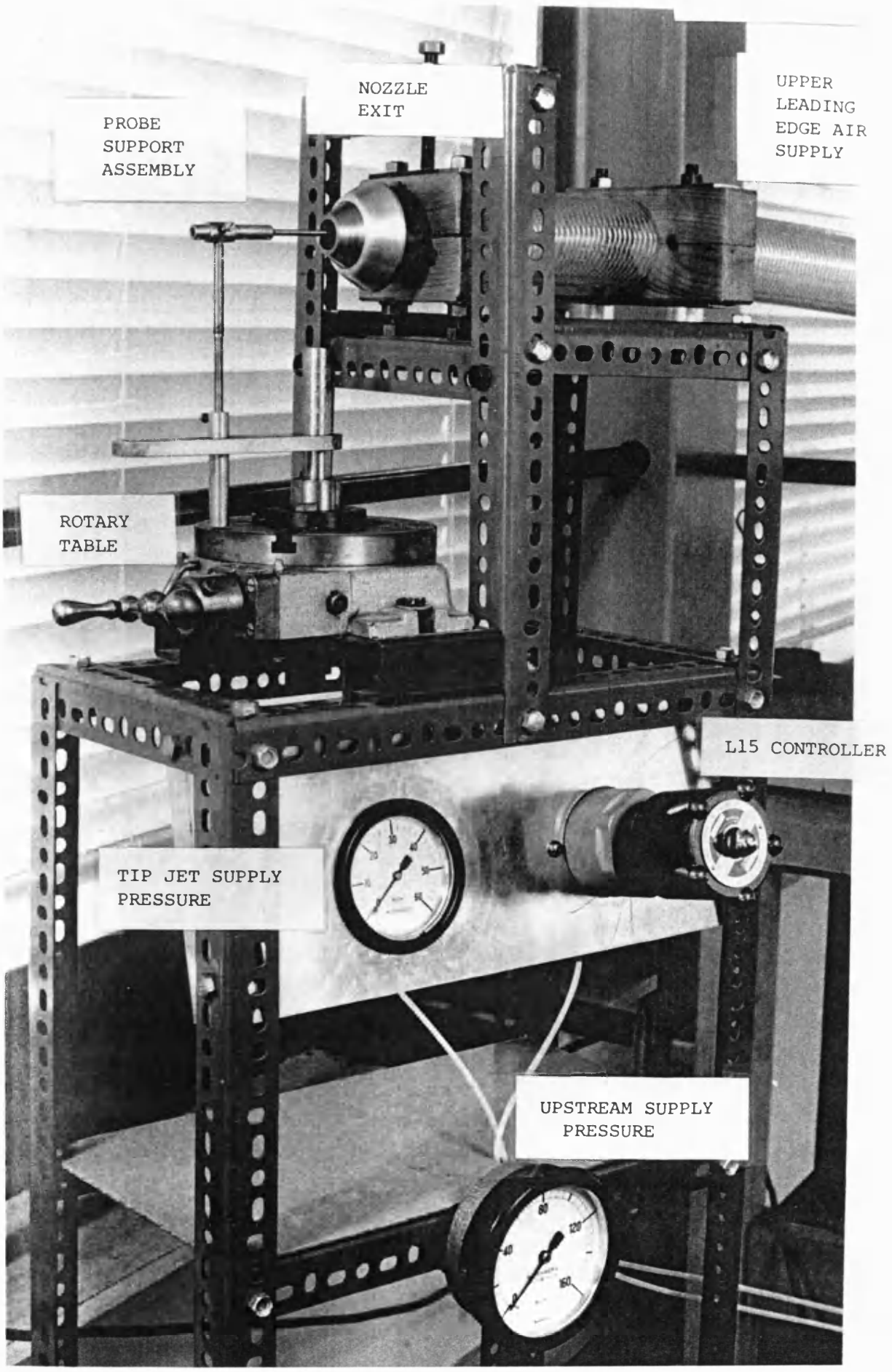

Figure 5.13 Steady flow calibration rig, Wood (1981)

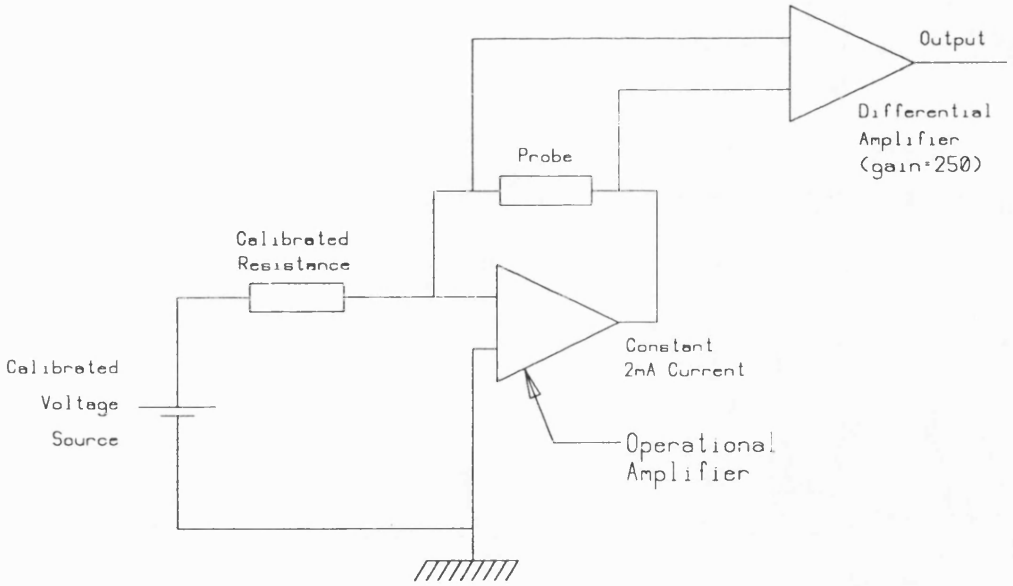

Figure 5.14 Resistance thermometer circuit

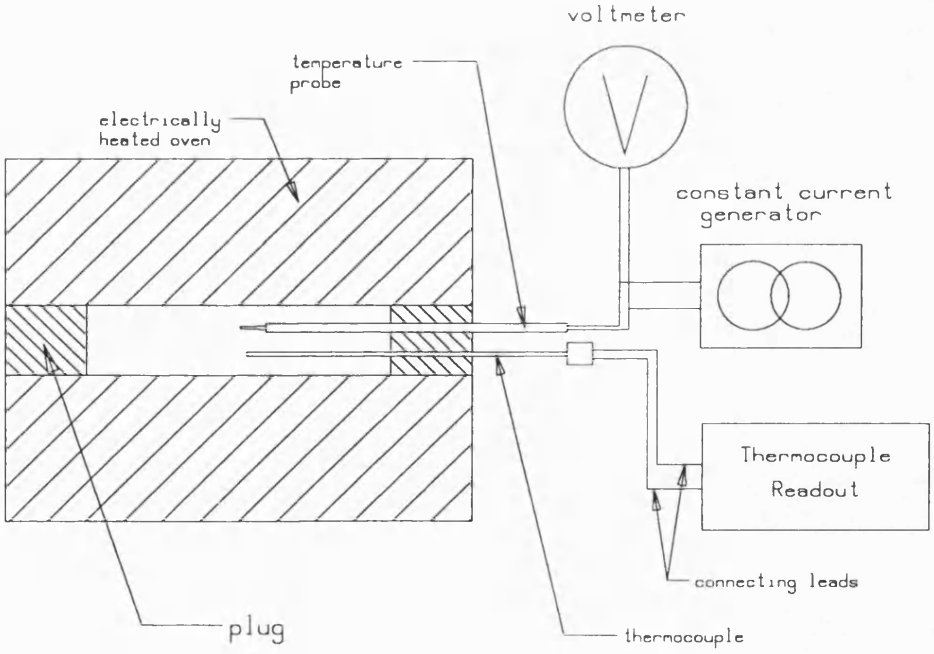

Figure 5.15 Standard oven test apparatus

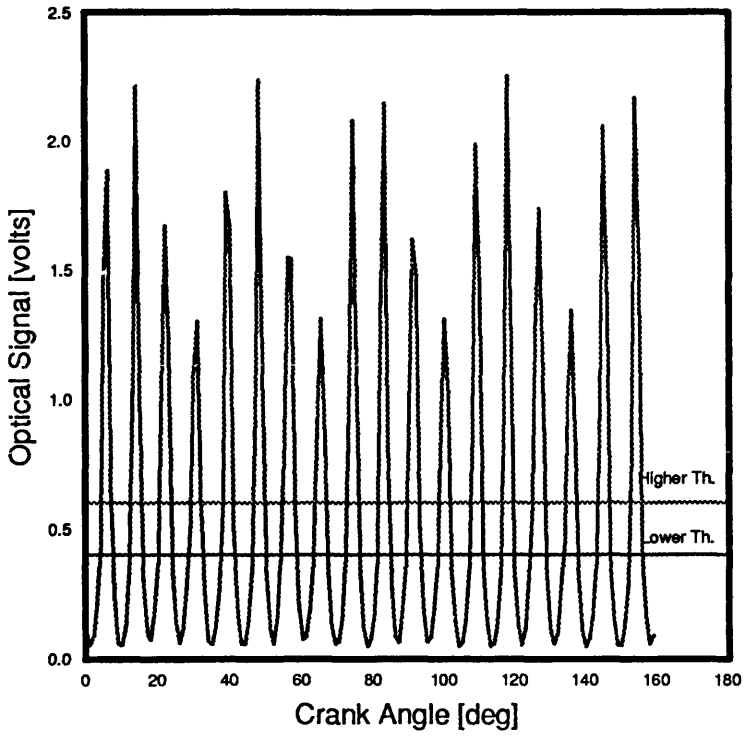

Figure 5.16 Vane anemometer raw signal

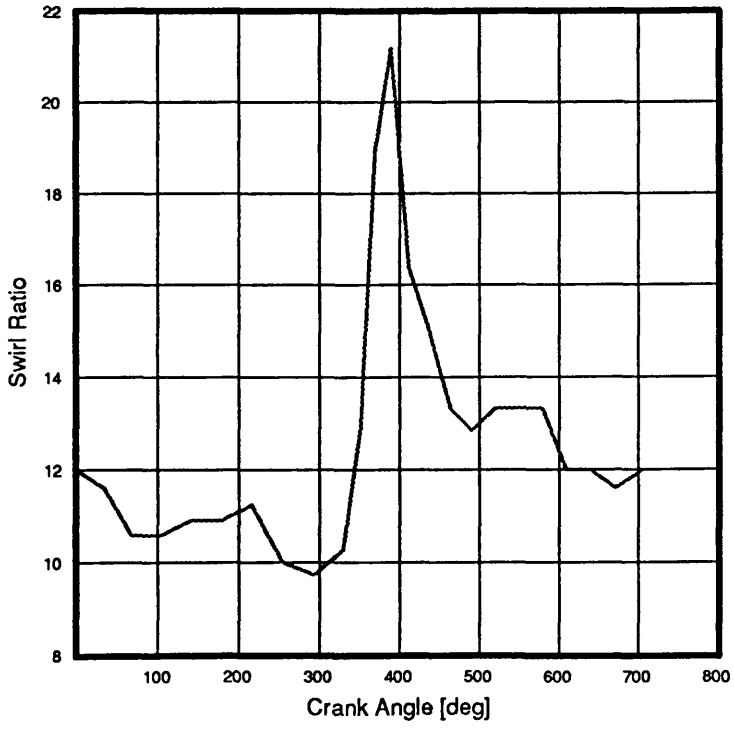

Figure 5.17 Swirl ratio measured by paddle wheel anemometer

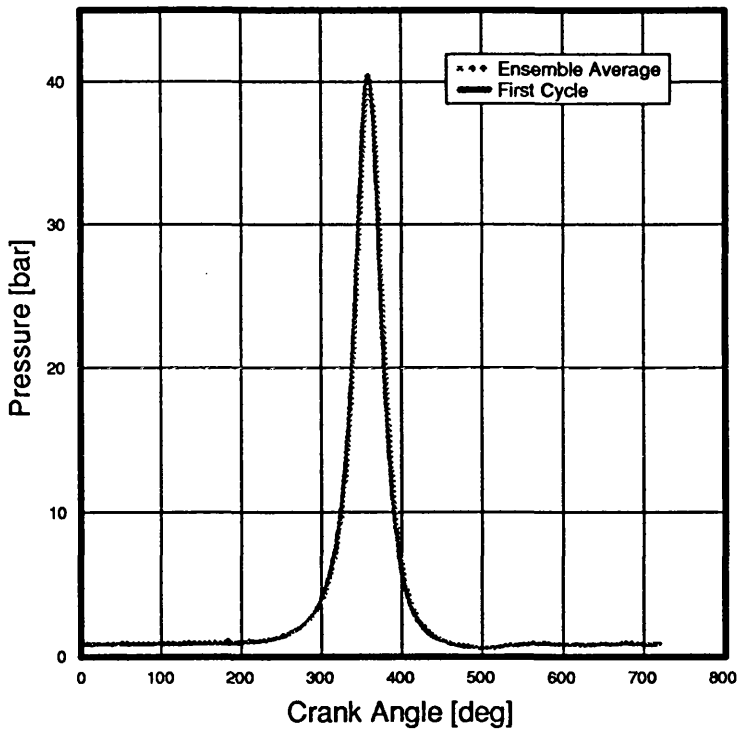

Figure 5.18 Single and mean gas pressure in the swirl chamber

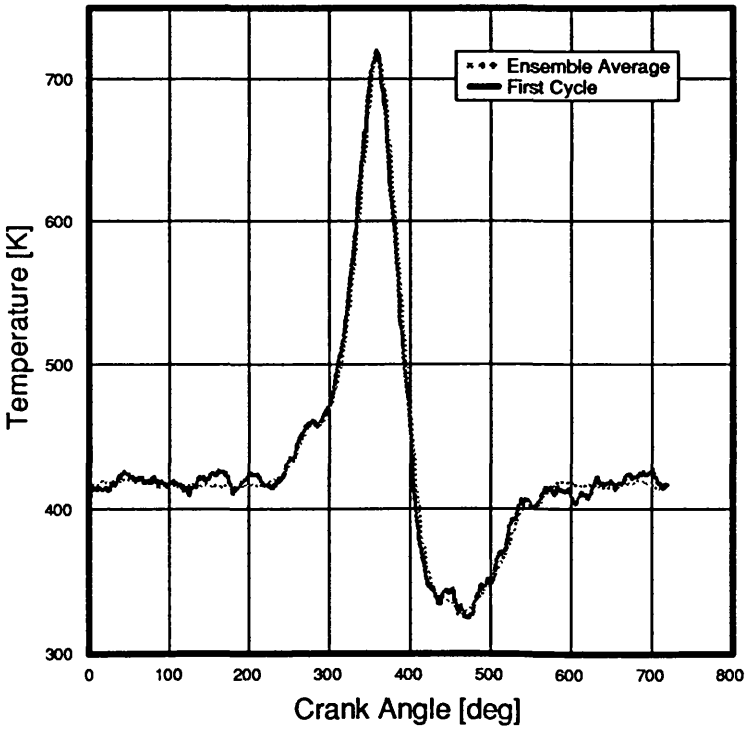

Figure 5.19 Single and mean gas temperature in the swirl chamber

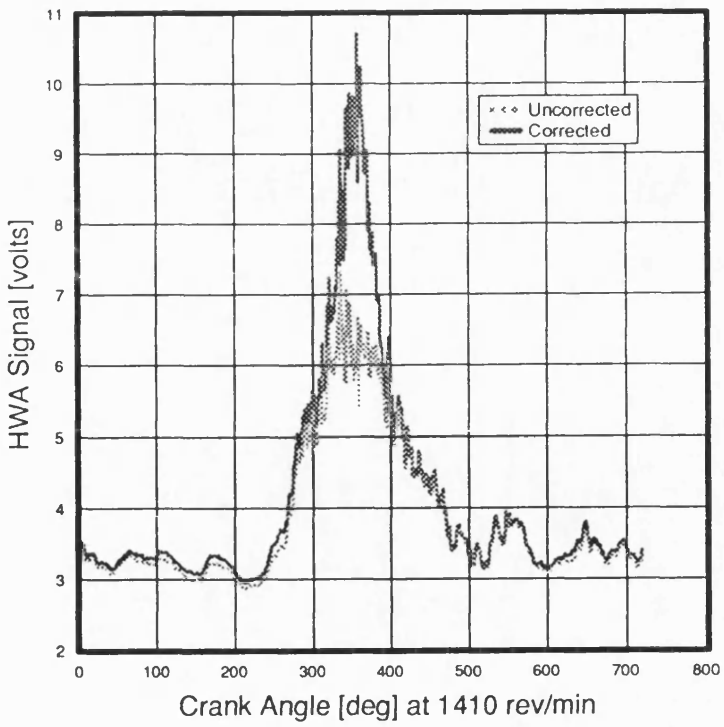

Figure 5.20 Corrected and uncorrected voltages

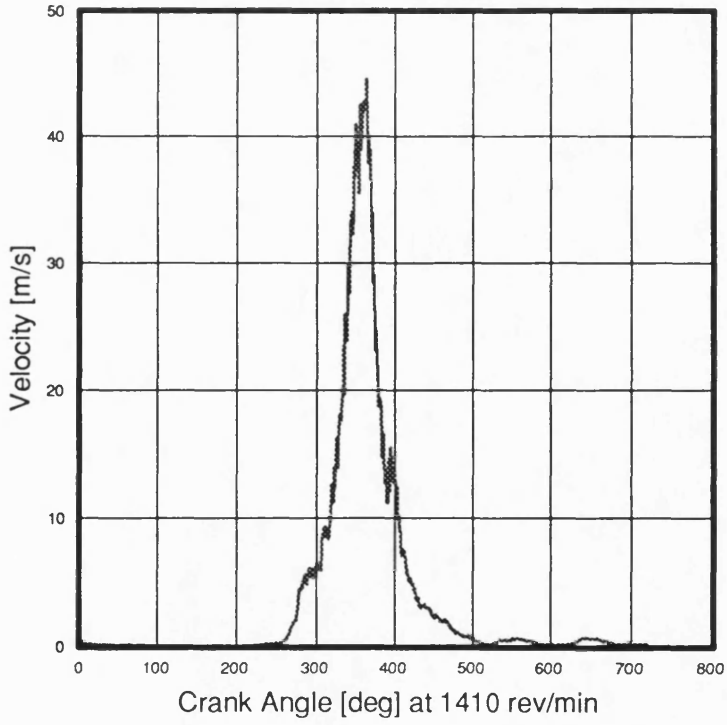

Figure 5.21 Mean velocity computed by ensemble average

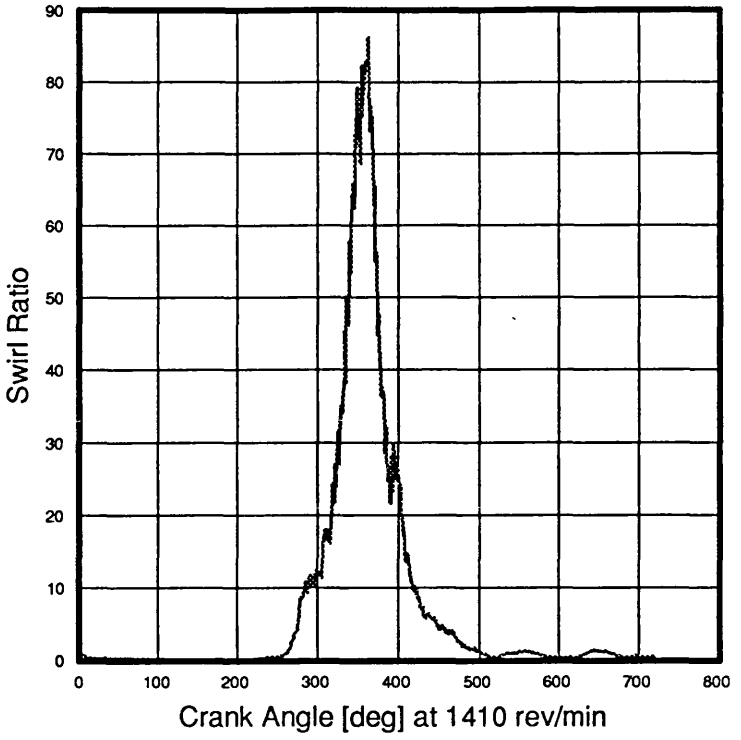

Figure 5.22 Swirl ratio versus crank angle

CHAPTER 6

EXPERIMENTAL RESULTS AND COMPARISON WITH THE MODEL

6.1 Introduction

The experimental facilities, data acquisition system and data processing techniques were described in Chapter 5. In this chapter the results of measurements made using both paddle wheel and hot wire anemometers are presented. Gas temperature measurements made in the swirl chamber with ceramic and standard insert are also presented. Comparison of the computed air swirl, temperature and pressure in the swirl chamber, is made with the experimental results. The chapter then ends with a brief summary.

6.2 Air Swirl

Figure 6.1 shows the variation of swirl ratio obtained by paddle wheel anemometer against crank angle for four engine speeds. Despite the absence of swirl over most of the cycle, as expected, the swirl ratio indicated by the wheel at no point falls below 9:1, due to the moment of inertia of the wheel. The paddle wheel anemometer has three disadvantages. Firstly, its moment of inertia severely limits frequency response. Secondly, at the speed encountered in this application the drag torque at the bearings prevents the wheel from attaining the mean swirl speed of the gas - by an unknown amount. Thirdly the wheel itself occupies a finite volume and thereby alters the compression ratio and the volume ratio. Nonetheless, the results from the paddle wheel are interesting and suggest that the swirl ratio is very largely independent of engine speed. The wheel is seen to accelerate over a relatively short period between 60 deg btdc up to tdc. Maximum swirl, despite all the drawbacks of the wheel, is about 21 times engine speed. The mean swirl indicated by the wheel is about 12.5:1, which for the reasons stated should be lower

than the actual mean swirl ratio. Figure 6.2 shows the variation of swirl ratio against time. As expected the swirl takes more time to increase to its maximum level and decay to its minimum level as engine speed decreases.

Figure 6.3 shows swirl ratio plotted against crank angle at a speed of 677 rev/min obtained by hot wire anemometry. The measurements were taken with the glow plug present, as shown in Figure 6.4. The firing tdc occurs at 360 degCA. As the anemometer probe is situated behind the glow plug in the swirl chamber, the effect of the glow plug intrusion in the swirl chamber is quite apparent. It can be seen from Figure 6.3 that the glow plug has managed to destroy the swirl during the exhaust and intake strokes, where swirl is expected to be low. The swirl increases sharply during the compression stroke and decays rapidly during the expansion stroke. It can be seen that when the glow plug is not present higher levels of swirl were obtained during the exhaust and intake strokes. The figure also shows that no considerable gain in swirl ratio is obtained by the end of the compression strokes when the glow plug is absent. This is probably due to the fact that the drag of the glow plug is overwhelmed by the high levels of swirl occurring at the end of the compression stroke such that its effect is hardly significant.

Figure 6.5 shows the swirl ratio plotted against crank angle for three engine speeds obtained by hot wire anemometry with the presence of the glow plug in the swirl chamber. In this graph the firing tdc occurs at 360 degCA. It may be seen that the swirl is negligible up until 100 deg btdc at which point it increases rapidly to attain a maximum value 65-85 times engine speed close to tdc. Beyond tdc the descent of the piston causes flow from the swirl chamber into the main chamber. The swirl diminishes rapidly during the expansion stroke, mainly due to viscous friction in the boundary layer at the swirl chamber wall. By 150 deg atdc the swirl has become negligible. Although the measurements were made at the same position for the three speeds, there is some variation in maximum swirl ratio between the three speeds. Since the swirl chamber is not quite spherical geometrically, it is very difficult to define the centre around which the air is

rotating in the swirl chamber. The swirl ratio calculation is based on the assumption that the centre of vortex in the three cases is constant. This assumption is probably not realistic and may explain the discrepancy between the maximum swirl ratio.

Figure 6.6 shows the same results as Figure 6.5 but in terms of velocity rather than swirl ratio. At tdc higher levels of air velocity are obtained at the highest engine speed as expected. The difference is not quite proportional to the engine speed, which agrees with the discrepancy in Figure 6.5.

In order to examine the velocity distribution in the swirl chamber, measurements were made at locations of 3, 5 and 7 mm from the geometrical centre of the swirl chamber. Figure 6.7 shows the comparison of velocity at three different positions in the swirl chamber at a speed of 670 rev/min. An examination of the figure shows that the velocity increases radially. If the assumption of solid body rotation is true the velocity is expected to increase linearly with the radius. Apparently this is not the case in Figure 6.7. Again it could be explained by the above argument that the centre of vortex in the swirl chamber is not stationary with time or speed. This would indicate that the measured velocity at a fixed geometrical position in the swirl chamber does not have to be the same as the actual position in the air vortex. Figure 6.8, which shows the swirl ratio of the velocities of Figure 6.7, shows that there is a discrepancy between the maximum swirl ratio at the three positions. The three curves in figure 6.8 should be identical if the solid body rotation assumption is true. This means that the velocity at the centre should be zero and maximum at the periphery. Ajakaiye (1976) found that the velocity near the centre of a cylindrical prechamber was not equal to zero. Figure 6.9 shows the radial distribution of the velocity in the swirl chamber at tdc and a speed of 670 rev/min. Since measurements were not made simultaneously it can not be stated that the solid body rotation assumption does not hold. It might also be possible that a combination of forced and free vortices exist in the swirl chamber. These areas may perhaps be probed in the future by using

simultaneously four probes in the swirl chamber two through the injector hole and two through the glow plug to measure the velocity at four different locations. Correlation of the resulting data may enable the centre of rotation to be located with time.

6.3 Gas Temperature

The variation of gas temperature in the swirl chamber measured by the fast response resistance thermometer is shown is Figures 6.10 and 6.11. Three materials (cast steel, syalon and aluminium titanate) have been used in the lower half of the swirl chamber (hot plug) at two engine speeds (677 and 1410 rev/min).

Both syalon and aluminium titanate are engineering ceramic materials. For all of the experimental tests the engine was motored and the jacket water was at a temperature of 20-30 degC. The temperature curves shown are the average of 44 cycles. It can be noticed from the curves that the temperature peak is coincident with the pressure peak which shows that there is almost no thermal lag at this time as discussed is section 4.6.1. Furthermore, as mentioned earlier, these temperatures were taken in the swirl chamber and not in the main chamber where the temperature at the end of induction (180 degCA) would be very close to the ambient temperature (20 degC).

During gas exchange (500-180 degCA) the gas in the swirl chamber is seen to pick up heat from the walls and to attain a temperature between 400 K and 500 K. Although the jacket water was not hot, the hot plug walls seem to be hot enough to heat the gas in the swirl chamber. This can be explained by the fact that there is an air gap between the hot plug and cylinder head which is designed to reduce heat transfer. In order to check this point we placed a thermocouple near the centre of the swirl chamber, at the same position of the hot wire, with a special adaptor through the injector hole. The thermocouple reading was 280 degC which represented the average temperature during the cycle. This seems to agree with the temperature measured by the resistance thermometer. When the cylinder head was removed from the engine, immediately after running, the swirl

chamber insert was hot even though the bulk coolant temperature was only 20-30 degC. Since the engine was motored for only a short time (less than 10 minutes) before measurements were made it is likely that the engine had not reached thermal equilibrium and it was passing through the thermal lag phase. As aluminium titanate has a larger temperature swing, see Figure 7.15, and a lower penetration depth than the other two materials it was probable that the small amount of air in the swirl chamber during gas exchange (less than 100 μg in mass) did not pick up as much heat from the hot plug as with cast steel which has a higher thermal diffusivity. Had the engine reached thermal equilibrium the story would have been different since aluminium titanate would have a hotter surface than the other two materials as shown in Figure 7.13.

Throughout the exhaust and intake strokes it is unlikely that any significant gas exchange occurs between the swirl chamber and the main chamber. At the beginning of the compression stroke, air temperature in the swirl chamber is seen to decrease slightly before it continues to increase again. This is due to the fact that as the air in the swirl chamber has picked up heat from the walls, during the intake and exhaust strokes, its temperature is higher than that of ambient air. At the beginning of the compression stroke air coming from the main chamber will reduce the temperature of the air in the swirl chamber. The coolest point in the cycle occurs at the end of the expansion stroke where temperatures of 330-380 K are observed.

During the compression stroke air temperature rises rapidly until it reaches its highest value at the end of the compression stroke. The ceramic materials were in the form of a monolithic hot plug, ie lower half of the swirl chamber only, within a steel sleeve to give support. The material with the lowest thermal conductivity, aluminium titanate, gave the highest temperature at the end of the compression stroke. Syalon and cast steel have similar thermal conductivities and hence peak temperatures. At the lowest speed (677 rev/min) the gas temperature was some 40 degC higher with the aluminium titanate hot plug, at the end of compression, which could assist cold starting. It is likely that this

temperature difference will increase when a full ceramic swirl chamber is used at cranking speed (500 rev/min). This may allow a reduction in compression ratio and hence a larger swirl chamber. Peak temperature difference is seen to decrease as engine speed increases, this is because less time is available for heat transfer and peak temperature will mostly be determined by compression ratio.

6.4 Comparison of Computed and Measured Results

In order to validate the mathematical model a comparison was made between the experimentally measured pressure, temperature and swirl and the computed values, in the swirl chamber, at 1410 rev/min engine speed. Since the engine was motored it was expected that some blowby would occur. This was confirmed by measuring the blowby through the engine breather. The blowby measured was about 8% of the induced air. Account had to be taken, in the model, of gas leakage past the piston by including a small flow path from the cylinder to the crank case. This was achieved by connecting a flow junction between the atmosphere and the control volume representing the cylinder. The leakage having previously been measured, and matched during simulation by adjusting the area of the leakage path.

Figure 6.12 compares the measured and computed gas pressure in the swirl chamber. The agreement is excellent, however, predicting the pattern of the pressure curve is not particularly difficult. In addition, account was taken of the blowby without which the peak of the pressure would have been over estimated.

Figure 6.13 shows a comparison of the measured and computed gas temperature in the swirl chamber. The experimental curve was obtained using the fast-response resistance thermometer described earlier, which measures the temperature of the gas at a single point within the chamber. The computed value represents the spatially averaged gas temperature for the entire swirl chamber, thus small differences should be expected. The temperature in the swirl chamber reaches a minimum at the end of the expansion stroke.

After the expansion stroke there is little flow into or out of the swirl chamber until the compression stroke. The gas held in the swirl chamber during the exhaust and induction strokes, having been cooled by expansion is heated gradually by the relatively hot chamber walls until the rapid in-flow from the main chamber begins. These effects are reasonably well predicted, as is the compression temperature rise, however, the peak temperature is overestimated by about 20 degC, probably due to poor performance of the heat transfer model in the main chamber.

Figure 6.14 shows a comparison of the experimentally measured swirl ratio and the computed swirl ratio. The peak level of swirl ratio is predicted reasonably well, as is the development of the swirl during the compression stroke. The experimentally measured swirl is shown to rise and decay very rapidly, lasting for only 240 degCA, whereas the computed swirl persists throughout the cycle, at no point falling below 10:1. Bearing in mind the predicted swirl is the mean swirl in the swirl chamber while the measured swirl is made at a single point in swirl chamber, see section 6.2.

6.5 Summary

This chapter has looked at the results acquired from the motored engine. Swirl measurements made in the swirl chamber using paddle wheel and hot wire anemometers are presented. Results of gas temperature measured by using a resistance thermometer in the swirl chamber with ceramic and the standard insert are discussed. The experimental and the theoretical computed results are compared.

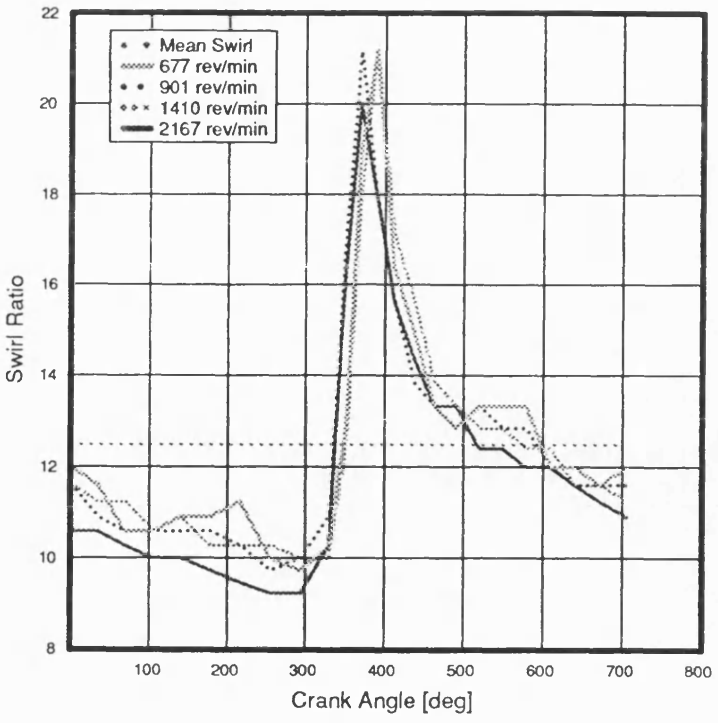

Figure 6.1 Instantaneous swirl versus crank angle measured with the paddle wheel anemometer

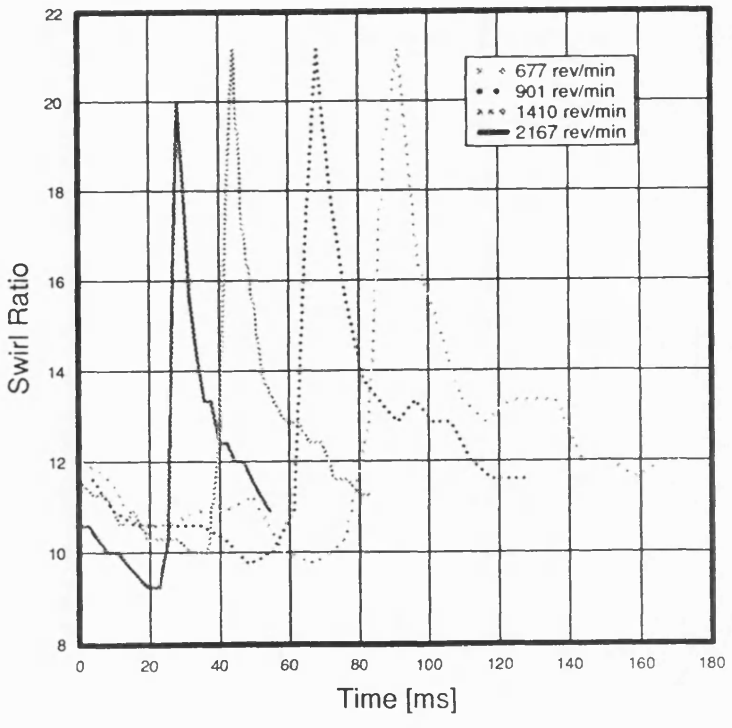

Figure 6.2 Instantaneous swirl versus time measured with the paddle wheel anemometer

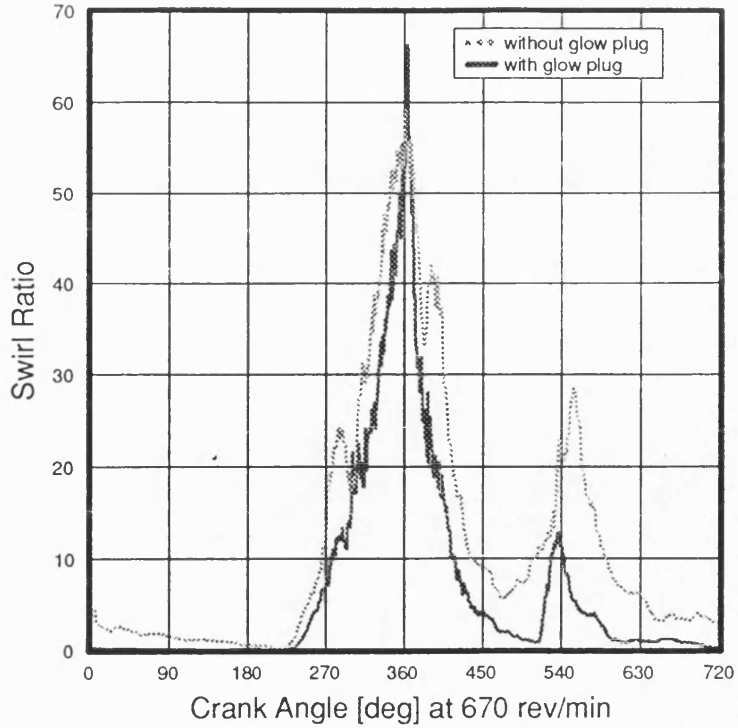

Figure 6.3 Instantaneous swirl versus crank angle measured by hot wire anemometer

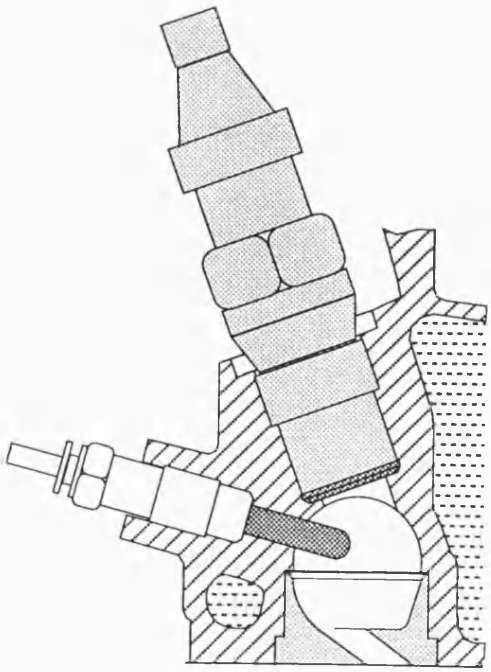

Figure 6.4 Cross-section of the Ford 1.6 litre IDI Comet swirl chamber

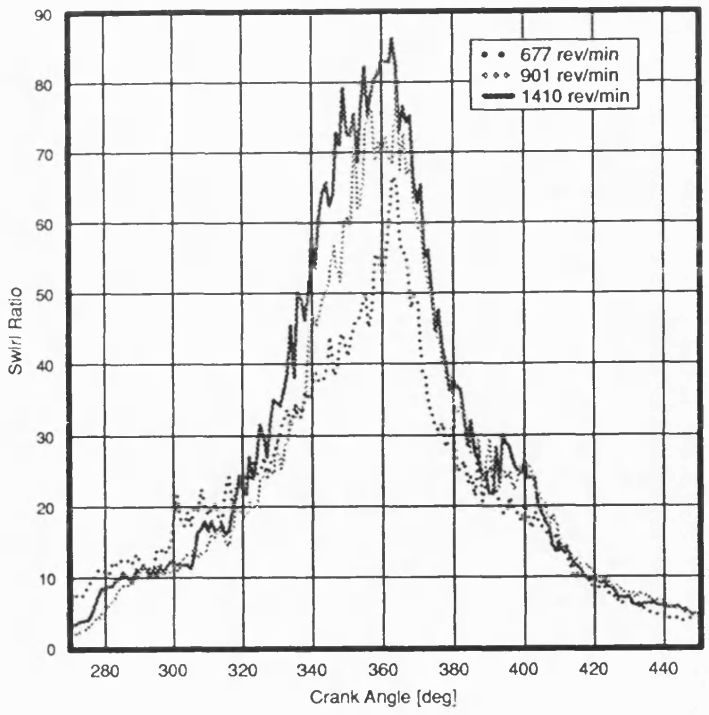

Figure 6.5 Swirl ratio at three engine speeds measured by hot wire anemometer

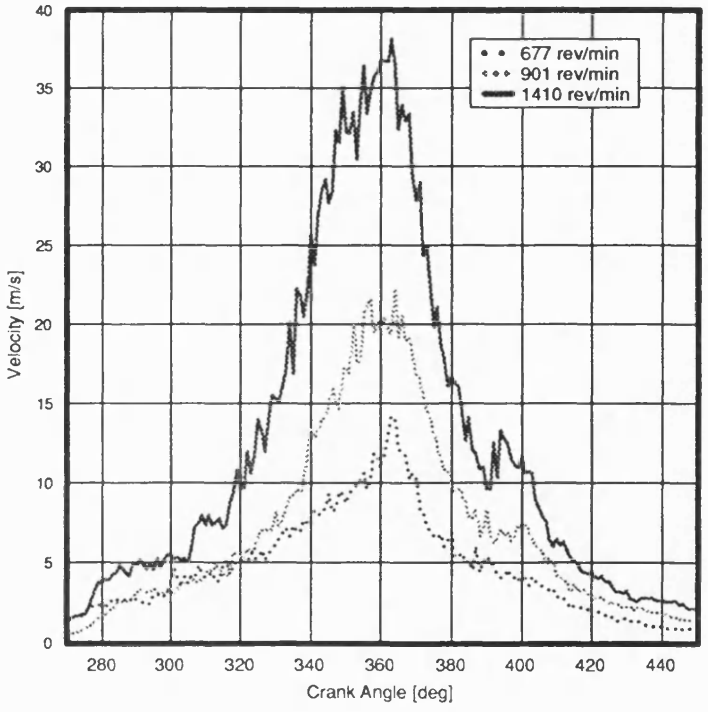

Figure 6.6 Air velocity at three engine speeds measured by hot wire anemometer

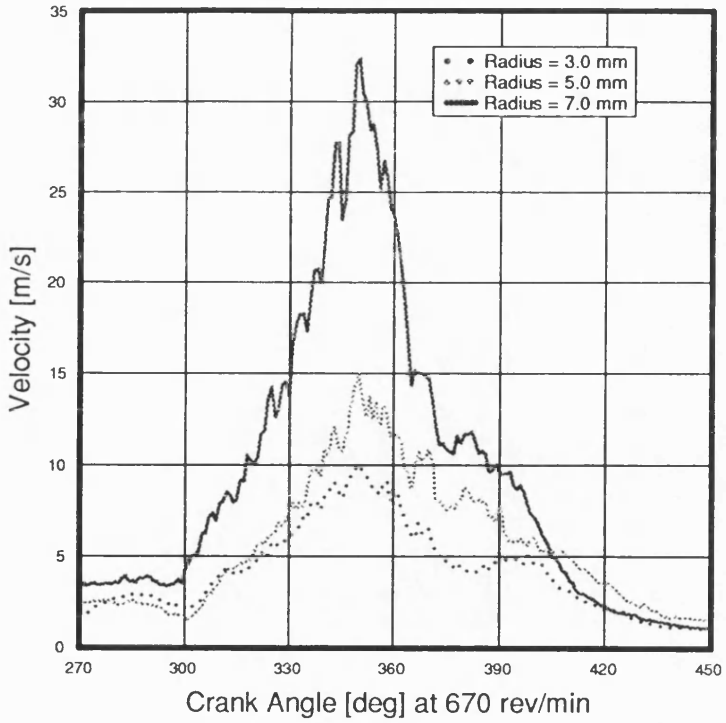

Figure 6.7 Measured air velocity at three different positions in the swirl chamber

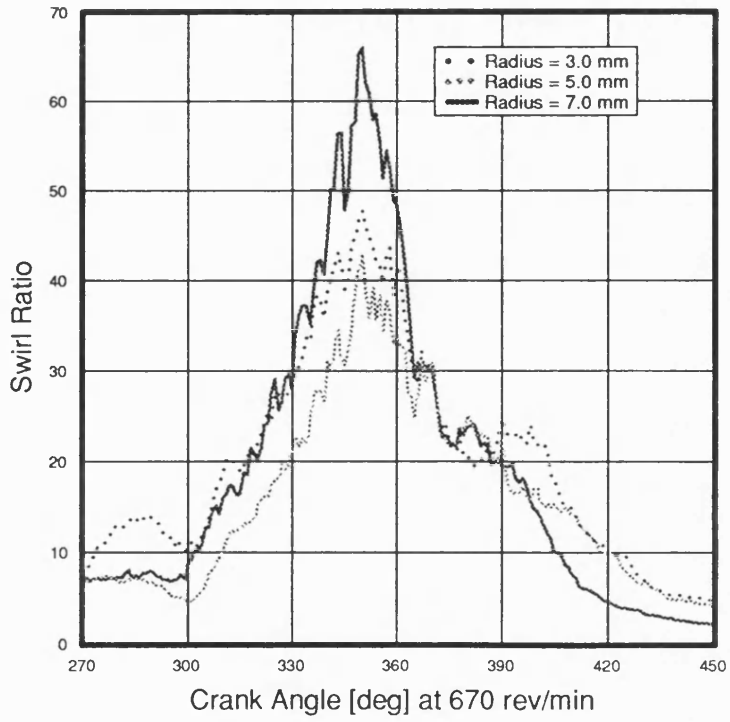

Figure 6.8 Swirl ratio at three different positions in the swirl chamber

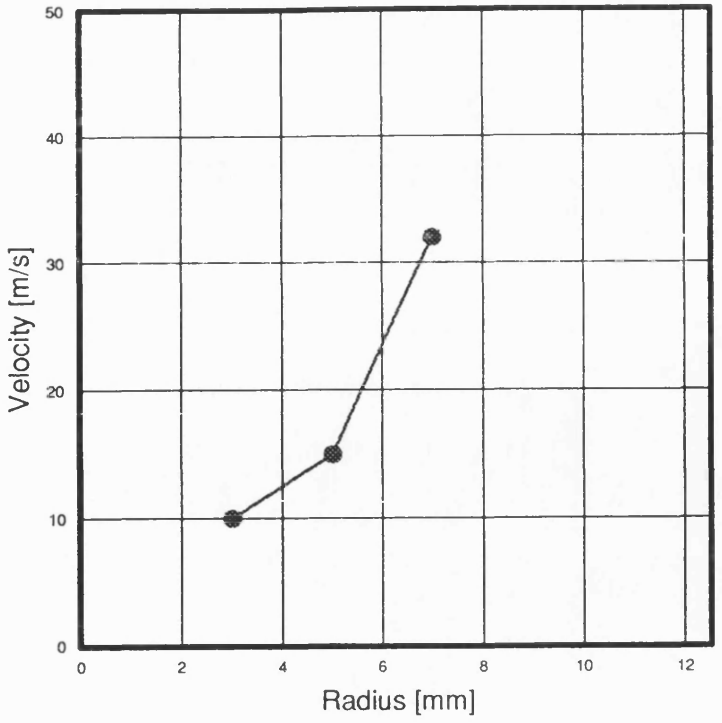

Figure 6.9 Radial profile of air velocity in the swirl chamber

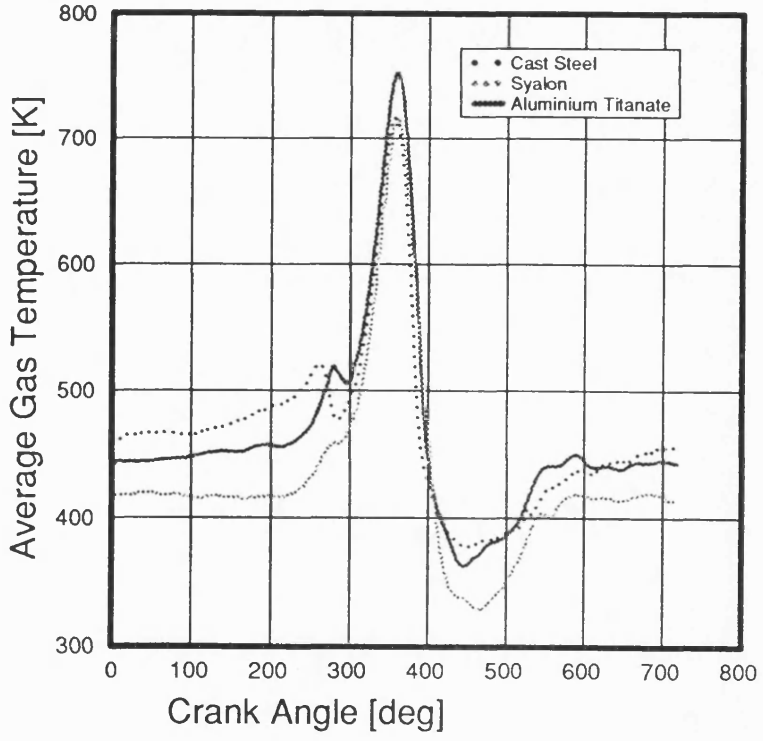

Figure 6.10 Measured instantaneous gas temperature versus crank angle at 677 rev/min

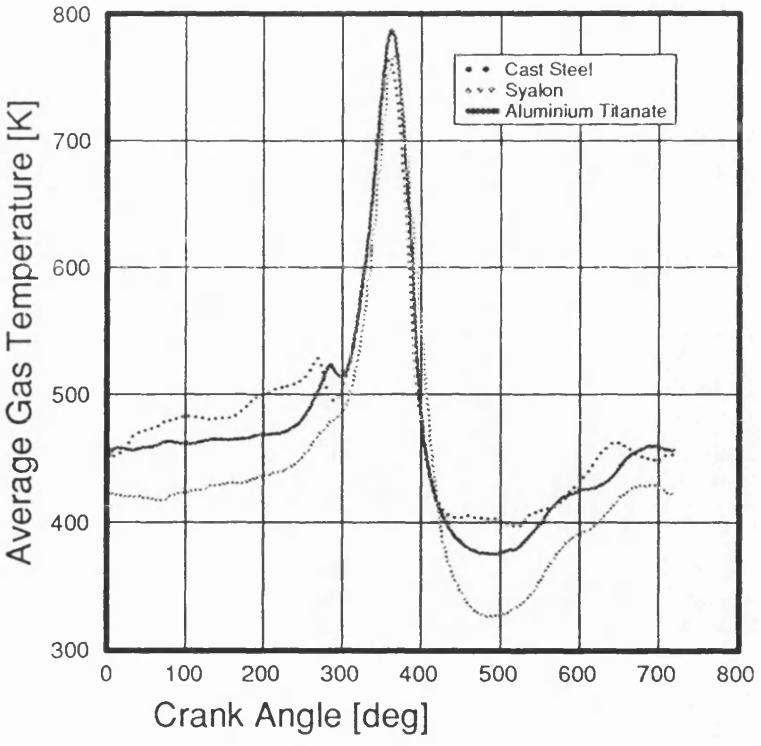

Figure 6.11 Measured instantaneous gas temperature versus crank angle at 1410 rev/min

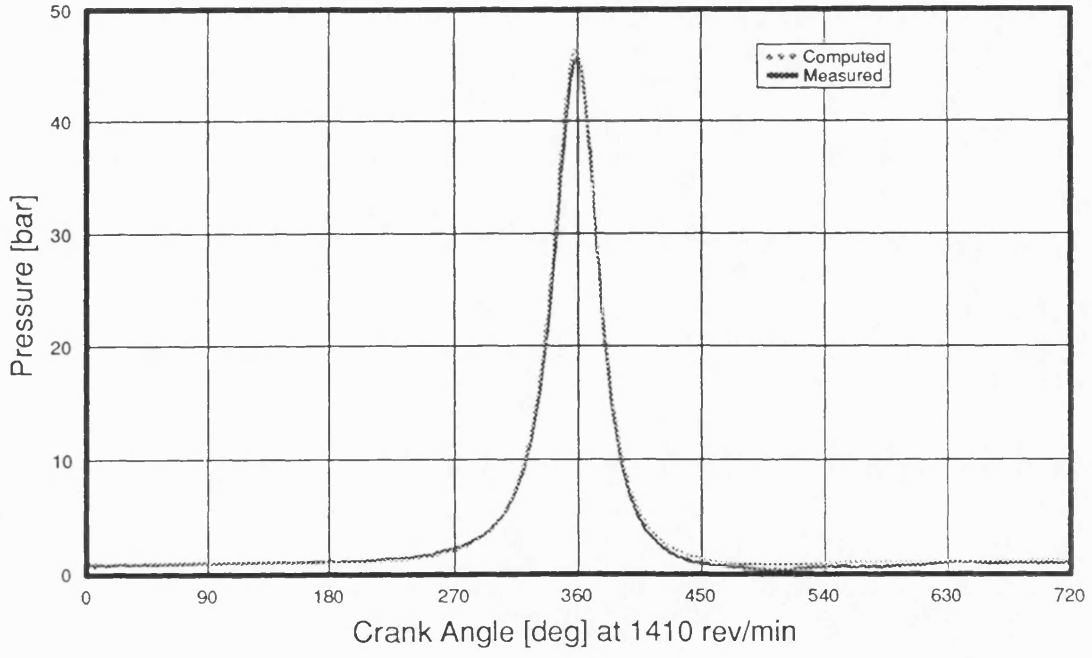

Figure 6.12 Comparison of measured and computed swirl chamber pressure

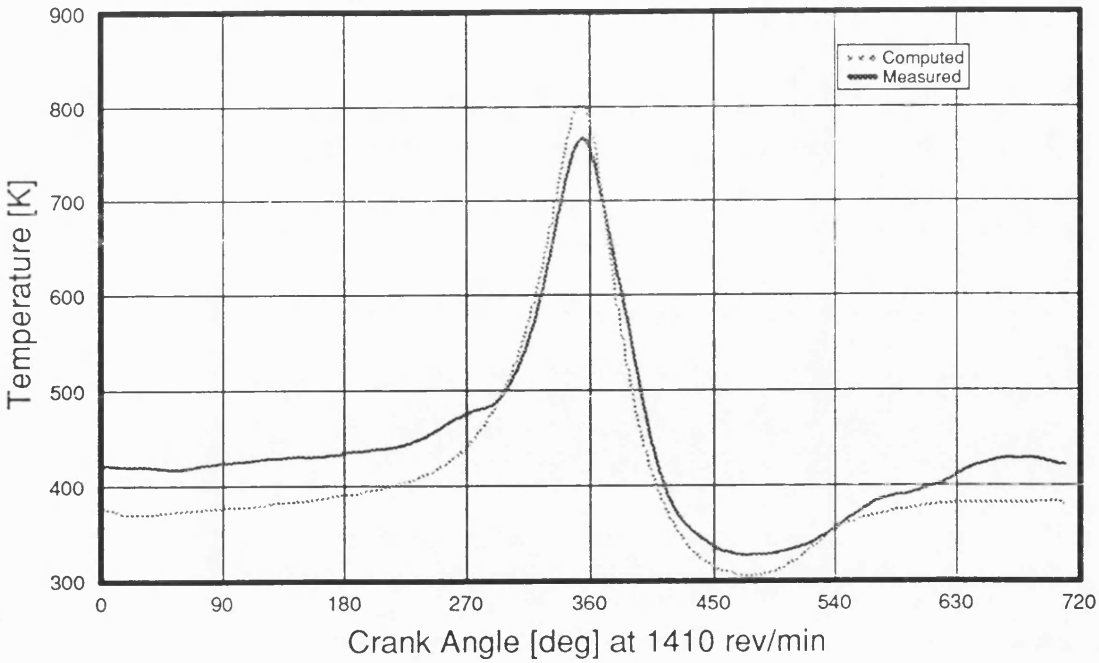

Figure 6.13 Comparison of measured and computed swirl chamber temperature

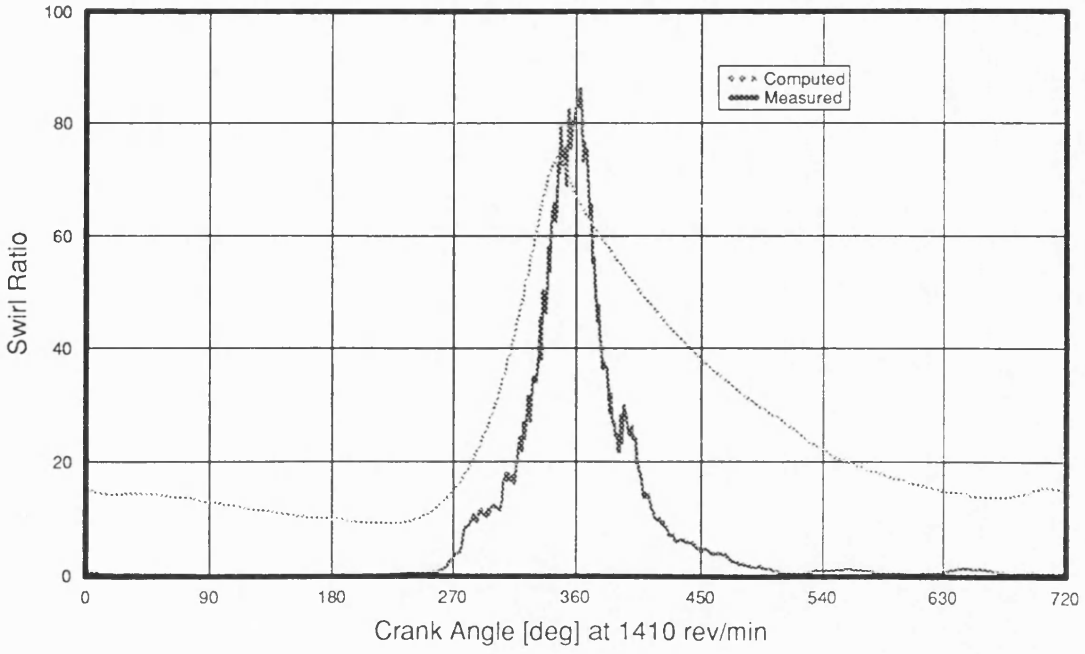

Figure 6.14 Comparison of computed swirl ratio and swirl ratio measured by hot wire anemometer

CHAPTER 7

PARAMETRIC STUDY

7.1 Introduction

A successful mathematical model should mimic the actual system in almost all the physical processes involved. In a real engine cycle, the output is very much dependent on certain engine input parameters such as geometry, speed and material properties. Therefore the predictions of an engine cycle simulation have to be sensitive to changes in the values of the input parameters. In the current simulator some empirical coefficients have been used in the internal sub-models. This chapter discusses the sensitivity of the cycle simulation results, under motored conditions, to values of input parameters and coefficients. A sensitivity analysis has been performed by varying each parameter, or coefficient, independently. The simulator was run for 10 cycles, to achieve equilibrium, in each case. The following is a description of the effects of the discharge coefficient, throat area ratio, friction factor and piston leakage on air swirl. In addition the heat transfer model was used to study the effect of swirl chamber material and heat transfer coefficient on swirl, surface temperature and heat flux.

7.2 Throat Coefficient of Discharge

The rate of mass flow through the connecting throat between the swirl chamber and the main chamber of the IDI engine, see equation (3.8), is described by the equation for the compressible flow through a flow restriction. Real gas flow effects are included by multiplying the geometric area by a discharge coefficient, usually experimentally determined, to produce the effective flow area. The value of the discharge coefficient is very important as the predicted behaviour of an IDI engine will depend on the effective flow area of the throat. Kamel (1977) found, from experimental steady flow tests, that the value of the discharge coefficient is a function of flow direction, pressure ratio and piston proximity. He stated that the effective area is much reduced when the piston

approaches the top dead centre position. This is shown in Figure 7.1. Mansouri (1981) investigated the effects of the value of the discharge coefficient in a prechamber engine. He found out that thermal efficiency and NO_x emissions levels are slightly sensitive to changes in the value of the discharge coefficient. However, he also found out that the pressures and the pressure differences between the two chambers are more sensitive to the same changes during the combustion and expansion processes.

In the current investigation the throat discharge coefficient was varied from 0.6 to 0.9 at an engine speed of 3000 rev/min. Figure 7.2 shows clearly that mean swirl ratio is much dependent on the value of the discharge coefficient, the relation is almost linear. As the value of discharge coefficient increases the effective area is increased which reduces mean swirl ratio. Mean swirl ratio drops from about 30.5:1 at a discharge coefficient value of 0.6 to about 23:1 when the discharge coefficient is 0.9. Figure 7.3 shows variations of instantaneous swirl ratio with values of discharge coefficient of 0.6 and 0.9. The difference in peak swirl ratio is about 30.

7.3 Throat Area ratio

The simulator was used to study the effect of varying the throat area at a constant discharge coefficient, taken as 0.62, and in order to speed up the simulation time the engine was run at 5000 rev/min. The throat area was increased from the datum by 10% and 20%. The result of the simulation is shown in Figure 7.4. In this case the firing tdc occurs at 180 deg CA and the non-firing tdc occurs at 540 deg CA. The smaller second peak is caused by the pressure build-up at the non-firing tdc because of the very low valve overlap of this engine. At the firing tdc the maximum swirl is reduced from 370,000 rev/min to 312,000 (-16%) as the area is increased by 20%.

7.4 Pumping Work

The pumping of the gas through the throat is a major factor which makes the IDI engine less efficient than the DI engine. The simulator has been used to investigate the effects of variation of engine geometry on pumping work. In order to isolate pumping losses the simulation was carried out with no heat transfer from the motored engine. An equivalent DI engine was modelled under the same operating conditions as that of the IDI. The difference between the brake power absorbed by the DI and the IDI engine was considered as the power needed to pump the gas through the throat. Two cases; throat area ratio D_{th}^2/D_{cyl}^2 and volume ratio V_{SW}/V_{cyl} were considered. The cases were applied over a range of engine speeds to predict the additional power, for the four cylinders, needed to fill the swirl chamber against the flow resistance of the throat. The results obtained are shown in Figure 7.5 and Figure 7.6. In an IDI engine the throat area is generally expressed as a percentage of the piston area. The throat area has been varied by 0.2% of the piston area on either side of the datum which has a throat area equivalent to 1% of the piston area.

Figure 7.5 shows that relatively small changes in throat area have marked effects on the predicted pumping power. The power is seen to increase sharply with engine speed, the relation being approximately cubic, as would be expected. This is due to the fact that at high engine speeds there is less time available to pump the gas through the throat. For the smallest throat at the highest speed the pumping power is almost 3 kW, for an engine output of 40 kW, compared with 1.75 kW for the standard design. In addition to the excessive power requirement the maximum pressure in the main chamber was increased from 60 to 66 bar under these conditions. On the other hand, using a larger throat decreases pumping power but at the same time it reduces maximum swirl as shown in Figure 7.4.

Figure 7.6 shows the predicted relationship between pumping power and volume ratio. Again, relatively small changes in volume ratio are shown to have significant effects on

pumping power. This is due to the fact that as the swirl chamber is enlarged, at constant compression ratio, so the mass transferred to the swirl chamber increases. Of course it is desirable to have a larger swirl chamber as more air will be present in the swirl chamber to improve mixing and oxygen availability , which reduces particulate and soot emissions. Unfortunately, as can be seen from Figure 7.6, the IDI engine would pay the penalty in terms of pumping losses.

7.5 Engine Speed

The predicted variation of swirl ratio with engine speed is shown in Figure 7.7. This indicates that the peak swirl ratio is quite independent of engine speed. The rate of decay of swirl ratio does, however, depend on engine speed, the lower engine speeds having a slightly higher rate of decay in crank angle, but, as shown in Figure 7.8, a much slower rate of decay on a time basis as would be expected. It can also be seen from Figure 7.7 that the smaller second peak, which is caused by the pressure build up at the non-firing tdc, at the highest engine speed is not present at the lowest engine speed.

7.6 Friction Factor

The calculation of the total viscous torque is defined in section 3.3. The friction factor, in equation 3.13, is determined by the value of the empirical constant λ , which allows for differences between the flat plate and cylinder wall conditions. This constant, with a value of 1.5 at the basic condition, has been varied from 0 (slip condition) to 4 at an engine speed of 4800 rev/min. The results are shown in Figures 7.9 and 7.10. It can be seen from Figure 7.10 that with the slip condition the swirl seems to increase steadily from 80 degCA btdc to a maximum value at 8 degCA btdc and then to decrease to a constant level at tdc. The swirl stays at this level during the expansion stroke as there is no viscous friction. The swirl then falls steadily during the exhaust stroke and it stays at a constant level during most of the intake stroke before falling again steadily until about 80 degCA btdc. This behaviour can be explained with the help of the throat velocity

curve and the instantaneous swirl chamber mass curve, shown in Figures 7.11 and 7.12. The throat velocity determines the momentum flux entering or leaving the swirl chamber. For a given angular momentum, swirl is inversely proportional to the mass of air in the swirl chamber, ie. larger mass will slow down swirl in the swirl chamber. This explains the dip in the swirl curve close to tdc, shown in Figure 7.10. As the piston is slowing down towards tdc, the throat velocity, decreases rapidly until it reaches a minimum value at tdc, shown in Figure 7.11. In the mean time, the instantaneous mass of the air in the swirl chamber increases to a maximum value at tdc, shown in Figure 7.12. The combination of both effects result in the reduced swirl.

In Figure 7.9, it is seen that the rate of decay of swirl depends significantly on wall friction. Mean swirl ratio was reduced from 64:1 with a slip condition to 30:1 at basic condition ($\lambda = 1.5$). At low levels of swirl during the engine cycle the effect of wall friction is quite apparent. As swirl increases the effect of wall friction on swirl is reduced.

7.7 Heat Transfer

There is substantial interest in using ceramic materials in the IDI engine, since they could operate at much higher temperatures, and reduce heat loss from the working fluid to the cooling water. The study was conducted on the three materials (cast steel, syalon and aluminium titanate) discussed in section 6.3 with their properties described in Table 5.3.

Figure 7.13 shows the predicted variation of surface temperature in the hot plug of the swirl chamber for the three materials. It can be seen that aluminium titanate, which has the lowest thermal conductivity, increases the surface temperature by some 200 degC over the other two materials. The thermal energy is transferred from the hot gases in the swirl chamber to the swirl chamber wall during the compression and expansion strokes. This energy is stored in a thin layer adjacent to the surface. Some of the thermal energy diffuses through the wall, but much of it is transferred back to the swirl chamber contents, which will be at a lower temperature, during the intake and exhaust strokes.

The thermal wave penetrates the skin of the material until the amplitude of the wave dies out at a certain depth. The penetration depth δ is proportional to $\sqrt{\alpha/\omega}$ where α is the thermal diffusivity and ω the fundamental frequency of the wave (proportional to the engine speed). Figure 7.14 shows the effect of engine speed on the penetration depth.

Since the gas temperature is fluctuating, this in turn causes the amplitude of the surface temperature to fluctuate. According to Heywood (1988) the surface temperature fluctuation is a source of thermal stress. The magnitude of the temperature fluctuation is proportional to $(\delta\rho c)^{-1}$ which varies as $(\kappa\rho c)^{-1/2}$. Figure 7.15 shows the temperature swing for the three materials. It is clear that aluminium titanate, as expected, has a larger swing than syalon and cast steel.

The instantaneous heat transfer coefficient was computed in this work, see chapter 3, according to either the empirical definition given by Hassan (1968) or the classic correlation for convection heat transfer over a flat plate. Figure 7.16 shows the variation of instantaneous heat transfer coefficient in the swirl chamber for the three materials at an engine speed of 700 rev/min. Since heat transfer coefficient depends largely on a Reynolds-Nusselt correlation, it is greatly influenced by the value of swirl in the swirl chamber. It is clear from the Figure that wall material, and hence wall temperature, does not affect the value of heat transfer coefficient.

Figure 7.17 shows the variation of heat transfer coefficient in the swirl chamber at an engine speed of 700 rev/min calculated by both the Hassan and flat plate correlations. It is seen that the flat plate correlation has a maximum value higher than the maximum value obtained by the Hassan correlation.

Figure 7.18 shows instantaneous heat flux in the swirl chamber at an engine speed of 700 rev/min computed for the three materials. Heat flux is a function of the difference between the gas temperature and surface temperature. It is seen that the heat flux is

below zero when the surface temperature is higher than the gas temperature. Insulating the swirl chamber reduces the heat flux because the surface temperature is higher than standard temperature.

7.8 Summary

This chapter has tested the sensitivity of the mathematical model to values of input parameters and coefficients, under motored conditions. The effects of the discharge coefficient, throat area ratio, friction factor and piston leakage on air swirl are presented. The model has also been used to study the effect of swirl chamber material and heat transfer coefficient on swirl, surface temperature and heat flux.

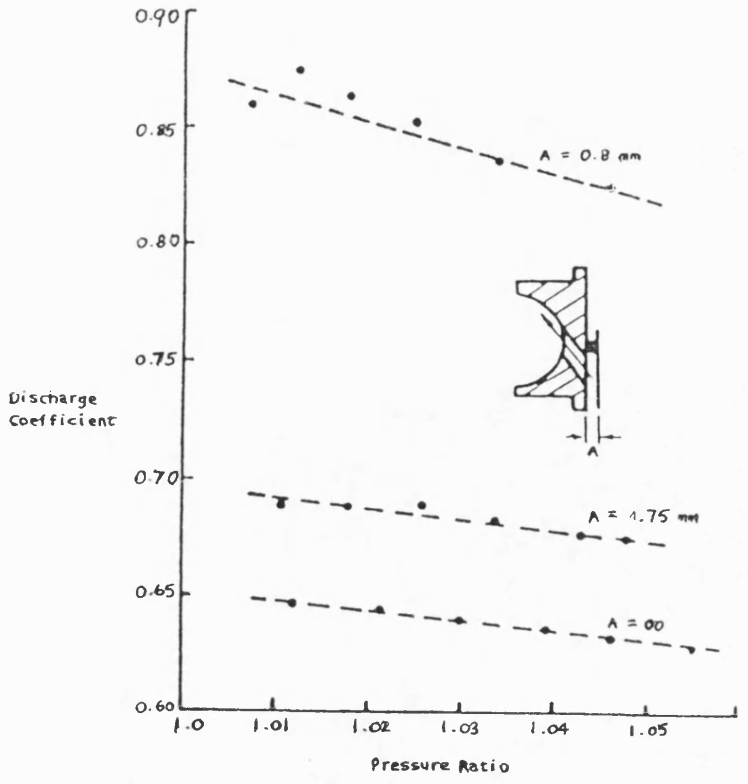

Figure 7.1 The effect of piston position on discharge coefficient, Kamel (1977)

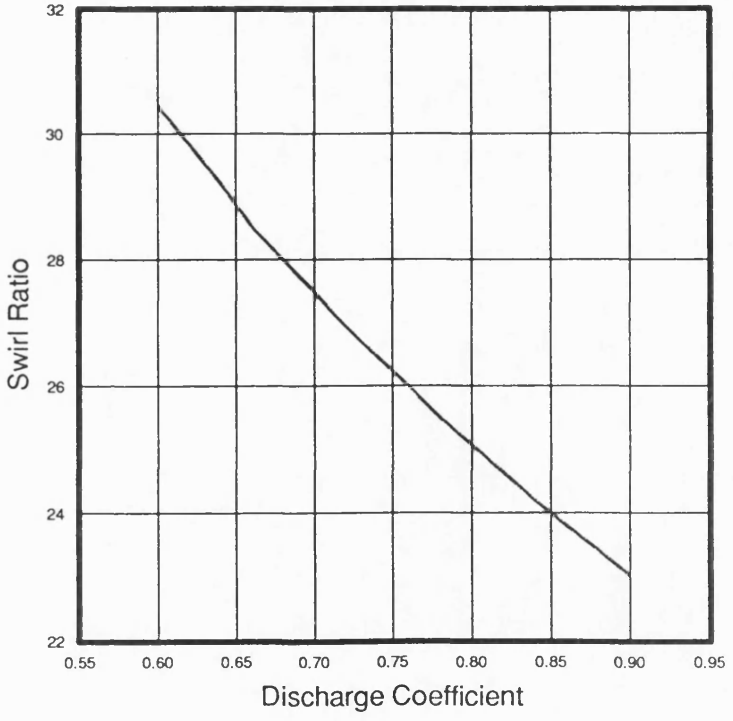

Figure 7.2 Effect of discharge coefficient on mean swirl ratio

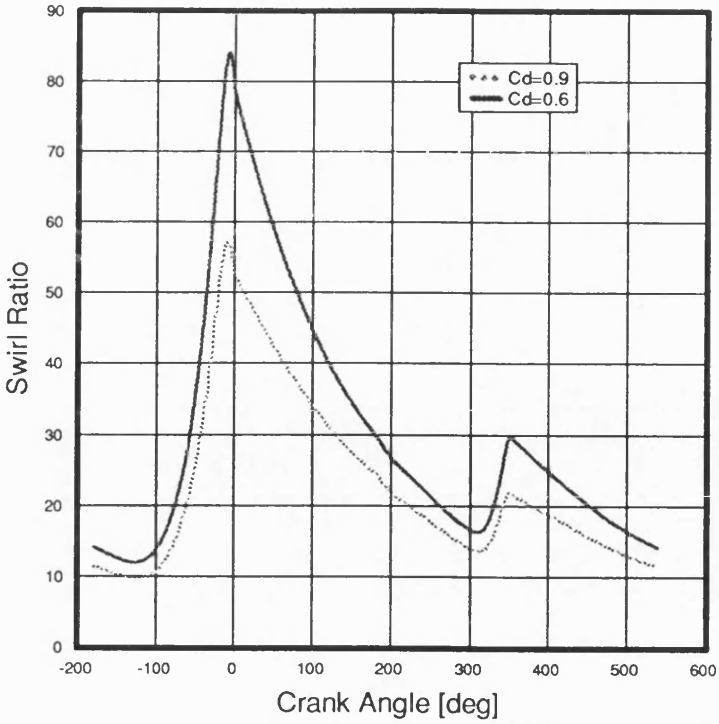

Figure 7.3 Variation of instantaneous swirl ratio with discharge coefficient

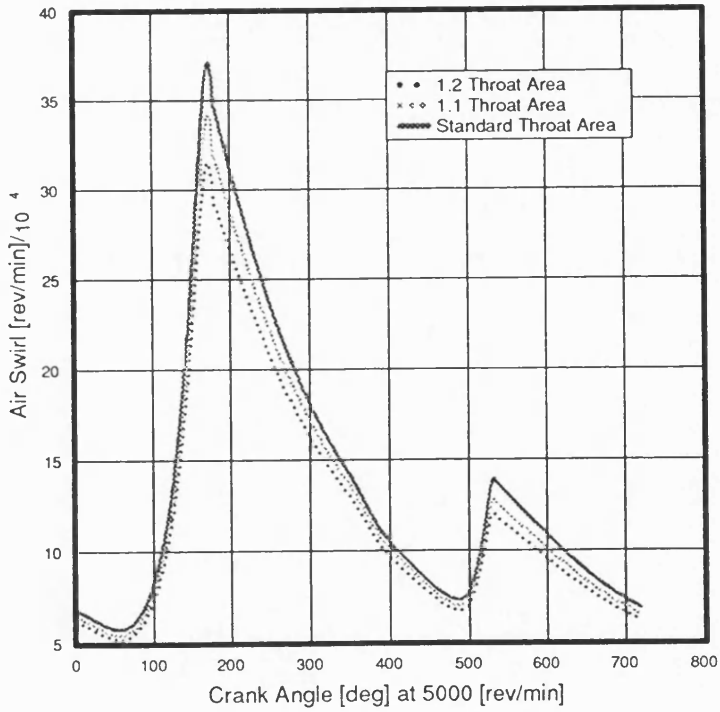

Figure 7.4 Computed variation of swirl with throat area ratio

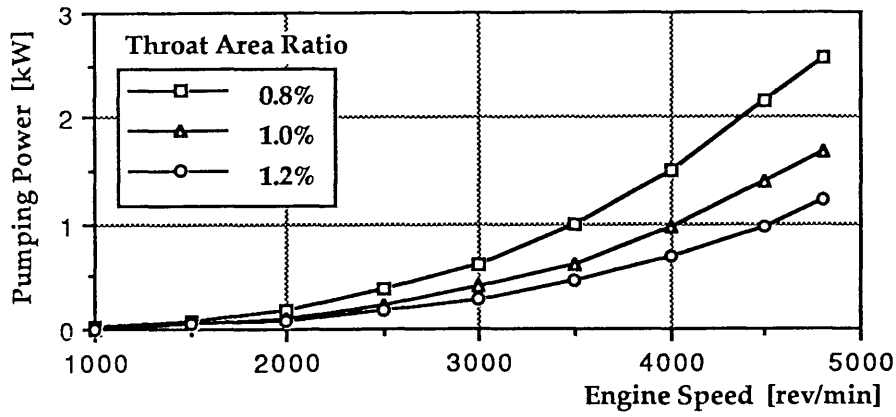

Figure 7.5 Computed pumping work versus swirl chamber throat area ratio

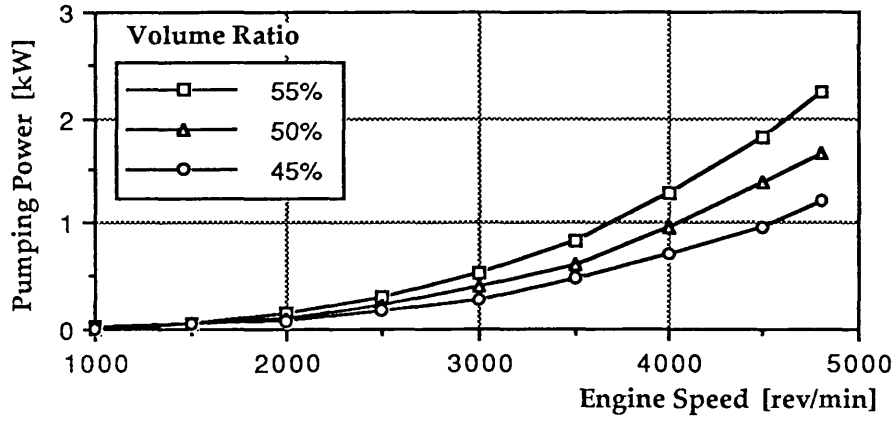

Figure 7.6 Computed pumping work versus swirl chamber volume ratio

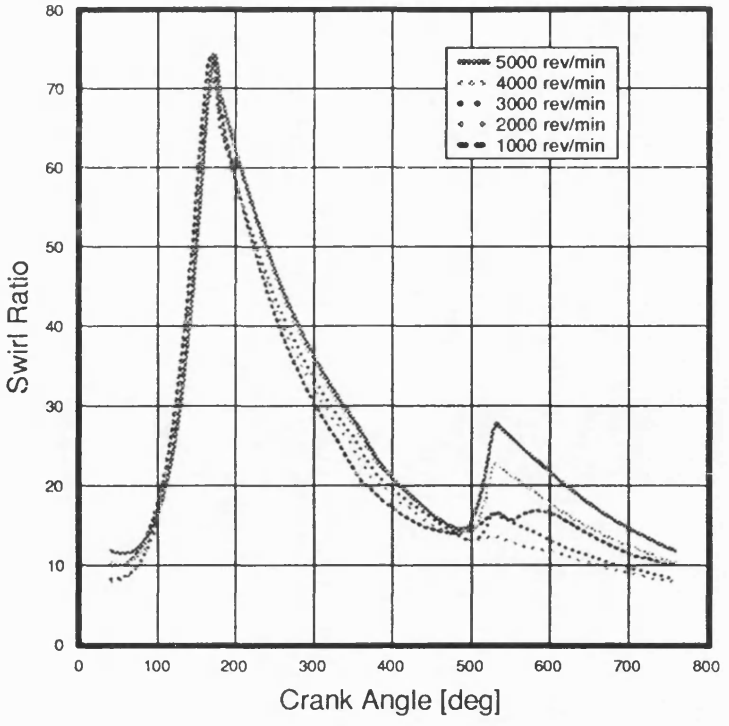

Figure 7.7 Computed variation of swirl ratio with engine speed (crank angle basis)

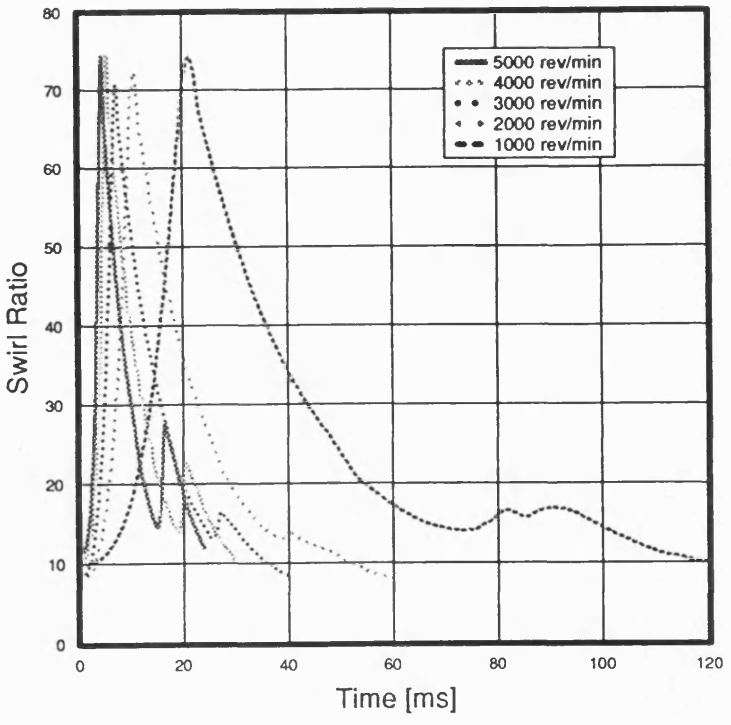

Figure 7.8 Computed variation of swirl ratio with engine speed (time basis)

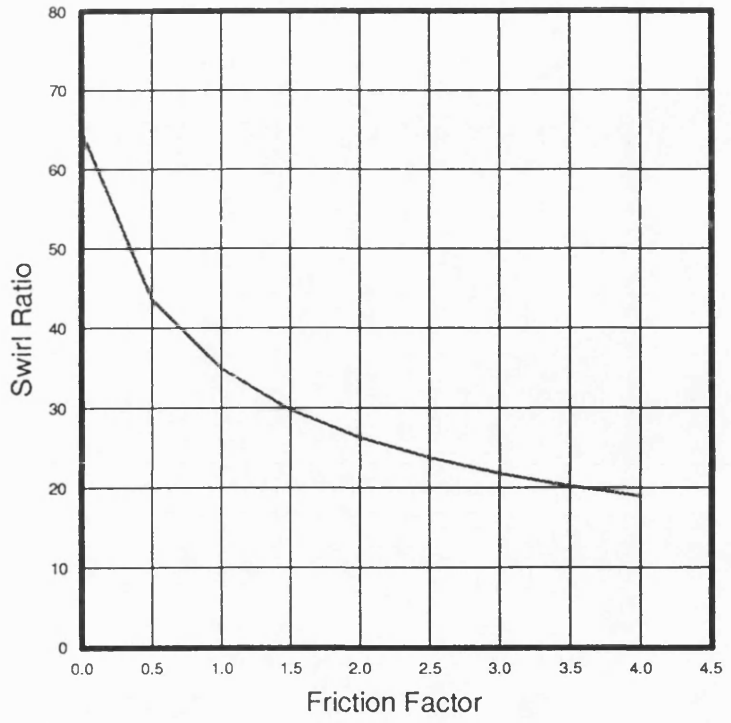

Figure 7.9 Mean swirl ratio versus friction factor

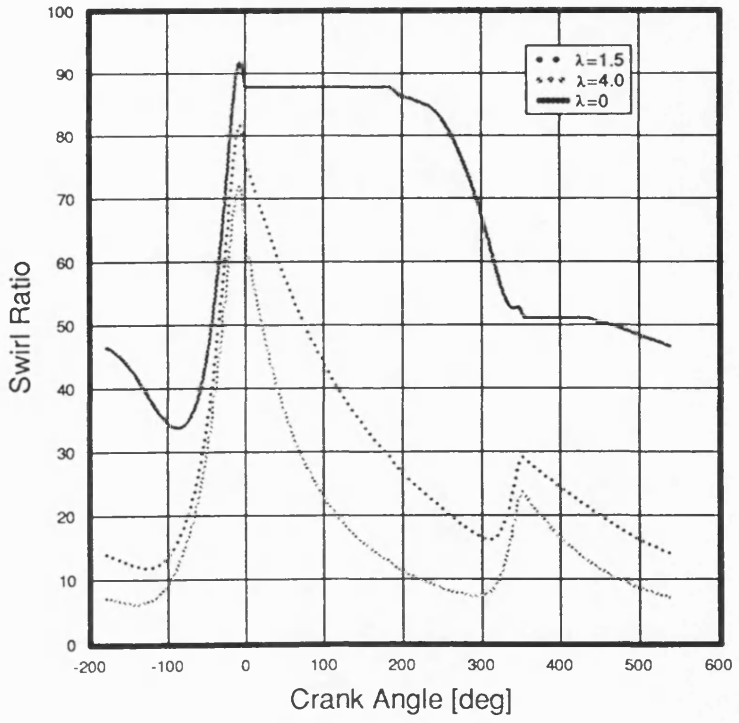

Figure 7.10 Variation of instantaneous swirl ratio with friction factor

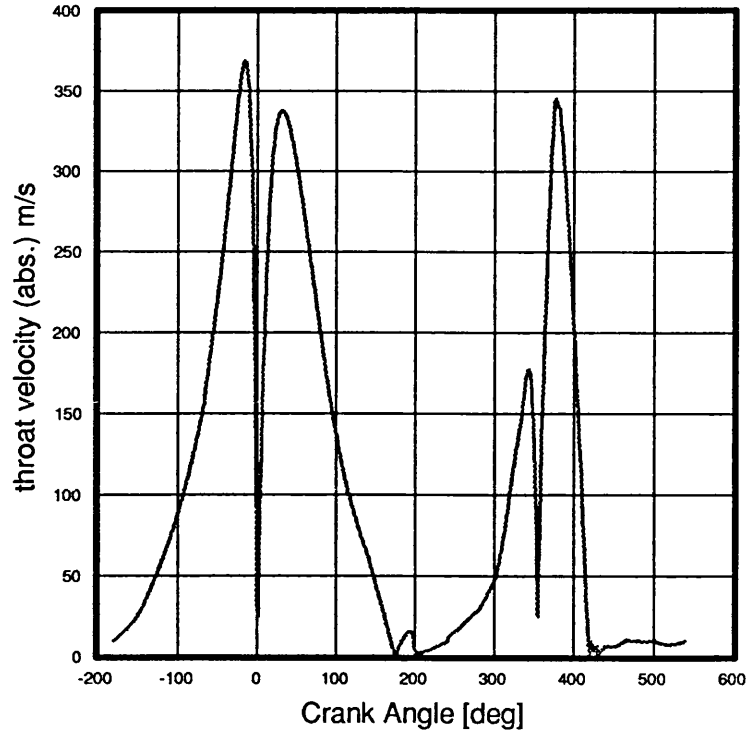

Figure 7.11 Absolute value of velocity through the throat during one cycle

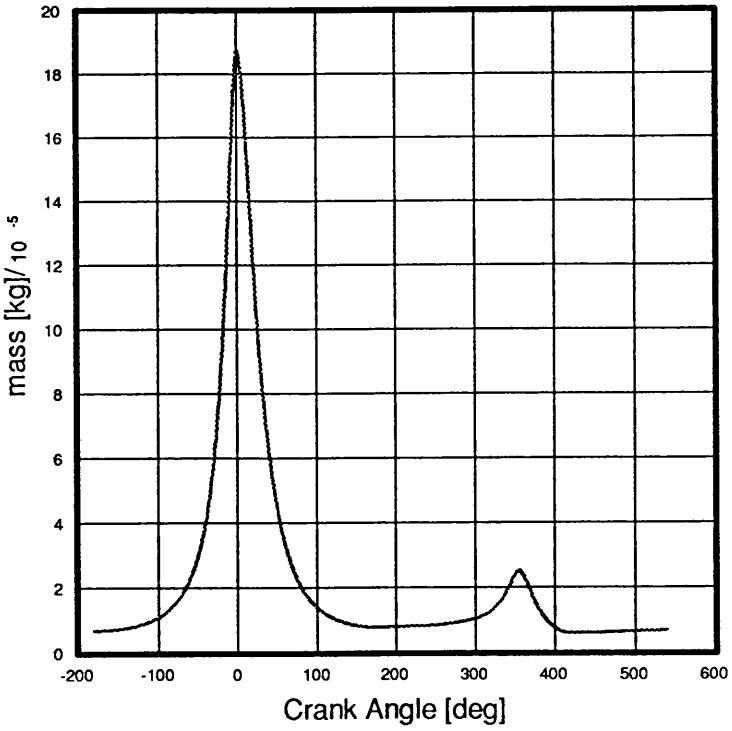

Figure 7.12 Air mass in the swirl chamber

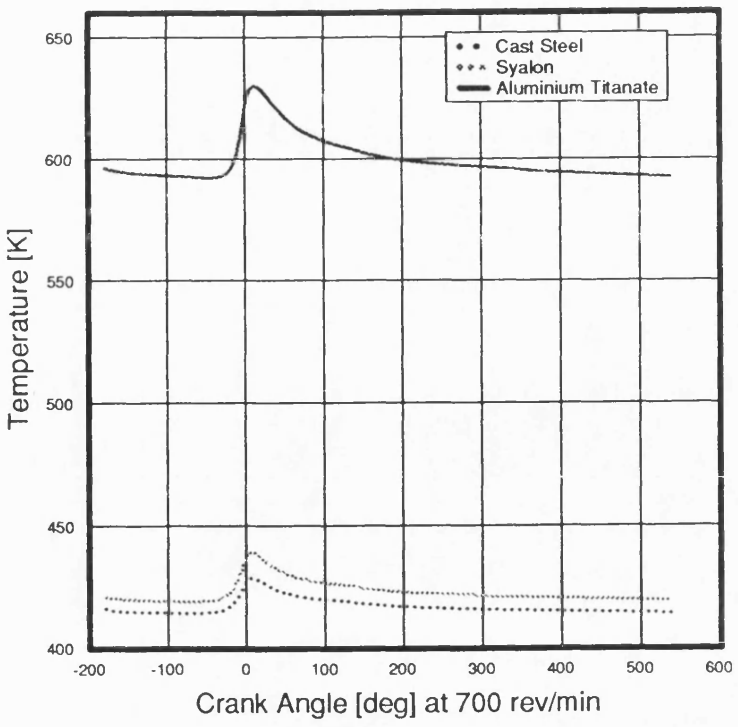

Figure 7.13 Surface temperature profile in the swirl chamber

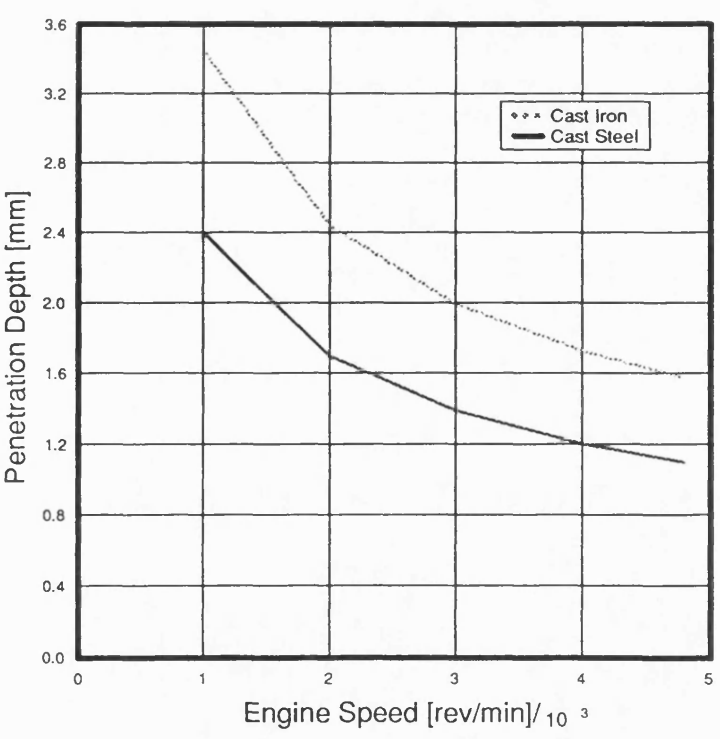

Figure 7.14 Variation of penetration depth with engine speed

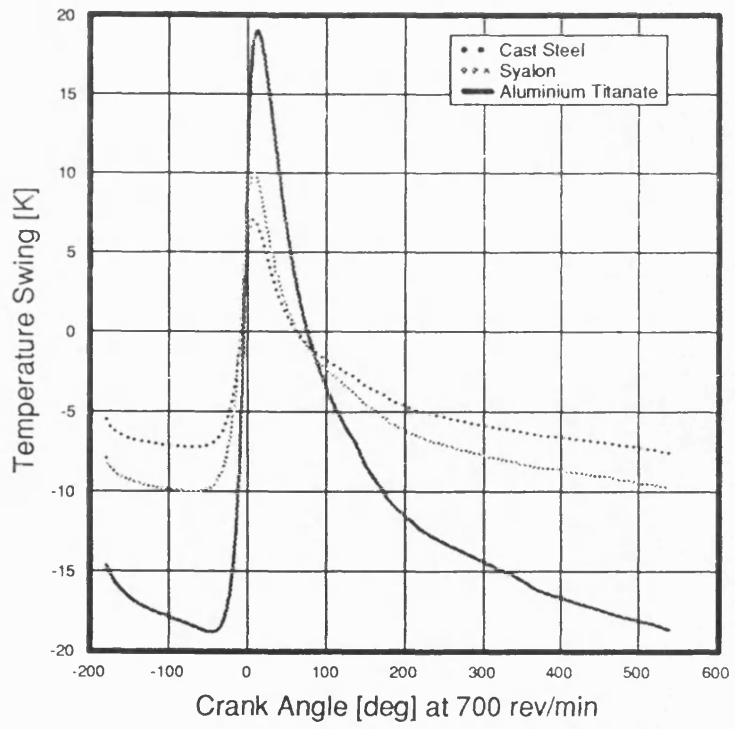

Figure 7.15 Surface temperature swing in the swirl chamber

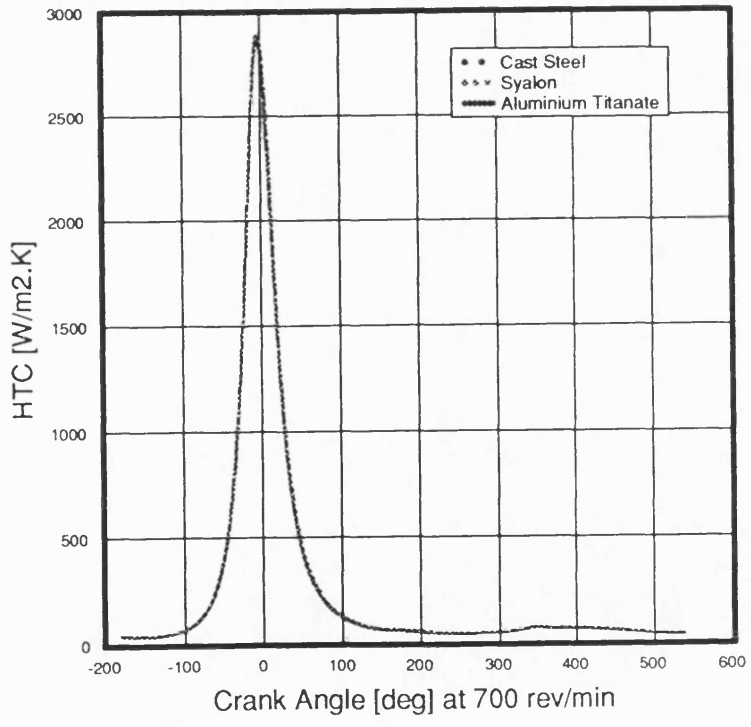

Figure 7.16 Variation of heat transfer coefficient with swirl chamber material

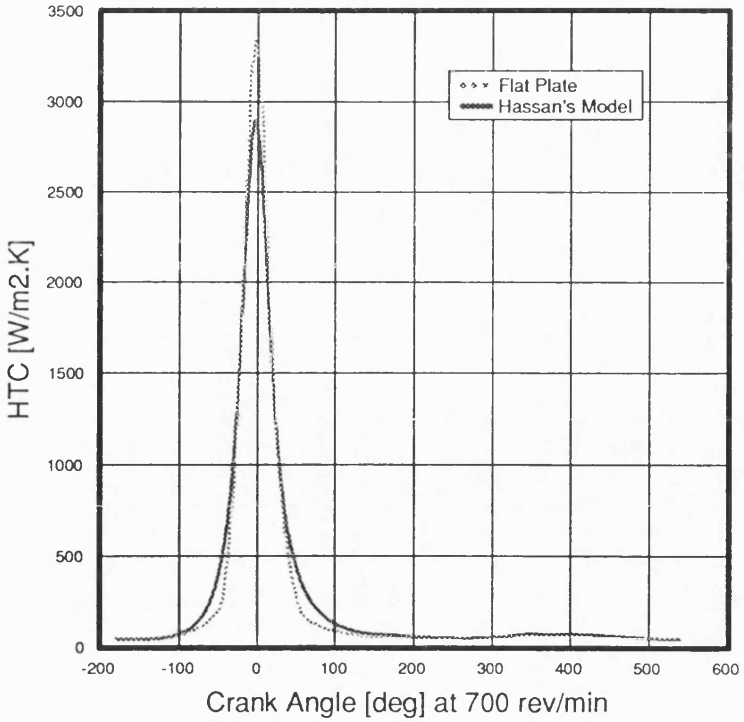

Figure 7.17 Comparison of calculated heat transfer coefficient between flat plate and Hassan (1968) correlations

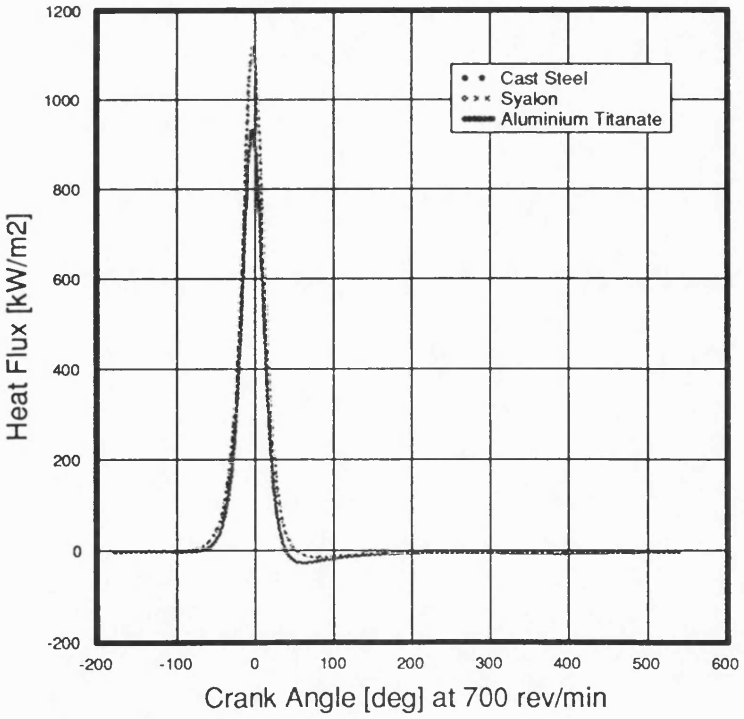

Figure 7.18 Variation of heat flux with swirl chamber material

CHAPTER 8

DISCUSSION AND CONCLUSIONS

8.1 Introduction

This chapter discusses the work, theoretical and experimental, presented in this thesis. The chapter also discusses further development of the theoretical model which is taking place by other workers. Finally the chapter ends by drawing a number of conclusions.

8.2 Discussion

A detailed investigation of air motion and heat transfer in a motored indirect injection (IDI) diesel engine has been carried out in four parts. In the first part a thermodynamic model, which simulates the air motion and heat transfer of the IDI diesel engine, has been successfully developed. In the second part an experimental rig has been constructed for the measurement of air motion and gas temperature in a motored IDI engine. In the third part a validation of the mathematical model was carried out and comparisons made with experimental data. In the fourth part the model was used to explore the effect of certain parameters such as engine geometry, speed and swirl chamber materials on pumping losses, swirl, swirl chamber gas and wall temperature and heat flux.

The mathematical model was written in FORTRAN77. This language was found to be, in comparison with a number of other languages, adequate for the purpose of the work. Using the debugging facility provided by the compiler, during program development, cut down the development time considerably. Another useful lesson which was learned from this project was to write the software in a structured way and to try to document the program in-source whenever possible. Since the program was developed and successfully run on more than one operating system, it was very helpful to write the program in standard FORTRAN77 to cope with different compilers.

When satisfied with the simulation program it was used to conduct a parametric study. This shows that using software for engine simulation is very useful in providing a great deal of information in a short time and at minimum cost. By changing only a few parameters in the data file the engineer could obtain a lot of performance data which would have taken a great deal more time and money to obtain experimentally. However, the author does not believe that engine simulation can, in his lifetime, entirely replace experimentation.

At the start of the project no previous knowledge or facilities were available in the School for hot wire anemometry to measure air velocity and temperature in engines. It was found very easy to gain experience in the manufacture, repair and use of hot wires in a short time. It was also found that it is not advisable to use proprietary probes in an engine application if the facility for repairing them in house is not available. Much time, and money, will be wasted waiting for the probes to be repaired by the manufacturer. After reasonable skill has been gained in making and using hot wires in engines the wire durability improves. Repairing a wire usually requires less than 5 minutes.

The purpose of developing the existing model, for motored engines, was to allow extension to fired engines in the future, and work on this subject is still continuing by other workers at Bath University. A heat release model has been added to the program by introducing suitable functions for fuel burning rate in the swirl chamber and the main chamber. The model has been used for design of a turbocharged two-stroke IDI diesel engine. The results obtained are encouraging.

The model is also being used to provide boundary conditions for a CFD model of the IDI diesel engine. A sample of the velocity vectors generated by the CFD model is shown in Figure 8.1. The model developed in this project was used to predict instantaneous conditions inside the cylinder and swirl chamber of a fired 4-stroke IDI engine. The results of the simulation are shown in Figures 8.2 at a speed of 4825 rev/min. The

figure shows; main chamber and swirl chamber pressures, gas temperature in each chamber, heat flux and swirl ratio in the swirl chamber under both motored and fired conditions and charge mass and rate of heat release in both chambers.

It is seen from the figure that the pressure in the main chamber is higher than that of the swirl chamber during compression and until the start of combustion. When combustion starts, immediately atdc in this case, the pressure in the swirl chamber rises rapidly to a value higher than that of the main chamber. The pressure difference between the main chamber and the swirl chamber reaches a maximum value of 5 bar at 7 degCA atdc. At 15 degCA atdc the pressure difference falls to 1 bar with the swirl chamber pressure staying higher than that of the main chamber until the end of the expansion stroke.

The swirl chamber temperature remains above 700 K throughout the cycle. The maximum temperature in the swirl chamber leads the main chamber temperature by 28 K and is about 660 K higher. This figure is very useful as it provides significant information which will reduce the running time of a CFD model.

The heat flux figure shows that the heat flux under motored conditions is higher than that under fired conditions from 70 degCA btdc until tdc. This is because the swirl chamber wall temperature is much closer to the gas temperature under fired conditions than under motored conditions. After combustion starts the maximum heat flux is more than double that under motored conditions. The heat is transferred from the hot combustion gases to the swirl chamber walls until 35 degCA abdc whereas under motored conditions the swirl chamber wall temperature becomes hotter than the gas temperature at 50 degCA atdc.

Swirl ratio is seen to be similar under both motored and fired conditions for most of the compression stroke. The fuel jet energy is not added to the swirl chamber kinetic energy, see section 3.4.3, in this case. The rate of decay of swirl ratio is higher under fired

conditions as combustion gases are discharged quicker and viscous friction action to decelerate the motion of the smaller mass becomes greater. By the end of the expansion stroke and during the induction stroke swirl ratio is higher under motored conditions as the low pressures in the swirl chamber cause gas to flow through the throat which raises swirl levels.

Mass flow between the swirl chamber and the main chamber is seen to be a mirror image. The mass flow between both chambers is dictated by the pressure difference. Mass flow from the main chamber to the swirl chamber is seen to continue until immediately atdc before it starts to flow in the reverse direction. This indicates that reverse flow exists atdc.

The imposed rate of heat release curve for the swirl chamber starts to rise at tdc when combustion starts. It is seen to rise sharply to its maximum value, higher than the main chamber peak, before it decays rapidly lasting for 34 degCA. The heat release curve for the main chamber starts 5 degCA later and it continues longer than the swirl chamber curve lasting for 115 degCA. The rate of heat release curves exhibit reasonable trends although fuel burning in this case seems to last for a long time in the main chamber. As mentioned earlier the heat release is handled by introducing suitable fuel burning rate functions for the swirl chamber and the main chamber based on empirical results.

8.3 Conclusions

The major conclusions that can be drawn from this investigation are :

(i) An experimental rig has been constructed for the measurement of air motion and gas temperature in a motored indirect-injection (IDI) diesel engine. Swirl, in the swirl chamber of the motored engine, has been measured, using paddle wheel and hot wire anemometers. Instantaneous gas temperature has been measured using a fast response resistance thermometer.

(ii) A computer model of a motored IDI diesel engine has been written and used to study a number of parameters. For example the effects of throat area and volume ratio on swirl chamber pumping power, swirl and the effects of swirl chamber materials on heat transfer.

(iii) Good agreement between the predicted values and experimentally measured swirl chamber pressure and gas temperature was obtained, with the exception of the swirl ratio which is overpredicted because no account is taken of the drag caused by the presence of the glow plug.

(iv) The pumping power associated with filling the swirl chamber increases cubically with speed and may reach 1-3kW (5%) for a 4 cylinder engine at 4800rev/min.

(v) The maximum swirl ratio of the standard swirl chamber has a value between 70 and 80:1 and does not vary significantly with engine speed.

(vi) Insulating the swirl chamber would help both cold starting and ignition. Swirl ratio in the swirl chamber is not affected by swirl chamber insulation and depends solely on swirl chamber geometry.

(vii) The mathematical model is being used to assist the design of a two-stroke IDI engine and to provide data for a CFD model of a fired IDI engine. The preliminary results obtained from both applications have been encouraging.

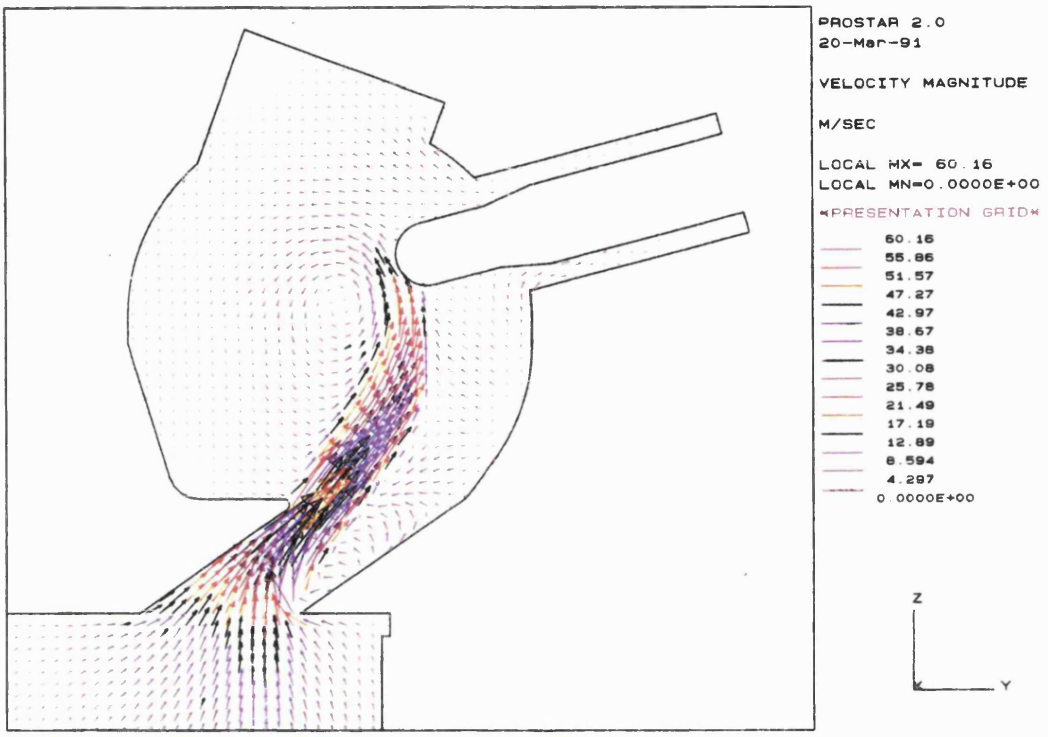

Figure 8.1 Velocity vectors predicted by the CFD model

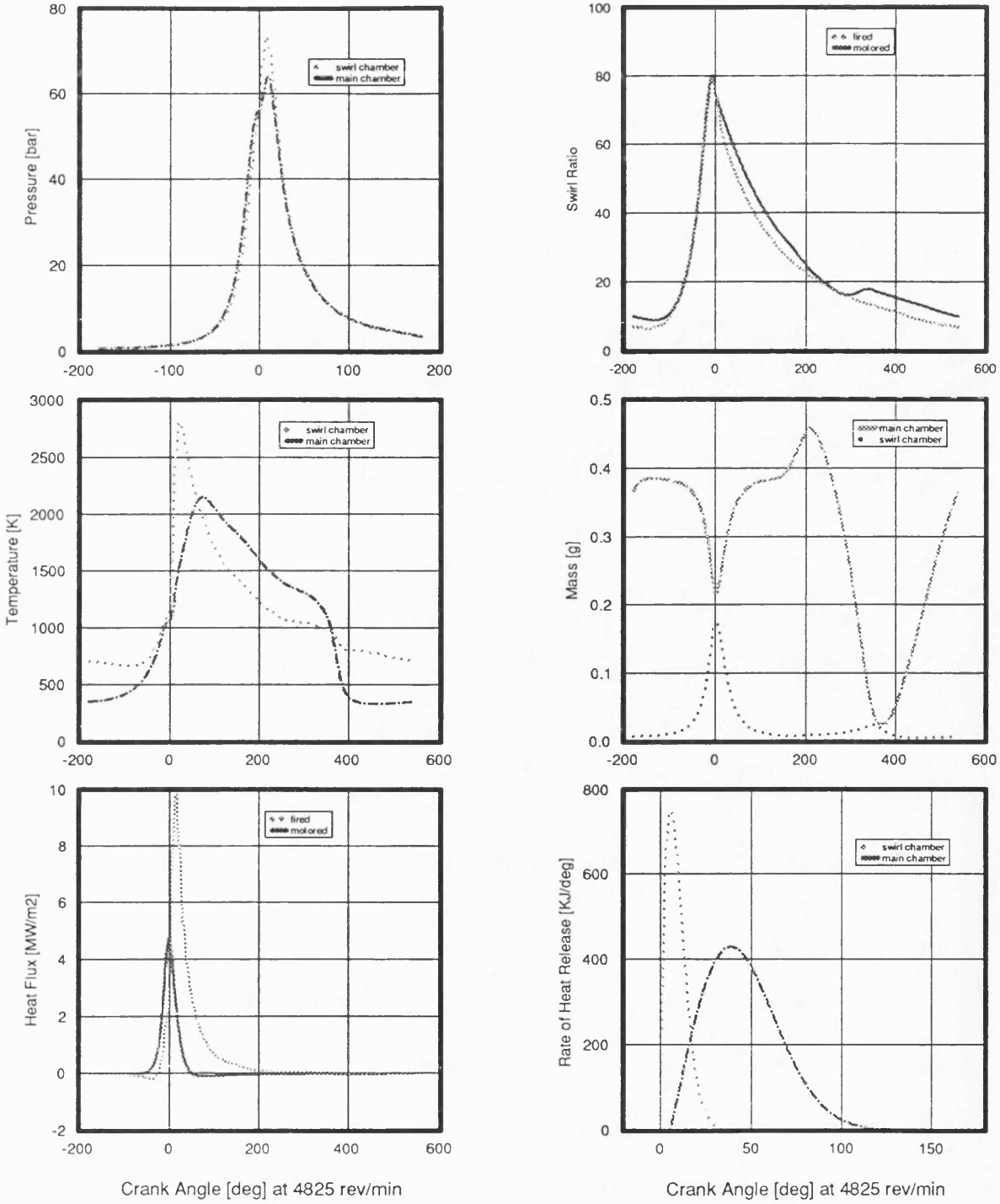

Figure 8.2 Full cycle predictions for an IDI diesel engine

REFERENCES

Abou-Ellail , *M.M.M.* and Elkotb, M.M. (1981). Prediction and measurement of flow and heat transfer in motored diesel engine swirl chambers. Proc. 3rd Symposium on Turbulent Shear Flows, Springer, Berlin.

Abou-Romia, *M.* and Tien, C. (1967). Appropriate mean absorption coefficients for infrared radiation of gases. Trans. ASME, Vol. 89, series C, No. 4.

Ajakaiye, B *A.* (1976). Air Motion in an indirect injection diesel engines. Ph.D. Thesis, University of Technology, Loughborough.

Ajakaiye, B *A.* and Dent, J.C. (1981). A Correlation of air motion in cylindrical prechambers of diesel engines. ASME, Journal of Engineering for Power, 103, 499-504.

Alcock, J.F. (1934). Air swirl in oil engines. Proc. Of the IMechE, Vol. 128, pp. 123-193.

Alcock, J.F. and Scott, W.M. (1963). Some more light on diesel combustion. Proc. IMechE, Auto. Div., 1962-63, 5, 179-191.

Arcoumanis, *C.* (1988). Internal Combustion Engines. Academic Press Ltd., London.

Bowden, C.M. , Samaga, B.S. and Lyn, W.T. (1970). Rate of heat release in high speed indirect injection diesel engines. Proc. IMechE, 184, Pt. 3J, paper 12.

Bastress, E.K. Chng, K.M. and Dix, D.M. (1971). Models of combustion and nitrogen oxide formation in direct and indirect injection compression ignition engines". SAE, paper 719053.

Champagne, *F.H.*, Sleicher, C.A. and Wehrmann O.H. (1967). Turbulence measurements with inclined hot-wires. Part 1: Heat Transfer Experiments with Inclined Hot-Wire. J. Fluid Mech., 28, 153-176.

Charlton, S *J.* (1986). SPICE, user manual. University of Bath, School of Mechanical Engineering.

Collis, D.C . and Williams, M.J. (1959). Two-dimensional convection from heated wires at low Reynolds numbers. J. Fluid Mech., 6, 357-384.

Corrsin, S. (1943). Investigation of flow in an axially symmetrical heated jet of air. Wartime Rept. W94, NACA.

Crank, J. and Nicolson, P. (1947). A practical method for numerical evaluation of solutions of partial differential equations of the heat conduction type. Proc. Camb. Phil. Soc., 43, 50-67, (17).

Croft, D. and Lilly, D. (1977). Heat transfer calculations using finite difference equations. Applied Science publishers Ltd, London.

Davies, P.O .A.L and Fisher, M.J. (1964). Heat transfer from electrically heated cylinders. Proc. Roy. Soc. A, 280, 486-527

Davis, M.R. (1970). The Dynamic response of constant resistance anemometers. Journal of Physics E: Si, 3.

Dent, J.C. and Salama, N. (1975). Turbulence structure in the spark ignition engine. IMechE, Conference on Combustion in Engines, paper No. C83/75. Cranfield.

DISA, (1982). Probe Catalog, Publ. No. 2201 E.

Durst, F. and Zare', M. (1974). Removal of pedestals and directional ambiguity of optical anemometer signals. Journal of Applied optics, 13, 2562-2579; through Witze (1980).

Eichelberg, G. (1939). Some new investigations on old combustion engine problems. Engineering, London, 148, 463-547.

El-Khafaji, *A.H.A.*, Tindal, M.J. and Williams, T.J. (1972). Engine cylinder gas flow measurements by hot-wire anemometers. Symposium on 'Flow - its measurements and control in science and industry', Pittsburgh.

Furubayashi, *M.*, Sato, Y. and Ishida, S. (1986). Combustion Control of a swirl-chamber type diesel engine by early ignition of residual fuel from the previous cycle. SAE, No. 861183.

French, G. and Scott, W. (1985). Giving the IDI a Fresh start. SAE, No. 850452.

Greeves, G. and Wang, C. (1981). Origins of diesel particulate mass emission. SAE, No. 810260.

Greeves, G., Wang, C., Partridge, I. and Black, J. (1988). Improvements to indirect injection diesel combustion. IMechE, No. C41/88.

Gosman, A.D., Johns, R., Tipler, W. and Watkins, A. (1979). Computer simulation of in-cylinder flow, heat transfer and combustion: a progress report. 13th International Congress on Combustion Engines.

Gosman, A.D. (1986). Flow processes in cylinders. The thermodynamics and gas dynamics of internal combustion engine volume II. Edited by J.H. Horlock and D.E. Winterbone. Clarendon Press. Oxford.

Gosman, A.D. (1989). Lecture notes for course on experimental and computational techniques for internal combustion engines. Imperial College, England.

Haddad, S.D. and Watson, N. (1984). Design and applications in diesel engineering. Ellis Horwood Ltd., England.

Hassan, H. (1969). Unsteady heat transfer in a motored internal combustion engine. Ph.D. Thesis, University of Technology, Loughbrough. University, 1969.

Hassan, H. (1971). Unsteady heat transfer in a motored internal combustion engine cylinder. Proc. IMechE, Vol. 185 80/71.

Hassan, H. and Dent, J.C. (1971). The Measurement of air velocity in a motored internal combustion engine using a hot-wire anemometer. IMechE, 185 50/71.

Heywood, J.B. (1988). Internal combustion engine fundamentals. MacGraw-Hill Book Company. New York.

Hinze, J.O. (1959). Turbulence. McGraw-HILL Book Company. New York

Hiroyasu, H. and Matsunari, F. (1968). Development and evaluation of the simulation of the fuel injection system. Trans. JSME, Vol. 34 No. 260.

Hiroyasu, H. and Kadota, T. (1979). Models for combustion and formation of nitric oxide and soot in direct injection diesel engines. SAE, paper 760129.

Hiroyasu, H., Yoshimatsu, A. and Arai, M. (1982). Mathematical model for predicting the rate of heat release and exhaust emissions in IDI diesel engines. IMechE, C102/82.

Hiroyasu, H., Nishida, K., Matsouka, T. and Yamauchi, H. (1986). characterization of combustion processes in the prechamber and main chamber of an indirect injection diesel engine by high-speed photography. SAE, No. 861181.

Holman, J.P. (1981). Heat Transfer. MacGraw-Hill, Inc., Fifth Edition. Printed in the United States of America.

Horlock, J. H. and Winterbone, D. E. (1986). The Thermodynamics and Gas Dynamics of Internal Combustion Engines. VolumeII, Clarendon Press, Oxford.

Hunsaker, J.C. and Rightmire, B.G., (1947). Engineering application of fluid mechanics. MacGraw-Hill, Inc., New York and London.

Ikegami, M., Komatsu, G. and Nishiwaki, K. (1986). Numerical Simulation of flow in an engine cylinder, 1st Report, formulation and algorithm. Bulletin of JSME, Vol. 29, No. 248.

Kamel, M. (1977). Thermodynamic analysis of indirect injection diesel engine operation. Ph.D. Thesis, Imperial College, University of London.

Kamel, M. and Watson, N. (1979). Heat transfer in the indirect injection diesel engine. SAE, paper 790826.

Knight, B.E. (1965). The problem of predicting heat transfer in diesel engines. Proc. IMechE, Vol. 179, Pt. 3C.

Kort, R.T., Mansouri, S.H., Heywood, J.B. and Ekchian, A. (1982). Divided-chamber diesel engine, Part II: Experimental validation of a predictive cycle-simulation and heat release analysis. SAE, paper 820274.

Kunitomo, T. and Kodama, K. (1974). Radiation from luminous flame at high pressures. Bulletin of the JSME, Vol. 17, No. 113.

Kunitomo, T., Matsuoka, K. and Oguri, T., (1975). Prediction of radiative heat flux in a diesel engine. SAE Paper 750786.

Kyriakides, S.C. (1984). Cylinder air motion in direct injection diesel engines. Ph.D. thesis, King's College, University of London.

Lancaster, D., (1976). Effects of engine variables on turbulence in a spark-ignition engine. SAE, paper 760159

Lakshminaray an, P. and Dent, J. C. (1983). Interferometric Studies of Vapourising and Combusting Sprays. S.A.E, No. 830244.

Lefferts (1978). Linear brief 39. National Semiconductors, Linear Application Handbook.

Lilley, L. C.R. (1984). Diesel engine reference book". Butterworth, London.

Lomas, C.G. (1986). Fundamentals of hot wire anemometry. New York : Cambridge University Press.

Lyn, W.T. and Valdmanis, E. (1962). The Application of high speed schlieren photography to diesel combustion research. J. of Photographic Science, 10, 74.

Lyn, W.T. and Valdmanis, E. (1967). The effects of physical factors on ignition delay. IMechE , Vol. 181, Pt 2A, No. 1.

Mansouri, S.H. (1981). Divided-chamber automotive diesel engine: Development and validation of a performance and emission model. Ph.D. Thesis, Department of Mechanical Engineering, Massachusetts Institute of Technology.

Mansouri, S.H. ,Heywood, J.B. and Radhakrishnan, K. (1982). Divided-chamber diesel engine, Part I: A cycle-simulation which predicts performance and emissions. SAE, paper 820273, 1982.

Meintjes, K. and Alkidas, A.C. (1982). An experimental and computational investigation of the flow in diesel prechambers. SAE, paper 820275, SAE Trans., vol. 91.

Monaghan, M .L. (1981). The high speed direct injection diesel for passenger cars. SAE, No. 810477.

Monaghan, M .L. (1982). The best high speed direct injection diesel system for light duty application. IMechE C105/82.

Nagao, F., Ikegami, M. and Shinzato, T. (1967). Air motion and combustion in a swirl chamber type diesel engine. Bulletin of JSME, Vol. 10, No. 41, 1967.

Nakajima, K., Kajiya, S. and Nagao, F. (1969). An experimental investigation of the air swirl motion and combustion in the swirl chamber of diesel engines. Bulletin of the JSAE, 195-209.

Oguri, T. and Inaba S., (1972). Radiant heat transfer in diesel engines. SAE No. 720023.

Oguri, T. and Kunitomo, T. (1975). Prediction of radiative heat flux in a diesel engine. SAE, No. 750786.

Özisik, M.N., (1985). Heat Transfer A Basic Approach. MacGraw-Hill, Inc. Printed in the United States of America.

Packer, J.P. (1983). Diesel type combustion studies in high swirl chambers. Ph.D. thesis, School of Engineering, University of Bath.

Pinchon, P. (1989). Three dimensional modelling of combustion in a prechamber diesel engine. SAE Paper 890666.

Rask, R.B. (1979). Laser-doppler anemometer measurements in an internal combustion engine. SAE Paper No. 790094.

Rask, R.B. (1981). Comparison of window, smoothed-ensemble, and cycle-by-cycle data reduction techniques for laser doppler anemometer measurements of in-cylinder velocity. Proc. Of the ASME Symposium on Fluid Mechanics on Combustion Systems.

Rogers, G.F.C and Mahew, Y.R., (1980). Thermodynamic and transport properties of fluids. Basil Blackwell.

Scadion, M.D. and Warshawsky, I, (1952). Experimental determination of time constants and Nusselt numbers for bare wire thermocouples in high velocity air streams and analytic approximation of conduction and radiation errors. N.A.C.A. Tech. Note 2599.

Scott, N.M. (1973). Noise of small indirect injection diesel engine. International Automotive Engineering Congress, Detroit, Michigan, paper 730242.

Scott, N.M. (1984). Design and applications in diesel engineering. Edited by Haddad and Watson. Ellis Horwood Ltd., England.

Schmidt, E. M. and Cresci, R.J. (1971). Hot wire anemometer in low-density flows. AIAA J., 9, 2019-2027.

Shephard, W., Charlton, S.J., Cook, G. and Watts, M. (1990). The effect on performance of thermal insulation of the IDI diesel engine. Proc. CARE Consortium Conference, Jaguar Cars Limited, Coventry.

Sitkei, G. (1972). A rational approach for calculation of heat transfer in diesel engines. SAE Paper 720027.

Sitkei, G. (1974). Heat transfer and thermal loading in internal combustion engines. Akademiai Kaido, Budabest.

Smith, G.D. (1965). Numerical solution of partial differential equations. Oxford University Press. London.

Stone, R. (1989). Motor vehicle fuel economy. Macmillan Education Ltd., London.

Syed, S.A. and Bracco, F.V. (1979). Further comparisons of computed and measured divided chamber engine combustion. SAE, paper 790247.

Tabaczynski, R.J. (1988). Internal Combustion Engines. Edited by Arcoumanis, C. Academic Press Ltd., London.

Tamura, H., Hashimoto, M., Maekawa, M. and Imoto, K. (1989). New systems of IDI diesel engine for passenger car application. SAE, No. 890262.

Tanaka, T., Sugihara, K. and Ueda, T. (1986). Improvement of IDI diesel engine combustion through dual-throat jet swirl chamber. SAE, No. 861184.

Tarabad, M., (1983). Diesel engine cycle simulation. Internal report; School of Mechanical Engineering, University of Bath.

Tawfig, M.E., Charlton, S.J. and Prest, P.H., (1991). An investigation of air motion and gas temperature in a motored IDI diesel engine. IMechE C433/002, London.

Taylor, G.I. (1935). Statistical theory of turbulence. Proc. Roy. Soc. of London, A 151, pp. 421.

Taylor, G.I. (1938). The spectrum of turbulence. Proc. Roy. Soc. of London, A 164, pp. 476-490.

Tindal, M., Brown, O.G. and Kyriakides, S.C. (1982). An Investigation of swirl and turbulence in the cylinders of direct injection diesel engines. IMechE, C127/82.

Tropea, C. (1988). Perspective on temperature effects in thermal anemometry. Lecture 4,UMST Manchester.

Wade, W.R. (1980). Light duty NO_x-HC-Particulate trade-off studies. Diesel combustion and emissions, Proceedings P.86, Congress and Exposition Cobo Hall, Detroit.

Watson, N. and Kamel, M. (1979). Thermodynamic efficiency evaluation of an indirect injection diesel engine. SAE, No. 790039.

Watson, N. and Janota, M.S. (1982). Turbocharging the Internal Combustion Engine. Macmillan Education Ltd., London.

Watson, N. (1982). Comparative thermodynamic efficiency of direct and indirect injection diesel engines. Entropie, No. 105.

Williams,T.J. and Tindal, M.J. (1980). Gas flow studies in direct injection diesel engines with re-entrant combustion chambers". SAE, paper 800027.

Witze, P.O. May (1977a). Hot-wire measurements of the turbulence structure in a motored spark-ignition engine. SAND77-8233, Sandia Laboratories, Livermore, CA.

Witze, P.O. (1977b). Measurements of the spatial distribution and engine speed dependence of turbulent air motion in an I.C. Engine. SAE Paper No. 770220.

Witze, P.O. (1980). A critical comparison of hot-wire anemometry and laser-doppler velocimetry for I.C. Engine application. SAE Paper No. 800132.

Wood, N. (1981). Aerodynamic Motion. Ph.D. thesis, School of Engineering, University of Bath.

Yamaguchi, J. (1986). Diesel with all-ceramic swirl chamber meets American particulate limit. Automotive Engineering.

Zellat, M., Rolland, Th. and Poplow, F. (1990). Three dimensional modeling of combustion and soot formation in an indirect injection diesel engine. SAE, No. 900254.

Zimmerman, D.R., (1983). Laser anemometer measurements of the air motion in the prechamber of an automotive diesel engine. SAE, No. 830452.

APPENDIX A

COMPUTER PROGRAM SUBROUTINES

```
C       ---------------------
C       subroutine PCTW01.FOR
C       ---------------------
C       This routine determines the wall temperature as a function of time
C       for a one-dimension heat transfer through a solid wall which
C       transfers heat from one side to the other.
C       The routine uses an explicit method which requires the bulk gas
C       temperature and htc from the previous iteration in order to compute
C       the current temperature distribution.
C            <IZONE> = 1   HOT PLUG
C            <IZONE> = 2   UPPER HALF
C            <IZONE> = 3   THROAT
        SUBROUTINE PCTW01 (KVOL,IZONE,HTC,TMP,TWALL)
C------ PARAMETERS
        INCLUDE 'GLOBALS.INC'
C------ VARIABLE TYPING
        REAL HTPREV(3),TMPREV(3)
C------ TIME STEP FOR FINITE DIFFERENCE
        DELT = TSTEP
C------ IF FIRST ITERATION USE CURRENT VALUES IN PLACE OF PREVIOUS VALUES
        IF(TMPREV(IZONE).EQ.0.0) TMPREV(IZONE) = TMP
        IF(HTPREV(IZONE).EQ.0.0) HTPREV(IZONE) = HTC
C------ WALL PROPERTIES
        DELX   = RES(3,IZONE,VOLS(14,KVOL))/(NGRID-1)
        CP     = RES(6,IZONE,VOLS(14,KVOL))
        DENSIT = RES(5,IZONE,VOLS(14,KVOL))
        THCOND = RES(4,IZONE,VOLS(14,KVOL))
        ALPHA  = THCOND/(DENSIT * CP)
        FO     = (ALPHA*DELT)/(DELX*DELX)
C------ BIOT NUMBER FOR GAS AND COOLANT
        BIOTG  = (HTPREV(IZONE)*DELX)/THCOND
        BIOTC  = (RES(1,IZONE,VOLS(14,KVOL))*DELX)/THCOND

        TEXP(1,IZONE,KVOL) = 2.0 * FO *
     1     (TSLAB(2,IZONE,KVOL) + BIOTG*TMPREV(IZONE)
     1   + (1.0/(2.0*FO) - BIOTG-1.0)*TSLAB(1,IZONE,KVOL))
        DO 101 I=2,NGRID-1
           TEXP(I,IZONE,KVOL) = FO * (TSLAB(I-1,IZONE,KVOL)
     1       + TSLAB(I+1,IZONE,KVOL)
     1       + (1.0/FO-2.0)*TSLAB(I,IZONE,KVOL))
101      CONTINUE
        TEXP(NGRID,IZONE,KVOL) = 2.0 * FO * (TSLAB(NGRID-1,IZONE,KVOL)
     1                  + BIOTC * RES(2,IZONE,VOLS(14,KVOL))
     1                  + (1.0/(2.0*FO)-BIOTC-1.0)
     1                  * TSLAB(NGRID,IZONE,KVOL))

        DO 3000 IN=1,NGRID
        TSLAB(IN,IZONE,KVOL) = TEXP(IN,IZONE,KVOL)
 3000   CONTINUE
C------ WALL TEMPERATURE
        TWALL = TSLAB(1,IZONE,KVOL)
C------ SAVE HTC AND TMP FOR NEXT ITERATION
        TMPREV(IZONE) = TMP
        HTPREV(IZONE) = HTC

        RETURN
        END



C       TSLAB.......TEMPERATUTE OF THE WALL GRID              [K]
C       TWALL.......TEMPERATURE OF THE WALL AT THE GAS SIDE   [K]
C       TMP.........GAS TEMPERATURE                           [K]
C       HTC.........COEFFICIENT OF HEAT TRANSFER OF THE GAS   [W/m*2 K]
C       CP..........SPECIFIC HEAT CAPACITY OF THE METAL       [J/kgK]
C       DENSIT......DENSITY OF THE METAL                      [Kg/m*3]
C       THCOND......THERMAL CONDUCTIVITY OF THE METAL         [W/mK]
C       DELX........LENGTH OF SPACE BETWEEN GRIDS             [m]
C       ALPHA.......THERMAL DIFFUSIVITY                       [m2/s]
C       FO..........FOURIER NUMBER
C       KVOL........VOLUME NUMBER
```

```
C       ---------------------
C       subroutine PCTW02.FOR
C       ---------------------
C       This routine determines the wall temperature as a function of time
C       for a one-dimension heat transfer through a solid wall which transfers
C       heat from one side to the other.
C       The routine uses an Crank-Nicolson method which requires the bulk gas
C       temperature and htc from the previous iteration in order to compute
C       the current temperature distribution.
C            <IZONE> = 1   HOT PLUG
C            <IZONE> = 2   UPPER HALF
C            <IZONE> = 3   THROAT

         SUBROUTINE PCTW02 (KVOL,IZONE,HTC,TMP,TWALL)

C------ PARAMETERS
         INCLUDE 'GLOBALS.INC'

         DIMENSION BETA(200,NVOLS),GAMMA(200,NVOLS),A(200,NVOLS),
     1            B(200,NVOLS),C(200,NVOLS),D(200,NVOLS)

C------ VARIABLE TYPING
         REAL HTPREV(3),TMPREV(3)

C------ TIME STEP FOR FINITE DIFFERENCE
         DELT = TSTEP

C------ IF FIRST ITERATION USE CURRENT VALUES IN PLACE OF PREVIOUS VALUES
         IF(TMPREV(IZONE).EQ.0.0) TMPREV(IZONE) = TMP
         IF(HTPREV(IZONE).EQ.0.0) HTPREV(IZONE) = HTC

C------ WALL PROPERTIES
         DELX   = RES(3,IZONE,VOLS(14,KVOL))/(NGRID-1)
         CP     = RES(6,IZONE,VOLS(14,KVOL))
         DENSIT = RES(5,IZONE,VOLS(14,KVOL))
         THCOND = RES(4,IZONE,VOLS(14,KVOL))
         ALPHA  = THCOND/(DENSIT * CP)
         FO     = (ALPHA*DELT)/(DELX*DELX)

C------ BIOT NUMBER FOR GAS AND COOLANT
         BIOTG  = (HTPREV(IZONE)*DELX)/THCOND
         BIOTC  = (RES(1,IZONE,VOLS(14,KVOL))*DELX)/THCOND

C------ POINT 1 REFERS TO THE WALL ADJACENT TO  GAS

         A(1,KVOL) = 0
         B(1,KVOL) = BIOTG*FO + FO + 1.
         C(1,KVOL) = -FO
         D(1,KVOL) = BIOTG*FO*(TMPREV(IZONE)+TMP) +
     1              FO*TSLAB(2,IZONE,KVOL) -
     1              (BIOTG*FO+FO-1.)*TSLAB(1,IZONE,KVOL)

C------ FOR POINTS 2 TO N-1 CONDUCTION COEFFICIENTS ARE USED

         DO 1000 I=2,NGRID-1
           A(I,KVOL) = -FO
           B(I,KVOL) = 2. + 2.*FO
           C(I,KVOL) = -FO
           D(I,KVOL) = FO*(TSLAB(I-1,IZONE,KVOL)+
     1                  TSLAB(I+1,IZONE,KVOL)) +
     1                  (2.-2.*FO)*TSLAB(I,IZONE,KVOL)
 1000    CONTINUE

C------ FOR THE LAST POINT

         A(NGRID,KVOL) = -FO
         B(NGRID,KVOL) = BIOTC*FO + FO + 1.
         C(NGRID,KVOL) = 0.0
         D(NGRID,KVOL) = BIOTC*FO*(2*RES(2,IZONE,VOLS(14,KVOL))) +
     1                  FO*TSLAB(NGRID-1,IZONE,KVOL) -
     1                  (BIOTC*FO+FO-1.)*TSLAB(NGRID,IZONE,KVOL)

C------ USE THOMAS ALGORITHM OF DIRECT ELIMINATION

         BETA(1,KVOL) = B(1,KVOL)
         GAMMA(1,KVOL) = D(1,KVOL)/B(1,KVOL)

       DO 2000 I=2,NGRID
            BETA(I,KVOL) = B(I,KVOL)-(A(I,KVOL)*C(I-1,KVOL))/
     1                     BETA(I-1,KVOL)
            GAMMA(I,KVOL) = (D(I,KVOL)-A(I,KVOL)*
     1                      GAMMA(I-1,KVOL))/BETA(I,KVOL)
 2000    CONTINUE

         TSLAB(NGRID,IZONE,KVOL) = GAMMA(NGRID,KVOL)

C------ BACK SUBSTITUTION

       DO 3000 I=NGRID-1,1,-1
         TSLAB(I,IZONE,KVOL) = GAMMA(I,KVOL)-(C(I,KVOL)*
     1                         TSLAB(I+1,IZONE,KVOL)/
     1                         BETA(I,KVOL))
 3000    CONTINUE

C------ WALL TEMPERATURE
         TWALL = TSLAB(1,IZONE,KVOL)
```

```
C------ SAVE HTC AND TMP FOR NEXT ITERATION
         TMPREV(IZONE) = TMP
         HTPREV(IZONE) = HTC
         RETURN
         END



C       TSLAB.......TEMPERATUTE OF THE WALL GRID                [K]
C       TWALL.......TEMPERATURE OF THE WALL AT THE GAS SIDE     [K]
C       TMP.........GAS TEMPERATURE                             [K]
C       HTC.........COEFFICIENT OF HEAT TRANSFER OF THE GAS     [W/m*2 K]
C       CP..........SPECIFIC HEAT CAPACITY OF THE METAL         [J/kgK]
C       DENSIT......DENSITY OF THE METAL                        [Kg/m*3]
C       THCOND......THERMAL CONDUCTIVITY OF THE METAL           [W/mK]
C       DELX........LENGTH OF SPACE BETWEEN GRIDS               [m]
C       ALPHA.......THERMAL DIFFUSIVITY                         [m2/s]
C       FO..........FOURIER NUMBER
C       KVOL........VOLUME NUMBER
```

APPENDIX B

INPUT DATA AND RESULT FILES

INPUT DATA FILE

```
* TEST 1: PRECHAMBER MODEL:  {bsrun9 speed = 4825
* CONTROL DATA
1                                   /mode
1                                   /reference cylinder
C ncyc step nv nj ns nh ng nht nv
   10 0.25  2  3  1  2  3   2  2
* PRINT AND PLOT CONTROLS
10 10
1 4 0 2 4 0
1 2
1 2 3 4
* VOLUME DATA
0  1  1  1  1 540  4  0  3  11  2  / cylinder
2  2  2  2  1   0  4  0  3  16  0  / swirl chamber
* JUNCTION DATA
8  3  0  1  0  0  0  2  0          / throat
1  1  0  0  0  0  0  1  1          / intake valve
1  2  0  1  0  0  0  0  1          / exhaust valve
* SHAFT DATA
1  0  0
* HEAT RELEASE SETS
1.0   5 300 43e6 18e-6 100 0.0 0.0 0.0   / cylinder heat release
1.0 720  60 43e6  8e-6  20 0.0 0.0 0.0   / swirl chamber heat release
* GEOMETRIC DATA SETS
0.0825  0.08 21.5 0.13  0 0             / cylinder      / bore /stroke / cr /con-rod length
0.000009682 0.00202 0.0124 30 1.5 128    / swirl chamber vol / surf area / rad /swirl/fric
fac/grid
0.0000371 0.0102 0.0083 0.8495 0.000355  / throat eff area / offset / eff dia /sfgrav/thoat
surf area
* CHAMBER SURFACE AREAS AND TEMPERATURES
C heat transfer data for the cylinder
5
C hcool Tcool      x   k    R     Cp    To  factors
    800   353  0.020 160  0.0  0.0050  450     0.70
   2000   353  0.008  50  0.0  0.0050  500     0.00
   2000   353  0.008  50  0.0  0.0189  500     0.02
   2000   353  0.008  50  0.0  0.0189  500     0.06
   2000   353  0.008  50  0.0  0.0189  500     0.08
C heat transfer data for the swirl chamber
3
C hcool Tcool     x     k  rho    Cp  To  zero
   2000   350 0.010 20.94 7800 481.5 423     0
   2000   350 0.008 50.94 7200 480.0 423     0
   2000   350 0.030 20.94 7800 481.5 423     0
* VALVE DATA SETS
C intake
13 0 1 1
350 370 390 410 430 450 470 490 510 530
550 570 590
0 22E-6 133E-6 265E-6 280E-6 319E-6 336E-6 319E-6 283E-6 241E-6
127E-6 23E-6 0
C exhaust
13 0 1 1
130 150 170 190 210 230 250 270 290 310
330 350 370
0 85E-6 213E-6 271E-6 291E-6 299E-6 311E-6 299E-6 291E-6 270E-6
213E-6 86E-6 0

* ENTRY AND EXIT CONDITIONS
.998E+5   299   1.06E+5   299                    * BOUNDARY PRESS AND TEMP
* Initial Shaft Speeds
   4825.000
* Initial Pressure / Temperature / Fuel-Air Ratio
   99511.03   323.6493  6.4224207E-04
   99506.39   772.6531  3.1704837E-02
```

RESULT FILE

```
**************************************************************************
**** SPICE II    ENGINE SYSTEM SIMULATOR ************** UNIVERSITY OF BATH ****
**** Version 1.02    APRIL 1989 ********************************************
**************************************************************************

Date and Time : 12-04-1991     14:53.23          Simulation Mode = 1
Title :
* TEST 1: PRECHAMBER MODEL:  (bsrun9 speed = 4825
Duration of simulation (s)=   0.248705  Thermofluid time step  (s)=   0.000009
Number of control volumes =    2        Number of th'fluid junc's =    3
Number of shafts          =    1
==========================================================================

END-OF-CYCLE SUMMARY OF RESULTS (CYCLE 10)
------------------------------

Cylinders :  1
SIMULATION TIME   0.248705 [SEC]     ELAPSED TIME  16.18 [MIN]
CYLINDERS - 4 STROKE
---------
IMEP BMEP FMEP PMEP  ISFC BSFC  EFFICIENCY  POWER [kW]  VOL.EFFICIENCY SCAV.
       [BAR]          [g/kWh]   b.Th  MECH  IND.  BRAKE  TRAPD O/ALL  RATIO
 8.5  6.0 2.54-1.15 257.0 366.4 22.85 70.14  14.6  10.3  72.9  72.7   0.9972

CYLINDERS
---------
CYL. Pmax & ANG AFtr  Tmax  Tmean hmean    Qw1   Qw2   QW3    QW4   QW5   Qinj
     [BAR]              [K]   [K] [W/m2K]          [J/cycle]
 1    64.   9.8  13.7 2150. 1240.8 410.0    53.   39.   36.    0.    0.   1118.

SWIRL CHAMBER   2
-------------
Vol  Pmax & ANG  AFtr Tmax  mx.swirl mn.swirl  swirl
     [BAR]             [K]      [rev/min]      ratio
 2    73.   8.0  12.5 2813.  382678.  112662.  23.35
Region        Tgmean  hmean     Q      Twmean   Twmax   Twmin   Tcool P.Depth
                [K]   [W/m2K] [J/cyc]    [K]     [K]     [K]     [K]    [mm]
Hot Plug     1582.5 1031.3   15.767   970.7   994.6   961.4   666.5   0.966
Upper Half   1582.5 1031.3   18.893   849.4   868.1   842.9   728.9   1.571
Throat       1480.4 1030.5    3.454  1104.0  1115.6  1093.3   544.7   0.966

COMBUSTION SUMMARY
------------------
VOL. PmID  TmID   ID    ID   Lpipe CAstat  CAinj CAcomb  BETA
    [bar]   [K]  [ms]  [deg]  [m]   [deg]  [deg]  [deg]
 1               0.03   1.00                 4.0    5.0  0.0000

HEAT TRANSFER SUMMARY  New surface temperatures [K]
---------------------
CYL.  PISTON CYL.HD       LINER                    ADDITIONAL AREAS
                    UPPER   MID   LOWER
 1    481.4   542.1  556.7  459.9  408.6    0.0    0.0    0.0    0.0    0.0

ADDITIONAL SYSTEM DATA
----------------------
CYL SHAFT SPEED          VALVE FLOW            INLET...MANIFOLDS...EXHAUST
       [rev/min] INLET [kg/cycle] EXHAUST  NO. P[bar] T[K] NO. P[bar] T[K]
 1    1 4825.00  2   0.00036  3   0.00039  0   0.00   0.00 0   0.00    0.00

JUNCTIONS - Mean Values
---------
JUN.  FLOW    MN.MACH MN.VEL. MN.POWER  EFFIC P-RATIO    MFParam  U/C JUNC.TYPE
     [kg/s]           [m/s]    [kW]
 1  -0.00030  0.0070  -10.6                                          THROAT
 2   0.01448  0.6748  218.8                                          VAR.AREA
 3   0.01553  0.8222  577.2                                          VAR.AREA

SHAFTS - Mean Values
------
SHAFT     TORQUE VALUES   [Nm]     POWER TRANSMITTED [kW]  MN.SPEED   MN.ACCEL
 NO.    NET     INPUT    OUTPUT     NET    INPUT  OUTPUT  [rev/min] [rev/min/s]
 1       0.0      0.0       0.0     0.00    0.00    0.00    4825.0  0.0000E+00

SYSTEM MASS BALANCE                  SYSTEM ENERGY BALANCE  [J]       [%]
-------------------                  ---------------------
AIR ENTERING SYSTEM    = 0.00036016  ENERGY OF FUEL        1117.8    100.00
FUEL ENTERING SYSTEM   = 0.00002599  ENERGY TO EXHAUST      589.2     52.71
EXHAUST LEAVING SYSTEM = 0.00038622  ENERGY TO COOLANT      165.3     14.79
       MASS BALANCE    = 0.9998      USEFUL WORK            255.4     22.85
                                     FRICTION WORK          108.7      9.73
                                     INTERCOOLERS             0.0      0.00
                                     SHAFT LOSSES             0.0      0.00
                                     ENERGY BALANCE   =       0.9992
```

```
INITIAL CONDITIONS - FOR RESTART
--------------------
* Initial Shaft Speeds
    4825.00
* Initial Pressure / Temperature / Fuel-Air Ratio
    79540.5     349.864     1.17928E-03
    79387.1     709.271     4.16002E-02
```